

CONFERENCE PROGRAMME

All speakers will have 15 minutes to give their presentation. There will be 3-4 minutes available for questions following each presentation. Presenters are asked to contact the support staff (these will be made known to you) well in advance of their presentation slot so that any files can be up-loaded onto the AV system. Maybe not everyone will want to use computer-generated slides; we very much welcome seeing hand-drawn presentations using coloured marker pens in the style of Mike Crisfield. The sessions have purposefully been arranged to embrace diverse topics such that we are exposed to a variety of analysis methods, numerical techniques and engineering applications.

WEDNESDAY 10TH APRIL 2019 P1-P10 B200

- 12:30-1:30pm *Registration (Main Entrance Northampton Square, EC1V 0HB) and Lunch*
- 1:30-1:40 Welcome and Introduction

P1 1:40-2:00 Chris Pearce (Glasgow) *Fracture Propagation in Nuclear Graphite*

P2 2:00-2:20 Carlos Azua-Gonzalez (Cardiff) *A combined Micromechanics Strong-Discontinuity approach for Modelling Distributed and Localised Fracture in Cementitious Materials*

P3 2:20-2:40 Jinlong Fu (Swansea) *Resolution Effect: An Error Correction Model for Intrinsic Permeability of Sandstones Estimated from Lattice Boltzmann Method*

P4 2:40-3:00 Emilio Martinez Paneda (Cambridge) *Phase Field Modelling of Hydrogen Assisted Cracking*

- 3:00-3:30 *Tea*

P5 3:30-3:50 Stephen Smith (Queen's Belfast) *Simulating A Large Deformation Forming Processes using a Meshfree Method based on a Total-Lagrangian Kernel*

P6 3:50-4:10 Chennakesava Kadapa (Swansea) *Novel Unified Finite Element Schemes for Computational Solid Mechanics based on Bézier Elements*

P7 4:10-4:30 Ahmed Abdulaziz (Cardiff) *Parametric Study of Honeycomb Composite Structure using Open Source Finite Element Software*

P8 4:30-4:50 Alireza Ahangar Asr (Salford) *The Joint Influence of the Presence of Cavities and Rapid Drawdown on the Discharge Rate through Earth Dams*

P9 4:50-5:10 Chrysanthi Stropouli (City) *An Aerostatic Approach to Include the Effect of Adaptable Wind Barriers in Wind-Vehicle-Bridge Interaction Analysis*

P10 5:10-5:30 Ganesh Diwan (UCL) *Computational Studies on the Acoustics of the Womb*

- 5:30-6:30 *UKACM Executive Committee Meeting*

THURSDAY 11TH APRIL P11-P31 B200

- P11 8:40-9:00 Mokarram Hossain (Swansea) *Experimental Characterization and Constitutive Modelling of Transparent Polyurethane*
- P12 9:00-9:20 Thomas Adams (Durham) *An hp-Adaptive Discontinuous Galerkin Level Set Method*
- P13 9:20-9:40 Ashutosh Bhokare (Swansea) *Numerical Analysis of SCC Flow: The Bingham Model and Beyond*
- P14 9:40-10:00 Lok Chan (Exeter) *Optimisation of a Conceptual Aircraft Model using a Genetic Algorithm and 3D CFD*
- P15 10:00-10:20 Peter Grassl (Glasgow) *On the Influence of Fibres on Tensile Laps of Reinforcement Loops*
- 10:20-10:40 *Tea*
- P16 10:40-11:00 Twana Kamal Haji (Birmingham) *Challenges Associated with Finite Element Methods for Forward Modelling of Unbounded Gravity Fields*
- P17 11:00-11:20 Mebratu Wakeni (Glasgow) *Modelling and Computation of the Thermoelastic Response of the Skin at Finite Strains with Non-Fourier Effects*
- P18 11:20-11:40 Rui Zhang (Sheffield) *Use of Non-Linear Failure Criteria to Extract Stress Data from Upper Bound Plasticity Solutions*
- P19 11:40-12:00 Ge Yin (Cambridge) *Cad-Compatible Structural Topology Optimisation*
- P20 12:00-12:20 Jinsheng Wang (Swansea) *An Efficient Algorithm that combines Surrogate Model and Maximum Entropy Method for Structural Reliability Analysis*
- 12:30-1:20 *Lunch (UKACM Board Meeting)*
- P21 1:20-1:40 Andrei Shvarts (Glasgow) *FEM Implementation for Navier-Stokes Equations for an Incompressible Steady Flow using Hierarchical Basis Functions*
- P22 1:40-2:00 Abdul Majid (Karachi) *Simulation of Soap Film with Flexible Boundary*
- P23 2:00-2:20 Zhi Li (Swansea) *An Unsymmetric Solid-Shell Element for Geometric Nonlinear Analysis*
- P24 2:20-2:40 Mohammad Khanjanpour (Exeter) *An Investigation of a γ -type MTD Stirling Engine Prototype*
- P25 2:40-3:00 Prashant Saxena (Glasgow) *Instabilities in the Deformation of Magnetoelastic Membranes*
- 3:00-3:30 *Tea*
- P26 3:30-3:50 Ignatios Athanasiadis (Glasgow) *Mortar Contact Formulation for Hierarchical Basis Functions using Smooth Active Set Strategy*
- P27 3:50-4:10 Mohammad Akrami (Exeter) *Analysing Greenhouse Ventilation using CFD*
- P28 4:10-4:30 Yanan Sun (Swansea) *An Investigation of Stepwise Crack Tip Advancement*
- P29 4:30-4:50 Liang Yang (Imperial) *Unified One-Fluid Formulation for Multibody Dynamics and Multiphase Flow Interaction*
- P30 4:50-5:10 Zhaowei Liu (Glasgow) *Topology Optimisation of Sound Absorbing Materials using an Isogeometric Boundary Element Method through Subdivision Surfaces*
- P31 5:10-5:30 Savvas Triantafyllou (Nottingham) *A Material Point Method for the Robust Simulation of Rocking Induced Damage*
- 6:30-7:00 *Reception Goldsmiths' Hall (15 minutes walk from the University)*
 - 7:00-9:00 *Conference Dinner Goldsmiths' Hall*

FRIDAY 12TH APRIL P32-P51 B200

- P32 8:40-9:00 Yew Wong (City) *Layered-Shell NLFEM of the Nearly Incompressible Orthotropic Myocardium*
- P33 9:00-9:20 Nur Hashim (Durham) *An Implicit Non-Ordinary State-Based Peridynamics for Large Deformation Analysis*
- P34 9:20-9:40 Matthew Ellison (Exeter) *Developing a Finite Element Model to Investigate Second Metatarsal Stress During Running*
- P35 9:40-10:00 Jovana Veletic (City) *On the Use of Hierarchical Sub-Structuring for the FEA of Tall Slender Buildings*
- P36 10:00-10:20 Neeraj Chakshu (Swansea) *Combining Computational Mechanics and Machine Learning Techniques to Calculate Fractional Flow Reserve*
- P37 10:20-10:40 Lucasz Kaczmarczyk (Glasgow) *Mixed Formulation with Stresses in h -div Space for Large Strains*
- 10:40-11:00 *Tea*
- P38 11:00-11:20 Antonis Zervos (Southampton) *Some Effects of Particle Shape on the Mechanical Behaviour of Granular Materials*
- P39 11:20-11:40 Sizeng You (Swansea) *Establishment and Application of the Quantified Relationship between Concrete Properties and Workability Tests*
- P40 11:40-12:00 Eky Febrianto (Cambridge) *Immersed B-Spline Finite Elements for Complex Geometries*
- P41 12:00-12:20 Qili Fang (Imperial) *Resolution of Discontinuity in Shell Models of Folded Plates*
- 12:30-1:20 *Lunch*
- P42 1:20-1:40 Lei Fan (Durham) *The Local Maximum Entropy Point Collocation Approach for Membrane Analyses*
- P43 1:40-2:00 Sanjay Komala Sheshachala (Swansea) *A Complementary Low and High Order Scheme for Unsteady Flow Simulations in Coarse Meshes*
- P44 2:00-2:20 Karol Lewandowski (Glasgow) *Modelling of Crack Propagation in Heterogeneous Materials Like Bones*
- P45 2:20-2:40 Daniel Thomson (Oxford) *A Study on Fibre Kinking Criteria for Unidirectional CFRPs under Off-Axis Compression at Quasi-Static and Dynamic Loading Rates*
- P46 2:40-3:00 Lei Wang (Durham) *On Improving the Accuracy of the Material Point Method with Simplex Elements*
- 3:00-3:30 *Tea*
- P47 3:30-3:50 Hoang Nguyen (Glasgow) *Vibrational Behaviours of Small-Scale Structures using Gradient Elasticity*
- P48 3:50-4:10 Antonios Parasyris (Loughborough) *Mathematical and Numerical Modelling of a Water Purification System*
- P49 4:10-4:30 Yuxuan Chen (Cambridge) *A Multigrid Approach that is Robust with respect to Mesh Quality*
- P50 4:30-4:50 Tim Charlton (Durham) *Development of a Constitutive Model for Modelling Wind Turbine Foundations in Unsaturated Soils*
- P51 4:50-5:10 Sathiskumar Anusuya Ponnusami (City) *Computationally-Derived Design Guidelines and Crack Healing Models for Self-Healing Materials*
- 5:10-5:15 *Closure*

CONFERENCE ATTENDEES

Thomas Adams	Durham	Chennakesava Kadapa	Swansea
Alireza Ahangar Asr	Salford	Mohammad Khanjanpour	Exeter
Katsuhiko Akahori	iKlKA LLC	Sanjay Komala Sheshachala	Swansea
Mohammad Akrami	Exeter	Omar Laghrouche	Heriot-Watt
Ahmed Abdulaziz	Cardiff	Karol Lewandowski	Glasgow
Sathiskumar Anusuya Ponnusami	City	Rhydian Lewis	Swansea
Ignatios Athanasiadis	Glasgow	Zhi Li	Swansea
Charles Augarde	Durham	Zhaowei Liu	Glasgow
Carlos Azua-Gonzalez	Cardiff	Abdul Majid	Karachi
Ashutosh Bhokare	Swansea	Emilio Martinez Paneda	Cambridge
Alfredo Camara	City	Hoang Nguyen	Glasgow
Neeraj Chakshu	Swansea	Antonios Parasyris	Loughborough
Christophe Chalons-Mouriesse	Glasgow	Chris Pearce	Glasgow
Lok Chan	Exeter	Giuliano Pretti	Durham
Tim Charlton	Durham	Prashant Saxena	Glasgow
Yuxuan Chen	Cambridge	Rubén Sevilla	Swansea
William Coombs	Durham	Andrei Shvarts	Glasgow
Roger Crouch	City	Stephen Smith	Queen's Belfast
Ganesh Diwan	UCL	Chrysanthi Stropmouli	City
Olga Doeva	Limerick	Yanan Sun	Swansea
Matthew Ellison	Exeter	Daniel Thomson	Oxford
Lei Fan	Durham	Savvas Triantafyllou	Nottingham
Qili Fang	Imperial	Zahur Ullah	Queen's Belfast
Asaad Faramarzi	Birmingham	Jovana Veletic	City
Eky Febrianto	Cambridge	Mebratu Wakeni	Glasgow
Jinlong Fu	Swansea	Jinsheng Wang	Swansea
Peter Grassl	Glasgow	Lei Wang	Durham
Twana Haji	Birmingham	Yew Wong	City
Nahiene Hamila	INSA Lyon	Liang Yang	Imperial
Nur Hashim	Durham	Ge Yin	Cambridge
Mokarram Hossain	Swansea	Sizeng You	Swansea
Anthony Jefferson	Cardiff	Antonis Zervos	Southampton
Lucasz Kaczmarczyk	Glasgow	Rui Zhang	Sheffield

FRACTURE PROPAGATION IN NUCLEAR GRAPHITE

*Chris J. Pearce¹, Hoang Nguyen¹ and Lukasz Kaczmarczyk¹

¹Glasgow Computational Engineering Centre, School of Engineering, University of Glasgow

*chris.pearce@glasgow.ac.uk

Summary

This paper presents an enhanced theoretical formulation and associated computational framework for brittle fracture in nuclear graphite within the context of configurational mechanics. A new condition for crack front equilibrium is exploited that leads to an implicit crack propagation formulation. This paper focuses on an extension of our previous work, whereby the complex internal stress state in a nuclear reactor is the primary driver for crack propagation in individual graphite bricks. The resulting crack path is resolved as a discrete displacement discontinuity, where the material displacements of the nodes on the crack front change continuously, without the need for enrichment techniques. Performance of the formulation is demonstrated by means of a representative numerical simulation, demonstrating both accuracy and robustness.

Key Words: *fracture propagation; configurational mechanics; graphite; internal stresses*

Introduction

Understanding the behaviour of Advanced Gas-Cooled Reactor (AGR) graphite cores with multiple cracked bricks is paramount to the assessment of structural integrity, safe operation and life extension. In this paper, the latest developments in the finite element modelling and simulation of crack propagation in graphite bricks are briefly presented.

Configurational mechanics (CM) provides the theoretical basis for our work on crack propagation. This approach has a strong physical motivation, exploiting the 1st and 2nd laws of thermodynamics to establish crack front equilibrium and the crack path direction. The authors have also developed the numerical techniques to implement this theory within a finite element analysis software framework (MoFEM[9]). This provides the ability to simulate propagating cracks in 3D solids that are discretely and continuously resolved by adapting the FE mesh in a smooth manner (exploiting the crack front equilibrium condition), thereby avoiding the need for enrichment.

CM dates back to the original work of Eshelby and his study of forces acting on material defects [1]. The concept of configurational (or material) forces is now a well established method to evaluate defects in a material providing a unified framework for the analysis of material imperfections and has been adopted by, amongst others, Maugin [2]. Steinmann [3] developed a computational strategy for the assessment of fractured bodies. Miehe et al. [4, 5] and Kaczmarczyk et al. [6, 8] built on this work to establish a finite element methodology for crack propagation.

Crack Propagation Problem

To formulate the crack propagation problem within the framework of configurational mechanics, two related kinematic descriptions are defined in the spatial and material settings. In the former, the classical conservation law of linear momentum balance is described, where Newtonian forces are work conjugate to changes in the spatial position, at fixed material position (i.e. no crack propagation). In the material setting, which represents a dual to the spatial setting, an equivalent conservation law is described, where configurational forces are conjugate to changes in material position but with no spatial motion. This decomposition of the behaviour is proven to be a simple but powerful methodology for describing crack propagation. The authors' previous paper [6] describes the mathematical formulation for crack propagation and a methodology for resolving the evolving crack path within the context of

the finite element method, and represented an advancement of the work of Miehe et al. [4, 5]. The current paper briefly explains how this previous work has been extended for internal stresses as the driver for crack propagation.

Key features of our work to date include:

- Griffith's fracture criterion is expressed correctly in terms of configurational forces.
- An expression for equilibrium of the crack front is established, balancing the configurational forces on the crack front with the resistance of the material. This is exploited so that the crack front can advance continuously.
- To maintain mesh quality, a mesh smoothing strategy, with surface constraints, is presented as a continuous process as part of a problem-tailored Arbitrary Lagrangian Eulerian formulation.
- The spatial and material displacement fields are both discretised using the same finite element mesh, although we adopt different levels of approximation for the two fields.
- The resulting discretised weak form of the two conservation equations represent a set of coupled, nonlinear, algebraic equations that is solved in a monolithic manner using a Newton-Raphson scheme.
- An arc-length method is adopted to trace the dissipative load path for brittle fracture propagation, using crack area rather than displacements as a control.

The current material coordinates \mathbf{X} are mapped onto the spatial coordinates \mathbf{x} via the familiar deformation map $\varphi(\mathbf{X}, t)$. The physical displacement is:

$$\mathbf{u} = \mathbf{x} - \mathbf{X} \quad (1)$$

$\Xi(\chi, t)$ maps the reference material coordinates χ on to the current material coordinates \mathbf{X} , representing a configurational change, i.e. extension of the crack due to advancement of the crack front. Φ maps the reference material coordinates χ on to the spatial coordinates \mathbf{x} . The current material and spatial displacement fields are given as:

$$\mathbf{W} = \mathbf{X} - \chi \quad \text{and} \quad \mathbf{w} = \mathbf{x} - \chi \quad (2)$$

Finite element approximation is applied to the displacements in both the current material and physical spaces. Three-dimensional domains are discretised with tetrahedral finite elements. In the spatial domain, hierarchical basis functions of arbitrary polynomial order are applied, following the work of Ainsworth and Coyle [7]. This enables the use of elements with variable, non-uniform orders of approximation, with conformity enforced across element boundaries. In the material domain, linear approximation is adopted, as this is sufficient for describing the crack front.

Kaczmarczyk et al. [8] derived a new expression for equilibrium of the crack front:

$$\dot{\mathbf{W}} \cdot (\gamma \mathbf{A} - \mathbf{G}) = 0 \quad (3)$$

where γ is the surface energy, \mathbf{A} is a dimensionless kinematic state variable that defines the current orientation of the crack front [6, 8] and \mathbf{G} is the configurational force calculated as the integral of the Eshelby stress Σ around the crack front:

$$\mathbf{G} = \lim_{|\mathcal{L}_n| \rightarrow 0} \int_{\mathcal{L}_n} \Sigma \mathbf{N} \, dL \quad (4)$$

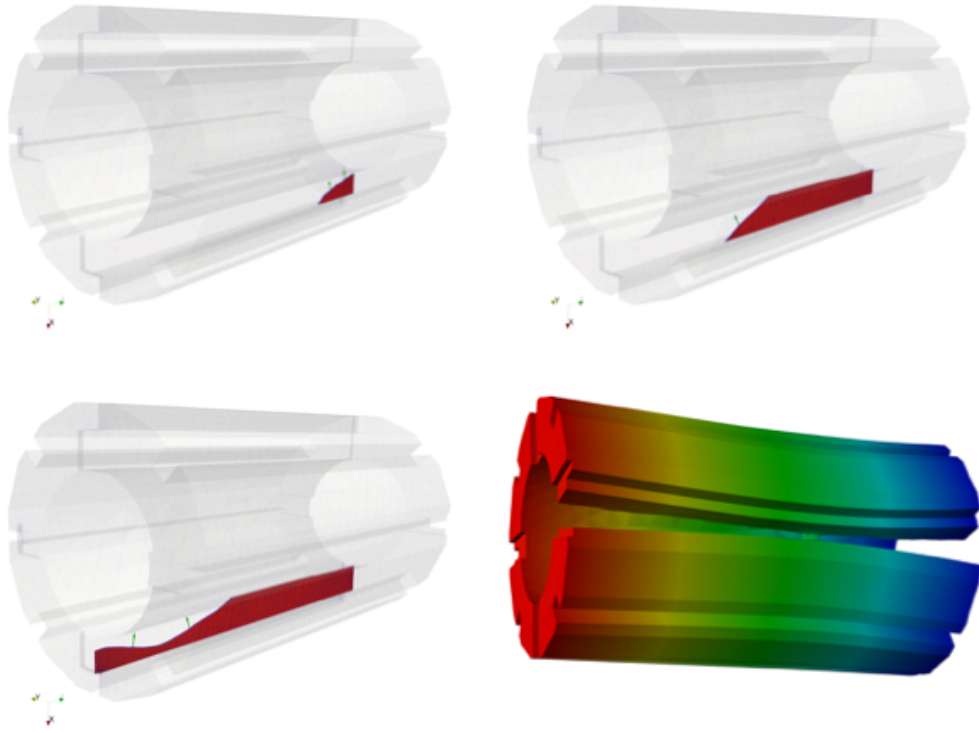


Figure 1: Progression of keyway root crack driven by internal stresses.

where This crack front equilibrium condition balances the configurational forces on the crack front with the resistance of the material. This is exploited so that the crack front can advance continuously, re-establishing the crack front to the physically correct position each load step, without recourse to any kind of crack tracking algorithm, and without influence from the finite element mesh.

Internal stress driven crack propagation

To account for the influence of internal stresses, the residual, discretised equations for spatial and material equilibrium are modified to become:

$$\mathbf{r}_s = \mathbf{f}_{s,int} - \mathbf{f}_{s,ext} + \lambda \mathbf{F}_r \quad (5)$$

$$\mathbf{r}_m = \mathbf{G} - \mathbf{f}_{m,res} + \lambda \mathbf{G}_r \quad (6)$$

$\mathbf{f}_{s,int}$ and $\mathbf{f}_{s,ext}$ are the standard vectors of nodal spatial internal and external forces. $\mathbf{f}_{m,res}$ is the material resistance, which is a function of the surface energy and the crack front orientation. λ is the load factor. \mathbf{F}_r and \mathbf{G}_r are additional terms that are included in the equilibrium equations to account for the internal stresses.

Numerical example

An example of a keyway root crack in a nuclear graphite brick, driven by internal stresses, is shown in the figure. The stress state is the result of operating at full power of 30 years. The crack is initiated at one end of the brick at a keyway root. The brick is only restrained to remove rigid body motion. The crack front advances simultaneously inwards to the free surface of the bore and along the length of the brick. Young's modulus, $E = 9600$ MPa, Poisson's ratio, $\nu = 0.2$, and fracture energy, $\gamma = 145$ J/m². The analysis was undertaken using MoFEM[9].

Conclusions

A novel formulation for brittle fracture in elastic solids within the context of configurational mechanics has been presented for the prediction of crack paths in nuclear graphite. The previous formulation [6, 8] has been extended to account for internal stresses as a driver for crack propagation. The formulation has been tested on single graphite brick subjected to internal stresses.

Acknowledgements

This work was supported by EDF Energy Nuclear Generation Ltd and The Royal Academy of Engineers. The views expressed in this paper are those of the authors and not necessarily those of EDF Energy Nuclear Generation Ltd.

References

- [1] J.D. Eshelby, *The force on an elastic singularity*, Philosophical Transactions of the Royal Society London A , 224, 87-112, 1951.
- [2] G.A. Maugin, *Material Inhomogeneities in Elasticity*, Chapman & Hall, London, 1993.
- [3] P. Steinmann, *Application of material forces to hyperelastic fracture mechanics. I. Continuum mechanical setting*, International Journal of Solids & Structures, 37, 7371-7391, 2000.
- [4] C. Miehe, E. Gürses and M. Birkle, *A computational framework of configurational-force-driven brittle fracture propagation based on incremental energy minimization*, International Journal of Fracture, 145, 245-259, 2007.
- [5] E. Gürses and C. Miehe, *A computational framework of three-dimensional configurational-force-driven brittle crack propagation*, Computer Methods in Applied Mechanics and Engineering, 198, 1413-1428, 2009.
- [6] Ł. Kaczmarczyk, M. Mousavi Nezhad, C.J. Pearce, *Three-dimensional brittle fracture: configurational-force-driven crack propagation*, International Journal of Numerical Methods in Engineering, 97, 531-550, 2012.
- [7] M.A. Ainsworth and J. Coyle, *Hierarchic finite element bases on unstructured tetrahedral meshes*, International Journal for Numerical Methods in Engineering, International Journal for Numerical Methods in Engineering, 58:14. 2103–2130, 2003.
- [8] Ł. Kaczmarczyk, Z. Ullah and C.J. Pearce, *Energy consistent framework for continuously evolving 3D crack propagation*, Computer Methods in Applied Mechanics and Engineering, 324, 54-73, 2017.
- [9] L. Kaczmarczyk, et al., *MoFEM [Computer Software]*, <https://doi.org/10.5281/zenodo.438712>.

COMPUTATIONAL STUDIES ON THE ACOUSTICS OF WOMB

*Ganesh C. Diwan¹, Eric Jauniaux², Julian Henriques³, Aude Thibaut⁴ and Pierre G lat⁵

¹Medical Physics and Biomedical Engineering, UCL, Gower Street, London WC1E 6BT.

²Institute for Womens Health, UCL, London WC1E 6AU.

³Goldsmiths, University of London, London SE14 6NW.

⁴Sonic Womb Productions Ltd, London.

⁵Department of Mechanical Engineering, UCL, Gower Street, London WC1E 6BT.

*g.diwan@ucl.ac.uk

Summary

A better understanding of the fetal auditory environment is critical for pregnant mothers to avoid exposing their babies to damaging levels of noise. After birth, when caring for premature neonates, exposure to non-physiological noise is also considered an environmental risk factor. For biomedical engineers, it is paramount to design incubators that reduce noise and simulate the physiological acoustic environment *in utero*. This research work focuses on the development and validation of computational models describing the propagation of acoustic waves from external sources into the womb, in view of helping to quantify their effects on the developing fetus. The propagation of acoustic waves is governed by the well-known Helmholtz equation. The numerical solution of the Helmholtz equation is a computationally challenging task. Complex interfaces/anatomical features (such as different tissue types with varying density and sound speed) lead to multiple scattering effects and attenuation of sound waves. We study the sound pressure levels experienced inside the womb due to plane incident acoustic field. The computational results confirm the findings of *in vivo* measurements on pregnant sheep and indicate that the womb/abdomen system undergoes resonant behaviour at frequencies within the human audio range.

Key Words: *in utero Acoustics, Finite Element Method, Helmholtz equation, Attenuation*

Introduction

The auditory development of the fetus starts as early as 12 weeks into gestation and takes place in two stages viz. structural changes in the inner ear followed by development of the peripheral sensory system [1]. These stages are highly dependent on the external auditory stimulus a fetus receives during gestation and even after birth. The external noise is in most cases unavoidable and aside from hearing damage in the fetus [2] could lead to serious health conditions and in the pregnant mother, such as cardiovascular diseases, sleep disorder and hypertension [3]. The public is routinely exposed to equivalent continuous sound pressure levels in excess of 85 dBA, see [4] for an overview of noise related morbidity. In the case of infants under care in a Neonatal Intensive Care Unit (NICU), it has long been argued that developmental problems experienced at the school-going age may be related to the exposure to unwanted noise levels at the NICU [5]. For biomedical engineers, it is therefore important to better understand the fetal auditory environment for developing incubators with better acoustical properties. There have been several studies attempting to quantifying the *in utero* acoustical environment using ovine models [6]. The experiments in [7] indicate on average an attenuation of 3 dBA above 10 kHz. Frequencies between 100-1000 Hz have also been reported to undergo low levels of attenuation, whereas frequencies between 1000 Hz and 10 kHz are attenuated by up to 6 to 10 dB. Setting up experiments on pregnant animals is a time consuming, costly and complex procedure, with ethical ramifications. Measured quantities are dependent on the position of hydrophones, the sensitivity and bandwidths of microphones/loudspeakers, hence generating uncertainties in attenuation estimates. In this study, we develop a finite element model for *in utero* acoustics to provide further insight into the propagation of incident sound fields into the womb across the human audio range.

Equations

Consider Ω to be an open bounded domain in \mathbb{R}^3 where $\partial\Omega$ is the domain boundary. We consider the time harmonic wave problem where the scalar acoustic potential, ϕ is governed by the Helmholtz equation in Ω subject to some boundary conditions: find $\phi \in H^1(\Omega)$ s.t.,

$$\rho \nabla \cdot \left(\frac{1}{\rho} \nabla \phi \right) + k^2 \phi = 0, \quad \text{in } \Omega \quad (1)$$

$$\frac{\partial \phi}{\partial \mathbf{n}} + \beta \phi = g \quad \text{on } \partial\Omega, \quad (2)$$

where $k = 2\pi f/c$ is the wavenumber with f being the frequency of the time-harmonic wave, c as the wave speed and ρ the density of medium. Also, \mathbf{n} is the unit outward normal on $\partial\Omega$ and β is chosen such that it the Sommerfeld's radiation condition can be approximately satisfied. Clearly, the variational statement for (2) is, find $\phi \in H^1(\Omega)$, s.t.,

$$\int_{\Omega} \left(\frac{1}{\rho} \nabla \phi \nabla \bar{\psi} - \frac{1}{\rho} k^2 \phi \bar{\psi} \right) d\Omega + \beta \int_{\Gamma} \frac{1}{\rho} \phi \bar{\psi} d\Gamma = \int_{\Gamma} \frac{1}{\rho} g \bar{\psi} d\Gamma, \quad \forall \psi \in H^1(\Omega). \quad (3)$$

For a discrete space $V_h \subset H^1(\Omega)$, the finite element method is given by, find $\phi_h \in V_h$, s.t.,

$$\int_{\Omega} \left(\frac{1}{\rho} \nabla \phi_h \nabla \bar{\psi} - \frac{1}{\rho} k^2 \phi_h \bar{\psi} \right) d\Omega + \beta \int_{\Gamma} \frac{1}{\rho} \phi_h \bar{\psi} d\Gamma = \int_{\Gamma} g \bar{\psi} d\Gamma, \quad \forall \psi \in V_h. \quad (4)$$

Let $\{\mathcal{N}_A, A = 1, \dots, N\}$, be the set of N basis functions whose linear combination forms the discrete space V_h (i.e. $\dim(V_h) = N$). Thus, letting $\phi_h = \sum_{A=1}^N \phi_A \mathcal{N}_A$, we get

$$\sum_{A=1}^N \phi_A \left[\int_{\Omega} \left(\frac{1}{\rho} \nabla \mathcal{N}_A \nabla \bar{\psi} - \frac{1}{\rho} k^2 \mathcal{N}_A \bar{\psi} \right) d\Omega + \beta \int_{\Gamma} \frac{1}{\rho} \mathcal{N}_A \bar{\psi} d\Gamma \right] = \int_{\Gamma} \frac{1}{\rho} g \bar{\psi} d\Gamma, \quad \forall \psi \in V_h. \quad (5)$$

Clearly, (5) is true for any $\psi \in V_h$, therefore, it must also be true for all the basis functions, say $\mathcal{N}_B, B = 1, \dots, N$ that form the space V_h . Therefore,

$$\sum_{A=1}^N \phi_A \int_{\Omega} \left(\frac{1}{\rho} \nabla \mathcal{N}_A \nabla \bar{\mathcal{N}}_B - \frac{1}{\rho} k^2 \mathcal{N}_A \bar{\mathcal{N}}_B \right) d\Omega + \beta \int_{\Gamma} \frac{1}{\rho} \mathcal{N}_A \bar{\mathcal{N}}_B d\Gamma = \int_{\Gamma} \frac{1}{\rho} g \bar{\mathcal{N}}_B d\Gamma, \quad \text{for } B = 1, \dots, N \quad (6)$$

To implement (6), we define \mathcal{T}_h to be a set of decompositions dividing Ω into non-overlapping and non self-intersecting elements where h is the diameter of any $E \in \mathcal{T}_h$. Rewriting (6) in matrix notation

$$\mathbf{A} \mathbf{u} = \mathbf{f} \quad (7)$$

where, \mathbf{A} is called the global coefficient matrix, \mathbf{f} the global load vector and \mathbf{u} the global solution vector. Note that the matrix $\mathbf{A} \in \mathbb{C}^{N \times N}$ is complex valued non-Hermitian, sparse symmetric matrix and is generally indefinite for large values of wavenumber k .

Numerical studies

We consider a computational model built with anatomical scans of a pregnant mother with 20 weeks of pregnancy. The finite element meshes for the model are obtained by performing the image segmentation

on the MRI scans and a representative mesh is shown in Figure 1a. Note that since we need to solve an exterior acoustic scattering problem, we use the first order Bayliss-Gunzburger-Turkel (BGT) approximation for $\beta = ik - \frac{1}{2R}$ where R is the radius of the truncation boundary, see [8]. For the 3D problems in the current case, $\partial\Omega$ is a sphere of radius R . The computational model contains the uterus as the inner most region which is embedded inside the abdominal cavity. A sphere of radius R filled with air is used to represent the homogeneous exterior medium. The physical properties of different fluid regions are given in Figure 1. We consider a plane wave $\phi^{inc} = e^{ikx}$ with $i = \sqrt{-1}$ impinging upon the configuration shown in Fig. 1a. The radius R is chosen such that at any given frequency, the sphere boundary is always one wavelength in air away from the scattering object, in this case the abdominal wall. A better approximation for Sommerfeld's radiation condition is of course possible in the form of higher order NRBC or Perfectly Matched Layer (PML) etc. However, we chose the first order condition for the current problem as the convergence studies for canonical scattering problems show between 6-8% errors in the numerical solution. Figures 1b-1c show the magnitude of acoustic pressure $p = -2\pi i \rho \phi f$ for the considered incident wave. We consider $f = 9000$ Hz and 10040 Hz. We chose these values as the wavelength in uterine tissue at these frequencies is very close to the length scale of the uterus. The maximum of the acoustic pressure magnitude is close to 0.16 Pa or 67.4 dB¹ at 9000 Hz. However, at 10040 Hz, the maximum pressure magnitude inside the abdomen (see Fig 1c) is almost 40 times higher than at 9000 Hz, i.e. 6.1 Pa or 99 dB. Although we have not taken into account the natural acoustic damping present in tissue, the experimental studies on pregnant sheep indicate peaks in the acoustic response around 10000 Hz. This indicates that at certain frequencies well within the human audio range, the acoustic pressure may undergo amplification. See Table 1 for attenuation levels in dB with reference to the incident field.

Frequency	9000	9489	10040	10346	11387
Uterus in air (dB)	-18.4	1.03	-18	-18	-16
Uterus in abdomen (dB)	-16.1	-13.5	16.6	8.5	27.7

Table 1: Attenuation levels (dB) with reference to incident field

A modal analysis of the uterus and abdomen shows that there are several modes between 9000 to 12000 Hz viz. 9867.5 Hz, 10153.96 Hz and 10376.55 Hz. One of the possible explanations for this effect therefore is that the natural modes of the uterus and abdomen model being excited by the incident wave.

Conclusions

We have developed a finite element model to study womb acoustics, based on the Helmholtz equation with a first order absorbing condition. The computational results and the experiments support the hypothesis of resonant behavior reported in [6, 9]. However, to achieve better accuracy, improved NRBCs need to be implemented. The resonant behaviour of womb can result in unphysical pressure amplitudes if the attenuation effects are not considered. Therefore, future work will involve incorporating physical effects such as attenuation (i.e. complex wave number) and additional soft tissue and bone domains. The work is in progress to acquire anatomical meshes of pregnant women at various stages of pregnancy.

¹dB relative to the incident field magnitude

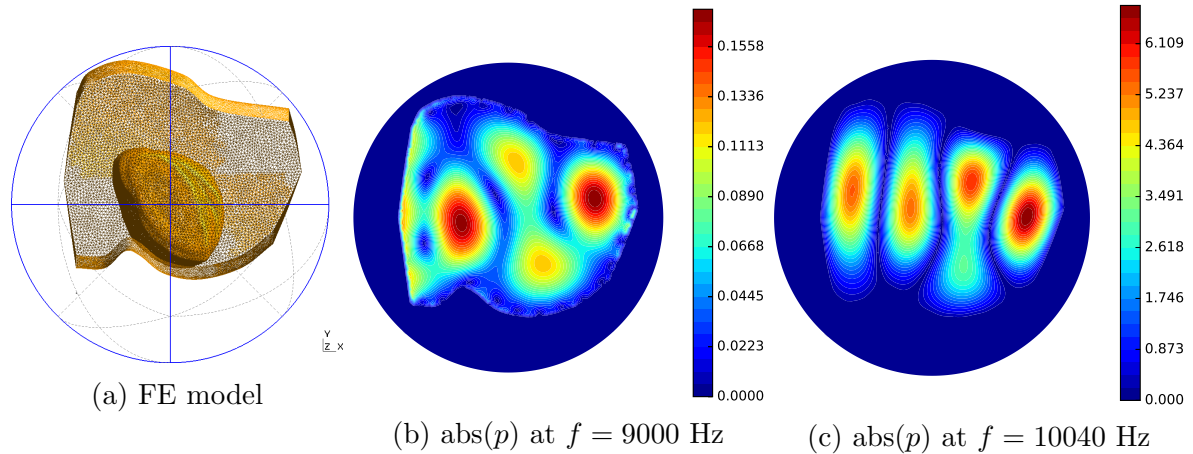


Figure 1: Acoustic scattering from uterus and abdomen in air, $c_{air} = 340$ m/s, $c_{abdomen} = 1440$ m/s, $c_{uterus} = 1500$ m/s, $\rho_{air} = 1.2$ kg/m³, $\rho_{uterus} = \rho_{abdomen} = 1000$ kg/m³. Uterus dimensions: 16 cm \times 18 cm \times 12 cm.

References

- [1] Peter G Hepper and B Sara Shahidullah. The development of fetal hearing. *Fetal and Maternal Medicine Review*, 6(3):167–179, 1994.
- [2] Mathias Basner, Wolfgang Babisch, Adrian Davis, Mark Brink, Charlotte Clark, Sabine Janssen, and Stephen Stansfeld. Auditory and non-auditory effects of noise on health. *The Lancet*, 383(9925):1325 – 1332, 2014.
- [3] Thomas Münzel, Tommaso Gori, Wolfgang Babisch, and Mathias Basner. Cardiovascular effects of environmental noise exposure. *European heart journal*, 35(13):829–836, 2014.
- [4] Mark P Matheson and Stephen A Stansfeld. Noise pollution: non-auditory effects on health. *British Medical Bulletin*, 68(1):243–257, 12 2003.
- [5] Amanda J Symington and Janet Pinelli. Developmental care for promoting development and preventing morbidity in preterm infants. *Cochrane database of systematic reviews*, (2), 2006.
- [6] Kenneth J Gerhardt and Robert M Abrams. Fetal hearing: characterization of the stimulus and response. In *Seminars in perinatology*, volume 20, pages 11–20. Elsevier, 1996.
- [7] Jean-Pierre Lecanuet, Bernard Gautheron, Alain Locatelli, Benoist Schaal, Anne-Yvonne Jacquet, and Marie-Claire Busnel. What sounds reach fetuses: biological and nonbiological modeling of the transmission of pure tones. *Developmental Psychobiology: The Journal of the International Society for Developmental Psychobiology*, 33(3):203–219, 1998.
- [8] Alvin Bayliss, Max Gunzburger, and Eli Turkel. Boundary conditions for the numerical solution of elliptic equations in exterior regions. *SIAM Journal on Applied Mathematics*, 42(2):430–451, 1982.
- [9] Joanna J Parga, Robert Daland, Kalpashri Kesavan, Paul M Macey, Lonnie Zeltzer, and Ronald M Harper. A description of externally recorded womb sounds in human subjects during gestation. *PloS one*, 13(5):e0197045, 2018.

EXPERIMENTAL CHARACTERIZATION AND CONSTITUTIVE MODELLING OF TRANSPARENT POLYURETHANE

Zisheng Liao¹, *Mokarram Hossain² and Xiaohu Yao¹

¹ School of Civil Engineering and Transportation, South China University of Technology, China

²Zienkiewicz Centre for Computational Engineering (ZCCE), Swansea University, UK

*mokarram.hossain@swansea.ac.uk

Summary

Transparent polyurethane has been widely applied in laminated windshield glasses as the interlayer material to enhance the reliability due to its outstanding impact resistance. Under impact loading such as bird strike, the interlayer undergoes large tensile deformation at wide range of strain rates. In addition, the interlayer is on service over a wide range of temperatures for a plane traveling around the world. The mechanical behavior of transparent polyurethane under these conditions is not fully understood. In this study, systematical experiments were performed on transparent polyurethane. The viscoelasticity of the material was firstly verified by several quasi-static cyclic tests. Then a series of large tensile deformation and tensile failure experiments were conducted under various strain rates using a servo-hydraulic high-speed tensile machine. All strain data were acquired by the Digital Image Correlation (DIC) technique. The experimental results show that tensile stress-strain curves and failure behaviors are significantly temperature and strain rate dependent. Finally, a phenomenological-based finite strain viscoelastic model is developed. After parameter identifications, one-dimensional equations are fitted to experimental data that yield good predictions.

Key Words: *Transparent polyurethane; Temperature dependence; Strain rate dependence*

Introduction

Bird strikes are fatal accidents threatening the safety of aeronautical structures and flight crews, and cause annual commercial loss of \$193 million merely in US [1]. A measure to minimize the damage of bird strike is to employ laminated glass as a windshield, which consists of two panes of glass bonded by a polymer interlayer in the simplest case. The interlayer plays a key role on diverse attributes of the windshield, such as transparency, sound attenuation, and mitigation of post-fracture glass fallout. One favourable choice is transparent polyurethane. Polyurethane is a segregated by soft and hard segments. The transparent polyurethane discussed in this paper possesses well elasticity with large deformation capacity, well viscosity with large hysteretic loop, strong impact resistance, low glass transition temperature, firm adhesion, sufficient light transmittance, and so forth. These excellent properties contribute to more extensive applications of transparent polyurethane than many conventional interlayer materials. Structural design is an effective mean to exploit the advantages of laminated glass to the full, which bases on a thorough understanding of involved material such as polyurethane. Under impact loading such as bird strike, the material is in certain conditions. For example, according to experimental results from [1], the speeds of bird strike on aircraft generally ranged from 70 m/s to 250 m/s, which results in strain rate of 10^0 /s to 10^1 /s loaded on the structure. Under a blast loading, the interlayer material of laminated glass was at strain rates from 30 /s to 100 /s. Similar to many polymers, polyurethane shows strong strain rate and temperature sensitivity. Taking these factors into account, investigations on large tensile deformation of transparent polyurethane at various intermediate strain rates and temperatures are essential.

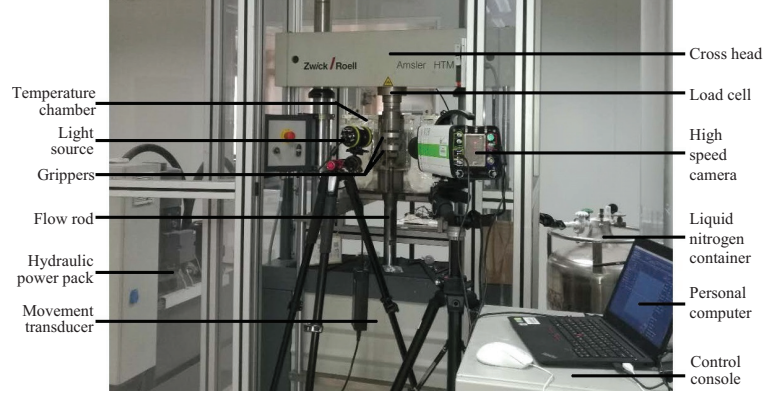


Figure 1: Zwick/Roell HTM-2512 servo-hydraulic tensile machine and a high speed camera.

Experimental study

In this study, S-123 transparent polyurethane provided by the company PPG was investigated. The material was based on dicyclohexylmethane-4,4-diisocyanate (HMDI), and polytetramethylene ether glycol (PTEG). The light transmittance was over 90% and the density was $1180 \text{ kg}\cdot\text{m}^{-3}$. Our specimens were designed in flat dumbbell shape in case they broke in the grippers. The specimen had a 10 mm longer gauge section and a 10 mm fillet radius of the arc section. It was 3 mm in thickness and 6 mm in width. Quasi-static tensile experiments were conducted on an Instron 5567 universal testing machine. Note that in quasi-static tests, the low strain rate loading induced more compliant behavior of the specimens than in dynamic tests. As a consequence, the specimens were hard to be gripped tightly. To tackle this problem, specimens were bonded to aluminum shims with glue before being mounted to the grippers. In this study, the tensile experiments at various strain rates were performed on a Zwick/Roell HTM-2512 servo-hydraulic dynamic tensile machine as shown in Fig 1. The tensile force is measured by the inbuilt piezo-electric load cell in the crosshead. There is an embedded transducer to measure the displacement of the gripper. Thanks to the hydraulic system, the test machine can maintain constant stretching speeds available from 0.03 m/s to 12 m/s. The speeds covered the corresponding strain rates from 10^0 /s to 10^2 /s.

Constitutive modelling

The key ingredient of finite strain based constitutive modelling for polymeric materials is a strain energy function, which can be decomposed as an isochoric contribution and a volumetric as

$$\Psi(\mathbf{C}, \mathbf{A}) = \tilde{\Psi}_{vol}(J) + \tilde{\Psi}_{iso}(\bar{\mathbf{C}}, \mathbf{A}) = \tilde{\Psi}_{vol}(J) + \tilde{\Psi}_{iso}^e(\bar{\mathbf{C}}) + \sum_{i=1}^s \tilde{\Psi}_{iso,i}^v(\bar{\mathbf{C}}, \mathbf{A}_i) \quad (1)$$

where $J = \det \mathbf{F}$, $\bar{\mathbf{C}} = J^{-2/3} \mathbf{C}$ and \mathbf{A} is an internal variable. Similar to the decoupled representation of the energy function, the corresponding decoupling of the stress tensor yields

$$\mathbf{S} = \mathbf{S}_{vol} + \mathbf{S}_{iso} = 2 \frac{\partial \Psi_{vol}}{\partial \mathbf{C}} + 2 \frac{\partial \Psi_{iso}}{\partial \mathbf{C}}. \quad (2)$$

In Eqn. (2), we have $\mathbf{S}_{vol} = Jp \mathbf{C}^{-1}$, where the hydrostatic pressure $p = \partial \Psi_{vol}(J) / \partial J$ has been introduced. In the case of incompressibility, $J = 1$ and p serves as a Lagrange multiplier

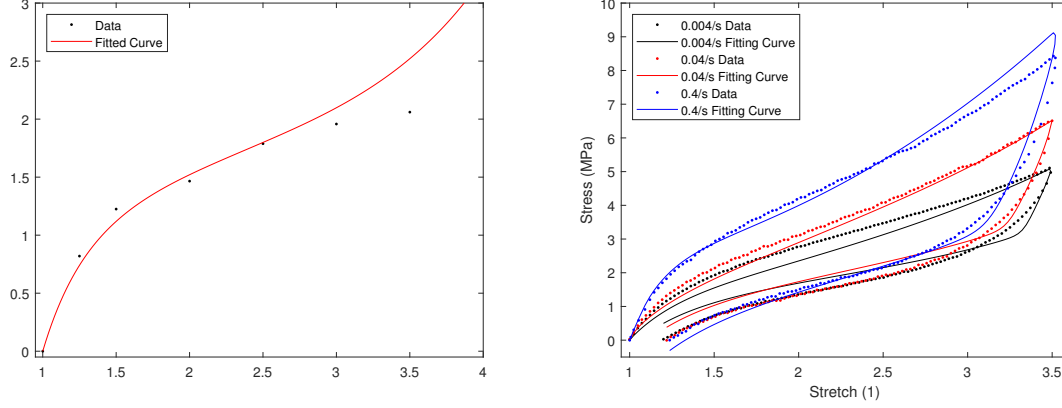


Figure 2: A complete set of material parameter identification using (Left) Elastic data, (Right) Viscoelastic data at various strain rates of 250% deformation

to satisfy this kinematic constraint on the deformation field. The isochoric energy function Ψ_{iso} is expressed in terms of the isochoric right Cauchy-Green tensor $\bar{\mathbf{C}} = \bar{\mathbf{F}}^t \bar{\mathbf{F}}$, $\bar{\mathbf{F}} = J^{-1/3} \mathbf{F}$. The definition of the stress tensor $\bar{\mathbf{S}} = 2\partial\Psi_{iso}(\bar{\mathbf{C}}, \mathbf{A})/\partial\bar{\mathbf{C}}$ is introduced and the isochoric stress \mathbf{S}_{iso} is related to the previous one via the fourth-order projection tensor $\mathbb{P} = \partial\bar{\mathbf{C}}/\partial\mathbf{C}$ by

$$\mathbf{S}_{iso} = J^{-\frac{2}{3}} \mathbb{P} : \bar{\mathbf{S}} \quad \text{with} \quad \mathbb{P} = \mathbb{I} - \frac{1}{3} \mathbf{C}^{-1} \otimes \mathbf{C} \quad , \quad \mathbb{I}_{ijkl} = \delta_{ik} \delta_{jl} \quad (3)$$

where δ_{ij} is a Kronecker delta. The stress $\bar{\mathbf{S}}$ is further decomposed into elastic and viscous parts, i.e. $\bar{\mathbf{S}} = \bar{\mathbf{S}}^e + \bar{\mathbf{S}}^v$. A Carrol type elastic energy is chosen as

$$\Psi_{iso}^e(\bar{\mathbf{C}}) = aI_1 + b\bar{I}_1^4 + c\sqrt{\bar{I}_2} \quad (4)$$

where a, b, c are material parameters. Lubliner [3] proposed a viscous energy function as

$$\Psi_{iso}^v = \sum_{i=1}^s \frac{1}{2} \mu_i^v [(\mathbf{A}_i : \bar{\mathbf{C}} - 3) - \ln \det(\mathbf{A}_i)] \quad (5)$$

where μ_i^v is a viscous shear modulus and \mathbf{A}_i are the strain-like tensorial variables associated with viscous Maxwell elements. A thermodynamically consistent evolution ansatz for the internal variable of a single element follows

$$\dot{\mathbf{A}}_i = \frac{1}{\tau_i} [\bar{\mathbf{C}}^{-1} - \mathbf{A}_i] \quad , \quad (6)$$

where τ_i is the relaxation time. All of the tests presented in the previous section are of uniaxial type. Therefore, the constitutive model discussed above needs to be formulated in one-dimensional form in order to identify the material parameters as well as to validate the model. From the incompressibility condition, i. e. $\det \mathbf{F} = \det \bar{\mathbf{F}} = \lambda_1 \lambda_2 \lambda_3 = 1$ and the assumption of symmetry the complementary principal stretches follow as $\lambda_2 = \lambda_3 = \lambda^{-1/2}$. Therefore, the complete deformation gradient reads $\mathbf{F} = [\lambda, \lambda^{-1/2}, \lambda^{-1/2}]$. The total stress can be obtained as

$$\mathbf{P} = \left[2a + 8b[2\lambda^{-1} + \lambda^2]^3 + c[1 + 2\lambda^3]^{-\frac{1}{2}} \right] [\lambda - \lambda^{-2}] + \sum_{i=1}^s \mu_i^v \left[\lambda \lambda_i^{2,A} - \frac{1}{\lambda^2 \lambda_i^A} \right] \quad , \quad (7)$$

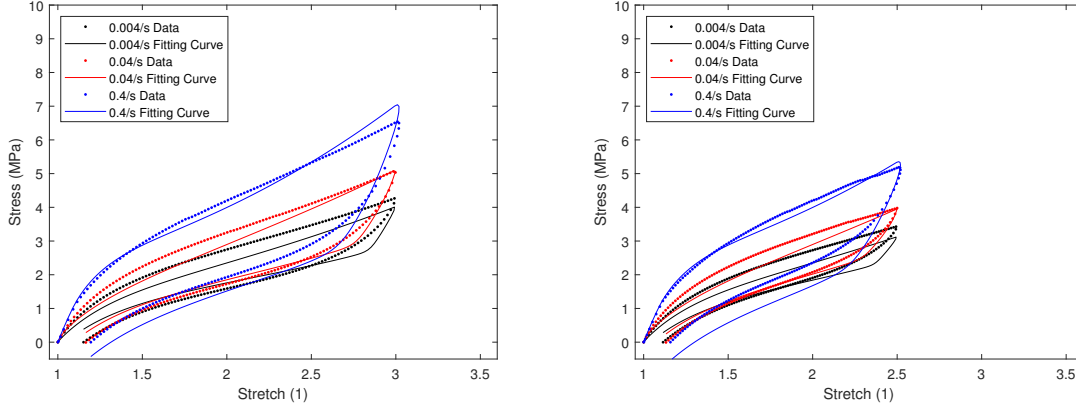


Figure 3: Model validation with other strains (Left) 200% deformation, (Right) 150% deformation

Table 1: Identified elastic and viscoelastic material parameters, respectively; μ , μ_i^v in [MPa] and τ_i in [s]

a	b	c	μ_1^v	μ_2^v	μ_3^v	μ_4^v
2.29e-01	5.93e-06	1.67	2.68e-1	1.4	9.71e-2	8.14e-2
-	-	-	τ_1	τ_2	τ_3	τ_4
-	-	-	1.36e-3	1.88	3.63e2	5.36e4

Similar to the one-dimensional formulation of the total stress, the evolution law is derived:

$$\dot{\lambda}_i^{2,A} = \frac{1}{\tau_i} \left[\lambda^{-2} - \lambda_i^{2,A} \right]. \quad (8)$$

Now a parameter identification algorithm is used to find a complete set of parameters of the model in Eqn 7. At first, the elastic part of the equation is used to identify parameters a, b, c . Elastic parameter fitting is shown in Fig 2(left). Afterwards, another set of data is incorporated to identify viscous parameters μ_i, τ_i , see Fig 2(right). During the viscous parameter identification, the elastic parameters are kept frozen. A complete set of identified parameters is presented in Table 1. With the identified parameters, other set of data are compared with the model to find model validation which find good agreements, see Fig 3.

Conclusions

In this study, a comprehensive experimental study was conducted to characterise viscoelastic behaviours of a widely used polymeric material, i.e., Transparent Polyurethane. After that, a large strain-based material model is proposed which predicts many data that are not included in the parameter identification process.

References

- 1 Liao Z S, Yao X H, Zhang L H, Hossain M, Wang J, Zang S. *International Journal of Impact Engineering*, 129:152-167, 2019.
- 2 Linder C, Tkachuk M, Miehe C, *Journal of the Mechanics and Physics of Solids*, 59:2134-2156, 2011
- 3 Hossain M, Vu D K, Steinmann P, *Computational Materials Science*, 59:65-74, 2012

AN *hp*-ADAPTIVE DISCONTINUOUS GALERKIN LEVEL SET METHOD*Thomas Adams¹, Stefano Giani¹ and William M. Coombs¹¹Department of Engineering, Durham University, Lower Mountjoy, South Road, Durham, DH1 3LE, UK.

*thomas.d.adams@durham.ac.uk

Summary

The level set (LS) method is a popular technique used for representing and tracking evolving interfaces in computer simulations with many varied and interesting applications. Discontinuous Galerkin (DG) methods are a class of nonconforming finite element methods which have seen growing popularity over the last few decades due to a number of advantages this lack of conformity affords. In particular, DG methods have both a high level of parallelisability and the ability to easily incorporate *hp*-adaptivity which enable one to develop methods which are both efficient and high-order accurate. The ultimate aim of this work is to advance the level set methodology through the adoption of a DG discretisation, for use with topology optimisation problems. This paper presents an *hp*-adaptive DG LS methodology.

Key Words: *Level Set Method; Discontinuous Galerkin; hp-adaptivity; Narrow Band.*

Level set method

The LS method works by defining an interface implicitly as the intersection of a function, called the level set function, ϕ , with the hyperplane that is the computational domain. This hyperplane corresponds to the plane on which the LS function equals zero. The interface can then be tracked or evolved by computing an appropriate advection velocity field, \mathbf{b} , over the problem domain and using this to drive the level set evolution equation,

$$\frac{\partial \phi}{\partial t} + \mathbf{b} \cdot \nabla \phi = 0. \quad (1)$$

Level set reinitialisation

The first required component of the DG LS methodology was the development of a high-order accurate DG LS reinitialisation method. Level set reinitialisation is a technique by which one can ensure that at any point during evolution, that the LS function has desirable numerical qualities; specifically that the LS function is a signed distance function (SDF) to the interface and thus satisfies the Eikonal equation,

$$|\nabla \phi| - 1 = 0. \quad (2)$$

The ability to ensure that for all pseudotime, t , during evolution, that the LS function is a SDF is advantageous for a number of reasons. One reason is that it allows the LS evolution equation, (1), to be simplified as follows,

$$\frac{\partial \phi}{\partial t} = -b, \quad (3)$$

where b is the magnitude of the advection velocity vector, \mathbf{b} . This is beneficial as it means that the LS evolution equation no longer contains spatial derivatives, allowing for evolution using a simple explicit temporal discretisation. Another advantage is that as a SDF will, by definition, satisfy (2), it removes a known issue with the LS method by which large variations in the gradient of the LS function lead to numerical instabilities [1]. DG LS reinitialisation methods have been the subject of earlier works and the reader is referred to [2, 3], for greater detail.

Error estimation

The evolution of the interface at a given point occurs normal to the interface at that point. The

best case scenario then, in terms of accurately computing the next iteration of the evolution, is to ensure that the gradient of the LS function along the interface is equal to the unit outward normal of the interface at each point along the interface. This, is exactly the purpose of LS reinitialisation. As such determining the degree with which the mesh can accurately compute the next iteration of the LS evolution problem can be recast as determining the degree with which the mesh can accurately compute the LS reinitialisation problem, which is easy to quantify. The least squares residual to the Eikonal equation (2), which we refer to as the *signed distance error* can be computed over the domain, Ω , as follows,

$$E_{SD}^2 = \int_{\Omega} (|\nabla\phi| - 1)^2 \, dx. \quad (4)$$

One other component which will be necessary to ensure accurate computation of the evolution is that a satisfactory solution to the problem of computing the advection velocity field can be achieved. This will ultimately depend on the underlying problem driving the evolution and will therefore require its own error estimator and refinement strategy.

Narrow band

A key feature of the method presented here is the adoption of a narrow band approach. When using the LS method, the area of interest is the current position of the interface, and as such it is common practice to restrict the computational domain to a band of elements close to the interface. In this work we define the narrow band such that there are two layers of elements either side of the interface. One advantage of this approach is that ignoring irrelevant degrees of freedom will improve the efficiency of the method. Another benefit is that, far away singularities in the LS function, which lead to numerical instabilities, [2], and which will exist if the interface forms a closed loop on a simply connected subdomain, will be removed from the computational domain.

The cost of a narrow band is that all of the information about the LS function outside the narrow band has to be forfeited after each time step during its evolution. As the interface evolves, the set of elements comprising the narrow band evolves with it. As such, as elements move from outside to inside the narrow band, new information needs to be generated pertaining to the value of the LS function on these elements. To do this, one can once again exploit the fact that the LS function is a SDF to the interface by modifying the reinitialisation method, [2], and applying it to the elements which have moved from outside to inside the narrow band.

hp-adaptive refinement strategy

One of the main advantages of using a DG discretisation for solving these kinds of problems is that *hp*-adaptivity becomes easy to implement. The lack of conformity means that one can use elements with hierarchical modal basis functions for ease of *p*-refinement, and likewise an arbitrary number of hanging nodes as a result of *h*-refinement are dealt with implicitly by the method. The main features of the *hp*-adaptive refinement strategy in the proposed method are outlined below.

An initial flagging strategy is computed by which any elements with an error, computed using (4) elementwise, greater than some percentage, defined by the user, of the maximum error are flagged for refinement. The narrow band is also leveraged here such that all of the elements outside the narrow band are always flagged for derefinement.

The next step is to decide whether to refine in *p* or *h*. For a sufficiently smooth problem it is known that it is more efficient, in terms of the number of degrees of freedom, to refine in *p* than *h*, and vice versa [4]. In order to make this decision then, one can compute the Sobolev regularity of the portion

of the LS function on the element, which can be done by calculating the decay rate of the coefficients of the Legendre expansion of the LS function on that element [4].

It is known that for some problems, one in particular that we are interested in being topology optimisation of linear elastic structures, that it is preferable that the maximum number of levels of refinement different between adjacent elements be at most one [5]. That is enforcing a limit of one hanging node per edge, and ensuring neighbouring elements are at most one polynomial order different. If this is the case, then a smoothing algorithm can be applied iteratively to the flagging strategy (with a preference for refining over not refining, and for not refining over derefining) until such a condition will be satisfied, post-refinement.

Once the flags have been appropriately determined, the mesh can then be refined and the LS function L^2 projected onto the new mesh.

Algorithm

A coarse outline of the whole method is stated in Algorithm 1.

Algorithm 1 Coarse outline of the method.

```

1: Initialise mesh, level set function and other problem parameters
2: while time < final time do
3:   Compute advection velocity
4:   Evolve level set function
5:   time = time + dt
6:   while true do
7:     Update narrow band
8:     If  $\{E_{SD} < tolerance\}$  then {break}
9:     Reinitialise level set function
10:    If  $\{E_{SD} < tolerance\}$  then {break}
11:    Refine mesh

```

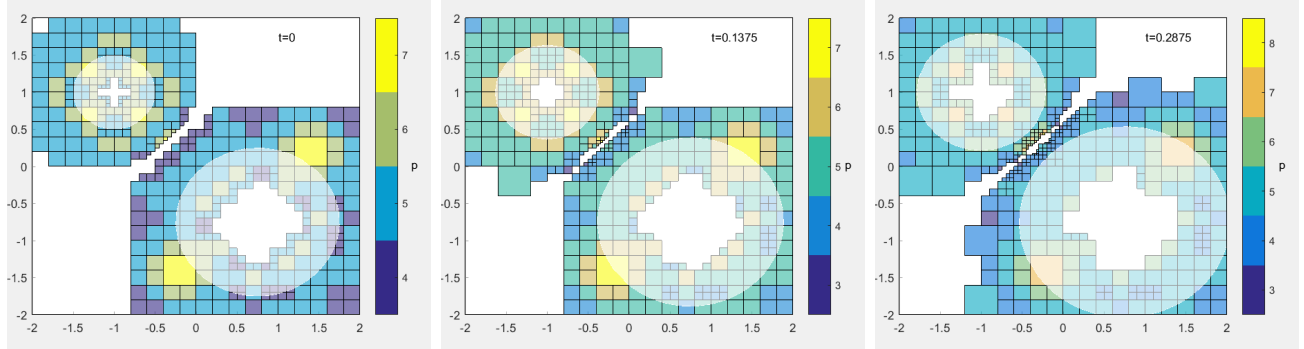
One can choose the initial LS function such that it is a SDF, and as such when generating the initial mesh, the same mesh refinement algorithm discussed above can be used exchanging the signed distance error with the projection error (that is the difference between the projected and analytical LS function in the L^2 norm) until a tolerance is satisfied. Then a time stepping loop through the evolution equation is computed. At the beginning of each iteration, the advection velocity will need to be computed for the current mesh; for a physics driven level set problem, this is where the physical problem will be computed. This is followed by computing the next iteration of the LS evolution equation.

After evolution it is likely that both the narrow band will need to be updated, and that the LS function will no longer satisfy the signed distance property and will need to be reinitialised. After modifying the narrow band, and running the reinitialisation problem until convergence, should the mesh still not satisfy a tolerance on the global error, the mesh will be refined and the narrow band once again updated. That loop will continue until the mesh is sufficiently refined to allow the reinitialisation problem to be computed to the desired degree of accuracy.

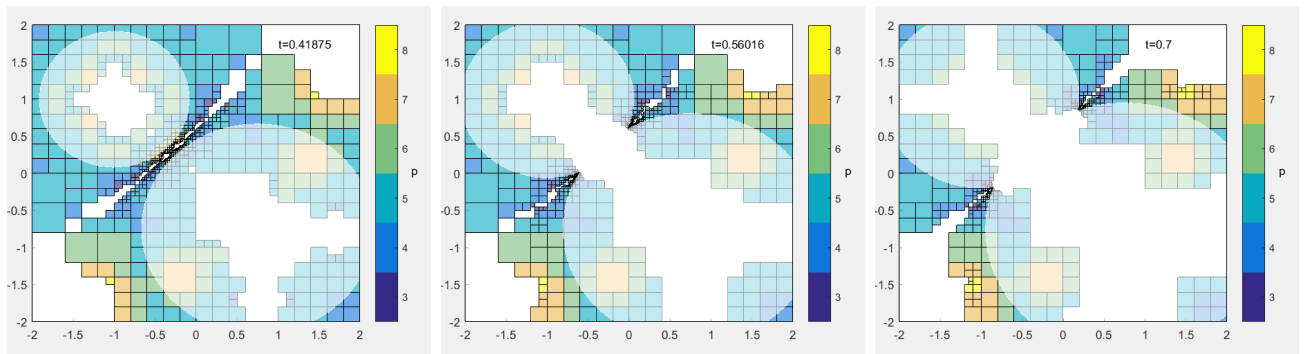
Numerical example: two growing circles

A numerical example is presented in which two circles of radii, 0.5 and 1, centred at $(-1, 1)$ and $(0.75, -0.75)$ respectively are evolved subject to an advection velocity, $b = 1$, everywhere such that

the two circles grow at a constant rate. As the circles grow they will undergo a topological change by which they will eventually merge. The threshold on the signed distance error to be enforced throughout is $E_{SD} < 10^{-6} \times \text{Area}$. The Area term refers to the area of the part of the domain inside the narrow band, and the error is normalised in this way as the size of the narrow band changes throughout the evolution. The problem is computed using the method outlined above; the resulting interface at roughly equal time steps between $t = 0$ and $t = 0.7$ is presented in Figure 1.



(a) LS interface and mesh at $t=0.00$ (b) LS interface and mesh at $t=0.14$ (c) LS interface and mesh at $t=0.29$



(d) LS interface and mesh at $t=0.42$ (e) LS interface and mesh at $t=0.56$ (f) LS interface and mesh at $t=0.70$

Figure 1: Evolution of LS interface using narrow banded and hp -adaptive mesh, for two growing and eventually merging circles. The colour of each element represents the polynomial order, p , corresponding to the colour bar besides each mesh.

Acknowledgements

This work was supported by the Engineering and Physical Sciences Research Council (grant EP/M507854/1).

References

- [1] W. Mulder, S. Osher, and J.A. Sethian, Computing interface motion in compressible gas dynamics. *J. Comput. Phys.* 100, pp. 209–228, 1992.
- [2] T. Adams, S. Giani, and W.M. Coombs, A high-order elliptic PDE based level set reinitialisation method using a discontinuous Galerkin discretisation. *J. Comput. Phys.* 379, pp. 373–391, 2019.
- [3] T. Adams, N. McLeish, S. Giani, and W.M. Coombs, A parabolic level set reinitialisation method using a discontinuous Galerkin discretisation. *Accepted Comput. Math. Appl.* 2019.
- [4] P. Houston, and E. Süli, A note on the design of hp -adaptive finite element methods for elliptic partial differential equations. *Comput. Meth. Appl. Mech. Eng.* 194(2-5), pp. 229–243, 2005.
- [5] R. Bird, W.M. Coombs, and S. Giani, A posteriori discontinuous Galerkin error estimator for linear elasticity, *Appl. Math. Comput.* 344: pp. 78–96, 2019.

NUMERICAL ANALYSIS OF SCC FLOW: THE BINGHAM MODEL AND BEYOND

***Ashutosh Bhokare¹, Sizeng You¹, Chenfeng Li¹**¹College of Engineering, Swansea University, SA1 8EN

*845973@swansea.ac.uk

Summary

The flow of self-compacting concrete (SCC) can be described as a multiphase flow with the constituents interacting at multiple scales to produce complex rheological behaviour. Successfully modelling SCC flow would deepen our understanding of SCC rheology and predict defects in SCC placement. The Bingham fluid model is the most widely used constitutive model to describe SCC flow. This paper aims to establish the advantages and disadvantages of the Bingham model in application to SCC flow. By means of a thorough parametric study, the paper proposes a correlation between the Bingham parameters and measurements taken from the V-funnel and slump flow tests. Further, the model is applied to a full-scale simulation of tremie concrete placement in a pile. This case-study establishes the Bingham model's ability to answer questions surrounding the 'bulk' flow patterns witnessed in the placement procedure, but also highlights its inability to capture phenomena such as segregation, blocking and bleeding. To capture such defect causing phenomena, the paper explores the use of a Eulerian-Lagrangian technique. The ability of the new approach to model segregation is demonstrated by simulating the unique column test.

Key Words: *Eulerian-Lagrangian, multiphase flow, SCC flow, Bingham model, FVM*

Introduction

The flow of SCC in placement processes of the construction industry is an example of multiphase flow. The main constituents of SCC, cement, aggregate, and water are simple ingredients which interact with each other at multiple scales to produce the complex rheological behaviour we see in SCC. Despite efforts by engineers to produce mix designs which match all workability and strength requirement, imperfections in concrete are witnessed on a regular basis. Placement of SCC in deep foundations suffers from the ill effects of segregation, granular blocking and bleeding. As structures get heavier, foundations get deeper, thus increasing the risk of defects in SCC placement. Defects in the placement process have cost the industry millions of pounds and put public safety at risk [3]. The mechanism of the defect causing phenomena are less understood and lab scale tests are limited in what they can indicate. Industrial scale experiments are expensive and hard to perform due to a lack of technology that can monitor them. Numerical simulations offer an alternative approach to study and understand SCC flow and predict defects in the placement process.

Summary of literature review

From a detailed literature review, we find that research on SCC flow simulation has mainly focussed on simulating field/lab tests like the V-funnel and slump flow tests [4]. Numerical strategies used can be classified as either continuum or non-continuum approaches. Finite volume method (FVM), finite element method (FEM), smooth particle hydrodynamics (SPH) are continuum-based approaches, while discrete element method (DEM) and lattice-Boltzmann method (LBM) are non-continuum-based approaches used to simulate SCC flow [1]. Regardless of the numerical strategy, most research has employed the Bingham fluid model. Although the Bingham fluid model is relatively simple to apply and describes the 'bulk' flow, it assumes the SCC to be homogeneous. Simulating defect causing phenomena like segregation and blocking is not possible with this assumption. There are also very few examples, in literature, applying simulation technology to industrial scale problems. Developing

sophisticated models to capture defect causing phenomena and applying them to full-scale problems is crucial in solving issues surrounding SCC placement.

The Bingham model

The Bingham model is characterised by two parameters and is usually used to describe the flow of fluids which exhibit yield properties. These parameters are the yield stress (τ_0) and plastic viscosity (μ). The relation between shear stress (τ) and strain rate ($\dot{\gamma}$) is:

$$\begin{aligned} \tau &= \tau_0 + \mu\dot{\gamma} & \text{if } \tau \geq \tau_0 \\ \dot{\gamma} &= 0 & \text{if } \tau \leq \tau_0 \end{aligned} \quad (1)$$

Since SCC can be interpreted as a fluid with yield properties, the Bingham model can be applied to it by assuming SCC to be a homogeneous material [2]. It is observed that the values of Bingham parameters are unique to a particular mix design. There is no existing procedure/test which gives values of these parameters for a particular mix and an attempt to do so is detailed in the next section.

Parametric study: A correlation between Bingham parameters and lab tests

In this section, a method to correlate measurements from standard SCC quality tests to the Bingham parameters is proposed. The Bingham model is implemented as a constitutive model in an in-house finite volume incompressible flow solver. Volume of fluid method (VoF) is used to model the interface between SCC and air. The V-funnel and slump flow tests are simulated numerous times using the in-house solver with a large range of values for plastic viscosity and yield stress. Figure 1 shows the flow diameter versus plastic viscosity for yield stresses varying from $10Pa$ to $500Pa$. From the figure, it is evident that flow diameter is more sensitive to yield stress than to plastic viscosity as it is more or less constant for a particular value of yield stress. This calibration data can be used to obtain a value of yield stress for a particular SCC mix, given its measured flow diameter in a slump flow test. Figure 2 shows the flow time versus yield stress for plastic viscosities from $10Pa \cdot s$ to $100Pa \cdot s$. Once a value of yield stress is obtained from the previous plot, the measured V-funnel flow time for that particular mix can be used to obtain a value of plastic viscosity from these calibration curves. Thus a correlation between Bingham parameters and measured experimental values is established. To validate this correlation, the Bingham parameters for a random SCC mix are obtained using the method mentioned above. These parametric values are used to simulate the slump cone and V-funnel test. The diameter and flow time obtained from the experiments are $641.25mm$ and $5.97s$ respectively while the values obtained from the simulations are $615.7mm$ and $5.96s$ respectively. The similarity in these values confirms that the calibration method proposed can be used to estimate the Bingham parameter values for a given SCC mix.

Full-scale simulation: Pushing the Bingham model to the limits

In this section, the Bingham fluid model along with the new correlation between experimental measurements and parameters is applied to a full-scale problem. In the problem, a $16m$ deep pile with diameter $1.5m$ is filled with SCC using a tremie pipe in three charges of volume $9m^3$ each. The pipe is lifted two times during the process. Figure 3 shows the mesh used in the simulation. The flow diameter and flow time for an SCC mix used in practice are used to obtain Bingham parameters with the aid of the calibration curves. The yield stress and plastic viscosity used in the simulation are $150Pa$ and $20Pa \cdot s$ respectively. Figure 4 shows the age of SCC in the pile in seconds. By observing the figure we see that SCC exiting the tremie is first forced down due to its momentum and then flows upwards towards the concrete surface. This forms a bowl-shaped flow pattern near the tremie. As SCC nears the surface, it flows towards the sides of the pile into the cover zone. We thus see older concrete towards the sides of the pile. Each time the tremie is lifted, older concrete below the tremie's new position gets 'locked' due

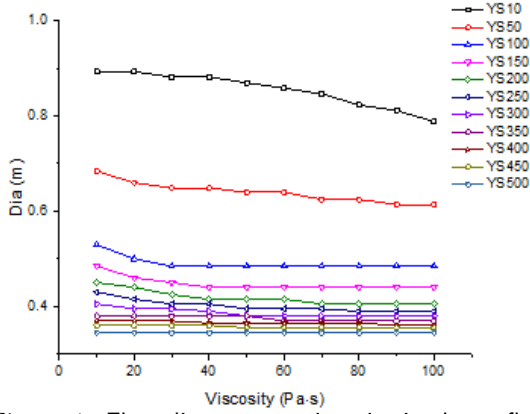


Figure 1: Flow diameter vs viscosity in slump flow

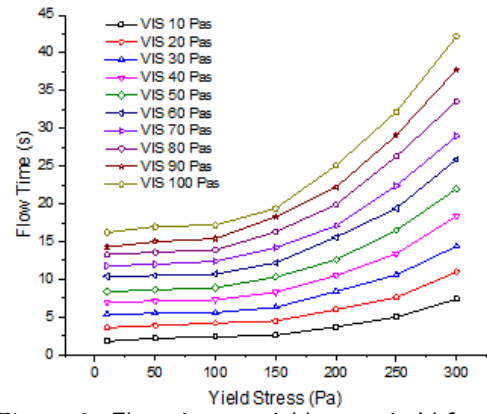


Figure 2: Flow time vs yield stress in V-funnel

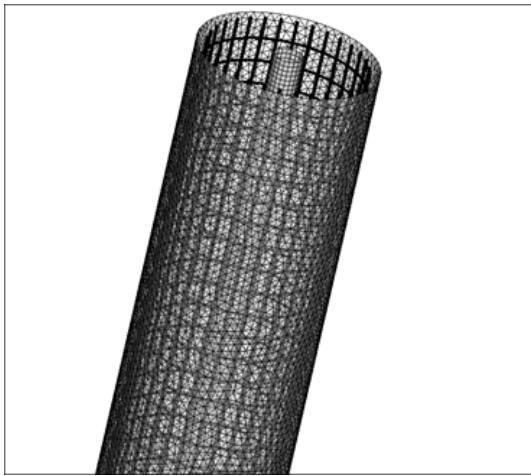


Figure 3: Close-up of mesh used in the simulation

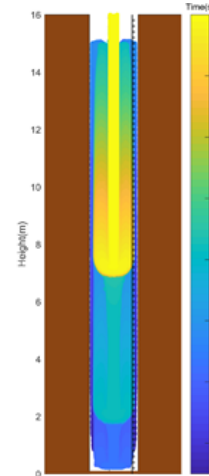


Figure 4: Age of concrete in the pile

to its yield properties while the new concrete forms the bowl-shaped flow pattern in the new position. This leads to the formation of bowls near the tremie opening where there is an abrupt change from old to new concrete. The Bingham model allows us to answer questions surrounding the 'bulk' flow of SCC in placement procedures but fails to answer questions regarding segregation and blocking.

Eulerian-Lagrangian approach: A fresh perspective

As stated earlier, the Bingham model and the homogeneous material assumption is unable to capture segregation and blocking. A Eulerian-Lagrangian approach, where the mortar is modelled as a continuum phase and coarse aggregate as the discrete phase (DEM), can be used to capture the effects of these phenomena. By introducing the volume fraction of the discrete phase in the Navier-Stokes equations we get

$$\frac{\partial(\rho_f \alpha_f)}{\partial t} + \nabla \cdot (\rho_f \alpha_f \mathbf{u}_f) = 0 \quad (2)$$

$$\frac{\partial(\rho_f \alpha_f \mathbf{u}_f)}{\partial t} + \nabla \cdot (\rho_f \alpha_f \mathbf{u}_f \mathbf{u}_f) = -\alpha_f \nabla p + \mathbf{R}_{f,p} + \nabla \cdot (\alpha_f \boldsymbol{\tau}_f) \quad (3)$$

where ρ_f is the density of fluid, α_f is the volume-fraction of fluid, u_f is the velocity, p is the pressure $\mathbf{R}_{f,p}$ is the momentum exchange term and $\boldsymbol{\tau}_f$ is the stress. The governing equations of DEM particles are given by

$$m_p \ddot{\mathbf{x}}_p = \mathbf{F}_p \quad (4)$$

$$I_p \frac{d\boldsymbol{\omega}_p}{dt} = \mathbf{r}_{p,c} \times \mathbf{F}_{p,t} \quad (5)$$

where m_p is the mass of the particle, x_p is the displacement, F_p is the force, I_p is the moment of inertia, ω_p is the angular velocity, $r_{p,c}$ is the distance from the point of contact and $F_{p,t}$ is the tangential force on the particle. The in-house flow solver is coupled with an in-house DEM solver and both are solved by time-marching in a staggered manner. It is used to simulate the unique column test. The result is shown in Figure 5 which depicts the position of coarse aggregates at the end of 15 minutes and their diameter. The segregation ratio is found to be 7.19%. This value is within the practical range of values found in practice. The Eulerian-Lagrangian approach to modelling SCC flow thus has the potential to model segregation and blocking.

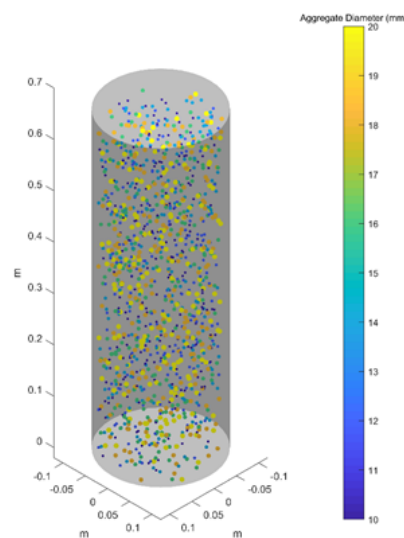


Figure 5: Unique column test simulation

Conclusions

Simulating SCC flow accurately, can increase our understanding of concrete rheology and enable us to predict defects in the placement procedure. The Bingham fluid model with the assumption that SCC is homogeneous is the most popular approach to model SCC flow and it is able to answer questions related to the 'bulk' flow of concrete. The Bingham parameters for a particular SCC mix can be estimated using the calibration curves obtained in this paper. However, since the Bingham model is unable to capture defect causing phenomena like segregation and blocking, other techniques must be developed in order to model them. The Eulerian-Lagrangian approach has the potential to model segregation and blocking.

References

- 1 N. Roussel, A. Gram. *Simulation of fresh concrete flow*. RILEM State-of-the-Art Reports, 15, 2014.
- 2 G. Tattersall, S. Bloomer. *Further development of the two-point test for workability and extension of its range*. Magazine of concrete research, 31(109):202-210, 1979.
- 3 EFFC, DFI. *EFFC/DFI concrete task group: Best practice guide to tremie concrete for deep foundations*. 2018.
- 4 N. Roussel, M. Geiker, F. Dufour, L. Thrane, P. Szabo. *Computational modelling of concrete flow: general overview*, Cement and concrete research, 37(9):1298-1307, 2007.

OPTIMISATION OF A CONCEPTUAL AIRCRAFT MODEL USING A GENETIC ALGORITHM AND 3D COMPUTATIONAL FLUID DYNAMICS

Lok Chun Chan, *Mohammad Akrami, Akbar A. Javadi, Gavin Tabor, Mahdiah Dibaj,
Mohammad Hassan Khanjanpour
Department of Engineering, University of Exeter, Exeter, EX4 4QF, UK
*m.akrami@exeter.ac.uk

Summary

Aircraft design is fundamentally a multidisciplinary design activity which involves different models and tools for various aspects of the design. This paper uses a Multidisciplinary Design Optimisation (MDO) for design of a simplified commercial aircraft, aiming to optimise the objectives of cost, weight and drag. NSGA-II is used to optimise the weight and cost by changing the geometry to introduce lightweight airframe materials and composites with lower density. Reducing weight of the structure is one of the major ways to improve the performance of aircraft. Lighter, stronger material will allow a higher speed and greater range which may contribute to reducing operational costs. Drag reduction is also a major factor in aircraft design. Reduction of drag in an aircraft means that it can have a lower fuel consumption or travel at higher speed, both of which are beneficial to plane performance. A smart structural optimisation algorithm helps to optimise the cost, weight and drag, while drag is analysed based on CFD modelling results. The results are validated against some wind tunnel tests.

Key Words: Optimisation, aircraft, NSGA-II, CFD

Introduction

The first commercial aircraft started back on 1st January 1914. It operated between St. Petersburg and Tampa, yet only lasted for four months. Since then, engineers and scientists start to design and investigate different methods to improve the performance of aircraft. The original aims are to increase the distance of travel and the capacity of the aircraft. Nowadays, commercial aircrafts are fairly developed and improved compared to the first commercial aircraft. Even though the aircrafts have massively improved compared to the earlier designs, but there are still areas to improve. Designers always try to come up with better designs and the aims have changed from achieving basic performance to improving the performance of flight such as reducing the fuel consumption. To achieve these aims, designers have applied various techniques and technologies to assist with their design works. For example, the use of computational simulation, wind tunnel experiment and mathematical models has helped to refine, improve and optimise the aircrafts in terms of their structure, material choice and geometry in order to achieve a “better” design. Aircraft design always contains more than one objective; e.g., reduction of fuel consumption, reduction of weight and increase in the payload; and involves various disciplines such as structure dynamics, fluid dynamics and materials engineering. In this paper, MDO is used to optimise a simplified model of a commercial aircraft in order to reduce weight, drag and cost, simultaneously.

Materials and Methods

During the conceptual design, ideas were formulated, rephrased, rejected or modified. Traditionally, aircraft design is separated into different areas of focus, such as structure, materials, dynamics and cost and there are aims and constraints in each area.

For example, the design of airframe focuses on structure and shape while the design of the wing will focus on lift and drag. All parts of an aircraft are closely related and interlinked with each other. Therefore, achieving one objective might have an adverse effect on the other design objective. For instance, replacing aluminium alloy by light-weight materials such as carbon fibre and other composites to achieve a weight reduction will have a trade-off of increased production cost. A complex design, such as aircraft, need to achieve different design objectives while there are different trade-offs. An MDO is a methodology to achieve the “best” solution by changing the design variables and maintaining different design constraints [1].

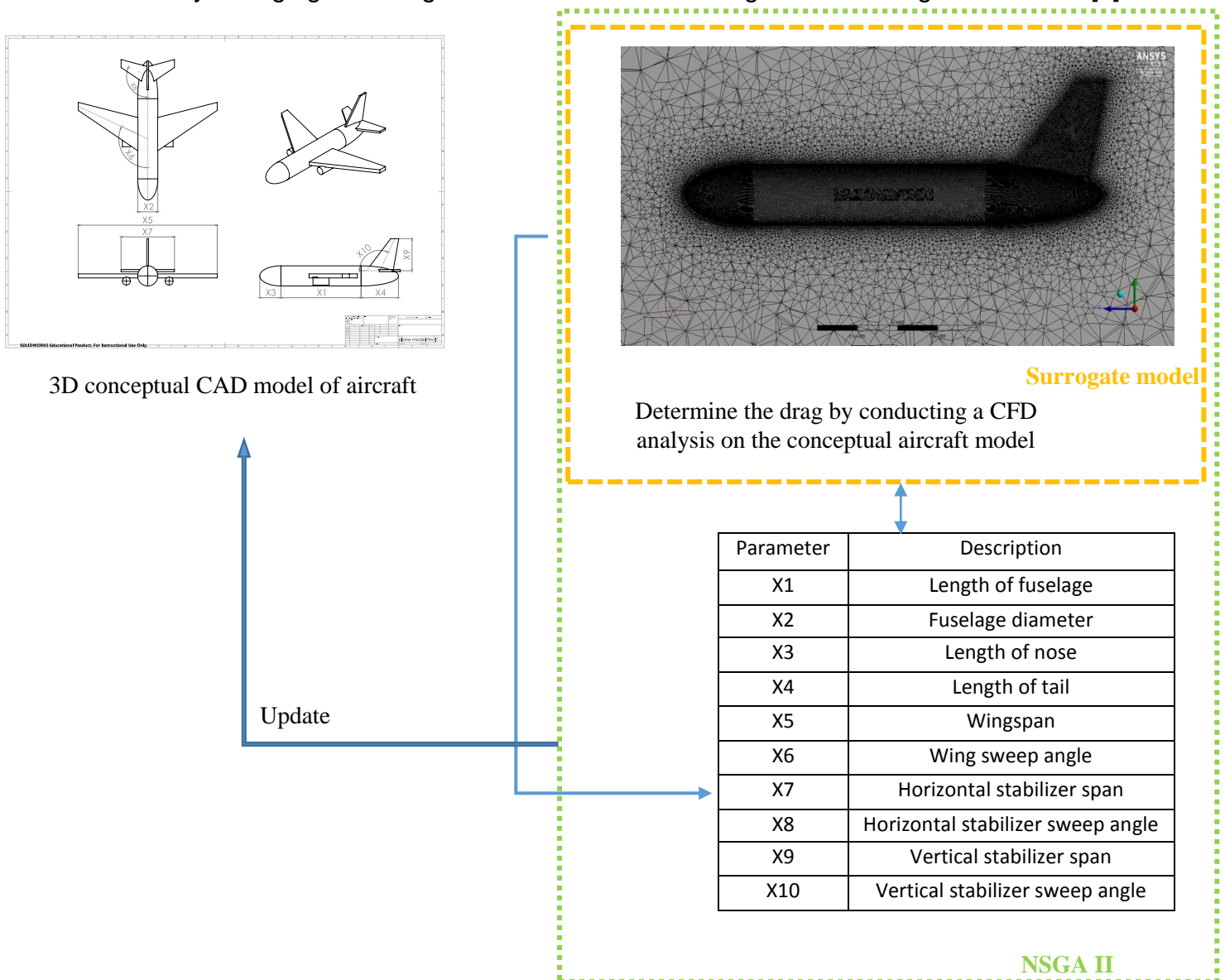


Figure 1: Application of the NSGA-II algorithm and the assigned parameters in the model

Traditionally, design is a process focusing on one area at a time and the areas down the stream are heavily dependent on the previous results. As modern design has developed and become more complex, it has become very difficult to optimise multiple design objectives. MDO is a design process which evaluates all design variables simultaneously and considers the trade-off and interaction between different objectives and disciplines. MDO is a methodology for the design of complex engineering systems that are governed by mutually interacting physical phenomena and made up of distinct interacting subsystems in their design.

The rapid development in the computational analysis in recent years has been largely influencing MDO. Many simulation results can now be linked and considered in the calculation process, which could be a significant aid, especially in aircraft design. Areas like wing lift and drag can be more easily considered during the design process. Apart from CFD or FEA, MDO can also involve diverse tools such as cost modelling and even experimental results. Non-dominated Sorting Genetic Algorithm (NSGA-II) is a modified version of NSGA which is a multi-objective optimisation model and was one of the first evolutionary algorithms [2, 3]. It generates a set of solutions, also known as Pareto-optimised solutions, which are superior to the rest of the solutions. There is no absolute better solution within this Pareto-optimised solutions and hence the choice of an optimal solution over the others requires problem knowledge and other problem factors. In this study, the ten initial parameters (Figure 1) were defined in order to optimise the three main objectives. These ten parameters will update in each iteration based on the geometrical parameters' ranges of the aircraft models to generate the optimal solution. Also, a surrogate model was constructed based on the initial results from the CFD model and the remaining simulations were analysed based on this model predictions to observe and choose the most promising ones until a "good design" can be achieved. By generating a surrogate model using CFD simulation which has been validated by the wind tunnel results (Figure 2) and adapted in the NSGA-II model, the range of optimal solutions are generated.

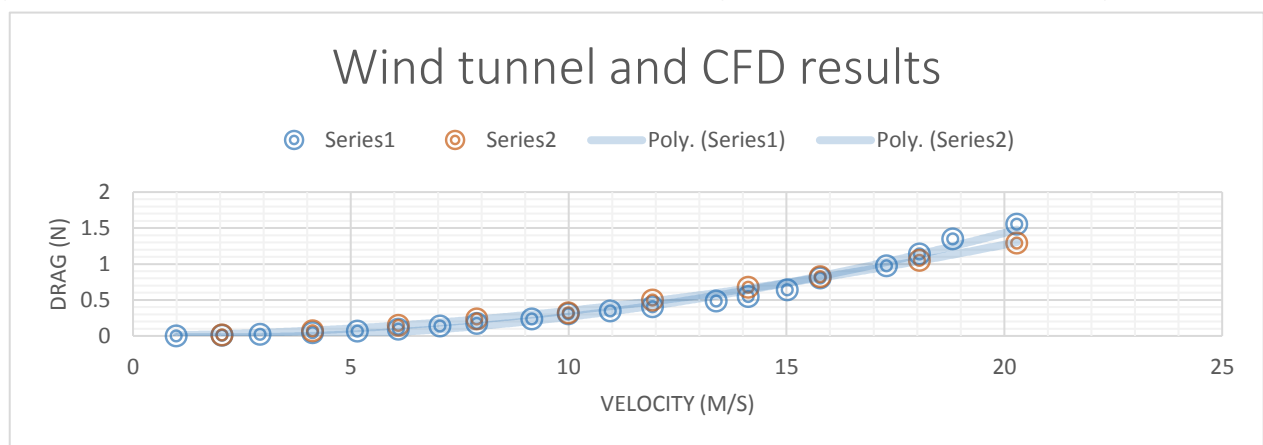


Figure 2: Validating the CFD model against the wind tunnel results based on the Drag force (N) and the Velocity (m/s)

Results and conclusion

By combining the surrogate optimisation model generated by multiple CFD simulations and NSGA II, multiobjective genetic algorithm, a Pareto front is generated which clearly shows a trade-off between different objectives. There is a significant trade-off between weight and cost, as weight decreases, the costs increases (Figure 3) [4, 5]. This trend clearly exists between the weight and Fuselage volume and also cost and the volume. The results help to find a range of solutions in order to optimise the the topology of the structure [6].

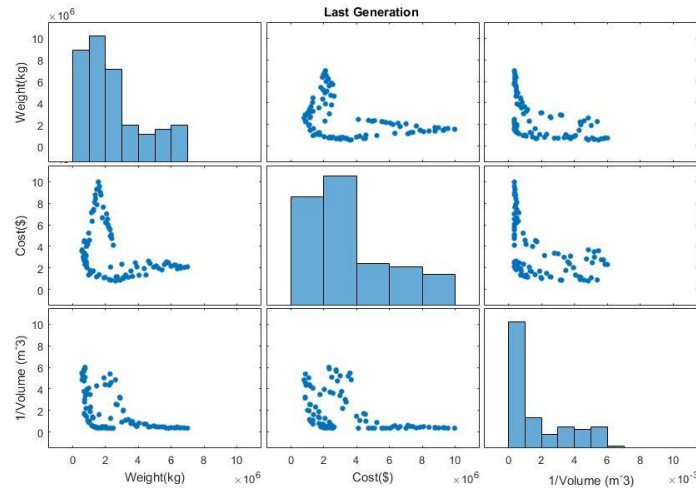


Figure 3: Optimisation results from the NSGA-II algorithm for the three main objectives of Cost, Weight and Fuselage volume

Based on the developed algorithm, the optimised ranges for the main 10 parameters are illustrated (Table 1) in order to minimise the aforementioned objectives.

Parameters	Initial range	Optimised range
X1	15 – 50	36.86 – 50
X2	3.76 – 8.5	6.648 – 8.5
X3	3.96 – 5	4.173 – 5
X4	7 – 15	8.115 – 13.473
X5	26 – 80	26 – 31.62
X6	90 – 125	105.03 – 123.23
X7	10 – 30	10 – 15.834
X8	115 – 140	119.694 – 127.67
X9	6 – 15	6 – 10.559
X10	115 – 140	115 – 139.07

References

1. Sobieszczanski-Sobieski, J., Multidisciplinary Design Optimization: An Emerging New Engineering Discipline, Advances in Structural Optimization (483-496), Kluwer Academic Publishers, the Netherlands, 1995
2. N. Srinivas, Kalyanmoy Deb, Multiobjective Optimization using Non-dominated sorting in Genetic Algorithms, 1994
3. Deb, K., Pratap, A., Agarwal, S. and Meyarivan, T. A fast and elitist multiobjective genetic algorithm: NSGA-II. Evolutionary Computation, IEEE Transactions on, 6, 2 (2002)
4. Wang X, Hirsch C, Kang S, Lacor C. Multi-objective optimization of turbomachinery using improved NSGA-II and approximation model. Computer Methods in Applied Mechanics and Engineering. 2011;200(9-12):883-95.
5. Bellary SAI, Adhav R, Siddique MH, Chon B-H, Kenyery F, Samad A. Application of computational fluid dynamics and surrogate-coupled evolutionary computing to enhance centrifugal-pump performance. Engineering Applications of Computational Fluid Mechanics. 2016;10(1):171-81.
6. Niemann, S., Kolesnikov, B., Lohse-Busch, H., Hühne, C., Querin, O.M., Toropov, V.V. and Liu, D., 2013. The use of topology optimisation in the conceptual design of next generation lattice composite aircraft fuselage structures. *The Aeronautical Journal*, 117(1197), pp.1139-1154.

```

function [y, cons] = TP_CONSTR_objfun(x)
[Ane, Ate]= elliptical (x);
Abo=pi*x(1)*x(2); An=integral(Ane,-x(3),0);Ata=integral(Ate,-x(4),0);
Awis= ((x(5)/4)+1.5)*(x(5)/2);
Awint= (2*((x(5)/2)/sind(x(6)))+1.5)*0.75;
Awi=Awis+2*Awint; Astas= ((x(7)/2.5)+1.5)*(x(7)/2);
Astat=(2*((x(7)/2)/sind(x(8)))+1.5)*0.4;
Asta=Astas+2*Astat; Arus=((x(9)/1.2)+1.5)*x(9)/2;
Arut=(2*((x(9)/2)/sind(x(10)))+1.5)*0.3;
Aru=Arus+Arut; En= (1.5/2)^2*pi*3;
tbl = readtable('test2.xlsx','range','A1:K101','ReadVariableNames',false);
tbl.Properties.VariableNames =
{'X1','X2','X3','X4','X5','X6','X7','X8','X9','X10','drag'};
gprMd =
fitrgp(tbl,'drag','KernelFunction','squaredexponential','FitMethod','fic','Predict
Method','exact','Standardize',1);
C={x(1),x(2),x(3),x(4),x(5),x(6),x(7),x(8),x(9),x(10),[]};
T = cell2table(C);
T.Properties.VariableNames =
{'X1','X2','X3','X4','X5','X6','X7','X8','X9','X10','drag'};
y = [0,0,0];
cons = [0,0];
y(1) = predict(gprMd,T);
y(2) =
((x(11)/(x(11)+x(12)+x(13)))*1750+(x(12)/(x(11)+x(12)+x(13)))*2800+(x(13)/(x(11)+x
(12)+x(13)))*7850)*0.5*((Abo)+(abs(An))+(abs(Ata))+(2*Awi)+(2*Asta)+(2*Aru)+(2*En
));
y(3) =
((x(11)/(x(11)+x(12)+x(13)))*1750*6.38+(x(12)/(x(11)+x(12)+x(13)))*2800*1.38+(x(13
)/(x(11)+x(12)+x(13)))*7850*0.3)*(0.5*((Abo)+(abs(An))+(abs(Ata))+(2*Awi)+(2*Asta
)+(2*Aru)+(2*En)));
c(1)= x(1)*(x(2)/2)^2*pi;
c(2)= x(1)*(x(2)/2)^2*pi;
%c(3)= y(3);
if(c(1)<150)% new deisgn has a lower payload than the original Boeing 737 100
cons(1) = abs(c(1)-150)*100000;
if (c(2)>=150)
cons(2)=150/((abs(c2)-150)*100000);
end
%if (c(3)<=0)
% cons(3)=0.001/((abs(c2)-150)*100000);
%end
end
clear All
boundary
options = nsgaopt(); % create default options structure
options.popsize = 100; % populaion size
options.maxGen = 100; % max generation
options.numObj = 2; % number of objectives
options.numVar = 13; % number of design variables
options.numCons = 2; % number of constraints
options.lb = lb; % lower bound of x
options.ub = ub; % upper bound of x
options.objfun = @TP_CONSTR_objfun; % objective function handle
options.plotInterval = 5; % interval between two calls of
"plotnsga".
result = nsga2(options); % begin the optimization!
%plotting
%optimisation_history
function varargout = plotnsga(varargin)
gui_Singleton = 1;
gui_State = struct('gui_Name', mfilename, ...
'gui_Singleton', gui_Singleton, ...
'gui_OpeningFcn', @plotnsga_OpeningFcn, ...
'gui_OutputFcn', @plotnsga_OutputFcn, ...
'gui_LayoutFcn', [], ...

```

```

'gui_Callback', []);
if nargin && ischar(varargin{1})
    gui_State.gui_Callback = str2func(varargin{1});
end
if nargin
    [varargout{1:nargout}] = gui_mainfcn(gui_State, varargin{:});
else
    gui_mainfcn(gui_State, varargin{:});
end
function plotnsga_OpeningFcn(hObject, eventdata, handles, varargin)
handles.output = hObject;
guidata(hObject, handles);
handles.bLoadFromFile = 0;
if( isempty(varargin) )
    error('PLOTNSGA:ParamError', 'Error: plotnsga should be called :
plotnsga(result, curGen) or plotnsga(''pops.txt'')');
elseif(length(varargin) == 1)
    if( isstruct(varargin{1}) )
        handles.result = varargin{1};
        handles.currentGen = 1;
        elseif( ischar(varargin{1}) )
            global oldresult;
            oldresult = loadpopfile(varargin{1});
            evalin('base', 'global oldresult');

            handles.bLoadFromFile = 1;
            handles.strPopFile = varargin{1};
            handles.result = oldresult;
            handles.currentGen = 1;
        end
    elseif(length(varargin) == 2)
        if( isstruct(varargin{1}) && isscalar(varargin{2}) )
            handles.result = varargin{1};
            handles.currentGen = varargin{2};
        else
            error('PLOTNSGA:ParamError', ...
                'Error: plotnsga should be called : plotnsga(result, curGen) or
plotnsga(''pops.txt'')');
        end
    end
popsize = size(handles.result.pops, 1);
strList = repmat({''}, [1,popsize]);
for i = 1:popsize
    strList{i} = sprintf('%d', i);
end
curSel = handles.currentGen; set(handles.listPop, 'string', strList);
set(handles.listPop, 'value', curSel);
dispState(handles, curSel);
plotPopulation( handles, curSel );
guidata(hObject,handles);
function varargout = plotnsga_OutputFcn(hObject, eventdata, handles)
varargout{1} = handles.output;
function btnStop_Callback(hObject, eventdata, handles)
global STOP_NSGA;
STOP_NSGA = 1;
function btnPause_Callback(hObject, eventdata, handles)
if isempty(getappdata(0,'gadsSolverState'))
    setappdata(0,'gadsSolverState','pause');
    set(hObject,'String','Continue');
    waitfor(hObject,'String');
else
    setappdata(0,'gadsSolverState','');
    set(hObject,'String','Pause');
end
end

```

ON THE INFLUENCE OF FIBRES ON TENSILE LAPS OF REINFORCEMENT LOOPS

P. Grassl

School of Engineering, University of Glasgow, G133RX

peter.grassl@glasgow.ac.uk

Summary

In reinforced concrete structures, connections between members are often critical for the performance in the ultimate limit state. The most common approach to provide force transfer across the connection is to overlap reinforcement bars to form a lap splice. Here, looped reinforcement laps subjected to tension were studied using a three-dimensional nonlinear finite element approach. For the constitutive model of concrete, a damage-plasticity approach was used. In this model, the input for the tensile response is given in the form of a stress versus crack-opening curve, which, for the case of concrete with fibres, is adjusted to consider the bridging effect of fibres. The influence of lap length and fibres on the mechanical response was investigated. The numerical results show that fibres significantly increase the strength and ductility of lap splices.

Key Words: *reinforcement loops, lap splices, reinforced concrete, cracking*

Introduction

Force transfer between members of reinforced concrete structures is commonly provided by reinforcement lap splices. Understanding the failure process of these lap splices is important for being able to develop design approaches which can be used with confidence. In tensile lap splices made of reinforcement loops, the loop provides additional force transfer which reduces the overall lap length required. However, for these loop laps, complex failure processes involving spalling of the concrete cover have been reported in experiments [2].

For understanding the nonlinear response of reinforced concrete structures, the nonlinear finite element method provides a powerful tool. By modelling separately the nonlinear response of concrete, steel and bond between concrete and steel, it is possible to provide a better understanding of the processes which govern the often highly nonlinear composite response. This analysis strategy relies on robust numerical techniques, and constitutive models, which describe the material responses well.

In the present study, the nonlinear finite element method was used to study failure process of tensile laps made of reinforcement loops. The main aim is to investigate the influence of fibres in concrete on the response of the tensile laps of reinforcement loops. This work complements recent research in which the influence of fibres on straight tensile laps was studied [4].

Method

For the nonlinear finite element analysis of tensile lap splices of reinforcement loops, an explicit dynamic solution approach with an incremental displacement control was applied. For concrete, constant stress tetrahedral finite elements with the damage-plasticity constitutive model CDPM2 [5] were used. Reinforcement was modelled by frame elements which were positioned independently of the finite element mesh of concrete. The constitutive model for the reinforcement was chosen to be elasto-plastic without hardening. The interaction between concrete and reinforcement was modelled by linking the degrees of freedom of frame elements to those of the concrete elements [8], with a bond-slip law between reinforcement and concrete.

For the concrete constitutive model CDPM2, the stress evaluation is based on the concept of damage mechanics concept with nominal and effective stress. The nominal stress is evaluated by a combination of damage and plasticity, whereas the effective stress in the undamaged material is determined using

plasticity only. For the nominal stress evaluation, tensile and compressive damage variables are applied to positive and negative components of the principal effective stress, respectively. The function for the tensile damage variable is derived from a bilinear stress-crack opening ($\sigma-w_c$) curve, so that the results of analyses of tensile failure in which strains localise in mesh-dependent regions are independent of the finite element mesh [1]. For fibre reinforced concrete, the parameters of the stress-crack opening curve were adjusted to consider the bridging stress of the fibres [6, 7]. Here, it was assumed that the steel fibres, which bridge cracks, are pulled out of the concrete, but do not yield. The presence of small steel fibre volume ratios considered in this study resulted in a small increase of the tensile strength, and a very large increase of the crack opening at which the stress becomes zero. This is also in agreement with meso-scale simulations carried out in [3].

Analyses and results

The tensile specimen consists of two pairs of symmetrically arranged overlapping reinforcement loops embedded in concrete (Figure 1).

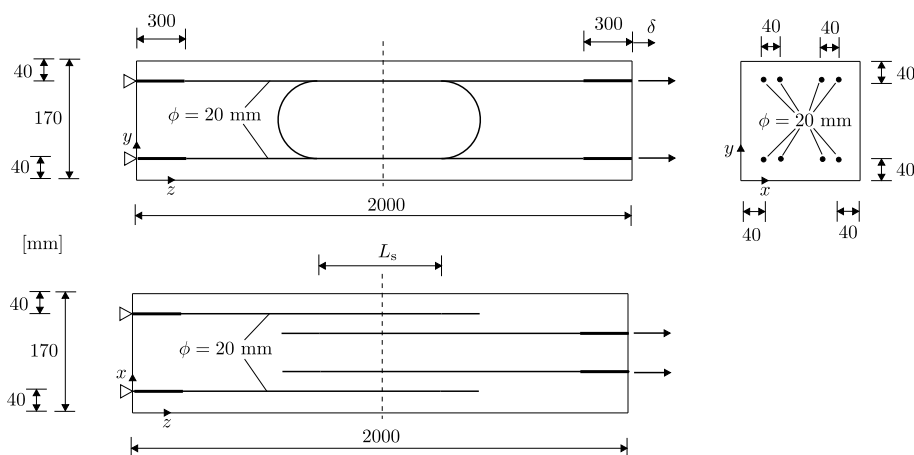


Figure 1: Geometry of splicing of reinforcement loops in direct tension.

In this short paper, selected results for one short lap length $L_s = 300$ mm with and without fibres are shown in the form of normalised load-displacement curves (Figure 2) and maximum principal strain contour plots representing cracks (Figure 3) for stages marked in Figure 2. The load and displacement are normalised by the force and displacement of four continuous reinforcement bars at yielding, respectively.

For concrete without fibres, the peak load is reached before the reinforcement bars yield, which indicates that the strength of the lap limits the overall strength of the specimen. The post-peak response is characterised by a reduction of load with increasing displacements. The crack patterns for the loop splices without fibres show the formation of longitudinal (in the direction of loading) splitting cracks within the lap length (Figure 3a). These cracks represent spalling planes which were experimentally reported in [2]. Outside the lap zone, tensile cracks perpendicular to the load direction are visible.

For concrete with fibres, the peak load exceeds the yield load of the reinforcement. In the post-peak regime, the load remains constant. This response indicates that yielding of the reinforcement limits the strength of the specimen. The maximum load is greater than the yield load of the steel bars, since the bridging stress of steel fibres across cracks contribute to the load transfer. Outside the lap zone, the tensile cracks perpendicular to the load direction have a smaller spacing than for plain concrete. Inside the lap region, almost no longitudinal cracks are visible.

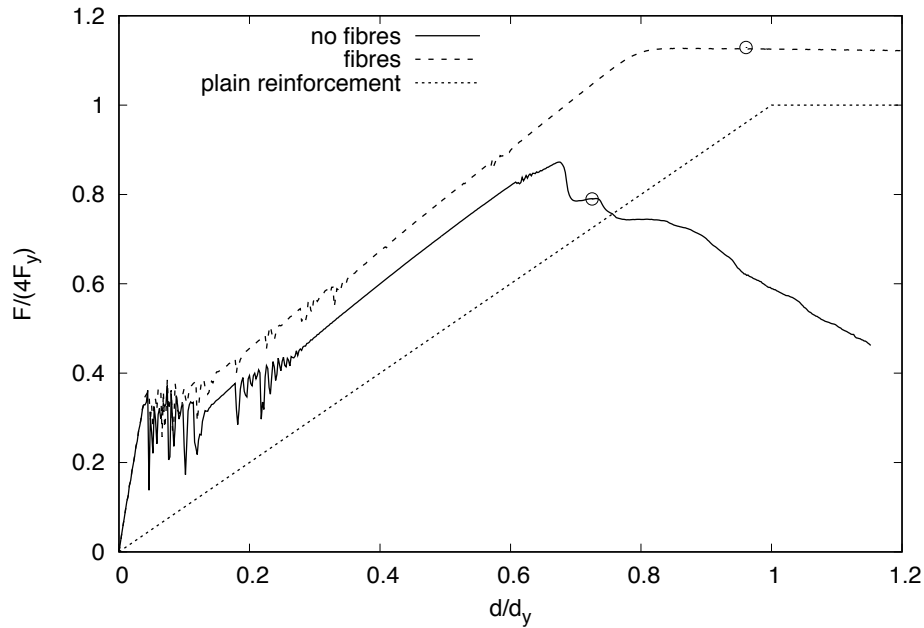


Figure 2: Load-displacement curves for lap splices of reinforcement loops in concrete with a lap length of $L_s = 300$ mm with and without fibres obtained from nonlinear finite element analyses with the concrete damage plasticity model CDPM2.

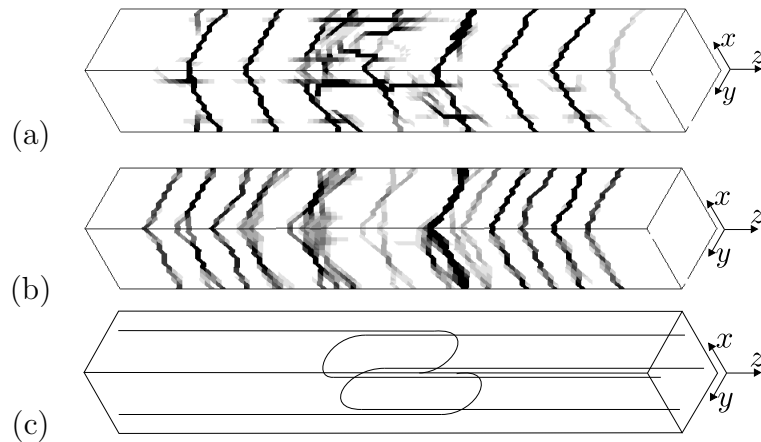


Figure 3: Contour plots of the maximum principal strain for lap splices (a) without fibres and (b) with fibres. Black indicates strains which correspond to crack openings greater than 0.3 mm. The geometry of the loops is shown in (c).

The differences in the crack patterns are further elucidated in Figure 4 by showing plots of only those elements with a maximum principal strain corresponding to a crack opening greater than 0.2 mm for stages marked in Figure 2. For concrete without fibres, the crack plane along the edge of specimen within the lap length is clearly visible, which indicates the onset of spalling.

For the low volume fraction of steel fibres ($V_f = 1\%$) used, the peak stress in tension is not significantly increased ($f_t = 3.22$ MPa for fibre reinforced concrete versus $f_t = 3$ MPa for plain concrete). Still, the bridging stress after cracking is sufficient to prevent spalling and to change considerably the crack pattern.

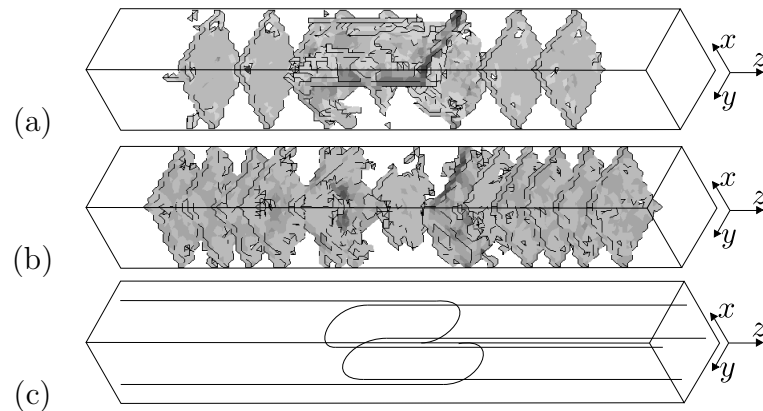


Figure 4: Finite elements with a maximum principal strain corresponding to a crack opening greater than 0.2 mm for lab splices (a) without fibres and (b) with fibres. The geometry of the loops is shown in (c).

Conclusions

The present nonlinear finite element analyses of a short lap splice of reinforcement loop in both plain and steel fibre reinforced concrete showed that 1 % of volume fraction of steel fibres has a strong influence on the mechanical response. For plain concrete, spalling cracks resulted in an abrupt drop of the load before yield load of the reinforcement could be reached. On the other hand, for steel fibre reinforced concrete, spalling was prevented so that yielding of the reinforcement occurred.

References

- [1] Bažant, Z. P. and Oh, B.-H. Crack band theory for fracture of concrete. *Materials and Structures*, 16:155–177, 1983.
- [2] Grassl, P. Splicing of reinforcement loops in beams: Experiments and non-linear finite element analyses. MSc thesis, Chalmers University of Technology, Göteborg, Sweden, 1999.
- [3] Grassl, P. and Antonelli, A. 3D network modelling of fracture processes in fibre-reinforced geomaterials. *International Journal of Solids and Structures*, 156-157:234–242, 2019.
- [4] Grassl, P. and Middlemiss, J. Finite element modelling of tensile reinforcement laps in steel fibre reinforced concrete. In *SEMC 2019: The seventh international conference on structural engineering, mechanics and computation*, 2019.
- [5] Grassl, P.; Xenos, D.; Nyström, U.; Rempling, R., and Gylltoft, K. CDPM2: A damage-plasticity approach to modelling the failure of concrete. *International Journal of Solids and Structures*, 50 (24):3805–3816, 2013.
- [6] Naaman, A. E. High performance fibre reinforced cement composites. *IABSE reports*, 55:371–376, 1987.
- [7] Naaman, A. E.; Namur, G. G.; Alwan, J. M., and Najm, H. S. Fiber pullout and bond slip. I: Analytical study. *Journal of Structural Engineering*, 117(9):2769–2790, 1991.
- [8] Phillips, D. V. and Zienkiewicz, O. C. Finite element non-linear analysis of concrete structures. In *Institution of Civil Engineers, Proceedings*, volume 61, 1976.

Challenges associated with finite element methods for forward modelling of unbounded gravity fields

Twana Kamal Haji*, Asaad Faramarzi
Farough Rahimzadeh, Nicole Metje, David Chapman
School of Engineering, College of Engineering and Physical Sciences,
University of Birmingham, Edgbaston, Birmingham, B15 2TT, United Kingdom
* t.k.haji@bham.ac.uk

April 2019

Abstract

Gravity forward modelling is the calculation of gravity field from a specific density distribution, and is essential for reconstructing ground density in an inversion process. Finite element (FE) methods have been effectively used for forward modelling of gravity data. In contrast to the closed-form and analytical methods, FEM can model complicated geometries and density distributions. Since the gravity field is an unbounded domain, numerical modelling of the boundary condition is the main challenge associated with the FE formulation of the gravity data. In the majority of numerical cases, the domain of the gravity is truncated at a relatively far distance from the zone of density contrast in order to reduce the effect of the boundary conditions on the results. Some researchers have applied a zero gravitational potential value to the boundary while others have applied an estimated gravitational potential value to the truncated edges. In both cases, a large zone of zero-density contrast has to be added around the zone of density contrast which considerably increases the computational time. Another type of the boundary condition, which is less developed in the field of gravity modelling, is the use of a single layer of infinite elements around the zone of density contrast to model the boundary. The scope of this paper is the discussion and comparison of the aforementioned types of modelling boundary conditions in FE analyses with respect to gravity field modelling. The advantages and disadvantages of each method, especially the infinite element boundary over the truncation methods, are presented. The results show that a trade-off between the size of the additional zero density zone around the zone of density contrast, and the meshing element sizes is essential for the truncation methods. Furthermore, the infinite element boundary is shown to have great potential to overcome the computational issues related to the truncation methods. A high accuracy in the results with less computational time can be obtained using infinite elements.

Keywords: gravity forward modelling, Finite element analysis, Boundary conditions, Infinite elements

1. Introduction

Modelling of gravity plays an important role to solve different issues, such as identifying and locating buried objects. Gravity values can be predicted from a specific distribution of ground density in a process called forward modelling of gravity data. Forward modelling is an essential stage of the inversion process in which the subsurface density is reconstructed using a non-destructive approach. Different methods can be used for gravity forward modelling, including closed-form solutions and numerical methods.

Numerical methods contain different techniques one of which is the finite element (FE) method, which is a powerful technique used for forward modelling of gravity. The importance of FE analysis becomes vital when the geometry of the problem and the density distribution are complicated. In such cases, the complexity of the problem makes it impossible to use simplified methods or closed-form solutions [2].

This paper is focused on the use of FE analysis for forward modelling of gravity, considering three different techniques within the FE method. The difference between the three techniques is related to the way the boundary conditions of the gravity field is modelled, since gravity is an unbounded problem. Background to the use of FE analysis, including the gaps in knowledge, is presented in Section 2. Utilising a set of rigorous numerical simulations, this work aims to evaluate the performance of FE methods to model gravity, and to introduce robust indicators to improve the numerical outcomes when using them for gravity forward modelling.

2. Background

FE modelling of gravity, as opposed to closed-form solutions, initially solves the gravitational potential, and then calculates the gravity values from the gradient of the potential field. This needs a solution for

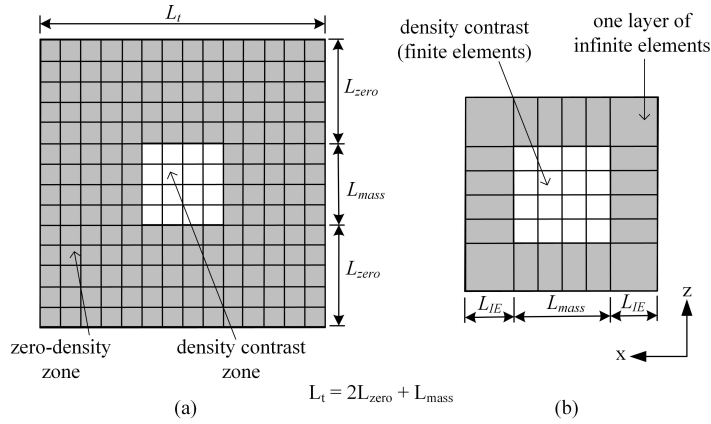


Figure 1: A typical numerical domain for (a) the truncation boundary and (b) an infinite element boundary (L_{mass} and L_{zero} are the lengths of the density contrast and the zero-density zones, respectively, and L_{IE} is the length of infinite elements)

an unbounded problem. The main concern associated with the FE modelling of such problems is the simulation of the boundary conditions since theoretically, it extends to infinity.

The truncation of the boundary at a far, but finite, distance from the zone of density contrast is the most popular technique used for the forward modelling of gravity. The space from the edge of the density contrast zone to the truncated boundary of the whole domain needs to be modelled with zero-density elements (zero-density here means no contrast within the density distribution). At the truncated boundary, either a zero gravitational potential is applied, as used by Jahandari and Farquharson [4] and Zhang et al. [8], or the gravitational potential is estimated and applied to the boundary, as proposed by Cai and Wang [2]. In the rest of this paper, the former method is called the zero-potential boundary, and the latter is called the Cai and Wang method. A typical numerical model of the truncation boundary is shown in Figure 1a. It is worth noting that a comparison of these two boundary modelling methods was made by May and Knepley [7] in their paper about forward models for the calculation of gravity anomalies. Their focus was mainly on the effect of the domain size on the results. A trade-off between the domain size and the mesh fineness, and the influence of the element size outside the zone of density contrast on the results were not discussed.

Another type of boundary condition, simulated with one layer of infinite elements around the zone of density contrast, was used by Gharti and Tromp [3] to model gravity in a spherical domain. It should be mentioned that this method is less developed in the field of gravity modelling. Furthermore, no comparison of this method with the truncation techniques is available in the literature.

This paper presents the results from a series of analyses investigating the infinite element boundary condition. A brief methodology of the numerical simulation of this boundary is presented in Section 3. Figure 1b shows a typical numerical domain with an infinite element boundary.

3. Methodology and Model Description

For details of the simulations by Cai and Wang, the reader is referred to reference [2] who originally proposed the method. This section presents some insight into the formulation of 2D infinite elements, which is then followed by a description of the model used in this paper.

The aim behind using infinite elements to model boundaries is that the infinity nature of the unbounded domains can be reproduced using only one layer of elements that have special types of shape functions. The coordinate ascent approach, in which an infinite element is compressed to become a conventional finite element [5], was used to formulate infinite elements in this paper.

The difference between a conventional finite element analysis and an infinite element formulation is the type of shape functions used to form the Jacobian matrix for the conversion between the global and local coordinate systems. In the local coordinate system, finite element shape functions are used to interpolate the field variables (in the case of gravity modelling, the gravitational potential, Φ). It is worth noting that when simulating infinite elements, an arbitrary position called the pole has to be specified. This position is used to find the length of the infinite elements, however it is not explicitly modelled. There is not a specific criterion to accurately determine the pole position. The factors that help with specifying this position include engineering knowledge, the problem characteristics (geometrical and physical), and fit to the decay pattern. More details about the pole position can be found in [6] and [9]. In this work, the

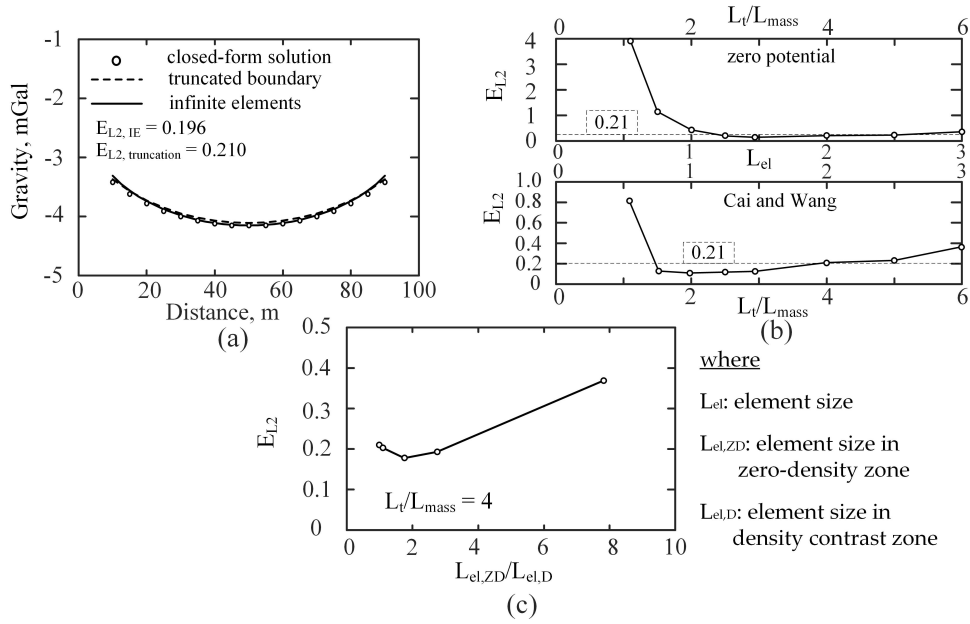


Figure 2: (a) Gravity values predicted by the infinite element and truncated boundary methods, (b) the combined effect of the mesh fineness and zero-density size, and (c) the effect of mesh non-uniformity on the truncated boundary results

infinite element formulation proposed by Marques and Owen [6] was used to model the boundary of the problem.

To simplify the problem and to focus on the intended aim of the paper, a simple domain of density contrast was simulated that had dimensions of $100 \text{ m} \times 100 \text{ m}$ (i.e. $L_{mass} = 100 \text{ m}$ in Figure 1), and a uniform density contrast of 1800 kg/m^3 . In all cases, the domain was discretised using 2D square elements with 4 nodes at their corners. All the numerical simulations were performed using MATLAB. Observation points were located at the top of the density contrast zone, starting from $x_{mass} = 10 \text{ m}$ to $x_{mass} = 90 \text{ m}$ where x_{mass} is the horizontal distance along the zone of the density contrast. The element and domain sizes were variable. Extra information is presented in Section 4 where the results are discussed. It should be mentioned that for the infinite element model, one layer of infinite elements were used to model the boundary of the problem. The length of these elements was 22.5 m (obtained from comparing the numerical results to the exact solution of the problem).

In order to validate the results, an exact solution of the problem was calculated using Equation 1 [1]. Furthermore, the error between the numerical and synthetic data was calculated using the L_2 norm, Equation 2.

$$g_{synth} = 2G\rho \iint \frac{z}{r^2} dx dz \quad (1)$$

$$E_{L_2} = \sqrt{\sum_{i=1}^{n_m} |g_{num,i} - g_{synth,i}|^2} \quad (2)$$

where $g_{synth,i}$ is the synthetic gravity at i^{th} observation point, G is Newton's gravitational constant, ρ is the density, z is the vertical distance, r is the distance between the mass and the observation point, n_m is the number of measurement points, and g_{num} is the gravity values computed numerically (i.e. FEM).

4. Results & discussion

Figure 2a shows the gravity prediction and L_2 error for the different numerical techniques. The zero-density size in the truncation methods was $L_t/L_{mass} = 4$ (L_t is the length of the whole numerical domain, as shown in Figure 1). The numerical domain was meshed uniformly with elements of 2 m side length. The total number of elements was $2,704$ and $40,000$ in the infinite element boundary and truncation methods, respectively. Figure 2a also states that $E_{L_2} = 0.196$ and 0.210 , respectively for the infinite element and the truncation boundaries. For the same meshing resolution, the infinite element boundary gives slightly better results than the truncation method, while using considerably fewer elements.

The results of Figure 2a indicate that substantially less computational cost is involved when modelling gravity using an infinite element boundary. It should be noted that when using infinite elements, the

choice of a suitable pole position has to be made carefully due to its impact on the results. In addition, for more complicated gravity problems, non-linear shape functions for the infinite elements could improve the results significantly.

Figure 2b presents the combined effect of the element and zero-density domain sizes on the results of the truncation boundaries. The total number of elements for all the simulations in Figure 2b was 40,000. The meshing was gradually made coarser as the zero-density domain was added to the model. The magnitude of E_{L_2} is large when there is no zero-density domain, despite having a very fine mesh in the zone of the density contrast. Adding the zero-density domain reduces the error up to a specific point (up to $L_t/L_{mass} = 2$ for the Cai and Wang method, and 3 for the zero-potential boundary). After this point, the error starts to bounce which shows the role of the element size in the analysis. It should be noted that after $L_t/L_{mass} = 4$, both the truncation methods give similar results.

The simulations linked with Figures 2a and 2b had uniform meshes throughout the domain whilst Figure 2c shows the results with non-uniform meshing. Figure 2c displays the effect of the element size in the zero-density domain on the results for the truncation methods with $L_t/L_{mass} = 4$. All the simulations are for a constant element number of 40,000. Figure 2c shows that the results improve as the ratio of the element size of the zero-density to that of density contrast zone, $L_{el,ZD}/L_{el,D}$, increases up to 1.75. After this point, an increase in the $L_{el,ZD}/L_{el,D}$ ratio results in a larger error. This effect is the same for both truncation methods, and shows that non-uniformity meshing could be helpful to improve the results.

5. Conclusions

This paper has presented insights into the forward modelling of gravity data using finite element methods with three types of boundary formulations: infinite elements, zero-potential and the Cai and Wang methods. The results showed that the infinite element boundary presented accurate predictions of gravity data with fewer elements compared to the zero-potential and Cai and Wang methods. This could lead to a considerable reduction in computational cost if proper infinite element shape functions and accurate pole positions are used.

Regarding the zero-potential and Cai and Wang methods, it was shown that a trade-off between the element size and the size of the zero-density domain is necessary to obtain optimal results. Furthermore, the results showed that the meshing does not need to be uniform throughout the domain. A finer mesh within the zone of the density contrast improves the gravity prediction of the truncation methods up to a specific limit. This limit can be determined by finding an optimal ratio between the element sizes within and outside the zone of the density contrast.

Acknowledgements

The authors would like to acknowledge the funding received for this project from QT Hub for Sensors and Metrology (EP/M013294), and EPSRC, and Innovate UK funded project (EP/R043574), and the support received from the OXEMS Limited.

References

- [1] R. J. Blakely. *Potential theory in gravity and magnetic applications*. Cambridge university press, 1996.
- [2] Y. Cai and C.-y. Wang. Fast finite-element calculation of gravity anomaly in complex geological regions. *Geophysical Journal International*, 162(3):696–708, 2005.
- [3] H. N. Gharti and J. Tromp. A spectral-infinite-element solution of poisson’s equation: an application to self gravity. *arXiv preprint arXiv:1706.00855*, 2017.
- [4] H. Jahandari and C. G. Farquharson. Forward modeling of gravity data using finite-volume and finite-element methods on unstructured grids. *Geophysics*, 78(3):G69–G80, 2013.
- [5] P. Kumar. Static infinite element formulation. *Journal of structural engineering*, 111(11):2355–2372, 1985.
- [6] J. Marques and D. Owen. Infinite elements in quasi-static materially nonlinear problems. *Computers & structures*, 18(4):739–751, 1984.
- [7] D. A. May and M. G. Knepley. Optimal, scalable forward models for computing gravity anomalies. *Geophysical Journal International*, 187(1):161–177, 2011.
- [8] J. Zhang, C.-Y. Wang, Y. Shi, Y. Cai, W.-C. Chi, D. Dreger, W.-B. Cheng, and Y.-H. Yuan. Three-dimensional crustal structure in central taiwan from gravity inversion with a parallel genetic algorithm. *Geophysics*, 69(4):917–924, 2004.
- [9] O. Zienkiewicz, C. Emson, and P. Bettess. A novel boundary infinite element. *International Journal for Numerical Methods in Engineering*, 19(3):393–404, 1983.

MODELLING AND COMPUTATION OF THE THERMOELASTIC RESPONSE OF THE SKIN AT FINITE STRAINS WITH NON-FOURIER EFFECTS

***Mebratu F. Wakeni¹, B. Daya Reddy² and Andrew T. McBride³**

^{1,3}Glasgow Computational Engineering Centre, Infrastructure and Environment, School of Engineering, The University of Glasgow, Glasgow G12 8QQ, United Kingdom

^{1,2,3}Centre for Research in Computational and Applied Mechanics (CERECAM), University of Cape Town, 7701 Rondebosch, South Africa

^{1,2}Department of Mathematics and Applied Mathematics, University of Cape Town, 7701 Rondebosch, South Africa

*mebratu.wakeni@glasgow.ac.uk

Summary

The coupling of the generalized, nonlinear thermal model accounting for non-Fourier effects and mechanical deformation at finite strains is applied to analyse the coupled response of human skin. Linearisation of the thermal part of the model gives the widely-used, classical thermal conduction model based on Fourier's law. A space-time discontinuous Galerkin (DG) finite element method with a staggered algorithm based on iso-entropy splitting is used for numerical realisation of the model [1, 5]. To illustrate the importance of the coupled response, a numerical example is considered in which a hot rigid indenter is in contact with the skin [3].

Key Words: *Non-Fourier; Finite strains; Iso-entropy splitting; Staggered algorithms; Space-time DG method*

Introduction

The Pennes equation [4] has been successfully used to model thermal transfer in biological tissues. It is based on the Fourier's law of heat conduction, along with various components accounting for external or internal thermal sources such as blood perfusion, sweating and surface cooling. However, non-Fourier effects such as wave mechanism of heat conduction have been observed experimentally in materials with non-homogeneous inner structure, which are similar in heterogeneity to biological tissue. Experimental results on biological tissue, for example [2], coupled with mathematical analysis have also shown that the temperature oscillation is better explained with the thermal wave analyses than the classical diffusion mechanism of thermal conduction by Fourier's law. The non-homogeneous inner structure together with the temperature oscillation commonly observed in biological tissue suggests the existence of a wave mechanism of thermal conduction in biological tissue. The problem of interest is the modelling of the skin tissue using the generalized (non-Fourier) thermoelastic model discussed in [5].

Governing equations and constitutive relations

Here the local form of the balance laws and the constitutive relations are summarised as follows. The balance of linear momentum, ignoring the inertial terms, reads as

$$\text{Div } \mathbf{P} + \mathbf{b} = 0, \quad (1)$$

where \mathbf{P} is the first Piola-Kirchhoffs stress tensor and \mathbf{b} denotes the body force.

The balance of energy (the first law of thermodynamics) in the strong form is expressed as

$$\Theta \dot{\eta} = -\text{Div } \mathbf{Q} + \Theta^{-1} \mathbf{Q}_E \cdot \nabla \Theta + \mathbf{r}, \quad (2)$$

where η is the entropy, \mathbf{Q} is the Piola heat flux vector, \mathbf{Q}_E is the energetic component of the heat flux, and \mathbf{r} is the heat source.

Motivated by the microscopic analysis of thermal propagation as phonon-phonon interaction model, we additively decompose the heat flux vector into energetic \mathbf{Q}_E and dissipative \mathbf{Q}_D components, that is,

$$\mathbf{Q} = \mathbf{Q}_E + \mathbf{Q}_D.$$

Moreover, following the Green-Naghdi theory, an additional scalar field quantity α , the so-called *thermal displacement*, is introduced and defined as $\dot{\alpha} = \Theta$.

Applying the local form of the second law of thermodynamics as free energy imbalance, the constitutive equations for \mathbf{P} , η , and \mathbf{Q}_E are derived from the free energy Ψ as

$$\mathbf{P} = \frac{\partial \Psi}{\partial \mathbf{F}}, \quad \eta = -\frac{\partial \Psi}{\partial \Theta}, \quad \text{and} \quad \mathbf{Q}_E = -\frac{\partial \Psi}{\partial \Lambda} \quad (3)$$

The thermodynamical restriction also imposes a type of Dhuvel's law inequality on the dissipative heat flux vector \mathbf{Q}_D , and with the assumption of isotropic conductivity, it is chosen to be

$$\mathbf{Q}_D = -J \kappa_d \mathbf{F}^{-1} \mathbf{F}^{-T} \nabla \Theta, \quad (4)$$

where κ_d is the spatial thermal diffusivity (accounting for the dissipative process).

The free energy for the generalized model can be written as

$$\Psi(\mathbf{F}, \Theta, \Lambda) = \hat{\Psi}(\mathbf{F}, \Theta) + \Psi^{NF}(\Lambda),$$

in which we assume a neo-Hookian type free energy for the classical part $\hat{\Psi}$ given by

$$\hat{\Psi}(\mathbf{F}, \Theta) = \frac{1}{2} \lambda (\ln J)^2 + \frac{1}{2} \mu [\mathbf{F} : \mathbf{F} - 3 - 2 \ln J] - 3 \omega \kappa \vartheta \frac{\ln J}{J} + c_F \left(\vartheta - \Theta \ln \left[\frac{\Theta}{\Theta_0} \right] \right) - \Xi_0 \vartheta,$$

where λ and μ are the Lamé constants, $\kappa = \lambda + \frac{2}{3} \mu$ is the bulk modulus, ω is the thermal expansion coefficient, and c_F is the specific heat capacity. Moreover, the non-Fourier contribution of the free energy is quadratic in Λ , given by

$$\Psi^{NF}(\Lambda) = \frac{1}{2} \kappa_e \Lambda \cdot \Lambda,$$

where κ_e is the energetic material thermal conduction coefficient.

Numerical discretisation

A stable staggered method is obtained by first decoupling the full problem using adiabatic operator split, into mechanical phase at constant entropy, i.e.,

$$\text{Div } \mathbf{P} + \mathbf{b} = 0, \quad \text{Subject to: } \dot{\eta} = 0, \quad (5)$$

and thermal phase of heat conduction under fixed configuration, i.e.,

$$\Theta \dot{\eta} = -\text{Div } \mathbf{Q} + \Theta^{-1} \mathbf{Q}_E \cdot \nabla \Theta + \mathbf{r}, \quad \text{Subject to: } \dot{\mathbf{u}} = \mathbf{0}. \quad (6)$$

The next step is to discretise the problems in each stage by an appropriate method to obtain stable schemes. Let the algorithm that transfers the solution of the mechanical problem from the time-step

t^n to t^{n+1} be denoted by \mathbb{A}_M , and correspondingly the algorithm to that of the thermal phase by \mathbb{A}_T . Then a stable first-order approximation can be obtained as the composition $\mathbb{A}_T^n \circ \mathbb{A}_M^n$ (referred to as *single pass*), that is,

$$\mathcal{X}^{n+1} = \mathbb{A}_T \circ \mathbb{A}_M(\mathcal{X}^n), \quad (7)$$

where \mathcal{X}^n represents the solution vector at the discrete time t^n .

In this work the sub-algorithms \mathbb{A}_M and \mathbb{A}_T are obtained by applying the space-time discontinuous Galerkin approach [6].

The discret problems corresponding to the algorithms \mathbb{A}_M and \mathbb{A}_T in the mechanical and thermal phase, respectively, are defined as

$$B_M(\bar{\mathcal{X}}^h, \mathcal{X}^h) = L_M(\bar{\mathcal{X}}^h), \quad \text{and} \quad B_T(\bar{\mathcal{X}}^h, \mathcal{X}^h) = L_T(\bar{\mathcal{X}}^h), \quad (8)$$

where

$$B_M(\bar{\mathcal{X}}^h, \mathcal{X}^h) = (\nabla \bar{\mathbf{u}}^h, \mathbf{P}^h)_\Omega, \quad \text{and} \quad L_M(\bar{\mathcal{X}}^h) = (\bar{\mathbf{u}}^h, \mathbf{b}) + (\bar{\mathbf{u}}, \mathbf{h})_{\Gamma_N \times [t^n, t^{n+1}]},$$

$$\begin{aligned} B_T(\bar{\mathcal{X}}^h, \mathcal{X}^h) &= \langle \bar{\alpha}^h(t^{n+}), \alpha^h(t^{n+}) \rangle + \langle \bar{\Theta}^h(t^{n+}), c_F \Theta^h(t^{n+}) \rangle + (\bar{\alpha}, \dot{\alpha}^h \text{Theta}^h) \\ &\quad + (\bar{\Theta}^h, c_F \dot{\Theta}^h - 1/\Theta^h \mathbf{Q}_E^h \cdot \nabla \Theta^h + \frac{\partial \mathbf{P}^h}{\partial \Theta^h} : \dot{\mathbf{F}}^h) - (\nabla \bar{\Theta}^h, \mathbf{Q}^h), \quad \text{and} \\ L_T(\bar{\mathcal{X}}^h) &= \langle \bar{\alpha}^h(t^{n+}), \alpha^h(t^{n-}) \rangle + \langle \bar{\Theta}^h(t^{n+}), c_F \Theta^h(t^{n-}) \rangle + (\bar{\Theta}^h, r), \end{aligned}$$

where the pairings (\cdot, \cdot) and $\langle \cdot, \cdot \rangle$ are integral inner-products over the space-time slab $\Omega \times [t^n, t^{n+1}]$ and the space Ω , respectively. The test and trial vector functions are represented by $\bar{\mathcal{X}}^h = (\bar{\mathbf{u}}^h, \bar{\alpha}^h, \bar{\Theta}^h)$ and $\mathcal{X}^h = (\mathbf{u}^h, \alpha^h, \Theta^h)$, respectively. For a detailed discussion of the formulation the method described in equation (4) the reader can refer the work by Wakeni et al [6].

Result

A cylindrical skin model consisting of four layers (namely, *Stratum Corneum*, *Epidermis*, *Dermis* and *subcutaneous fat*) having significantly differing mechanical and thermal properties is considered. The skin is subject to a hot indenter pressed down (frictionlessly) at a constant rate until the final depth of the indenter reaches 25%. The problem setup and parameters are taken from the paper by McBride et al [3]. In their work the thermomechanical response of the skin is modelled using the classical model. Exploiting the symmetry of the problem, the computational domain is a quarter of the full domain, as shown in Fig. 1.

Fig. 1 (c) & (d) show the temperature profile of four points each located at the mid-thickness of the layers along the axis of the cylinder. The temperature is tracked over the duration of the simulation and is calculated using the generalised and classical models. It is obtained that the result displayed in (d) is in good agreement with the literature. As expected the result in (c) shows non-Fourier behaviour.

Conclusion

The generalized model better explains the thermal oscillations observed in heterogeneous biological tissues. The staggered algorithm is unconditionally stable, however, it is limited to first-order despite the fact that the space-time DG discretisation of the subproblems is higher-order.

Acknowledgements

This work has been supported by the National Research Foundation of South Africa through the South African Chair in Computational Mechanics. This support is acknowledge with thanks.

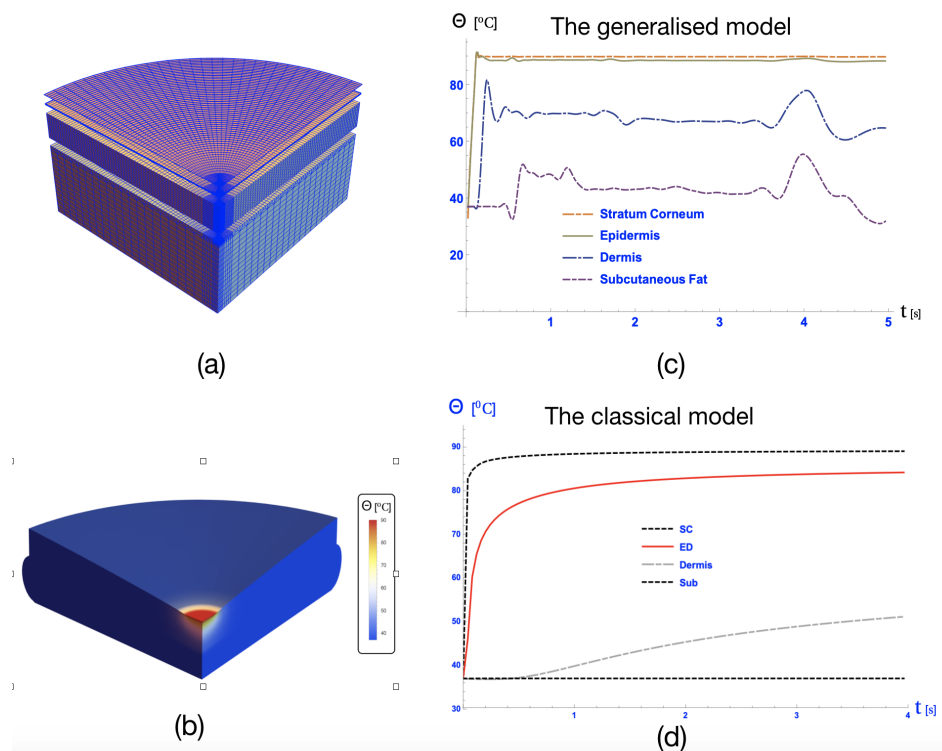


Figure 1: Thermal conduction in a skin specimen. (a) is the computational domain composed of the four layers, the gaps between layers shown are only for visualization purpose, (b) shows the temperature distribution in the specimen at the final time, (c) and (d) show the temperature profile of the four points along the axis of the cylinder each at the mid of each layer based on the generalised and the classical models, respectively.

References

- [1] F. Armero and J. C. Simo. A new unconditionally stable fractional step method for non-linear coupled thermomechanical problems. *International Journal for Numerical Methods in Engineering*, 35, 737–766, 1992.
- [2] H. Herwig and K. Beckert. Experimental evidence about the controversy concerning Fourier or non-Fourier heat conduction in materials with a nonhomogeneous inner structure. *Heat and Mass Transfer*, 36(5), 387–392, 2000.
- [3] A. T. McBride, S. Bargmann, D. Pond. and G. Limbert. Thermoelastic modelling of the skin at finite deformations. *Journal of Thermal Biology*, 62(part B), 201–209, 2016.
- [4] H.H. Pennes. Analysis of tissue and arterial blood temperatures in the resting human forearm. *Journal of applied physiology*, 1(2), 93–122, 1948.
- [5] M. F. Wakeni, B. D. Reddy, B and A. T. McBride. (2015). A thermodynamically consistent formulation of generalized thermoelasticity at finite deformations. *International Journal of Engineering Science*, 108, 1–8, 2016.
- [6] M.F. Wakeni, B. D. Reddy and A. T. McBride. An unconditionally stable algorithm for generalized thermoelasticity based on operator-splitting and time- discontinuous Galerkin finite element methods. *Computer Methods in Applied Mechanics and Engineering*, 306:425–451, 2016.

Non-linear upper bound failure mechanism analysis

A non-linear power-law failure criterion may be expressed as [1],

$$\tau = c_0(a + \sigma_n/\sigma_t)^{1/m} \quad (1)$$

In this study three exemplar materials will be modelled: (i) a loose sand (after [2] using a relative density index $I_D = 0$), (ii) a tropical lateritic clay (after [1]), and (iii) a Tresca material representing a metal with a shear strength 300 MPa. For a non-linear material any given slip-line separating two rigid bodies will normally be curved as shown in the kinematics in Fig.1 and may be described by a function $\eta = f(\xi)$, where for convenience the axes are aligned with the velocity jump across the slip-line. To ensure a kinematically compatible rigid block mechanism, in combination, the local dilation and the gradient of the curve must sum to a constant global secant dilation ψ_s which determines the general form of the curve. Following [6], the local dilation angle ψ at any point on a slip-line may be given by:

$$\tan \psi = \frac{d\tau}{d\sigma_n} = \frac{c_0(a + \sigma_n/\sigma_t)^{\frac{1-m}{m}}}{m\sigma_t} \quad (2)$$

Noting that $\cot \psi = \kappa f'(\xi)$, the normal stress at any point on the slip-line can be given by,

$$\sigma_n = -a \cdot \sigma_t + \sigma_t \left(\frac{c_0}{m\sigma_t} \right)^{\frac{m}{m-1}} [\kappa f'(\xi)]^{\frac{m}{m-1}} \quad (3)$$

where $\kappa = 1$ for the passive case and $\kappa = -1$ for the active case. Substituting Eq.(3) in Eq.(1) allows the shear stress also to be determined as follows:

$$\tau = c_0 \left(\frac{c_0}{m\sigma_t} \right)^{\frac{1}{m-1}} [\kappa f'(\xi)]^{\frac{1}{m-1}} \quad (4)$$

A conventional wedge type kinematic analysis may then be carried out using the secant AB to the curve, a coefficient of dissipation $\hat{C}(\psi_s, \theta, l)$ and a correction to the wedge weight above the secant $\hat{W}(\psi_s, \theta, l)$ to allow for the curvature of the line. \hat{C} is equivalent to the term cl for the linear case. Variational approaches are then used to determine the specific form of the curve that minimises the energy dissipation. These functions are straightforward to compute using a computer program [6].

Example problems

Three example problems are considered, active and passive smooth retaining walls retaining soil and the kinematically similar case of orthogonal metal cutting. The principles of the approach will be developed for the former as follows. Consider a frictionless vertical wall of height H with horizontal active or passive load F , and a surface surcharge q with a single wedge at angle θ to the horizontal and of area $0.5H^2/\tan \theta$ as shown in Fig.2 together with the hodograph. The slip-line length $l = H/\sin \theta$.

If the global dilation is assumed to be ψ_s , and the wedge moves at a velocity v_0 at an angle $\theta + \kappa\psi_s$ to the horizontal, the full energy equation may be expressed as [6]:

$$F\kappa v_0 \cos(\theta + \kappa\psi_s) = \left[\frac{H^2\gamma}{2 \tan \theta} - \kappa \hat{W}(\psi_s, \theta, l) + \frac{qH}{\tan \theta} \right] \kappa v_0 \sin(\theta + \kappa\psi_s) + \hat{C}(\psi_s, \theta, l) v_0 \cos \psi_s \quad (5)$$

This is identical to a conventional linear analysis with the addition of the \hat{W} term and the replacement of the cl term by \hat{C} . To find the optimal upper bound, it is necessary to find $\max F(\psi_s, \theta)$ for the active case and $\min F(\psi_s, \theta)$ for the passive case. The optimization must thus be done in two parameters (ψ_s, θ) rather than the one (θ) for the linear problem and was implemented in this work using MATLAB. Having found the optimum solution, equations (3) and (4) allow the determination of the shear and normal stresses with depth z on any non-linear slip-lines. These are plotted in in Fig.3 using materials

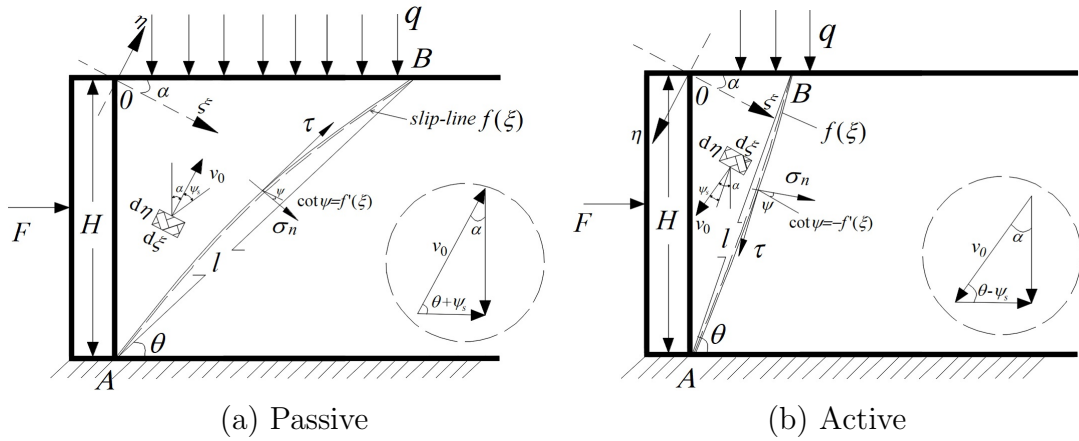


Figure 2: Upper bound failure mechanism analysis for frictionless retaining wall with hodograph.

(i) and (ii). For comparison predictions using a simple non-linear lower bound approach given in [6] are also given. This latter analysis assumes that principal stresses remain horizontal and vertical. The metal cutting problem (Fig. 4a) is kinematically similar to the passive wall problem and is solved in a similar way. However in this case two slip-lines were modelled using a non-linear yield function, the tool/wall interface as an almost linear frictionless interface and the slip-line through the metal as an almost linear Tresca material. The predicted stresses along the two slip-lines are given in Fig. 4b.

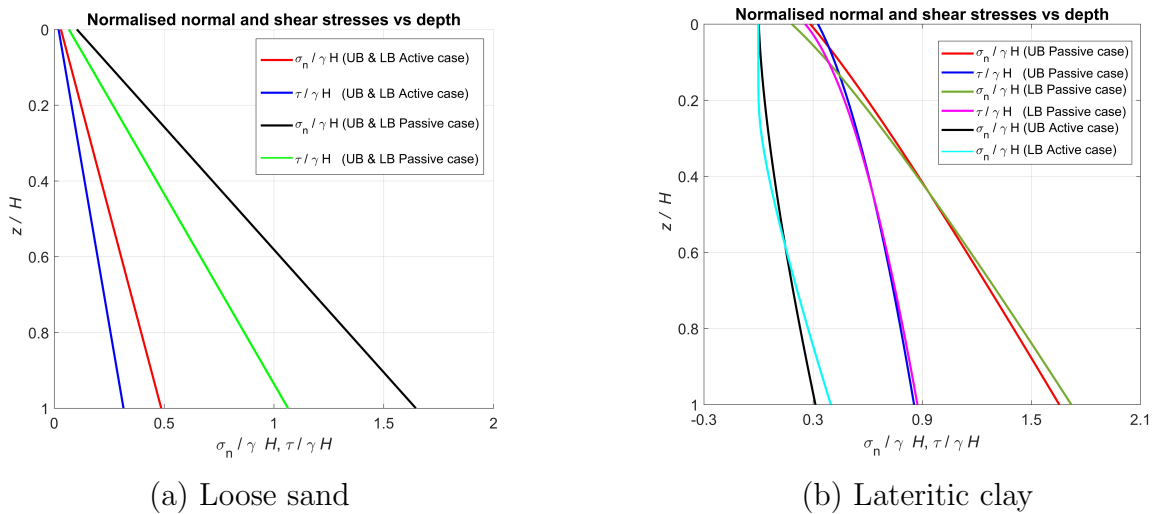
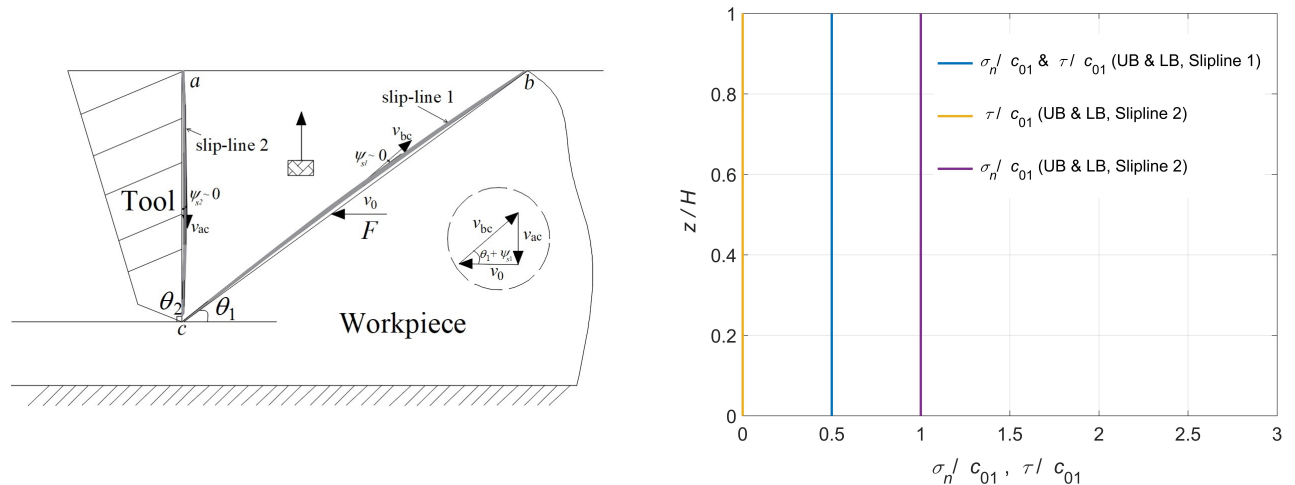


Figure 3: Predicted upper bound (UB) and lower bound (LB) normalised normal and shear stresses on the inclined failure slip-lines with depth z for retaining wall problem ($q = 5\text{kN/m}^2$ and $H = 5\text{m}$): loose sand case ($c_0 = 1 \text{ kN/m}^2$, $\sigma_t = 1.7321 \text{ kN/m}^2$, $\gamma = 15 \text{ kN/m}^3$, $m = 1.001$, $a = 0$); lateritic clay case ($c_0 = 1 \text{ kN/m}^2$, $\sigma_t = 0.053 \text{ kN/m}^2$, $\gamma = 18 \text{ kN/m}^3$, $m = 1.8282$, $a = 1.644$).

Discussion and Conclusions

From Figs 3 and 4b it can be concluded that the stress distribution from the upper bound solutions are near identical to those from the lower bound approach for an almost linear material, which corroborates with the almost identical collapse loads found. In contrast, for the non-linear case, the results are not identical, but are closely similar which also corroborates with the fact that limit loads are also similar but not identical (the difference is smaller than 0.3%). Some conclusions are drawn below:



(a) Metal cutting mechanism and hodograph

(b) Stress distributions

Figure 4: Predicted upper bound (UB) and lower bound (LB) normalised normal and shear stresses with depth z on two non-linear slip-lines for the metal cutting problem. Slip-line 1 properties: $c_{01} = 300 \text{ MN/m}^2$, $\sigma_{t1} = 3 \times 10^8 \text{ kN/m}^2$, $\gamma_1 = 0 \text{ kN/m}^3$, $m_1 = 1.001$, $a_1 = 1$. Slip-line 2 properties: $c_{02} = 1 \text{ kN/m}^2$, $\sigma_{t2} = 1 \times 10^5 \text{ kN/m}^2$, $\gamma_2 = 0 \text{ kN/m}^3$, $m_2 = 1.001$, $a_2 = 1$.

1. An overview of a fully general variational approach for the upper bound analysis of failure of in non-linear soils has been presented. The analysis follows the form of the classic upper bound multi-wedge analysis utilised for linear soils.
2. The upper bound solutions can generate good predictions of shear and normal stresses along multiple slip-lines, which is not normally obtained from an upper bound analysis and show strong consistency with related lower bound solutions. This provides a potentially useful way to extract more information from upper bound solutions when modelling linear and non-linear materials.

References

- 1 A. J. Anyaegbunam. Nonlinear power-type failure laws for geomaterials: Synthesis from 322 triaxial data, properties, and applications. *Int. J. of Geomechanics*, 15(1), 04014036, 2013.
- 2 M. Bolton. The strength and dilatancy of sands. *Geotechnique*, 36(1), 65-78, 1986.
- 3 W. F. Chen. *Limit Analysis and Soil Plasticity*, Elsevier, 1975.
- 4 M. Fraldi and F. Guarracino. Limit analysis of collapse mechanisms in cavities and tunnels according to the hoekbrown failure criterion. *International Journal of Rock Mechanics and Mining Sciences*, 46(4), 665-673, 2009.
- 5 C. Smith and M. Gilbert. Application of discontinuity layout optimization to plane plasticity problems. *Proceedings of the Royal Society of London A: Mathematical, Physical and Engineering Sciences*, 463(2086), 2461-2484, 2007.
- 6 R. Zhang and C. Smith. Upper bound limit analysis of soils with a non-linear failure criterion. *Canadian Geotechnical Journal*, under review, 2019.

CAD-COMPATIBLE STRUCTURAL TOPOLOGY OPTIMISATION

Ge Yin, Xiao Xiao and Fehmi Cirak

Department of Engineering, University of Cambridge, Trumpington Street, Cambridge, CB2 1PZ

gy241@cam.ac.uk

Summary

Topology optimization has been used in various engineering fields. The idea of optimising material distribution in topology optimisation tremendously contributes to fast and intuitive preliminary engineering design. The resulting topologically-optimised model generally consists of massive voxel or polygon mesh, which raises the difficulties in post-processing with CAD software. We introduce a new post-processing method combining homotopic thinning algorithm and beam optimisation to offer a CAD-compatible output. The thinning algorithm first extracts the homotopic structural skeleton modelled as a frame from topology optimisation result. Then the sequential of size and layout optimisations is applied on the frame model. The optimal frame can be easily constructed using geometric primitives in CAD software. It is convinced that, this method can transform a topology-optimised model into a frame model with lower compliance better structural performance and compatibility with CAD.

Key Words: *Topology Optimisation; Computer Aided Design; Digital Topology; Finite Elements*

1 Introduction

Topology optimization solves the problem how to distribute material within a prescribed design domain in order to obtain the best structural performance. The concept was initiated for mechanical design problems but has spread to a wide range of other physical disciplines, including fluids, acoustics, electromagnetics, optics and combinations thereof [1]. In general, topology optimization picks one objective function such as structural compliance, and the optimisation can deal with multiple loading problems [2]. For design and manufacturing, besides the mechanical performance, factors related to fatigue, manufacturing methods, user experience of the product, aesthetics are also taken into considerations. Formulating these factors all into optimisation process is impractical and significantly burdens the process. Therefore, the result of topology optimisation should be handed back to designers and engineers for further edition on the geometry. The existing software for topology optimisation is not able to offer a CAD-compatible optimal mode. The time and resource spent in manual or semi-automotive remodelling become bottlenecks for large popularity of topology optimisation.

2 One example

The cantilevered plate as in Figure 1 is one of the most widely studied benchmark examples in topology optimisation. The size of the chosen design domain is described into $150 \times 50 \times 4$ unit linear hexahedron elements. The left edge of the domain is fixed while all the others are free, and a force of $F = 100$ is applied along the centre of the right edge. The Young's modulus and Poisson's ratio of the solid material are 1.0 and $\nu = 0.3$. Using SIMP with the volume fraction of $\chi = 0.3$, the penalisation factor of $p = 3$, the minimum Young's modulus as $E_{\min} = 10^{-9}$ and the density filter radius as $R = 3$, topology optimisation gives the optimal shape as in Figure 2.

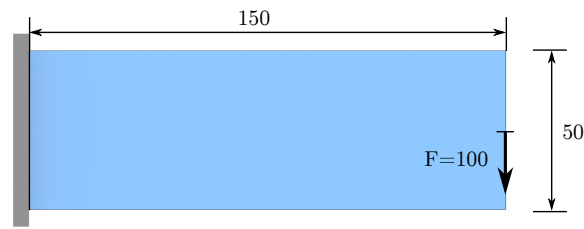


Figure 1: Geometry and boundary conditions of cantilever

The structural frame model can be obtained through skeletonisation process on the shape in Figure 2. The frame is shown as Figure 3 with initial sizes.

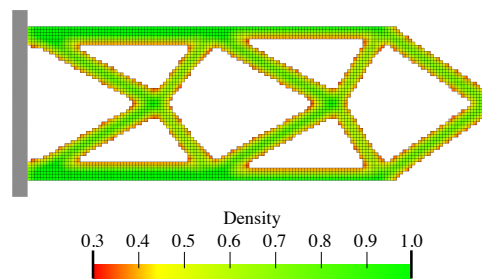


Figure 2: Topology optimised shape with threshold $\eta = 0.3$

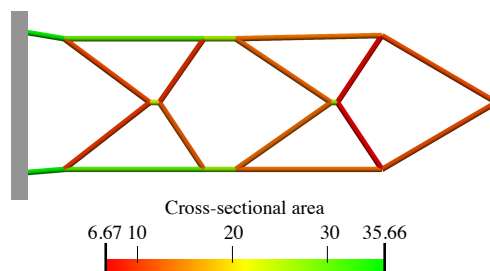


Figure 3: Initial size optimisation on beam model

After the size and layout optimisation, the optimal frame model can be converted into CAD-compatible format such as the STL format in Figure 4.

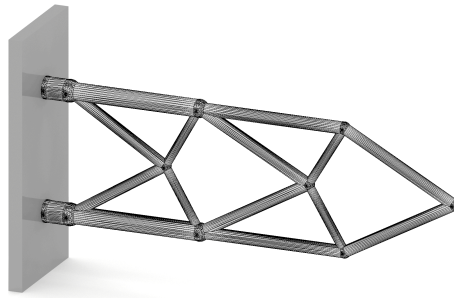


Figure 4: STL model of the cantilever

References

- [1] M.P. Bendsoe, Martin and O. Sigmund. Topology optimization: theory, methods and applications *Springer*, 2003.
- [2] H.A. Eschenauer and N. Olhoff. Topology optimization of continuum structures: a review. *Applied Mechanics Reviews*, 54, 331-390, 2001.

A COMBINED MICROMECHANICS STRONG-DISCONTINUITY APPROACH FOR MODELLING DISTRIBUTED AND LOCALISED FRACTURE IN CEMENTITIOUS MATERIALS

* **C.X. Azúa-González, I. Mihai and A.D. Jefferson**

School of Engineering, Cardiff University, Cardiff CF24 3AA

*Azua-GonzalezCX@cardiff.ac.uk

Summary

Traditional non-linear Finite Element (FE) constitutive models for cementitious materials, based on macroscopic theories, tend to capture failure states phenomenologically. This type of approach has, in the past, led to certain numerical inconsistencies, such as a lack of objectivity with respect to mesh grading. In this study, a novel framework is proposed, which aims to overcome the numerical issues of macroscopic-based constitutive models by using a more mechanistic approach. This new approach combines a micromechanics constitutive model with an Embedded Strong Discontinuity (ESD) approach. The resulting formulation uses additional degrees of freedoms (translational and rotational) at a crack axis within a special finite element. The coupling between the micro and macro cracking components of the model was derived using a variational principle, which ensures equilibrium across the embedded crack and provides an overall minimum energy solution. A number of numerical examples are presented to elucidate the performance of the numerical framework.

Key Words: *Fracture; Constitutive model; Nonlinear Finite Elements; Cementitious materials*

Introduction

In the past, macroscopic-based constitutive models (for quasi-brittle materials) led to numerical issues such as excessive mesh dependency of structural response in Boundary Value Problems (BVP). Many authors have proposed strategies to overcome such issue, e.g the crack band approach [2], gradient-enhanced models [3], micropolar continua [5] among others. In this study, a numerical strategy to couple a Micromechanics constitutive model [4] and the Embedded Strong Discontinuity (ESD) [7] approach is presented. The aim of this new formulation is to overcome the numerical issues of macroscopic-based constitutive models by using a more mechanistic approach.

Micromechanics-based damage constitutive model

The framework uses the basic constitutive model in [4]. This model considers a number of distributed (penny-shaped) microcracks, embedded in an elastic medium and aligned with microcrack-planes, according to the analytical solution in [6]. Each microcrack-plane uses a (local) damage surface, based on rotated normal and (engineering) shear strains $\boldsymbol{\varepsilon}_L = [\varepsilon_{Lr} \ \gamma_L]^T$, to trace the evolution of a (scalar) directional damage strain ζ_{Lp} . A *homogenised* secant (constitutive) stiffness $\bar{\mathbf{D}}_{sec}$ is obtained through integration over a (unit) semi-circle. The constitutive equation for this model is expressed as:

$$\boldsymbol{\sigma} = \mathbf{D}_e(\boldsymbol{\varepsilon} - \bar{\boldsymbol{\varepsilon}}^{add}) \quad (1)$$

$$\bar{\boldsymbol{\varepsilon}}^{add} = \frac{1}{\pi} \int_{\pi} \mathbf{N}_{\psi}^T \boldsymbol{\varepsilon}_{\psi}^{add} d\psi \approx \left[\sum_{i=1}^{n_{mc}} \frac{w_{Li}}{1 - w_{Li}} \mathbf{N}_i^T \mathbf{C}_L \mathbf{N}_i w_{intg_i} \right] \boldsymbol{\sigma} \quad (2)$$

where $\boldsymbol{\sigma}$ and $\boldsymbol{\varepsilon}$ are the stress and strain tensors in vector form; $\bar{\boldsymbol{\varepsilon}}^{add}$ represents the homogenised additional strain vector due to the presence of (evolving) microcracks; \mathbf{D}_e denotes the (undamaged) material stiffness; \mathbf{N}_{ψ} is a rotation matrix, which transforms the stress vector into local coordinates; $\boldsymbol{\varepsilon}_{\psi}^{add}$ represents the additional strain vector, in local coordinates, due to distributed microcracks aligned with a microcrack-plane; \mathbf{C}_L represents a (local) elastic compliance matrix; $w_L = w_L(\zeta_{Lp})$ is a (local) damage variable ($w_L \in [0, 1]$); n_{mc} is the total number of microcrack-planes considered for numerical integration; and w_{intg} is a coefficient used for numerical integration. Although the model has been published previously, for completeness, the main features in plane stress are presented in Box 1.

Box 1 Summary of Micromechanics-based damage constitutive model algorithm [4]

Constitutive equation: $\boldsymbol{\sigma} = \mathbf{D}_e(\boldsymbol{\varepsilon} - \bar{\boldsymbol{\varepsilon}}^{add})$

In the i -th microcrack-plane, $i = 1 \dots n_{mc}$:

Local damage parameter: $\zeta_{L_{eff},i}(\boldsymbol{\varepsilon}_{L_i}) = \frac{\varepsilon_{Lr,i}}{2} [1 + (\frac{\mu_\varepsilon}{r_\varepsilon})^2] + \frac{1}{2r_\varepsilon^2} \sqrt{(r_\varepsilon^2 - \mu_\varepsilon^2)^2 \varepsilon_{Lr,i}^2 + 4r_\varepsilon^2 \gamma_{L,i}^2}$; $\zeta_{Lp,i} \geq \zeta_0$

Local damage surface: $f_{L_i}(\zeta_{L_{eff},i}, \zeta_{Lp,i}) = \zeta_{L_{eff},i} - \zeta_{Lp,i}$

Local damage surface loading/unloading conditions: $\dot{\zeta}_{Lp,i} \geq 0$; $f_{L_i} \leq 0$; $\dot{\zeta}_{Lp,i} f_{L_i} = 0$

Constitutive tangent operator:

$$\mathbf{D}_{tan} = \bar{\mathbf{D}}_{sec} \left[\mathbf{I} - \sum_{i=1}^{n_{mc,ld}} \frac{1}{(1-w_{L_i})^2} \frac{dw_{L_i}}{d\zeta_{Lp,i}} \mathbf{N}_i^T \mathbf{C}_L \mathbf{N}_i \boldsymbol{\sigma} \{ \partial \zeta_{L_{eff},i} / \partial \boldsymbol{\varepsilon}_{L_i} \}^T \mathbf{N}_i w_{intg_i} \right]$$

$$\bar{\mathbf{D}}_{sec}(\mathbf{w}_L) = (\mathbf{I} + \mathbf{D}_e \bar{\mathbf{C}}^{add})^{-1} \mathbf{D}_e$$
; $\bar{\mathbf{C}}^{add}(\mathbf{w}_L) = \sum_{i=1}^{n_{mc}} \frac{w_{L_i}}{1-w_{L_i}} \mathbf{N}_i^T \mathbf{C}_L \mathbf{N}_i w_{intg_i}$

where r_ε and μ_ε represent stress ratios in equivalent strain terms; $n_{mc,ld}$ stands for the number of microcrack directions undergoing further micromechanical damage, i.e. if only if $\dot{\zeta}_{Lp,i} > 0$ as a consequence of the out-of-balance stress; \mathbf{I} is the identity matrix; the (local) elastic compliance matrix is expressed as $\mathbf{C}_L = \frac{1}{E} \begin{bmatrix} 1 & 0 \\ 0 & \frac{4}{2-\nu} \end{bmatrix}$; and damage evolution follows an exponential rule:

$$w_L(\zeta_{Lp}) = 1 - \frac{\zeta_0}{\zeta_{Lp}} e^{-c_1 \frac{\zeta_{Lp} - \zeta_0}{\zeta_m - \zeta_0}} \quad (3)$$

with ζ_0 being the strain at first (micromechanical) damage, and ζ_m the effective end of the stress-strain curve, both obtained from a uniaxial (tensile) stress-strain curve; and the constant $c_1 = 5$.

Formulation of a Micromechanics-ESD approach based on variational principles

The Micromechanics-ESD approach, as proposed here, ensures energetic balance across the crack plane and provides a minimum energy solution over a special finite element. This special finite element uses additional degrees of freedom $\widetilde{\mathbf{W}} = [\tilde{u}_{rc}, \tilde{u}_{sc}, \tilde{\alpha}_c]^T$ at a crack axis, which have been chosen to occur at the centre of the element. The crack formulation allows for opening (\tilde{u}_{rc}), sliding (\tilde{u}_{sc}) and rotation ($\tilde{\alpha}_c$) between the negative (Ω^-) and positive parts (Ω^+) of the element, see figure 1.

The strong discontinuity, which introduces a jump in the displacement field \mathbf{u} within an element, provides an additional strain vector component $\check{\boldsymbol{\varepsilon}}_{fr}$ ($\boldsymbol{\varepsilon} = \boldsymbol{\varepsilon}_{cont} + \check{\boldsymbol{\varepsilon}}_{fr}$). It was found convenient to allow this enrichment in the strain field, if the crack undergoes inelastic relative displacement $\check{\widetilde{\mathbf{W}}}$:

$$\check{\boldsymbol{\varepsilon}}_{fr} = \mathbf{M}_w \check{\mathbf{I}}_w \check{\widetilde{\mathbf{W}}} \quad (4)$$

where $\mathbf{M}_w = \sum_{i=1}^{n_{node_{\Omega^+}}} \mathbf{B}_i \mathbf{T}_w$; $n_{node_{\Omega^+}}$ stands for the number of nodes on the positive part of the element; $\check{\mathbf{I}}_w = \mathbf{I} - (\widetilde{\mathbf{K}}_\Gamma^{el})^{-1} \widetilde{\mathbf{K}}_\Gamma$; \mathbf{K}_Γ^{el} is the (elastic) local crack-plane stiffness matrix ($\mathbf{F}_{ck} = \mathbf{K}_\Gamma^{el} \mathbf{W}^{el}$); $\widetilde{\mathbf{K}}_\Gamma$ is the local crack-plane stiffness matrix ($\mathbf{F}_{ck} = \widetilde{\mathbf{K}}_\Gamma \widetilde{\mathbf{W}}$); $\mathbf{B}_i = \begin{bmatrix} \partial \tilde{N}_i / \partial x & 0 & \partial \tilde{N}_i / \partial y \\ 0 & \partial \tilde{N}_i / \partial y & \partial \tilde{N}_i / \partial x \end{bmatrix}^T$ with \tilde{N}_i being the i -th component of the interpolation vector $\tilde{\mathbf{N}}$; and \mathbf{T}_w is a transformation matrix, used to compute the (cartesian) additional displacement at each node for a given crack displacement $\widetilde{\mathbf{W}}$.

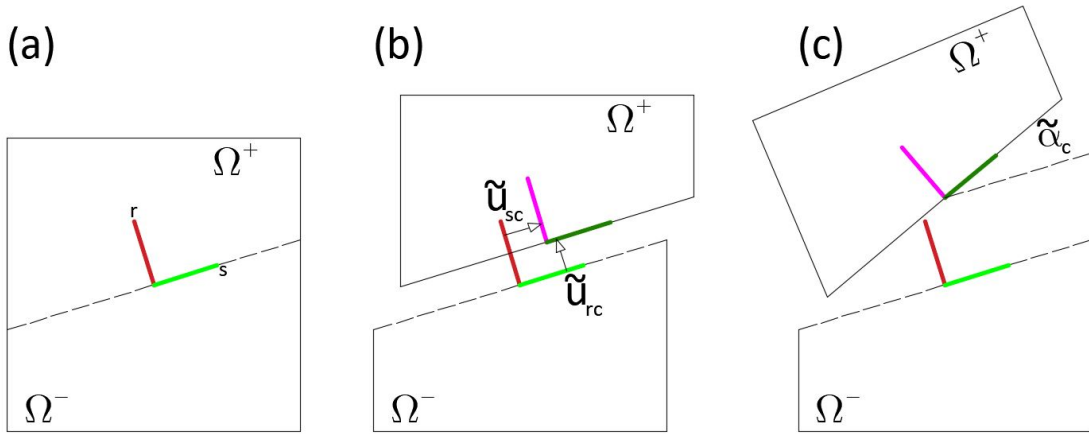


Figure 1: Four-noded element with an embedded crack: (a) local axis convention; element undergoing (b) crack opening and sliding, and (c) combined rotational and translational relative displacement.

It can be proved, based on **variational principles**, that there is a unique relation between the element degrees of freedom \mathbf{u} and the (local) crack displacement vector $\widetilde{\mathbf{W}}$:

$$\widetilde{\mathbf{W}} = \mathbf{B}_\Gamma^{-1} \mathbf{A}_\Gamma \mathbf{u} = \mathbf{C}_\Gamma \mathbf{u} \quad (5)$$

where $\mathbf{B}_\Gamma = \left(\int_\Omega \mathbf{M}_w^T \bar{\mathbf{D}}_{sec} \mathbf{M}_w t d\Omega \right) \check{\mathbf{I}}_w + \widetilde{\mathbf{K}}_\Gamma$; and $\mathbf{A}_\Gamma = \int_\Omega \check{\mathbf{I}}_w \mathbf{M}_w^T \bar{\mathbf{D}}_{sec} \mathbf{B} t d\Omega$ with t being the out-of-plane thickness. A pseudo-code for force recovery over an element is shown in algorithm 1. The combined Micromechanics-ESD stiffness matrix \mathbf{K}_{comb}^e , for one element, may be expressed as:

$$\mathbf{K}_{comb}^e = \int_\Omega (\mathbf{B} - \mathbf{M}_w \check{\mathbf{I}}_w \mathbf{C}_\Gamma)^T \bar{\mathbf{D}}_{sec} (\mathbf{B} - \mathbf{M}_w \check{\mathbf{I}}_w \mathbf{C}_\Gamma) t d\Omega + \mathbf{C}_\Gamma^T \check{\mathbf{I}}_w \widetilde{\mathbf{K}}_\Gamma \mathbf{C}_\Gamma \quad (6)$$

Numerical examples and discussion

A displacement-driven BVP has been performed, which involves an element of dimensions 100×100 (length in mm). The element has been stretched horizontally $u_{xx} = 0.06 \text{ mm}$, and squashed vertically $u_{yy} = -\nu u_{xx}$. The elastic constants have been set as $E = 31000 \text{ MPa}$ and $\nu = 0.2$; the tensile strength $f_t = 1.8 \text{ MPa}$; the strain at first micromechanical damage $\zeta_0 = f_{t,micro}/E$ with $f_{t,micro} = 1 \text{ MPa}$; the effective end of the softening branches: $u_m = 0.2 \text{ mm}$ (in the stress-displacement space, for macrocrack response) and $\zeta_m = u_m/(3d_{fa})$ (in the stress-strain space, for microcracks response), with the fine aggregate size $d_{fa} = 2 \text{ mm}$ dominating the width of the Fracture Process Zone (FPZ) at microcracks; the stress ratios in strain equivalences $r_\varepsilon = 6$ and $\mu_\varepsilon = 2.4$. The macrocrack damage evolution has been adjusted to follow a Smooth Unloading Reloading (SUR) response [1], using constants $a_p = 0.6$, $\nu = 0.75$ and a FPZ width ($3d_{ca}$) correlated to the coarse aggregate size $d_{ca} = 15 \text{ mm}$.

In figure 2, the response is predicted using solely the Micromechanics model; combined Micromechanics (without micromechanical damage) and ESD; and the proper Micromechanics-ESD response. The predicted response from the Micromechanics-ESD is shown to be more brittle than that of a solution obtained using just the micromechanics model. This may be explained by localisation of deformation at the macrocrack. Micromechanical damage, yields into a smaller gradient in the combined response within the pre-peak branch, when compared to the case of a fully undamage continuum.

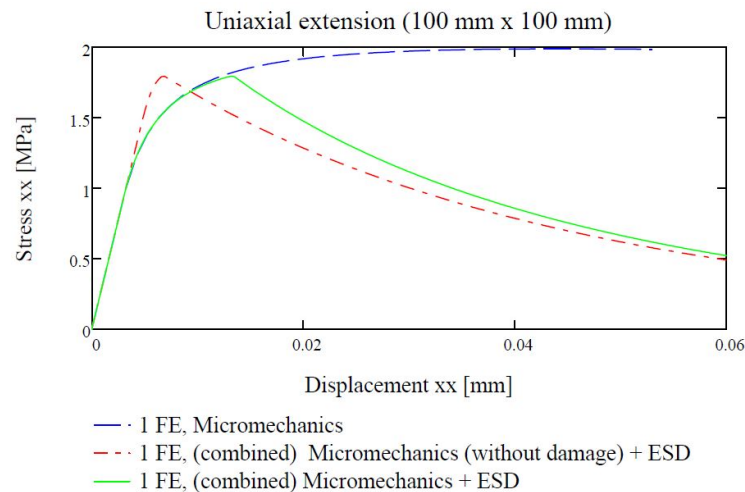


Figure 2: Uniaxial extension response in the stress-displacement space.

Conclusions

A novel Micromechanics-ESD framework has been proposed, which couples micro and macro crack components for modelling of cementitious materials. Preliminary numerical examples have shown, that the framework enables localisation of deformation at the macrocrack level.

Acknowledgements

The authors acknowledge the financial support by the EPSRC RM4L grant: <https://rm4l.com/>

References

- [1] W.F. Alnaas and A.D. Jefferson. A smooth unloading–reloading approach for the nonlinear finite element analysis of quasi-brittle materials. *Engineering Fracture Mechanics*, 152:105–125, feb 2016.
- [2] Z. P. Bažant and B. H. Oh. Crack band theory for fracture of concrete. *Matériaux et Constructions*, 16(3):155–177, may 1983.
- [3] R. de Borst, J. Pamin, R. H. J. Peerlings, and L. J. Sluys. On gradient-enhanced damage and plasticity models for failure in quasi-brittle and frictional materials. *Computational Mechanics*, 17(1-2):130–141, dec 1995.
- [4] A. D. Jefferson and T. Bennett. Micro-mechanical damage and rough crack closure in cementitious composite materials. *International Journal for Numerical and Analytical Methods in Geomechanics*, 31(2):133–146, 2007.
- [5] H. B. Mühlhaus and I. Vardoulakis. The thickness of shear bands in granular materials. *Géotechnique*, 37(3):271–283, sep 1987.
- [6] S. Nemat-Nasser and M. Hori. *Micromechanics: Overall Properties of Heterogeneous Materials*. North Holland, 1998.
- [7] J. C. Simo, J. Oliver, and F. Armero. An analysis of strong discontinuities induced by strain-softening in rate-independent inelastic solids. *Computational Mechanics*, 12(5):277–296, 1993.

Algorithm 1 Force recovery for the combined Micromechanics Strong-Discontinuity approach

```

1: procedure START WITH  $\mathbf{u}$ ,  $\{\zeta_{Lp}\}_{igp}$  FOR  $igp = 1 \dots ngp$ , AND  $\{\zeta_{ckp}\}$ 
2:   | Set a trial local displacement vector,  $\widetilde{\mathbf{W}} \leftarrow \widetilde{\mathbf{W}}_0$ ; and reset element force vector  $\mathbf{F}$ 
3:   | Update arrays along the crack temporarily: (i)  $\{\zeta_{ckp}\}$  and (ii)  $\{w_{ck}\}$ ; compute  $\widetilde{\mathbf{K}}_\Gamma, \check{\mathbf{I}}_w$ 
4:   | for  $igp = 1 \dots ngp$  do ▷ loop over Gauss points
5:     | Evaluate  $\check{\boldsymbol{\epsilon}}_{fr}, \boldsymbol{\epsilon}_{cont}, \bar{\mathbf{D}}_{sec}(\boldsymbol{\epsilon}_{cont})$ ; update arrays temporarily: (i)  $\{\zeta_{Lp}\}_{igp}$  and (ii)  $\{w_{Lp}\}_{igp}$ 
6:     | Accumulate terms for numerical integration of  $\mathbf{B}_\Gamma$  and  $\mathbf{A}_\Gamma$ 
7:   | Compute  $\mathbf{C}_\Gamma$ ; evaluate  $\phi_w \leftarrow \widetilde{\mathbf{W}} - \mathbf{C}_\Gamma \mathbf{u}$  and  $\bar{\phi}_w \leftarrow \phi_{wnorm}/\phi_{ref}$ 
8:   | while  $\bar{\phi}_w > Tol$  do ▷ Newton-Raphson scheme
9:     | Evaluate the tangent  $\partial\phi_w/\partial\widetilde{\mathbf{W}}$ , based on temporary arrays, using central differences
10:    | Compute  $\Delta\widetilde{\mathbf{W}} \leftarrow (\partial\phi_w/\partial\widetilde{\mathbf{W}})^{-1} \phi_w$ ; update  $\widetilde{\mathbf{W}} \leftarrow \widetilde{\mathbf{W}} + \Delta\widetilde{\mathbf{W}}$ 
11:    | Update temporarily against last converged arrays:  $\{\zeta_{ckp}\}$  and  $\{w_{ck}\}$ ; compute  $\widetilde{\mathbf{K}}_\Gamma, \check{\mathbf{I}}_w$ 
12:    | for  $igp = 1 \dots ngp$  do ▷ loop over Gauss points
13:      | Evaluate  $\check{\boldsymbol{\epsilon}}_{fr}, \boldsymbol{\epsilon}_{cont}, \bar{\mathbf{D}}_{sec}(\boldsymbol{\epsilon}_{cont})$ ; update temporarily:  $\{\zeta_{Lp}\}_{igp}$  and  $\{w_{Lp}\}_{igp}$ 
14:      | Accumulate terms for numerical integration of  $\mathbf{B}_\Gamma$  and  $\mathbf{A}_\Gamma$ 
15:      | Compute  $\mathbf{C}_\Gamma$ ; evaluate  $\phi_w \leftarrow \widetilde{\mathbf{W}} - \mathbf{C}_\Gamma \mathbf{u}$  and  $\bar{\phi}_w \leftarrow \phi_{wnorm}/\phi_{ref}$ 
16:    | Set temporary arrays as converged;
17:    | for  $igp = 1 \dots ngp$  do ▷ loop over Gauss points
18:      | Evaluate  $\check{\boldsymbol{\epsilon}}_{fr}, \boldsymbol{\epsilon}_{cont}, \bar{\mathbf{D}}_{sec}(\boldsymbol{\epsilon}_{cont})$ ; and  $\boldsymbol{\sigma} \leftarrow \bar{\mathbf{D}}_{sec} \boldsymbol{\epsilon}_{cont}$ 
19:      | Accumulate element force vector components  $\mathbf{F} \leftarrow \mathbf{F} + \mathbf{B}^T \boldsymbol{\sigma} t \det(\mathbf{J}) w_{intigp}$ 

```

AN EFFICIENT ALGORITHM THAT COMBINES SURROGATE MODEL AND MAXIMUM ENTROPY METHOD FOR STRUCTURAL RELIABILITY ANALYSIS

*Jinsheng Wang¹, Muhannad Aldosary² and Chenfeng Li¹

¹Zienkiewicz Centre for Computational Engineering, Swansea University, Swansea, SA1 8EN

²Dams and Water Resources Engineering, University of Anbar, Iraq

*844051@swansea.ac.uk

Summary

In this work, an efficient hybrid approach is proposed that combines the surrogate model technique (i.e. sparse polynomial chaos expansion, sparse PCE) with the maximum entropy method (MEM) for accurate failure probability evaluation of a structural system. In the proposed method, the statistical moments of the performance are furnished by sparse PCE, whereas the probability density function (PDF) is constructed using MEM under moment constraints. With the availability of the analytical expression of PDF, the failure probability of the structural system is obtained by a simple integral over the failure domain. The applicability of the proposed approach is investigated using a numerical example and its performance is compared with MCS. It is found that the proposed method can keep the trade-off between efficiency and accuracy for structural reliability analysis.

Key Words: *Structural reliability analysis; Sparse polynomial chaos expansion; Maximum entropy method; Statistical moments; Probability density function*

1. Introduction

Structural reliability analysis aims at evaluating the failure probability P_f of a structural system with respect to some specific performance criterion in the presence of uncertainty. The uncertain parameters involved in the structural system such as material properties, environmental factors and structural dimensions are usually modelled as a random vector $\mathbf{X} = \{X_1, X_2, \dots, X_N\}^T$ with prescribed joint probability density function (PDF) $f_{\mathbf{X}}(\mathbf{x})$. The state of the structural system is mathematically represented using a performance function (a.k.a. limit state function) $g(\mathbf{X})$ over the support of \mathbf{X} , which is defined such that $g(\mathbf{X}) \leq 0$ the failure domain and $g(\mathbf{X}) > 0$ the safe domain. The boundary between the safe domain and failure domain is the limit state surface defined by $g(\mathbf{X}) = 0$. Thus, the fundamental problem in structural reliability analysis can be formulated in terms of a multidimensional integral as [1]:

$$P_f = \text{Prob}[g(\mathbf{X}) \leq 0] = \int_{\{\mathbf{x}; g(\mathbf{x}) \leq 0\}} f_{\mathbf{X}}(\mathbf{x}) d\mathbf{X} \quad (1)$$

Despite the simplicity of the formulation in Eq.(1), the exact solution by integration is intractable if not impossible in reality due to the high dimensionality and implicit nature of the performance function, not even to mention that the joint PDF is sometimes unknown. Difficulty in calculating the failure probability by direct integration has led to the development of various approximation methods, among which the first-order reliability method (FORM) [2] and second-order reliability method (SORM) [3] are regarded as the most popular approaches to conduct reliability analysis. These approaches are generally sufficient for cases with moderate nonlinearity and small number of random variables. However, application of these methods may yield large errors for high dimensional/ nonlinearity problems. The simulation-based method known as the crude Monte Carlo simulation (MCS) is considered to be the most robust and accurate approach for reliability analysis. However, the computational demand could be prohibitively high for problems involved with complex Finite Element model (FEM), especially when the rare failure events if of concern. Therefore, this approach is merely applied to provide reference results for other approximation methods. Although some remarkable improvements on the efficiency of MCS have been made with the advent of more advanced simulation techniques such as importance sampling methods [4] and subset simulation [5], large computational effort may still be required for practical applications. In this regard, more efficient approaches in the category of surrogate model [6,7] and moment-based methods [8] have attract increasingly more attention in the structural reliability community.

The purpose of this study is to present a new efficient and accurate method for reliability analysis. Hence, a hybrid approach is proposed that combines the efficient sparse Polynomial Chaos Expansion (PCE) with the MEM for accurate PDF approximation and failure probability evaluation of a structural system. In the proposed method, the statistical moments of the random response are provided by sparse PCE with enhanced efficiency, whereas the PDF is constructed using MEM under moment constraints. With the availability of the analytical expression for PDF, the failure probability of the structural system is directly acquired by numerically integrating the PDF over the failure domain.

2. Sparse polynomial chaos expansion

PCE is an efficient surrogate model used to replace the originally true but computationally intensive model, based on which the origin model is represented using a series expansion consists of orthonormal polynomials:

$$Y = g(\mathbf{X}) \approx \sum_{\alpha \in \mathbb{N}^N} \eta_{\alpha} \psi_{\alpha}(\mathbf{X}) \quad (2)$$

where η_{α} 's are the unknown deterministic coefficients (also referred as coordinates in the space spanned by the polynomial basis) and the $\alpha \in \mathbb{N}^N$ is a multi-index vector that indicates the components of the multivariate polynomials $\psi_{\alpha}(\mathbf{X})$. For computational purpose, the expansion in Eq.(2) is usually truncated such that only those polynomials with total degree up to p are retained, i.e. $0 \leq |\alpha| = \sum_{i=1}^N \alpha_i \leq p$ [9]:

$$Y = \mathcal{M}(\mathbf{X}) \approx \mathcal{M}_{PC}(\mathbf{X}) = \sum_{0 \leq |\alpha| \leq p} \eta_{\alpha} \psi_{\alpha}(\mathbf{X}) \quad (3)$$

the above formulation leads to the so-called full PCE model, and the number of terms involved is given by $P = \binom{N+p}{p} = \frac{(N+p)!}{N!p!}$. In this study, the sparse PCE proposed in [9] is utilized to further improve the computational efficiency, in which the truncation scheme is formulated as:

$$\mathcal{A}^{N,p,q} = \left\{ \alpha \in \mathcal{A}^{N,p} : \|\alpha\|_q = \left(\sum_{i=1}^N \alpha_i^q \right)^{1/q} \leq p \right\} \quad (4)$$

where $0 < q < 1$ and $\mathcal{A}^{N,p} = \{ \alpha \in \mathbb{N}^N, 0 \leq |\alpha| \leq p \}$ (corresponds to the standard truncation scheme defined in Eq.(3) when $q = 1$).

3. Post-processing of sparse PCE

Once the optimal sparse surrogate model is ready, numerous simulation of the sparse PCE can be conducted to get the statistical estimation (e.g. statistical moments) of the model response at a negligible computational cost. Hence, the statistical moments that will be used as constraints in MEM can be calculated using the following equation:

$$m_Y^k \approx m_{Y,PC}^k = \frac{1}{M} \sum_{i=1}^M \mathcal{M}_{PC}^k(\mathbf{X}_i) \quad (5)$$

where m_Y^k and $m_{Y,PC}^k$ are the k^{th} raw moment of model response and its PC approximation, respectively; and M is the number of simulating samples which is set to be a large enough number in this study.

4. Maximum entropy method

Consider a random variable Y with PDF $f_Y(y)$, the differential entropy of $f_Y(y)$ is defined as:

$$\mathcal{H}[f_Y(y)] = - \int f_Y(y) \ln[f_Y(y)] dy \quad (6)$$

According to the principle of maximum entropy, the probability density that best describes the current state of knowledge is the one having largest entropy. Therefore, the derivation of $f_Y(y)$ is formulated as an optimization problem [10]:

$$\text{Maximize } \mathcal{H}[f_Y(y)] = - \int f_Y(y) \ln[f_Y(y)] dy \quad (7)$$

$$\text{Subject to } m_{\kappa_i} = \int y^{\kappa_i} f_Y(y) dy, \quad \kappa_i \in \mathbb{R}, \quad i = 1, 2, \dots, I \quad (8)$$

solving the above equation leads to a closed form solution of the maximum entropy PDF:

$$f_Y(y) = \exp \left[-\lambda_0 - \sum_{i=1}^I \lambda_i y^{\kappa_i} \right] \quad (9)$$

5. Basic steps of sparse PCE-based maximum entropy method

Mainly three steps are involved in the proposed method:

Step 1 consists in constructing the sparse PCE as a surrogate to replace the originally complex and/or time-consuming physical model of interest. In this step the Sobol sequences are used in the experimental design in view of its superior uniformity and better convergence property.

Step 2 consists in using the theory of maximum entropy method to recover the PDF of model response $f_Y(y)$. The moment constraints of the optimization problem are obtained through large number of runs of sparse PCE constructed in Step 1 using Eq.(5).

Step 3 consists in calculating the failure probability by integrating the PDF obtained in Step 2 over the failure domain:

$$P_f = \int_{-\infty}^0 f_Y(y) dy \quad (10)$$

6. Numerical example

In this example, a composite beam with an enhanced aluminium plate layer fastened to its bottom surface is considered. This composite structure have 20 independent random variables, including the cross-section parameters of beam (A and B) and the corresponding Young's modulus E_w ; the cross-section parameters of aluminium plate layer (C and D) and the corresponding Young's modulus E_a ; six external forces, namely P_1, P_2, P_3, P_4, P_5 and P_6 , are placed at six different locations with a distance of L_1, L_2, L_3, L_4, L_5 and L_6 from the left end of the structure; and the allowable stress is S . Please refer to [11] for the statistical information of the random variables, which is not given here for the sake of simplicity. The maximum stress of this composite beam can be derived explicitly in terms of these parameters and is given by:

$$\sigma_{max} = \frac{\left[\frac{\sum_{i=1}^6 P_i(L-L_i)}{L} L_3 - P_1(L_3 - L_1) - P_2(L_3 - L_2) \right] \left[\frac{0.5AB^2 + \frac{E_a}{E_w} CD(B+0.5D)}{AB + \frac{E_a}{E_w} CD} \right]}{\frac{1}{12} AB^3 + AB \left\{ \left[\frac{0.5AB^2 + \frac{E_a}{E_w} CD(B+0.5D)}{AB + \frac{E_a}{E_w} CD} \right] - 0.5B \right\}^2 + \frac{1}{12} \frac{E_a}{E_w} CD^3 + \frac{E_a}{E_w} CD \left\{ B + 0.5D - \left[\frac{0.5AB^2 + \frac{E_a}{E_w} CD(B+0.5D)}{AB + \frac{E_a}{E_w} CD} \right] \right\}^2} \quad (11)$$

To ensure the safety of the composite beam, the allowable stress S should larger than the maximum stress σ_{max} . Therefore, the performance function of interest for this composite structure is expressed as:

$$Y = \mathcal{M}(\mathbf{X}) = S - \sigma_{max} \quad (12)$$

The surrogate model of the performance function for the composite beam is constructed using 250 sampling pairs generated from Sobol sequence, and the optimal sparse PCE is of degree 3 with LOO error $\varepsilon_{LOO} = 4.571e - 6$. Following the procedure described in previous section, the first 14 raw moments of the performance function can easily be calculated using Eq.(5), which are utilized as the moment constraints in maximum entropy method. The derived PDF of the performance function and its corresponding CDF in logarithmic scale are depicted in Figure 1. It is observed that the PDF of the performance function derived by the proposed method perfectly matches the histogram evaluated using MCS. Moreover, the CDF in logarithmic scale obtained by the proposed method is in close agreement with that of MCS, which further confirms that the proposed method is well-suited for the approximation of the distribution and offers high accuracy in the entire investigated range. It should be emphasized that instead of requiring large number of functional calls to get the distribution function of the investigated performance function, the proposed approach only needs a rather small sample size to recover the entire distribution with sufficient accuracy, which is highly efficient.

With the availability of the PDF of performance function, the probability of failure can be readily obtained through numerical integration, or equivalently, directly evaluated from the CDF given in Figure 1(b). The probability of failure and the corresponding reliability index obtained from the proposed method are $1.7441e - 3$ and 2.9211 , respectively, both of which are quite close to those given by MCS, i.e. $1.7598e - 3$ and 2.9183 . Therefore, the proposed can achieve high accuracy with far less functional calls compared with MCS, which is especially attractive for practical application.

7. Conclusions

A hybrid approach that combines sparse PCE with MEM for reliability analysis is presented in this study. In this approach, the statistical moments of the performance function are calculated from sparse PCE with enhanced efficiency and the MEM is used to recover the PDF of performance function. With the availability of PDF, the failure probability of the structural system is directly obtained by simple one dimensional integral over the failure domain. According to the result of numerical example, it is observed that the proposed method can keep the trade-off between the efficiency and accuracy for structural reliability analysis, and has the capability to fully and accurately capture the uncertainty inherent in the performance function with a relatively small number of functional calls, which is especially attractive when the

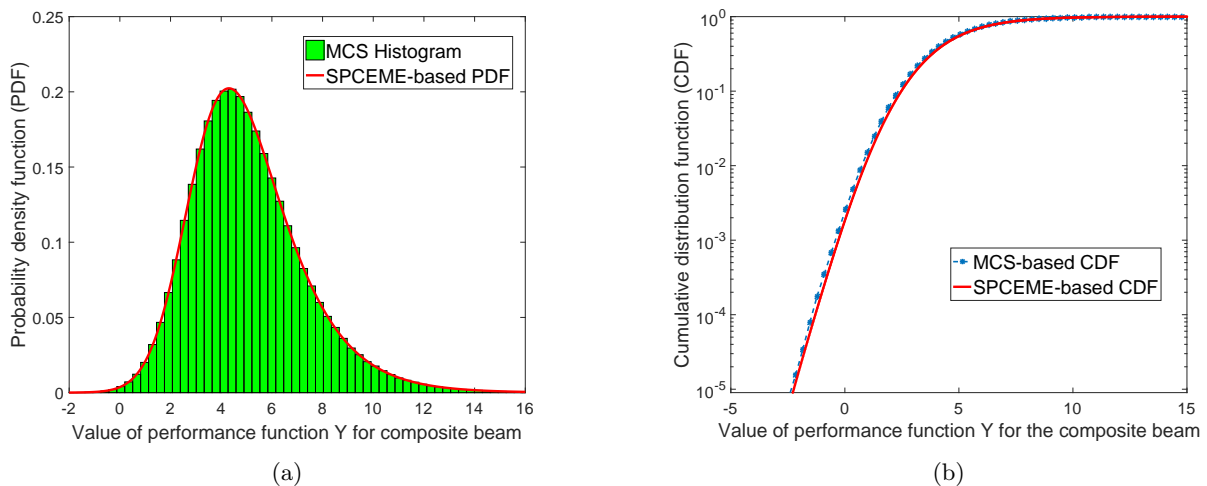


Figure 1: Comparison of PDFs and CDFs of performance function for the composite beam obtained by the proposed method and MCS (a) PDF of performance function (b) CDF of performance function

failure probabilities under different threshold are of concern. Therefore, for structural reliability analysis, the MEM is a proper choice to recover the entire range of performance function's PDF based on the higher-order statistical moments evaluated by the proposed approach. The framework proposed herein can readily be extended to accommodate other efficient surrogate model methods such as support vector machine, artificial neural network and Kriging, which is the scope of the future research.

Acknowledgements

The author gratefully acknowledges the financial support from College of Engineering and China Scholarship Council.

References

- 1 Madsen, Henrik O., Steen Krenk and Niels Christian Lind. *Methods of structural safety*, Courier Corporation (2006).
- 2 Lopez, R. H., A. J. Torii, L. F. F. Miguel, and JE Souza Cursi. *Overcoming the drawbacks of the FORM using a full characterization method*, Structural Safety 54 (2015): 57-63.
- 3 Huang, Xianzhen, Yuxiong Li, Yimin Zhang, and Xufang Zhang. *A new direct second-order reliability analysis method*, Applied Mathematical Modelling 55 (2018): 68-80.
- 4 Echard, B., Nicolas Gayton, Maurice Lemaire, and N. Relun. *A combined importance sampling and kriging reliability method for small failure probabilities with time-demanding numerical models*, Reliability Engineering & System Safety 111 (2013): 232-240.
- 5 Au, Siu-Kui, and James L. Beck. *Estimation of small failure probabilities in high dimensions by subset simulation*, Probabilistic Engineering Mechanics 16 (2001): 263-277.
- 6 Marelli, Stefano, and Bruno Sudret. *An active-learning algorithm that combines sparse polynomial chaos expansions and bootstrap for structural reliability analysis*, Structural Safety 75 (2018): 67-74.
- 7 Vazirizade, Sayyed Mohsen, Saeed Nozhati, and Mostafa Allameh Zadeh. *Seismic reliability assessment of structures using artificial neural network*, Journal of Building Engineering 11 (2017): 230-235.
- 8 Zhao, Yan-Gang, and Tetsuro Ono. *Moment methods for structural reliability*, Structural safety 23 (2001): 47-75.
- 9 Blatman, Graud, and Bruno Sudret. *Adaptive sparse polynomial chaos expansion based on least angle regression*, Journal of Computational Physics 230 (2011): 2345-2367.
- 10 Xu, Jun, Chao Dang, and Fan Kong. *Efficient reliability analysis of structures with the rotational quasi-symmetric point-and the maximum entropy methods*, Mechanical Systems and Signal Processing 95 (2017): 58-76.
- 11 Jinsheng Wang, Muhannad Aldosary, Chenfeng Li. *A hybrid approach combining sparse polynomial chaos with maximum entropy method for structural reliability analysis*. Engineering Computations (2019). (Submitted)

FEM IMPLEMENTATION FOR NAVIER-STOKES EQUATIONS FOR AN INCOMPRESSIBLE STEADY FLOW USING HIERARCHICAL BASIS FUNCTIONS

*Andrei G. Shvarts¹, Łukasz Kaczmarczyk¹ and Chris J. Pearce¹

¹Glasgow Computational Engineering Centre, School of Engineering, University of Glasgow

*andrei.shvarts@glasgow.ac.uk

Summary

We present an implementation of the finite-element method with hierarchical basis functions of arbitrary order for simulating incompressible steady-state fluid flow governed by Navier-Stokes equations (NSE). To verify the proposed formulation, we solved a problem of the fluid flow around a rigid sphere considering different velocity magnitudes. For a low-Reynolds-number flow the result coincides with the analytical solution for the Stokes flow, while for a higher Reynolds number a vortex is formed behind the sphere. The developed framework can be used to study the fluid flow in contact interfaces between solids with rough surfaces (e.g. in fractures) and compare the effect of the model describing the fluid flow (Reynolds, Stokes, or full NSE) on the transmissivity of these interfaces. The development is undertaken in MoFEM [1].

Key Words: *hierarchical basis functions; Navier-Stokes equations; flow past a sphere*

Introduction

Navier-Stokes equations (NSE), governing the motion of a viscous fluid, are used in various applications: from simulations of the flow in blood vessels to studies of the air flow around airplane wings and rotor blades, scaling up to models of ocean and atmospheric currents. Even in the case of an incompressible steady flow, NSE are non-linear due to the effect of the inertia, which is more pronounced in case of a higher Reynolds number. In this study we discuss the implementation of a viscous fluid model in the framework of the finite-element code MoFEM [1], which incorporates hierarchical basis functions of arbitrary order. This approach permits us to locally increase the order of approximation, enforcing conformity across finite element boundaries, without the need to change the implementation of an element. Moreover, the requirement of different approximation orders for primal (velocity) and dual (pressure) variables, necessary for a robust simulation of the flow, can be easily satisfied.

Problem statement

An incompressible isoviscous steady-state flow in a domain Ω is governed by the following equations:

$$\begin{cases} \rho (\mathbf{u} \cdot \nabla) \mathbf{u} - \mu \nabla^2 \mathbf{u} + \nabla p = \mathbf{f}, & (1a) \\ \nabla \cdot \mathbf{u} = 0, & (1b) \end{cases}$$

where (1a) are the Navier-Stokes equations, representing the balance of the momentum, and (1b) is the continuity equation; $\mathbf{u} = [u_1, u_2, u_3]^T$ is the velocity field, p is the hydrostatic pressure field, ρ is the fluid mass density, μ is fluid viscosity and \mathbf{f} is the density of external forces. The boundary value problem complements equations (1) by the Dirichlet and Neumann conditions on the boundary $\partial\Omega$:

$$\begin{cases} \mathbf{u} = \mathbf{u}_D & \text{on } \Gamma_D, & (2a) \\ \mathbf{n} \cdot [-p\mathbf{I} + \mu(\nabla\mathbf{u} + \nabla\mathbf{u}^T)] = \mathbf{g}_N & \text{on } \Gamma_N, & (2b) \end{cases}$$

where \mathbf{u}_D is the prescribed velocity on the part of the boundary $\Gamma_D \subset \partial\Omega$, and \mathbf{g}_N is the prescribed traction vector on the remaining part of the boundary $\Gamma_N = \partial\Omega \setminus \Gamma_D$, \mathbf{n} is an outward normal.

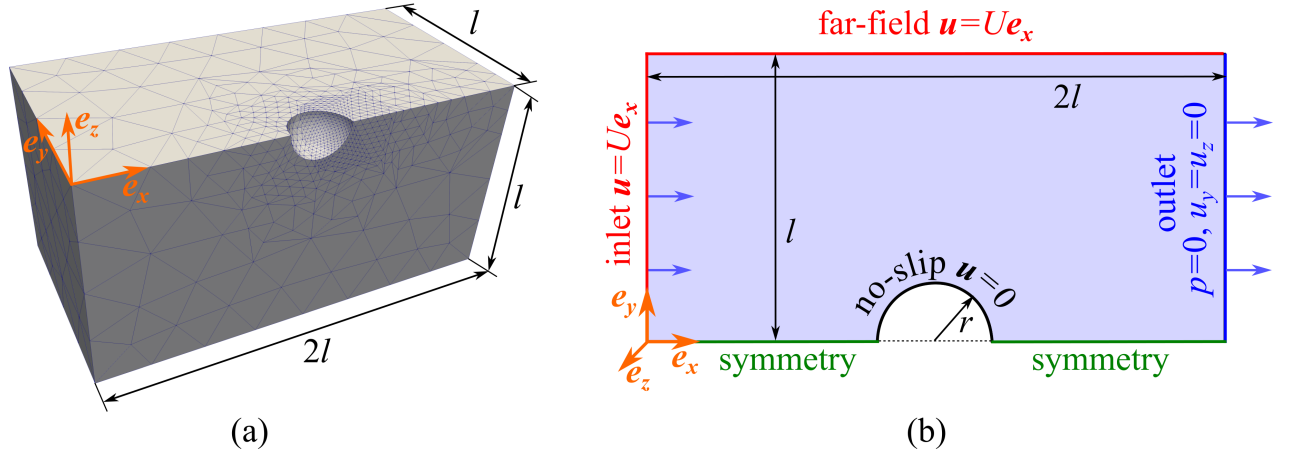


Figure 1: (a) Finite-element mesh used in simulations of fluid flow around a rigid sphere. (b) Sketch of the problem set-up on a section $z = 0$ of the mesh; parameters $r = 1$ m and $l = 7$ m were considered.

Finite-element implementation

The weak statement of the problem (1)-(2) reads: Find a vector field $\mathbf{u} \in \mathbf{V}$ and a scalar field $p \in \mathcal{P}$, such that for any test functions $\mathbf{v} = [v_1, v_2, v_3]^T \in \mathbf{V}$ and $q \in \mathcal{P}$:

$$\int_{\Omega} \rho (\mathbf{u} \cdot \nabla) \mathbf{u} \cdot \mathbf{v} d\Omega + \int_{\Omega} \mu \nabla \mathbf{u} : \nabla \mathbf{v} d\Omega - \int_{\Omega} p \nabla \cdot \mathbf{v} d\Omega - \int_{\Omega} q \nabla \cdot \mathbf{u} d\Omega = \int_{\Omega} \mathbf{f} \cdot \mathbf{v} d\Omega + \int_{\Gamma_N} \mathbf{g}_N \cdot \mathbf{v} d\Gamma_N, \quad (3)$$

while the particular choices for the spaces \mathbf{V} and \mathcal{P} will be discussed below. Upon finite-element (FE) discretization of the domain Ω , we consider interpolation of both unknown fields introducing shape functions on each element:

$$u_i = \sum_{\alpha=1}^{n_u} N_{\alpha} u_i^{\alpha}, \quad p = \sum_{\beta=1}^{n_p} \Phi_{\beta} p^{\beta}; \quad v_i = \sum_{\alpha=1}^{n_u} N_{\alpha} v_i^{\alpha}, \quad q = \sum_{\beta=1}^{n_p} \Phi_{\beta} q^{\beta}, \quad (4)$$

where n_u is the number of shape functions associated with the velocity field, and n_p is the similar number for the pressure field. Using the hierarchical basis approximation, the vector of the shape functions can be decomposed into four sub-vectors, consisting of shape functions associated with element's entities: vertices, edges, faces and the volume of the element, e.g. for the velocity field:

$$\mathbf{N}^{el} = [N_1, \dots, N_{\alpha}, \dots, N_{n_u}]^T = [\mathbf{N}^{ver}, \mathbf{N}^{edge}, \mathbf{N}^{face}, \mathbf{N}^{vol}]^T. \quad (5)$$

MoFEM [1] incorporates hierarchical basis functions of arbitrary order for tetrahedral meshes, based on Legendre [2], Lobatto [3] or Jacoby [4] polynomials, and approximations of \mathbf{H}^1 , $\mathbf{H}\text{-div}$, $\mathbf{H}\text{-curl}$ and \mathbf{L}^2 spaces can be considered. Furthermore, MoFEM provides functionality for iterating not only over all elements in the FE mesh, but also over shape functions associated with all entities of each element. Therefore, the resolution of a particular problem requires only the implementation of operators for computing the residual vector and the tangent matrix of each element, independent of the choice of the basis functions. Finally, the Newton method can be used for solving the non-linear problem.

Numerical results

In order to verify the proposed formulation, we solved the problem of the fluid flow around a rigid

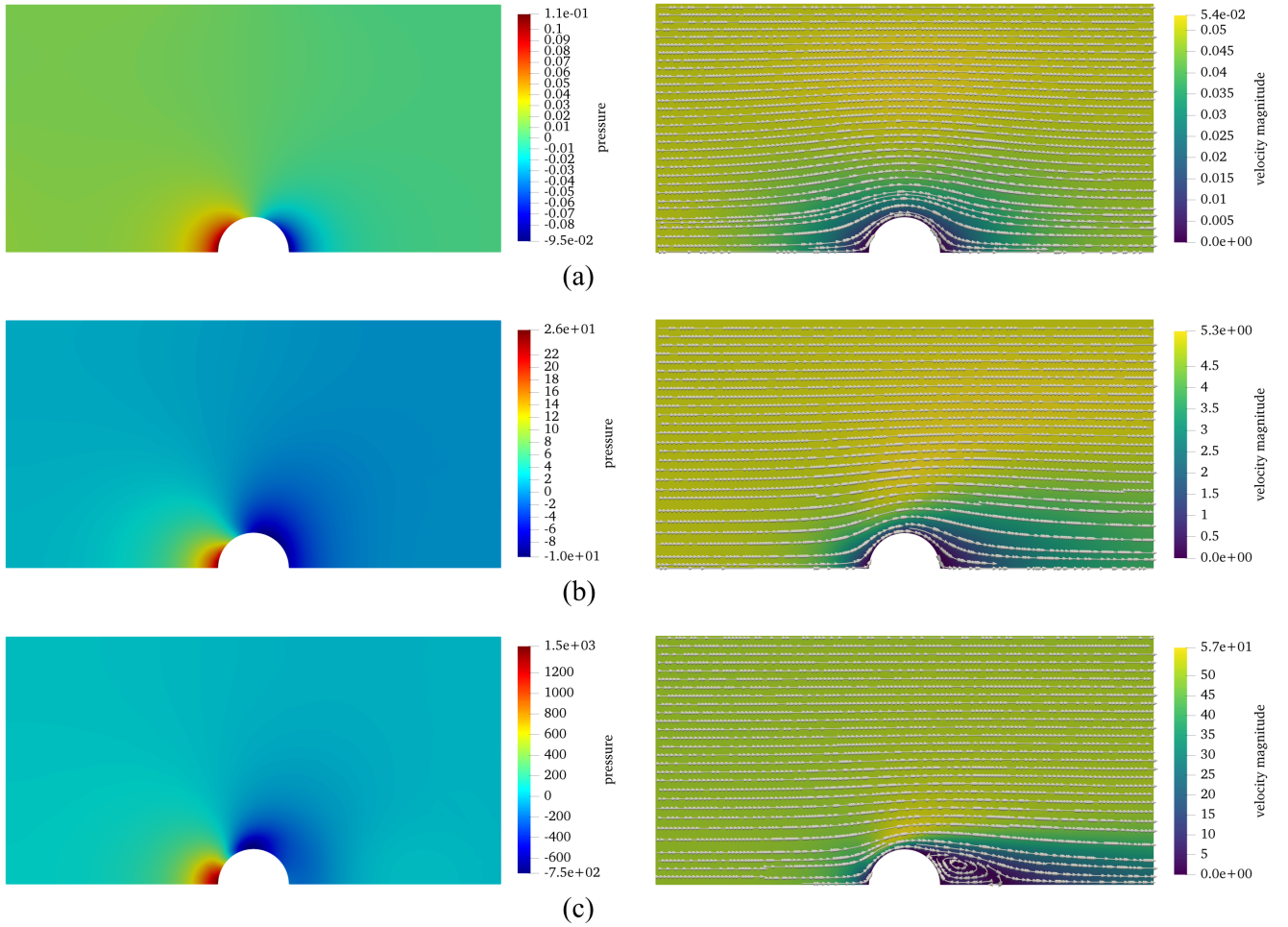


Figure 2: Results of simulations: the distribution of pressure (left) and velocity (right) on a section $z = 0$ of the mesh; (a) $U = 0.05$ m/s, $\mathcal{R} = 0.1$, (b) $U = 5$ m/s, $\mathcal{R} = 10$ and (c) $U = 50$ m/s, $\mathcal{R} = 100$.

sphere (see Fig. 1) of a radius r positioned in the centre of a cubic domain, the side length $2l$ of which is considered sufficiently large compared to r , so that a uniform far-field velocity on the exterior boundaries is valid (note that the body forces are neglected). Exploiting the symmetry of the problem, we used a quarter of the domain in our simulations. In Fig. 2 we present the numerical results obtained for three different values of far-field velocity magnitude: $U = 0.05, 5, 50$ m/s, which permits us to study the flow at different Reynolds numbers:

$$\mathcal{R} = \frac{2rU\rho}{\mu}, \quad (6)$$

where the diameter of the sphere $2r$ and the uniform far-field velocity magnitude U represent the length and the velocity scales, respectively. For a Reynolds number $\mathcal{R} = 0.1$ the solution is symmetric with respect to the plane $x = l$, in accordance with the analytical solution of the Stokes equation, which can be obtained neglecting the non-linear terms of NSE [5]. With $\mathcal{R} = 10$ the symmetry is broken, however, the flow remains laminar. For a higher Reynolds number $\mathcal{R} = 100$, we observe formation of a vortex behind the sphere. Note that in the presented example we considered Legendre polynomials [2] of the third order for velocity and of the second order for pressure, while the space \mathbf{H}^1 was used for both fields. Alternatively, the space \mathbf{L}^2 can be considered for the pressure field, however, in order to fulfil the necessary conditions of the patch test [6], a polynomial of even lower order must be used for approximating the pressure.

Perspectives

The proposed framework can be used to study the fluid flow in contact interfaces between solids with rough surfaces, which is relevant for numerous engineering and geophysical applications. The thin fluid flow is often described by the Reynolds equation, defined on the *lubrication surface*:

$$\nabla \cdot \left[\frac{h^3}{12\mu} \nabla p \right] = 0, \quad (7)$$

where h is the thickness of the fluid film, and the pressure p is assumed constant across the thickness, while the velocity profile is parabolic [5]. However, it has been pointed out that the Reynolds equation overestimates the fluid velocity (and, consequently, the fluid flux) in fractures, compared to the solution of full NSE, if the roughness of the surfaces is taken into account [7]. At the same time, the resolution of NSE becomes difficult if a fine discretization is used, necessary for a representative description of rough surfaces. The problem is further complicated if the contact between these surfaces is considered, resulting in a decrease of the film thickness under increasing external load. Nevertheless, the hierarchical basis approximation provides a possibility to consider the interfacial flow governed by NSE in a single layer of *prism elements*, using polynomials of an arbitrary order to interpolate the velocity profile across the thickness. Moreover, utilization of the hierarchical basis functions facilitates the use of more effective solvers (e.g. the multi-grid method), crucial for problems involving large number of unknowns, in particular, for simulations of fluid flow in rough contact interfaces.

Conclusions

In this study we showed how the model of a viscous fluid, governed by the Navier-Stokes equations, can be implemented in the finite-element framework using hierarchical basis approximation. To verify the proposed formulation, we solved a problem of the fluid flow around a rigid sphere. For a low-Reynolds-number flow, the solution coincides with the analytical solution for the Stokes flow, which neglects the non-linear terms, while under a higher Reynolds number a vortex is formed behind the sphere. Finally, we discussed a perspective application of the developed framework for studying the fluid flow described by Navier-Stokes equations in contact interfaces between solids with rough surfaces.

References

- [1] L. Kaczmarczyk, Z. Ullah, K. Lewandowski, X. Meng, X.-Y. Zhou, C. Pearce, I. Athanasiadis, H. Nguyen, C.-A. Chalons-Mouriesse, and E. Miur. Mofem-v0.8.16, November 2018. <http://mofem.eng.gla.ac.uk>.
- [2] M. Ainsworth and J. Coyle. Hierarchic finite element bases on unstructured tetrahedral meshes. *International Journal for Numerical Methods in Engineering*, 58(14), 2003.
- [3] H. Bériot, A. Prinn, and G. Gabard. Efficient implementation of high-order finite elements for helmholtz problems. *International Journal for Numerical Methods in Engineering*, 106(3), 2016.
- [4] F. Fuentes, B. Keith, L. Demkowicz, and S. Nagaraj. Orientation embedded high order shape functions for the exact sequence elements of all shapes. *Computers & Mathematics with Applications*, 70(4), 2015.
- [5] G.K. Batchelor. *An introduction to fluid dynamics*. Cambridge University Press, 1967.
- [6] O.C. Zienkiewicz and R.L. Taylor. *The finite element method: the basis*, volume 1. Butterworth-Heinemann, 2000.
- [7] S.R. Brown, H.W. Stockman, and S.J. Reeves. Applicability of the Reynolds equation for modeling fluid flow between rough surfaces. *Geophysical Research Letters*, 22(18), 1995.

SIMULATION OF SOAP FILM WITH FLEXIBLE BOUNDARY

A. Majid¹¹ Institute of Business Administration, Karachi, Assistant Professor

amajid@iba.edu.pk

Summary

The problem of finding a minimal surface spanning a rigid boundary is known as the Plateau problem. The generalization of the Plateau problem is known as the Euler Plateau [1] problem where the boundary is allowed to be flexible, however, it remains inextensible. In order to realize such minimal surfaces, consider a closed inextensible fishing line of fixed length, which is taken out after being immersed in soapy water. Depending upon the surface tension of the water, the bending rigidity and the length of the boundary, various shapes of the soap film are observed. For given values of surface tension and bending rigidity, fairly short length of the boundary results in the soap film tending to remain a circular disk. Owing to the fact that boundary is flexible, on increasing length of the boundary up to a critical value, the in plane bifurcation is noticed where circular disk becomes a stable non circular elliptic shape. On further increasing length beyond a critical value, it gives rise to the out of plane bifurcation where we get a twisted out of plane soap film. As we continuously increase length of the boundary, soap film keeps twisting and finally comes to first self contact in plane.

Nondimensionalization of the total energy brings about a dimensionless bifurcation parameter ν as in [2], responsible for various shapes of the soap film. In [1] and [2], it is analytically shown that for $\nu < 3$ the only stable equilibrium solution is a circular disk and the first non circular stable equilibrium solution is reported at $\nu = 3$. In this work, a discrete version of the energy is used to predict critical values of the bifurcation parameter at which transition from planar to a non planar shape takes place and the non planar shape becomes planar again after 180 degree twist, respectively. The two critical values of the bifurcation parameter ν are not known analytically.

Key Words: *Soap Film; Bifurcation; Minimization; Minimal Surface; Inextensibility.*

Model

In this section, the mathematical model [2] which describes the evolution of the soap films with flexible inextensible boundary is discussed. The simplest model where equilibrium shapes of the soap film are formed solely based on the surface tension of the soap film and curvature of the bounding loop is considered. In fact, surface tension pulls the boundary inward and minimizes the area, whereas the closed curve prefers to remain circular in order to minimize the bending energy. This competition of the forces gives rise to fascinating shapes depending upon the surface tension of the soap film, bending rigidity of the bounding loop and length of the bounding loop. The total energy of the system is sum of the surface energy and bending energy and it is given by

$$E = \int_{\Omega} \sigma dA + \frac{1}{2}a \int_{\partial\Omega} \kappa^2(s) ds, \quad (1)$$

subject to the constraint that boundary curve $\partial\Omega$ of the surface Ω is inextensible. In (1), $a > 0$ is the bending rigidity of the loop $\partial\Omega$, σ is the surface tension, κ is the curvature of the boundary and s is the arc length of the boundary curve $\partial\Omega$.

To facilitate future analysis, we nondimensionalize (1) by considering a circular disk of length $L = 2\pi R$ with radius R and introducing dimensionless quantities

$$\tilde{s} = \frac{s}{R}, \quad \tilde{A} = \frac{A}{R^2} \quad \text{and} \quad \tilde{\kappa} = R\kappa. \quad (2)$$

Using (2) in (1), we arrive at the dimensionless energy \tilde{E}

$$\tilde{E} = \frac{ER}{a} = \frac{\sigma R^3}{a} \int d\tilde{A} + \frac{1}{2} \int \tilde{\kappa}^2 d\tilde{s}, \quad (3)$$

where $\nu = \frac{R^3\sigma}{a}$ is the dimensionless parameter as in [2]. For the sake of clarity from now onwards the \sim symbol will not be used and the following energy will be used by assuming that all quantities are dimensionless.

$$E = \nu \int dA + \frac{1}{2} \int \kappa^2(s) ds. \quad (4)$$

The shapes and stability of the equilibrium solutions of (4) depend on the values of the parameter ν . Our aim is to discretize (4) and use some numerical approach to predict the critical value of the bifurcation parameter ν as accurately as possible.

Discrete Setting

Discrete differential geometry provides very powerful tools to transform a continuous model into discrete counterpart, suitable for numerical computations. This approach has been successfully applied to many physical problems of interest such as [3], [4], [5], etc. In this section, all components of the continuous model (4) namely: the surface energy, the bending energy and the inextensibility constraint will be discretized using differential geometry.

We divide the boundary curve $\partial\Omega$ of the surface Ω into $n+1$ discrete points starting from $\mathbf{r}_0, \mathbf{r}_1, \dots, \mathbf{r}_{n-1}, \mathbf{r}_n$. Since $\partial\Omega$ is closed we have $\mathbf{r}_0 = \mathbf{r}_n$ and $\mathbf{r}_{n+1} = \mathbf{r}_1$. Each edge is defined by $\mathbf{e}_i = \mathbf{r}_{i+1} - \mathbf{r}_i$ for $i = 0, \dots, n$. In order to define curvature at each \mathbf{r}_i we define the unit tangent vector corresponding to each \mathbf{r}_i as $\mathbf{t}_i = \frac{\mathbf{e}_i}{|\mathbf{e}_i|}$. The discrete pointwise scalar curvature κ_i at \mathbf{r}_i is defined as [6] the magnitude of the rate of change of the adjacent tangent vectors \mathbf{t}_{i-1} and \mathbf{t}_i .

$$\kappa_i = \frac{|\mathbf{t}_i - \mathbf{t}_{i-1}|}{l_i}. \quad (5)$$

Where $l_i = \frac{|\mathbf{e}_{i-1}| + |\mathbf{e}_i|}{2}$. Discrete bending energy is defined as the integrated squared curvature along the arc length which is given by

$$E_b = \frac{1}{2} \sum \kappa_i^2 l_i. \quad (6)$$

As for the inextensibility constraint, a penalty method approach proved to be the most suitable for this problem in comparison with Lagrange multiplier or projection method. It is very important for this problem that for each energy minimization step constraint is fully satisfied. We carefully choose a tuned penalty constant based on our numerical tests which gives the convergence and enforces the inextensibility constraint.

If d_i is some reference length for each edge length $|\mathbf{e}_i|$ the constraint for each edge is given by

$$\mathbf{e}_i \cdot \mathbf{e}_i - d_i^2 = 0, \quad (7)$$

and the corresponding penalty function is given by

$$E_p = \sum (\mathbf{e}_i \cdot \mathbf{e}_i - d_i^2)^2. \quad (8)$$

Our surface representation is a triangulated surface. If each triangle has area A_i the total surface energy E_A is defined as

$$E_A = \nu \sum A_i. \quad (9)$$

Numerical computations have uncovered a problem associated with Hessian of the surface area when an exact area formula is used. Using exact area formula for this problem gives a singular Hessian because the tangential movement of the interior vertices does not change the energy during minimization. The singularity of Hessian does not allow to minimize the energy by any numerical method which uses second variation of the energy functional such as Newton's Method. In order to deal with this problem we triangulate the initial configuration with approximately equilateral triangles and use a modified formula for the area of triangle.

Suppose a_i, b_i, c_i are three sides of triangle with area A_i , then

$$A_i = \left(\frac{a_i^2 + b_i^2 + c_i^2}{4\sqrt{3}} \right) AR_i, \quad (10)$$

where AR_i is the aspect ratio of the triangle. When $a_i \approx b_i \approx c_i$, for approximately equilateral triangles we have $AR_i \approx 1$ and the area formula (10) becomes

$$A_i \approx \frac{a_i^2 + b_i^2 + c_i^2}{4\sqrt{3}}. \quad (11)$$

The formula (11) provides a non singular Hessian and gives accurate results for equilateral triangles. In addition to begin with a very good mesh produced by Gmsh [8], an edge flipping strategy [7] has also been employed in each minimization step to ascertain that triangulation is approximately an equilateral triangulation.

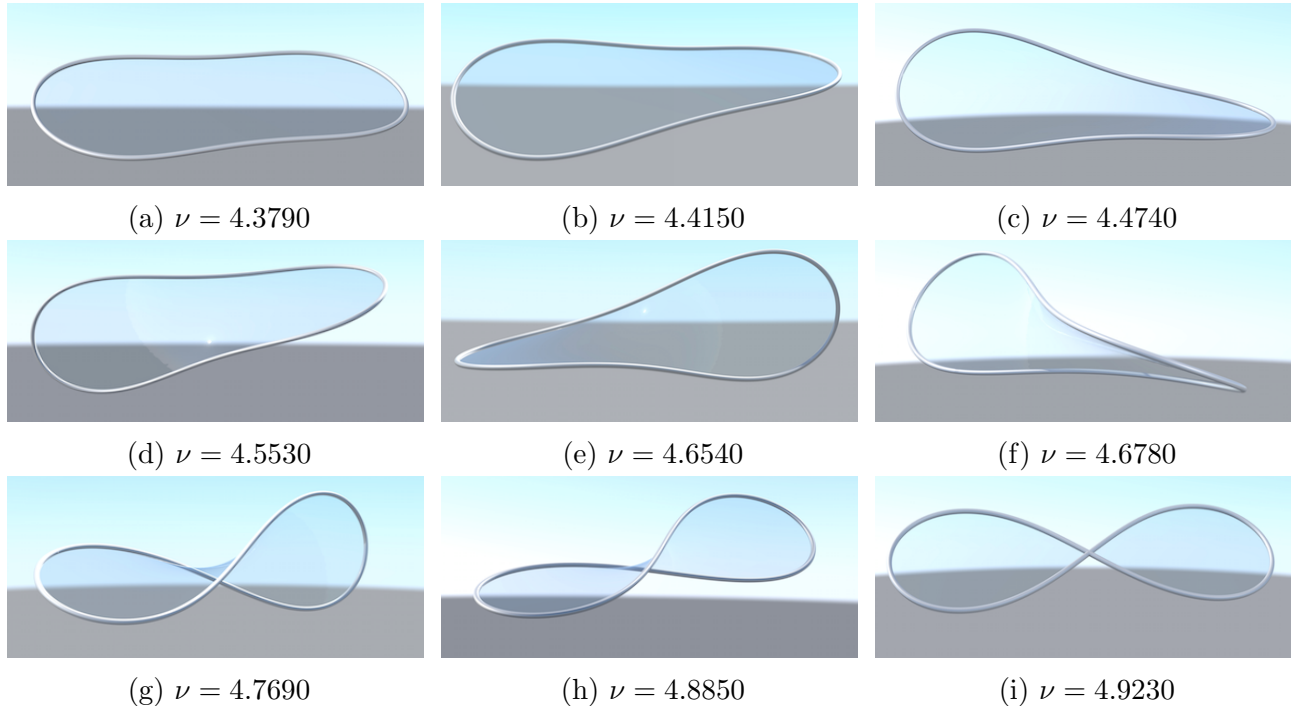


Figure 1: Stable equilibrium solutions of soap film with flexible and inextensible boundary for different values of the dimensionless parameter ν .

Conclusions

In order to predict two critical values of the bifurcation parameter ν , a combination of gradient and Newton's Methods has been used to minimize the discrete version of (4). It is found that first out of plane stable equilibrium solution is found at $\nu = 4.3790$, show in Fig 1a. As we progressively increase the values of ν ,

surface keeps twisting as shown in Fig 1, and we reach the first self contact in plane at $\nu = 4.9230$ as shown in Figure 1i. These values are not known analytically. The accuracy of the critical values of ν could be improved further with a better triangulation scheme which guarantees equilateral triangles at every step of minimization.

Due to the fascinating nature and flexible geometry of the minimal surface they have applications in architectural design and biological systems. As discussed in [9], morphology of a cell is subjected to various stiffnesses of the substrate. Cell constrained to more stiff substrates exhibits more flatter patterns than the soft substrates. Moreover, reference [10] provides good survey of the minimal surface applications in geometric modeling and material design.

References

- 1 L. Giomi and L. Mahadevan. Minimal surfaces bounded by elastic lines. *Proc. R. Soc. Lond. Ser. A, Math. Phys. Eng. Sci*, 468, 1851-1864, 2012.
- 2 Fried Y. C. Chen and E. Fried. Stability and bifurcation of a soap film spanning and elastic loop. *Journal of Elasticity*, 115(1), 75-100, 2013.
- 3 Bergou, M., Wardetzky, M., Robinson, S., Audoly, B. and Grinspun, E. Discrete Elastic Rods. *ACM Trans. Graph*, 63, 1-12, 2008.
- 4 Rony Goldenthal, David Harmon, Raanan Fattal, Michel Bercovier and Eitan Grinspun. Efficient Simulation of the Inextensible Cloth," *In ACM TOG*, 49.
- 5 Tim Hoffmann. Discrete Differential Geometry of Curves and Surfaces. 2008.
- 6 R. J. Renka. Constructing fair curves and surfaces with a Sobolev gradient method. *Computer Aided Geometric Design* 21, 137-149, 2004.
- 7 Øyvind Hjellev, Morten Daehlen. Triangulations and Applications *Springer*, 2006.
- 8 C. Geuzaine and J. F. Remacle. Gmsh: a three-dimensional finite element mesh generator with built-in pre- and post-processing facilities , *International Journal for Numerical Methods in Engineering*. 79, 1309-1331, 2009.
- 9 T. Yeung, P. C. Georges, L. A. Flanagan, B. Marg, M. Ortiz, M. Funaki, N. Zahir, W. Ming, V. Weaver, and P. A. Janmey. Effects of substrate stiffness on cell morphology, cytoskeletal structure, and adhesion. *Cell Motil. Cytoskel.*, 60, 24-34, 2005.
- 10 Pottmann, H., Brell-Cokcan, S., Wallner, J. Discrete surfaces for architectural design. *In: Curve and Surface Design: Avignon*, 213-234. Nashboro Press (2006).

AN UNSYMMETRIC SOLID-SHELL ELEMENT FOR GEOMETRIC NONLINEAR ANALYSIS

***Zhi Li^{1,3}, Song Cen^{1,2}, Chen-Feng Li³ and Yan Shang⁴**

¹Department of Engineering Mechanics, School of Aerospace Engineering, Tsinghua University, Beijing 100084, China

²Key Laboratory of Applied Mechanics, School of Aerospace Engineering, Tsinghua University, Beijing 100084, China

³Zienkiewicz Centre for Computational Engineering, Swansea University, Swansea SA1 8EN, UK

⁴State Key Laboratory of Mechanics and Control of Mechanical Structures, College of Aerospace Engineering, Nanjing University of Aeronautics and Astronautics, Nanjing 210016, China

*zli15@mails.tsinghua.edu.cn

Summary

A recent distortion-resistant unsymmetric 8-node hexahedral solid-shell element US-ATFHS8 is successfully extended to geometric nonlinear analysis. Owing to combining unsymmetric finite element method and analytical trial function method, the original linear elastic element can present highly accurate predictions for many shell problems. The extension is based on the co-rotational (CR) approach due to its simplicity and high efficiency, especially for geometric nonlinear analysis where the strain is still small. Since the analytical trial functions are employed to construct the element, the key of the whole work is that the co-rotational formulations of solid-shell element US-ATFHS8 are derived based on the updated Lagrangian (UL) framework, and an appropriate updated algorithm for analytical trial functions is designed. Numerical examples show that the present nonlinear element US-ATFHS8 also possesses high performance for various rigorous tests, no matter whether regular or distorted mesh is used.

Key Words: *finite element methods; unsymmetric solid-shell elements; geometric nonlinear analysis; co-rotational approach; mesh distortion*

Introduction

To date, the finite element method (FEM) is still considered as an efficient tool to simulate the complicated behaviors of shell, one kind of important and complex structures in engineering. More and more researchers and users prefer to use solid-shell elements in practical simulations, because such models have no rotational degrees of freedom and can be easily applied with general 3D constitutive laws. A recent locking-free unsymmetric solid-shell element US-ATFHS8 with high distortion tolerance is constructed by using the unsymmetric finite element method based on the analytical trial function method [1]. Since mesh distortions are more common in large strain, large displacement, or large rotation problems, a distortion-resistant finite element model is more expectative in nonlinear analysis. In present work, the co-rotational formulations of element US-ATFHS8 are constructed based on the updated Lagrangian framework for geometric nonlinear analysis.

Co-rotational Approach Based on Updated Lagrangian Framework

To find the co-rotational frame is one of main procedures in the co-rotational formulation based on the given deformable configuration. In this paper, the strategy to construct the best-fit co-rotational frames for 3D continuum finite elements proposed by Mostafa et al. [2], which is accomplished by minimizing deformations within the frame using a quaternion parametrization of rotations, is adopted. To clarify the element kinematics in the co-rotational formulation, a 2D element is shown in Figure 1. Based on the updated Lagrangian framework, the configuration at time t is considered as a reference configuration

instead of initial configuration in reference [2]. The displacement of a node I within the co-rotational frame is

$$\widehat{\mathbf{u}}_I = {}^{t+\Delta t}\widehat{\mathbf{R}}^T ({}^{t+\Delta t}\mathbf{x}_I - {}^{t+\Delta t}\mathbf{x}_O) - {}^t\widehat{\mathbf{R}}^T ({}^t\mathbf{x}_I - {}^t\mathbf{x}_O), \quad (1)$$

where ${}^{t+\Delta t}\mathbf{x}_O$ and ${}^t\mathbf{x}_O$ are the origin coordinates of the co-rotational frame at time $t + \Delta t$ and t , respectively. The essence of this strategy is to construct a co-rotational frame $({}^{t+\Delta t}\widehat{\mathbf{x}}_O, {}^{t+\Delta t}\widehat{\mathbf{R}})$ by minimize $\|\widehat{\mathbf{u}}\|^2$.

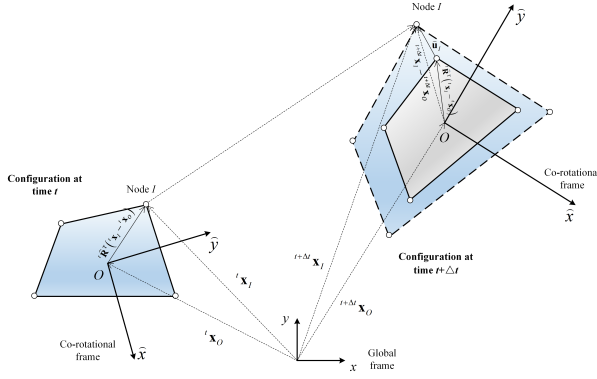


Figure 1: The element kinematics in the co-rotational formulation based on updated Lagrangian framework.

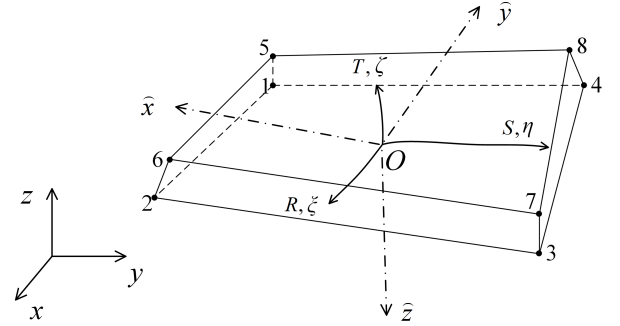


Figure 2: Local co-rotational coordinates, 3D oblique coordinates and natural coordinates in a solid-shell element.

The Construction of Element US-ATFHS8 for Geometric Nonlinear Analysis

An 8-node, 24-DOF hexahedral solid-shell is shown in Figure 3. $(\widehat{x}, \widehat{y}, \widehat{z})$, (R, S, T) , (ξ, η, ζ) are the local co-rotational coordinates, 3D oblique coordinates and natural coordinates respectively. For the unsymmetric element US-ATFHS8 [1], two different sets of interpolation functions for displacement fields are simultaneously used. Here, in the local co-rotational frame, the first set (test functions) is for the virtual displacement vector $\delta\widehat{\mathbf{u}}$ imposed on configuration ${}^{t+\Delta t}\widehat{V}$, which is constructed in natural coordinates by introducing proper shell assumptions and assumed natural strain modifications for transverse strains. The second set (trial functions) is for *real* incremental displacement vector $\widehat{\mathbf{u}}$, which is constructed in composite coordinates (local co-rotational coordinates and 3D oblique coordinates) with analytical trial functions:

$$\widehat{\mathbf{u}} = \begin{Bmatrix} \widehat{u}_x \\ \widehat{u}_y \\ \widehat{u}_z \end{Bmatrix} = \mathbf{P}\boldsymbol{\alpha} = \begin{bmatrix} 1 & 0 & 0 & {}^t\widehat{x} & 0 & 0 & {}^t\widehat{y} & 0 & 0 & {}^t\widehat{z} & 0 & 0 & {}^tU_{13} & \cdots & {}^tU_{21} & {}^tR^tS^tT & 0 & 0 \\ 0 & 1 & 0 & 0 & {}^t\widehat{x} & 0 & 0 & {}^t\widehat{y} & 0 & 0 & {}^t\widehat{z} & 0 & {}^tV_{13} & \cdots & {}^tV_{21} & 0 & {}^tR^tS^tT & 0 \\ 0 & 0 & 1 & 0 & 0 & {}^t\widehat{x} & 0 & 0 & {}^t\widehat{y} & 0 & 0 & {}^t\widehat{z} & {}^tW_{13} & \cdots & {}^tW_{21} & 0 & 0 & {}^tR^tS^tT \end{bmatrix} \begin{Bmatrix} \alpha_1 \\ \vdots \\ \alpha_{24} \end{Bmatrix}, \quad (2)$$

in which the first twelve terms in this interpolation are related to 3 translational rigid motions and 9 linear displacement fields, and the 13th-21st terms are the displacement solutions related to the 13th-21st stress solutions [1]. It should be noted that they depend on the configuration ${}^t\widehat{V}$ in present formulation. Then, the linear incremental strain tensor can be rewritten as Voigt notation:

$$\{ {}^t\widehat{\mathbf{e}} \} = {}^t\widehat{\mathbf{B}}\Delta\widehat{\mathbf{q}}^e. \quad (3)$$

The element stiffness matrix and the internal nodal force vector of solid-shell element US-ATFHS8 in the local co-rotational frame are given as follow:

$${}^t\widehat{\mathbf{K}}^e = \int_{{}^t\widehat{V}_e} {}^t\widetilde{\mathbf{B}}^T \left[{}^t\widehat{\mathbf{C}} \right] {}^t\widehat{\mathbf{B}} dV = \int_{-1}^1 \int_{-1}^1 \int_{-1}^1 {}^t\widetilde{\mathbf{B}}^T \left[{}^t\widehat{\mathbf{C}} \right] {}^t\widehat{\mathbf{B}} \left| {}^t\mathbf{J} \right| d\xi d\eta d\zeta, \quad (4)$$

$${}^t\widehat{\mathbf{F}}_{\text{int}}^e = \int_{{}^t\widehat{V}_e} {}^t\widetilde{\mathbf{B}}^T \left\{ {}^t\widehat{\boldsymbol{\sigma}} \right\} d^tV. \quad (5)$$

Since the linear deformation is assumed in the local co-rotational frame, the update of stress tensor is easy to handle:

$${}^{t+\Delta t}\widehat{\boldsymbol{\sigma}} = {}^t\widehat{\boldsymbol{\sigma}} + \Delta\widehat{\boldsymbol{\sigma}}. \quad (6)$$

Finally, the element stiffness matrix and the internal nodal force vector in the global frame can be calculated using Equations (41),(43) and (44) in reference [2].

Numerical Examples

Two numerical examples are presented in this section to assess the performance of the proposed formulation of solid-shell element US-ATFHS8 for geometric nonlinear analysis. As shown in Figure 3, a twisted beam is under out-of-plane end resultant force. Two mesh cases, 2×20 regular and distorted meshes, are considered. The results obtained by present element US-ATFHS8 and other solid-shell elements are given in Figure 4. It can be seen that US-ATFHS8 can agree very well with the reference results by using both coarse meshes (2×20 regular and distorted meshes), which are even better than the results obtained by using a finer mesh (4×24 regular mesh) in reference [3]. However, both SC8R and CSS8 elements in Abaqus cannot provide good results using the same regular coarse mesh. It can be found that CSS8 is very sensitive to the mesh distortion, worse results appear once mesh is distorted. In addition, although SC8R is insensitive to the mesh distortion as well as US-ATFHS8, it cannot provide good results even using regular coarse mesh.

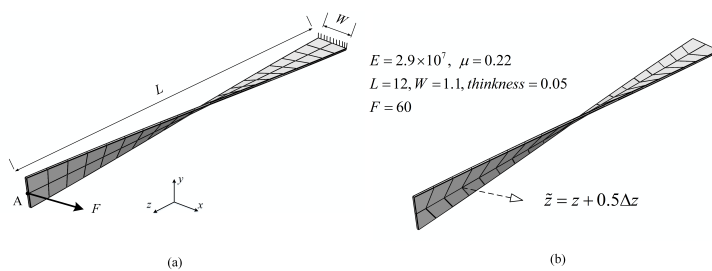


Figure 3: A twisted beam under out-of-plane end resultant force.(a) 2×20 regular mesh; (b) 2×20 distorted mesh.

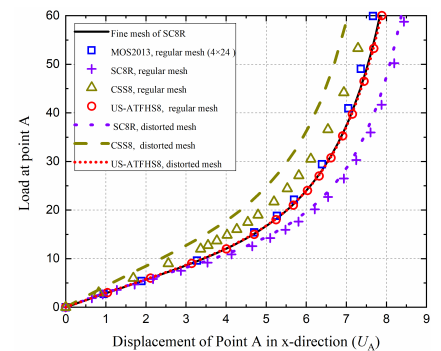


Figure 4: Load-displacement curves for a twisted beam under out-of-plane end resultant force

As shown in Figure 5, a segment of a cylindrical shell is hinged at the two edges and subjected to a concentrated load. Owing to symmetry, only a quarter of the model is considered. As reported in reference [4], the thickness is discretized with two elements when using solid-shell element to represent the hinged support. Two coarse meshes ($4 \times 4 \times 2$ regular and distorted elements) is used in present work. The load-displacement curves of US-ATFHS8 and other models [3, 4] are plotted in Figure 6 for comparison. In general, US-ATFHS8 can agree well with the reference results using both regular and distorted coarse mesh. The deviation appears when snap-through occurs at point A mainly because

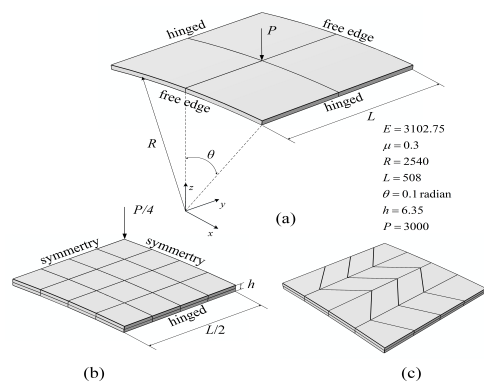


Figure 5: A hinged cylindrical shell under concentrated load. (a) Geometry; (b) Regular mesh; (c) Distorted mesh.

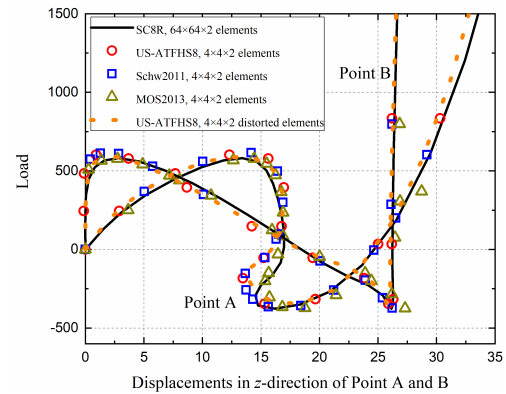


Figure 6: Load-displacement curves for a hinged cylindrical shell under concentrated load

the mesh is quite coarse such that the geometry discretization errors apply. On the other hand, no deviation appears when snap-through occurs at point B.

Conclusions

Based on the simple and efficient co-rotational approach, a recent distortion-tolerant unsymmetric 8-node hexahedral solid-shell element US-ATFHS8 [1] is successfully extended to geometric nonlinear analysis. The co-rotational formulations of element US-ATFHS8 are derived based on the updated Lagrangian framework, so that the analytical trial functions employed in this element can be updated during geometric nonlinear analysis. Numerical examples show that the present nonlinear element exhibits high-performance no matter whether regular or distorted mesh is used. It again demonstrates the advantages of the unsymmetric finite element method with analytical trial functions. How to generalize the unsymmetric element with linear analytical solutions to material nonlinear analysis is another interesting topic, and will be discussed in the near future.

Acknowledgements

The authors would like to thank for the financial supports from the National Natural Science Foundation of China (11872229), and the China Scholarships Council fellowship (201806210280) during the visit of Zhi Li to Swansea University.

References

- 1 J.B. Huang, S. Cen, Z. Li, C.F. Li. An unsymmetric 8-node hexahedral solid-shell element with high distortion tolerance: Linear formulations. *International Journal for Numerical Methods in Engineering*, 116, 759-783, 2018.
- 2 M. Mostafa, M.V. Sivaselvan. On best-fit corotated frames for 3D continuum finite elements. *International Journal for Numerical Methods in Engineering*, 98, 105-130, 2014.
- 3 M. Mostafa, M.V. Sivaselvan, C.A. Felippa. A solid-shell corotational element based on ANDES, ANS and EAS for geometrically nonlinear structural analysis. *International Journal for Numerical Methods in Engineering*, 95, 145-180, 2013.
- 4 M. Schwarze, S. Reese. A reduced integration solid-shell finite element based on the EAS and the ANS concept—Large deformation problems. *International Journal for Numerical Methods in Engineering*, 85, 289-329, 2011.

An investigation of a Υ -type MTD Stirling engine prototype

*M. H. Khanjanpour¹, M. Rahnama², A. A. Javadi¹, M. Akrami¹, A. R. Tavakolpour³
and M. Iranmanesh⁴

¹College of Engineering, Mathematics, and Physical Sciences, University of Exeter, EX4 4QF

²Department of Mechanical Engineering, Shahid Bahonar University of Kerman, 7618868366

³Department of Mechanical and Aerospace, Shiraz University of Technology, 75155713876

⁴International Centre for Science, High Tech. & Environmental Sciences Kerman, 7631818356
*mk592@exeter.ac.uk

Summary

Although thermal efficiency of moderate temperature differential (MTD) Stirling engines is higher than low temperature (LTD) engines, the complexity of design of MTD engines has led to the lack of research in this field. In this work, a prototype of Υ -type moderate-temperature differential Stirling engine was manufactured, evaluated and structurally optimised. A mathematical evaluation was carried out based on a finite-dimension thermodynamics approach. The swept volume ratio was optimised based on the temperature difference of 450^oC. A computer program was thus written to simulate the Stirling engine performance under the assumed working conditions. Based on the mentioned temperature difference, the swept volume ratio of the engine was found to be 3. The engine dimensions were then adjusted to fulfil the computed swept volume ratio. The bore and stroke for power piston were chosen as 60 mm and 40 mm, respectively. For the displacer, they were selected as 90 mm and 60 mm, respectively based on the chosen swept volume ratio.

Key Words: Stirling engine; Gamma-type; Swept volume ratio; finite-dimension thermodynamics

1. Introduction

The Stirling engine was invented by Robert Stirling approximately two centuries ago [1, 2]. The Stirling engine is a prominent candidate for power generation which uses both renewable and natural resources. According to the considered temperature difference, the Stirling engines can be categorized as the high-temperature differential (HTD), moderate temperature differential (MTD) and the low-temperature differential (LTD) designs. The high-temperature design represents the benchmark for solar energy to electricity conversion efficiency, typically around 30%. The thermal limit for the operation of high-temperature Stirling engines depends on the material used for its construction [3]. Engine efficiency ranges between 30% to 40%, resulting in a typical temperature range of 650-800 C^o, and the normal operating speed range is from 2000 to 4000 rpm [1]. However, it comes at a cost that can be as high as 10,000 \$/kW compared to 3000 \$/kW for the photovoltaic systems [3]. On the other hand, the low-temperature differential Stirling engines are not as successful as their high-temperature difference counterparts. The thermal efficiency of the low-temperature differential Stirling engines also cannot achieve the efficiency of the high-temperature Stirling engines [4]. Besides the high and low-temperature Stirling engines, the moderate temperature differential engine avoids the expensive alloys and complex design required in the high-temperature design, hence brings down the cost. Nevertheless, the thermal efficiency of moderate temperature is higher than that of the low temperature.

In this experimental study, a moderate temperature Stirling engine is modelled using the finite-dimension thermodynamics approach. According to the desired temperature

difference and using the mathematical model, the optimum swept volume ratio of the engine is estimated so as to maximise the objective functions (e.g. efficiency and work). Upon the obtained swept volume ratio, the prototype of the moderate temperature Stirling engine is developed and evaluated.

2. Optimization scheme

One of the first optimization goals concerning moderate temperature differential Stirling engines is to determine the optimum swept volume ratio (ξ). According to the guidelines provided in [5] and [6], the procedures of finite dimension thermodynamics were employed to calculate the efficiency of the engine η and dimensionless work W^* in order to find optimum swept volume ratio.

$$|W^*| = \frac{(1 - (1/\tau))m^*}{1 + \xi(1 + 2\sigma)(1 + 2\sigma)[1 + \xi(1 + 2\sigma)]} \quad (1) \quad \eta = \frac{-\ln(Z(\xi, \sigma, \tau))}{[(\tau \ln(Z(\xi, \sigma, \tau)))/(1 - \tau) + G(\xi, \sigma, \tau)]} \quad (2)$$

Where: $\tau = \frac{T_h}{T_c}$, σ : dead space volumes, m^* : dimensionless mass. T_h : cold outer space, T_c : cold inner space

Table 1, Reference parameters

$T_H(K)$	$T_C(K)$	$P_0(Pa)$	σ	$\nu (rev s^{-1})$	$y_0(mm)$	γ	η_{reg}
753	303	100000	0.1	2	60	1.4	0

Where: γ : gas heat capacity ratio, ν : frequency

For the given values of parameters in Table 1, the swept volume ratio was incremented so as to find the optimum value of ξ corresponding to maximum values of η and W^{**} . This was done by a computer program to determine the optimized swept volume ratio (Fig.1). In this work, an effort was made to design a moderate temperature differential around 450 °C and the sink temperature was assumed to be the ambient temperature.

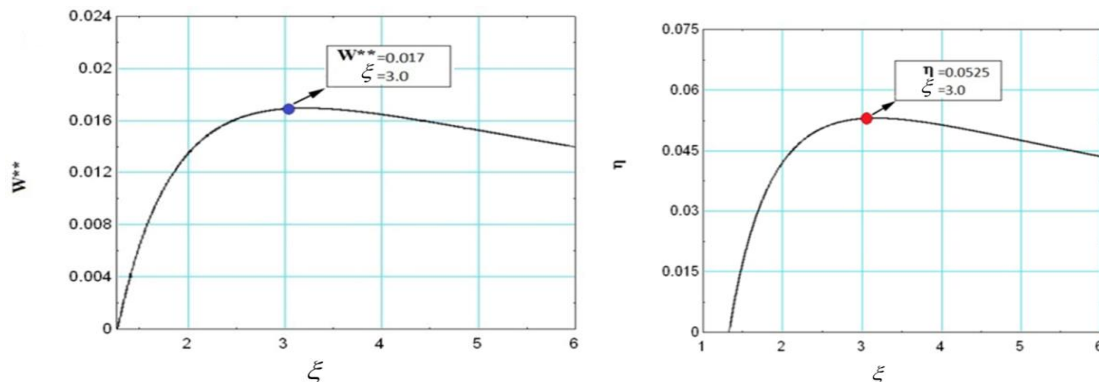


Fig. 1. (right) Efficiency and (left) dimensionless secondary work versus compression ratio

Table 2

Mechanical configuration	Displacer	Power piston	Phase angle	Swept volume ratio	Working gas	Cooling system
Gamma	Bore \times stroke (m) 0.09 \times 0.06	Bore \times stroke (m) 0.06 \times 0.04	90°	3	Air	Air cooled

3. Engine construction

According to the results obtained in the previous section, a moderate temperature Stirling engine with Gamma configuration was developed. The main engine design parameters are shown in Table 2. The power cylinder was made of a cast iron pipe and the power piston was made of an aluminium bar. The power piston was tuned to match the power cylinder bores. The clearance between the power piston and power cylinder was 0.5 mm. The displacer was built from aluminium. The displacer cylinder was made of a steel pipe. The clearance space between the displacer and the cylinder liner was 10 mm. The rod of the displacer was made of stainless steel. The cooling fins were built from aluminium. The two middle pages were made of aluminium with dimensions $20 \times 16 \times 2$ (cm) and were connected by 14 bolts and nuts. The flywheel was constructed from iron with 20 cm thickness and 2.3 kg weight. The prototype Stirling engine developed in this work is depicted in Fig. 2.

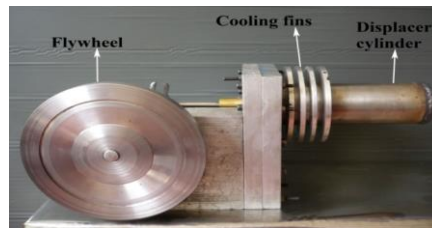


Fig. 2. Photographs of gamma-type Stirling engine

4. Indicated power and testing

The mean indicated power can be calculated approximately from equation 3:

$$P = \frac{W_{total} n_{mean}}{60} \quad (3)$$

where W_{total} is the total work done per cycle and n_{mean} is the mean engine speed at mean hot source temperature of 450°C and sink temperature of 30°C . n_{mean} was measured to be about 160 rpm. The developed Stirling engine was tested at thermodynamics Laboratory in order to evaluate the validity of the obtained swept volume ratio from the optimization study. Upon the presented optimization technique (Fig 1) the optimum swept volume ratio was found to be 3. Thus, the experimental investigation was organized with three swept volume ratios 2.5, 3 and 3.5 so as to see whether or not the swept volume ratio of 3 is optimal.

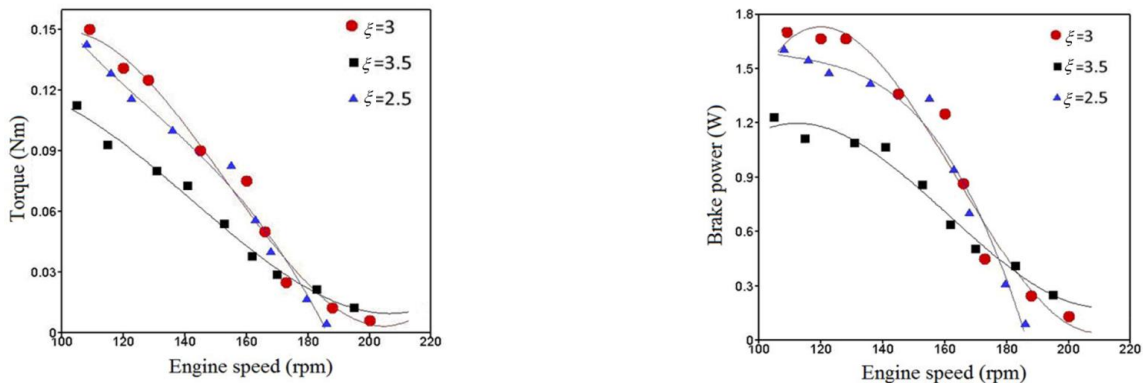


Fig. 3. (right) Brake power and (left) Engine torque versus engine speed

Fig. 3 demonstrates the variations of the engine torque and the brake power versus the engine speed for the three swept volume ratios. As can be observed, a higher engine torque and a higher brake power can be picked up at the lower engine speeds. Furthermore, around the engine speed of 120 rpm which is the considered speed in the optimization study (see Table 1), the swept volume ratio 3 showed some superiorities compared to other graphs through which the validity of the optimization scheme can be confirmed.

The brake power in Fig. 3 was calculated using the following equation [7]:

$$P_{Brake} = \frac{2\pi Tn}{60} \quad (4)$$

where n is the engine speed in rpm and T is the engine torque in Nm.

5. Conclusion

In this study, an optimization scheme which had been previously applied to the low-temperature differential Stirling engines based on the assumption of low-temperature difference [5] was used to optimize their moderate temperature counterparts. The optimized swept volume ratio was found to be 3 through the optimization study. A gamma-type moderate temperature differential Stirling engine with adjustable swept volume ratio was designed and constructed to evaluate the validity of the optimization method. The regenerator was omitted to determine the minimum possible output power and to simplify the engine structure. To validate the obtained optimum swept volume ratio, the engine was experimentally evaluated at different swept volume ratios including 2.5, 3 and 3.5. The results showed that the optimal swept volume ratio of the engine is 3 for the engine speed range of 100-160 rpm (in order to maximise the torque and brake power) and 3.5 when the engine speed is in the range of 160-200 rpm.

6. References

- 1 G. Walker, Stirling engines, Oxford: Clarendon Press; 1980.
- 2 G. Reader, T. and Hooper, C. (1983) Stirling Engines, E. & F. N.
- 3 I. Tlili, Y. Timoumi, SB. Nasrallah, Analysis and design consideration of mean temperature differential Stirling engine for solar application, Renewable Energy.33 (2008) 1911-1921.
- 4 S. Ishiki et al. The experimental study of atmospheric Stirling engines using pin-fin arrays' heat Exchangers, Power and Energy Systems. 2 (2008) 1198-1208.
- 5 A. R. Tavakolpour, A. Zomorodian and A. A. Golneshan, Simulation, construction and testing of a two-cylinder solar Stirling engine powered by a flat-plate solar collector without regenerator, Renewable Energy. 33 (2008) 77–87.
- 6 P. Rochelle LTD, Stirling engine simulation and optimization using finite dimension thermodynamic. In: Proceedings of the 12th international Stirling engine conference, Durham University, 2005.
- 7 JL. Meriam, LG.Karige, Engineering mechanics dynamics, Wiley, 1997.

INSTABILITIES IN THE DEFORMATION OF MAGNETOELASTIC MEMBRANES

Prashant Saxena

Glasgow Computational Engineering Centre, School of Engineering
 University of Glasgow, Rankine Building, Oakfield Avenue, Glasgow G12 8LT
 Email: prashant.saxena@glasgow.ac.uk

Summary

We study the inflation of weakly magnetizable isotropic membranes in the presence of externally applied magnetic field. The relevant governing equations, boundary conditions, and stability criteria are derived from a variational formulation and computational solutions are obtained for three geometries – circular, cylindrical, and toroidal membranes. It is observed that magnetic field can alter the onset of elastic limit point instability and introduce new magnetic limit points. Multiple stable equilibrium configurations are predicted for a given coupled load. We also observe induction of wrinkling in the membrane due to the magnetic field.

Key Words: *magnetoelasticity; membrane; instability; limit point; wrinkling*

1 Introduction

Magnetoelastic polymers are artificially fabricated composites that can change their mechanical attributes (shape/ stiffness etc.) upon the application of an external magnetic field. Nonlinear magnetoelastic membranes have applications in inflatable systems for energy harvesting and vibration absorption. We aim to develop a computational formulation to study the deformation of magnetoelastic membranes under coupled pressure and magnetic loading while focussing on development of instabilities in the system under these extreme deformation conditions.

2 Mathematical formulation

2.1 Kinematics

Figure 1 shows three cases of incompressible isotropic nonlinear magnetoelastic membranes. The membranes are inflated by a gas pressure as well as deformed by the externally applied magnetic field as shown in the figure. The right Cauchy–Green deformation tensor \mathbf{C} for each of the three cases of deformed toroidal, cylindrical, and circular membranes can be written, respectively, as

$$\begin{bmatrix} \frac{\rho^2 + \eta^2}{R_s^2} & 0 & 0 \\ 0 & \frac{\rho^2}{[R_b + R_s \cos\theta]^2} & 0 \\ 0 & 0 & \lambda_3^2 \end{bmatrix}, \begin{bmatrix} u'^2 + [1 + w']^2 & 0 & 0 \\ 0 & \frac{[R_0 + u]^2}{R_0^2} & 0 \\ 0 & 0 & \lambda_3^2 \end{bmatrix}, \begin{bmatrix} \rho'^2 + \eta'^2 & 0 & 0 \\ 0 & \frac{\rho^2}{R^2} & 0 \\ 0 & 0 & \lambda_3^2 \end{bmatrix}. \quad (1)$$

We refer the reader to the papers [2, 3, 4] for detailed derivations of above expressions. Here λ_3 is the stretch ratio in the thickness direction of the membrane, ρ and η are the parameters defining the profile for the toroidal and circular membrane upon deformation while u and w are the parameters defining the profile of cylindrical membrane upon deformation as shown in figure 1.

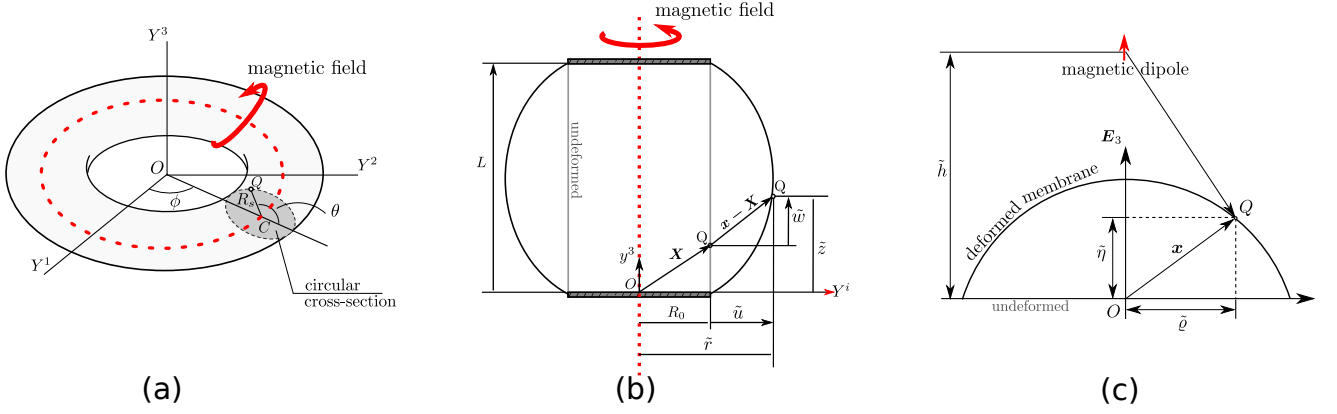


Figure 1: The three geometries studied in this work (a) Inflated toroidal membrane with magnetic field applied by a current carrying loop [2]. (b) Inflated cylindrical membrane with magnetic field applied by an infinite current carrying wire [3]. (c) Inflated circular membrane with magnetic field applied by a fixed dipole [4].

2.2 Governing equations and computational procedure

Under the thinness approximation, the total potential energy functional (E) of the system under consideration can be written as (see [1])

$$E = t_0 \int_{\Omega} \varrho \psi dA - t_0 \mu_0 \int_{\Omega} \mathbf{m} \cdot \mathbf{h}_a dA - \int_{V_0}^{V_0 + \Delta V} P dV, \quad (2)$$

where $\varrho \psi(\mathbf{F}, \boldsymbol{\mu})$ is the free energy per unit volume, \mathbf{F} is the deformation gradient, $\boldsymbol{\mu}$ is the material magnetization per unit mass, $\mathbf{m} = \varrho \boldsymbol{\mu}$ is the magnetization per unit current volume, \mathbf{h}_a is the externally applied magnetic field, P is the gas pressure used to inflate the membrane, Ω denotes the mid-surface of the undeformed membrane, t_0 is the initial thickness of the membrane, V_0 is the enclosed initial volume, and ΔV is the change in this enclosed volume. We use the following relations for a weakly magnetized membrane (self-generated magnetic field is negligible)

$$\frac{\partial \psi}{\partial \boldsymbol{\mu}} = \mu_0 \mathbf{h}_a, \quad \varrho \psi = W + \frac{\mu_0 \varrho^2}{2\chi} |\boldsymbol{\mu}|^2, \quad \mathbf{m} = \chi \mathbf{h}_a, \quad (3)$$

to simplify the above energy functional and then take the first variation to arrive at the relevant governing equations and boundary conditions for each of the three cases. Governing equations for the toroidal and circular membrane problems can be rewritten as ODEs in matrix form as

$$\mathbf{A} \mathbf{X}' = \mathbf{E}, \quad (4)$$

where \mathbf{X} is an $n \times 1$ column vector of the functions to be evaluated, \mathbf{A} is an $n \times n$ and \mathbf{E} is an $n \times 1$ matrix both of which depend on the material parameters, loading conditions and the state variable \mathbf{X} . We solve the above set of boundary value problem by converting it into an initial value problem using the shooting method and coupling it with an optimization routine.

Governing equations for the cylindrical membrane problem occur in the form of coupled ODEs that are more amenable to be solved using a finite difference method coupled with a cubic extrapolation arc-length technique.

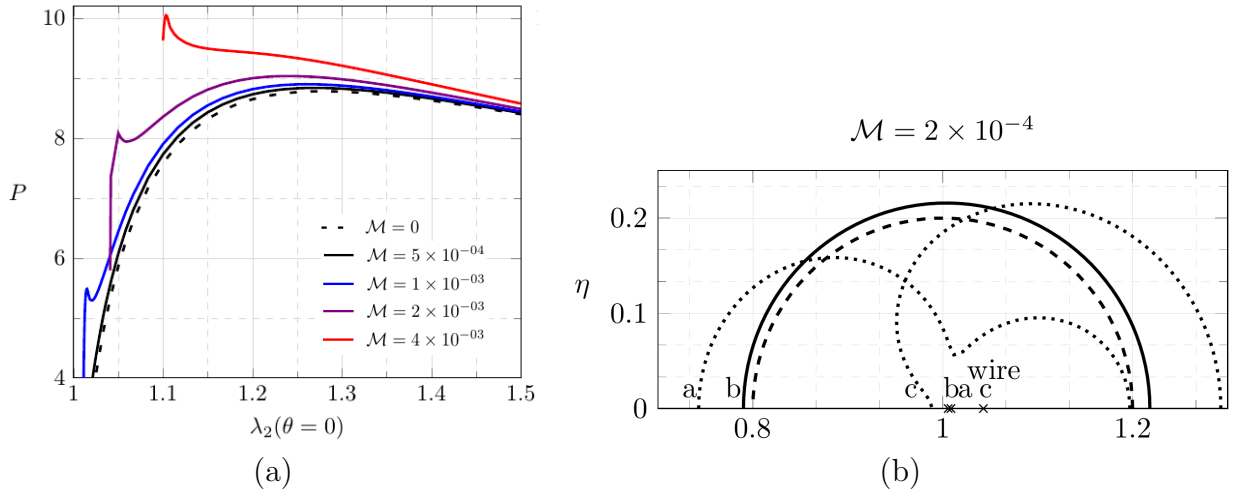


Figure 2: Results for toroidal membrane taken from [2]. (a) Pressure vs stretch plot shows change of limit point instability as magnetic loading \mathcal{M} is increased. (b) Multiple stable and unstable profiles of torus cross-section for a given magnetoelastic loading.

2.3 Stability of equilibrium

A necessary condition for the equilibrium state obtained in Section 2.2 is that it be a minimiser of the functional in equation (2). Corresponding to the two matrices \mathbf{P} and \mathbf{Q} given below

$$\mathbf{P} = \frac{1}{2} \begin{bmatrix} \mathcal{F}_{\rho'\rho'} & \mathcal{F}_{\rho'\eta'} \\ \mathcal{F}_{\eta'\rho'} & \mathcal{F}_{\eta'\eta'} \end{bmatrix}, \quad \mathbf{Q} = \frac{1}{2} \begin{bmatrix} \mathcal{F}_{\rho\rho} & \mathcal{F}_{\rho\eta} \\ \mathcal{F}_{\eta\rho} & \mathcal{F}_{\eta\eta} \end{bmatrix} - \frac{1}{2} \frac{d}{dr} \begin{bmatrix} \mathcal{F}_{\rho\rho'} & \mathcal{F}_{\rho\eta'} \\ \mathcal{F}_{\eta\rho'} & \mathcal{F}_{\eta\eta'} \end{bmatrix}, \quad (5)$$

the necessary condition for stability is that \mathbf{P} is positive definite while a sufficient condition requires that there is no conjugate point in the domain $r \in (0, 1)$. Here \mathcal{F} is the integrand of the functional in equation (2) and for the circular membrane problem it is given as

$$\mathcal{F} = W t_0 R_0^2 r - \frac{\chi}{2} \mu_0 |\mathbf{h}_a|^2 t_0 R_0^2 r + \frac{1}{3} P R_0^3 [\rho^2 \eta' - \rho \rho' \eta]. \quad (6)$$

Stability of all the solutions obtained for equations from Section 2.2 is checked via the above criteria. Expression for the total magnetoelastic (Cauchy) stress tensor is given by

$$\boldsymbol{\sigma} = \rho \psi_{,\mathbf{F}} \mathbf{F}^T + \mu_0 \left[\mathbf{h} \otimes \mathbf{h} - \frac{1}{2} [\mathbf{h} \cdot \mathbf{h}] \mathbf{i} \right] + \mu_0 \mathbf{h} \otimes \mathbf{m} - q \mathbf{i}, \quad (7)$$

where q is a Lagrange multiplier due to the constraint of incompressibility. Wrinkling instability is said to occur in a membrane as soon as zero or negative stresses are encountered. We record and demonstrate the location of wrinkles but are unable to update the solution due to lack of availability of a tension field theory [5] of magnetoelasticity.

3 Results and conclusion

For the toroidal membrane, we observe from figure 2(a) that magnetic field changes the location of limit point and additionally introduces an additional very early limit point. For very large magnetic field of $\mathcal{M} = 4 \times 10^{-3}$ the downward sloping curve indicates occurrence of magnetic limit point

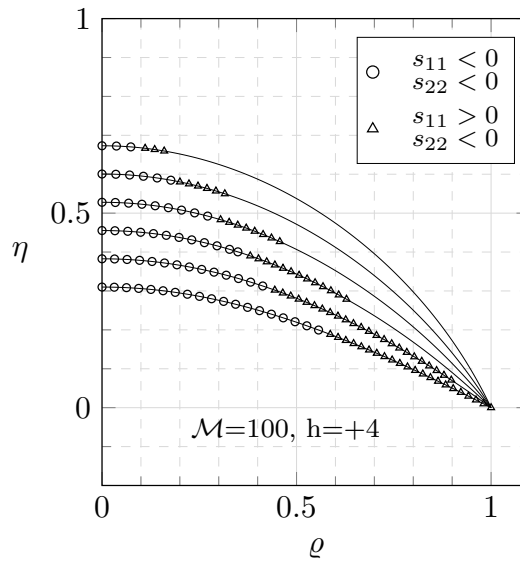


Figure 3: Profiles for circular membrane demonstrating regions of wrinkle development. Circles convey double wrinkling while triangles convey wrinkles in a single direction [4].

instability. Multiple stable and unstable equilibria for a given magnetoelastic load are shown in figure 2(b). Solid curve shows stable, dotted curve shows unstable while dashed curve represents the case where necessary condition is satisfied from section 2.3 but sufficient condition is violated. Wrinkling instability is demonstrated for circular membrane in Figure 3. We observe transition from a taut membrane (solid curve) to single wrinkles (triangles) to double wrinkles (circles) as one moves from edge of the membrane towards the centre.

Our results clearly demonstrate that magnetic loading can influence the location of limit points as well as induce additional limit point in the membrane. Occurrence of multiple stable and unstable equilibria for a given loading condition is an interesting result and needs to be studied further. We also show that compressive magnetoelastic stresses can induce wrinkles in both single and double directions in the otherwise taut membrane. We have only presented representative results here and a much more exhaustive analysis and discussion is given in references [2, 3, 4].

References

- [1] M. BARHAM, D. J. STEIGMANN, M. MCELFRISH, R. E. RUDD, *Limit-point instability of a magnetoelastic membrane in a stationary magnetic field*, Smart Materials and Structures, 17 (2008), p. 055003.
- [2] N. H. REDDY AND P. SAXENA, *Limit points in the free inflation of a magnetoelastic toroidal membrane*, International Journal of Non-Linear Mechanics, 95 (2017), pp. 248–263.
- [3] N. H. REDDY AND P. SAXENA, *Instabilities in the axisymmetric magnetoelastic deformation of a cylindrical membrane*, International Journal of Solids and Structures, 136-137 (2018), pp. 203–219.
- [4] P. SAXENA, N. H. REDDY, S. P. PRADHAN, *Magnetoelastic deformation of a circular membrane: wrinkling and limit point instabilities*, under review, (2019).
- [5] D. J. STEIGMANN, *Tension-Field Theory*, Proceedings of the Royal Society A: Mathematical, Physical and Engineering Sciences, 429 (1990), pp. 141–173.

MORTAR CONTACT FORMULATION FOR HIERARCHICAL BASIS FUNCTIONS USING SMOOTH ACTIVE SET STRATEGY

*Ignatios Athanasiadis¹, Łukasz Kaczmarczyk¹, Zahur Ullah² and Chris J. Pearce¹

¹Glasgow Computational Engineering Centre, School of Engineering, University of Glasgow, Glasgow

²School of Mechanical and Aerospace Engineering, Queen's University Belfast

*Ignatios.Athanasiadis@glasgow.ac.uk

Summary

This work focuses on 3D modelling of elastic two-body frictionless contact by means of the mortar method for small strains extended for hierarchical shape functions. Surfaces of two bodies discretised by tetrahedral elements are denoted as master and slave surfaces. When two triangular faces of tetrahedral elements are candidates for contact, with one face belonging to the master and the other to the slave surface, they are used to create a special prism element. These prisms are used as integration domains to solve the contact problem. For a given prism configuration, triangular faces can either be in contact or form a gap denoting an active or passive state, respectively. This state is determined by evaluation of the complementarity function proposed in [1], that is modified in the present work to yield a smooth Newton algorithm. Finally, results for sphere-to-sphere Hertz contact are compared to analytical solution for different orders of approximation.

Key Words: *Mortar Contact, Smooth Active Set, Hierarchical Basis Functions*

Introduction

Contact conditions are frequently observed in engineering applications. Even though contact has been an important research topic in computational mechanics for a long time, its modelling is still a challenge. Approaches that have been proposed are the so called node-to-node, node-to-segment and mortar contact, with the latter being the most promising method so far proposed. The majority of mortar contact related works involve usage of standard Lagrange shape functions or dual shape functions. In the present work, a mortar contact formulation using the active set strategy is presented for hierarchical shape functions for tetrahedral elements [2]. This paper is an extension of the work previously presented in [3]. Regularisation of non smoothness arising from the active set strategy formulation is proposed to avoid usage of semi-smooth Newton solver. This approach was chosen because it is well suited for integration within an already existing Arbitrary Lagrangian Eulerian fracture framework [4]. This future integration, will allow for investigation of influence of contact on crack propagation within nuclear graphite bricks.

Problem definition

The problem under consideration is schematically presented in Figure 1 where two bodies are potentially coming into contact. Current configuration of the two bodies is denoted by sets $\Omega^{(i)}$, where $i = 1, 2$. Furthermore, each body's surface, $\partial\Omega^{(i)}$, is divided into three sets, presented in Figure 1 with three different hatchings. The three sets are distinguished according to conditions applied and therefore there exist Dirichlet, Neumann and contact boundaries denoted by $\gamma_u^{(i)}$, $\gamma_\sigma^{(i)}$ and $\gamma_c^{(i)}$, respectively. Following assumptions presented in [1], the boundary sets are considered to be disjoint:

$$\partial\Omega^{(i)} = \gamma_u^{(i)} \cup \gamma_\sigma^{(i)} \cup \gamma_c^{(i)} \quad \text{and} \quad \gamma_u^{(i)} \cap \gamma_\sigma^{(i)} = \gamma_\sigma^{(i)} \cap \gamma_c^{(i)} = \gamma_c^{(i)} \cap \gamma_u^{(i)} = \emptyset \quad (1)$$

Moreover, the boundary value problem under consideration is described below

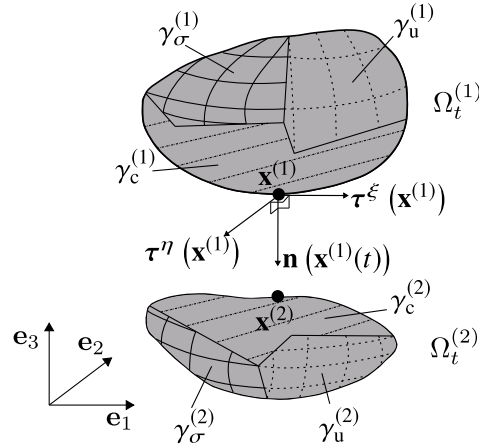


Figure 1: Schematic representation of 3D contact problem.

$$\operatorname{div} \boldsymbol{\sigma}^{(i)} = 0 \quad \text{in } \Omega^{(i)}, \quad \mathbf{u}^{(i)} = \bar{\mathbf{u}}^{(i)} \quad \text{on } \gamma_u^{(i)} \quad \text{and} \quad \boldsymbol{\sigma}^{(i)} \mathbf{n}^{(i)} = \bar{\mathbf{t}}^{(i)} \quad \text{on } \gamma_\sigma^{(i)} \quad (2)$$

where, $\boldsymbol{\sigma}^{(i)}$ is the Cauchy stress tensor, $\mathbf{n}^{(i)}$ is unit vector normal to $\gamma_u^{(i)}$ surfaces, $\bar{\mathbf{t}}^{(i)}$ is the vector of prescribed tractions on $\gamma_\sigma^{(i)}$ and $\mathbf{u}^{(i)}$ and $\bar{\mathbf{u}}^{(i)}$ are the unprescribed and prescribed displacement vectors, respectively. Vectors $\mathbf{u}^{(i)}$ and $\bar{\mathbf{u}}^{(i)}$ are evaluated as

$$\mathbf{u}^{(i)} = \mathbf{x}^{(i)} - \mathbf{X}^{(i)} \quad \text{on } \overline{\Omega^{(i)} \cap \gamma_u^{(i)}} \quad \text{and} \quad \bar{\mathbf{u}}^{(i)} = \bar{\mathbf{x}}^{(i)} - \mathbf{X}^{(i)} \quad \text{on } \gamma_u^{(i)} \quad (3)$$

where $\bar{\mathbf{x}}^{(i)}$ is the vector of prescribed current spatial positions on $\gamma_c^{(i)}$ and $\mathbf{x}^{(i)}$ and $\mathbf{X}^{(i)}$ are the vectors of current and reference unprescribed spatial positions, respectively. Furthermore, gap between the two bodies is evaluated as

$$g(\mathbf{x}) = -\mathbf{n}(\mathbf{x}^{(1)}) \cdot [\mathbf{x}^{(1)} - \mathbf{x}^{(2)}] \quad \text{where} \quad \mathbf{n}(\mathbf{x}^{(1)}) = \boldsymbol{\tau}^\xi(\mathbf{x}^{(1)}) \times \boldsymbol{\tau}^\eta(\mathbf{x}^{(1)}) \quad (4)$$

where g is the scalar gap function and $\boldsymbol{\tau}^\xi(\mathbf{x}^{(1)})$ and $\boldsymbol{\tau}^\eta(\mathbf{x}^{(1)})$ are two tangent vectors to surface $\gamma_c^{(1)}$ at $\mathbf{x}^{(1)}$. In addition, since contact is frictionless, only normal component, p_n , from contact tractions, \mathbf{t}_c , over $\gamma_c^{(1)}$ is taken into account and evaluated as

$$p_n = \mathbf{t}_c \cdot \mathbf{n}(\mathbf{x}^{(1)}) \quad (5)$$

The conditions that describe frictionless contact can be summarised by the Karun-Kuhn-Tucker (KKT) conditions as

$$g(\mathbf{x}) \geq 0, \quad p_n \leq 0, \quad p_n g(\mathbf{x}) = 0 \quad (6)$$

where the first inequality describes prohibition of penetration of the two bodies under consideration and the second one expresses development of normal tractions over the contact area. Moreover, the equality in (6) is a complementary argument that ensures gap closure when contact pressure is non-zero and zero pressure during gap opening.

Since it is computationally demanding to explicitly solve KKT conditions the three relationships in (6) can be captured by the alternative complementarity problem described by the complementarity function C as

$$C(\lambda, \mathbf{x}) = \lambda - \max(0, \lambda - c_n g) = \frac{1}{2} (\lambda + c_n g - |\lambda - c_n g|), \quad c_n > 0 \quad (7)$$

that was first presented in [1] for active set strategy that is well suited for semi-smooth Newton method. Here, λ is the so called Lagrange multiplier considered to be equal to p_n and c_n is a non-physical input parameter. In the present work, C function is regularised in order to avoid the primal dual active set strategy and usage of dual Lagrange multipliers. Regularisation is achieved by substituting the absolute (non-smooth) function with a strongly non-linear smooth function

$$\tilde{C}(\lambda, \mathbf{x}) = \frac{1}{2} \left(\lambda + c_n g - \frac{1}{r} |\lambda - c_n g|^r \right) \quad (8)$$

where \tilde{C} is the regularised C function and r is non-physical regularisation parameter whose values could be chosen between 1 to 1.1.

Contact element formulation

The central objective of the proposed formulation is for it to be integrated with mesh partitioning schemes. Therefore, when two triangular faces of tetrahedral elements are candidates to be in contact, with one face belonging to the master and the other to the slave surface, they are used to create a special prism element. No integration is performed within the prism volume therefore contact prisms can overlap and can be arbitrarily distorted. This approach resolves the problem where the master and slave triangle lie between two different partitions. More details of the generation process of the prism elements can be found in [3].

The present section focusses on the description of the contact element solely, while virtual work related to work on the elastic bodies is omitted. Virtual work related to contact development and for complementarity function are presented below

$$\mathbf{r}_x = \int_{\gamma_c^{(1)}} \lambda \delta g(\mathbf{x}) d\gamma_c^{(1)} = \int_{\gamma_c^{(1)}} \lambda (-\mathbf{n} \cdot (\delta \mathbf{x}^{(1)} - \delta \mathbf{x}^{(2)})) d\gamma_c^{(1)} \quad \text{and} \quad \mathbf{r}_\lambda = \int_{\gamma_c^{(1)}} \delta \lambda \tilde{C} d\gamma_c^{(1)} := 0 \quad (9)$$

Furthermore, the linearised system of equations is

$$\begin{bmatrix} \frac{\partial \mathbf{r}_x}{\partial \mathbf{x}}^{(n)} & \frac{\partial \mathbf{r}_x}{\partial \lambda}^{(n)} \\ \frac{\partial \mathbf{r}_\lambda}{\partial \mathbf{x}}^{(n)} & \frac{\partial \mathbf{r}_\lambda}{\partial \lambda}^{(n)} \end{bmatrix} \begin{bmatrix} \Delta \mathbf{x}^{(n+1)} \\ \Delta \lambda^{(n+1)} \end{bmatrix} = \begin{bmatrix} -\mathbf{r}_x^{(n)} \\ -\mathbf{r}_\lambda^{(n)} \end{bmatrix} \quad (10)$$

where n is the iteration number in the Newton algorithm within one step.

Results

Comparison of the model's results with the analytical solution for the Hertz problem for two spheres coming into contact is presented. The problem setup is schematically presented in Figure 2a) where only an eighth of each sphere is considered. Input parameters are: radius of the two spheres $R = 10$ [m], Young's modulus $E = 10$ [Pa], Poisson ratio $\nu = 0$, $c_n = 10$ and $r = 1$. All planar surfaces of the two bodies are fixed in their perpendicular direction except for one where uniform normal displacements are applied incrementally (Figure 2a)). For each displacement increment, the total quarter surface force is calculated via summation of reaction forces of the nodes prescribed with non-zero displacements. Four analyses were run using the same mesh for increasing orders of approximation and having both fields of Lagrange multipliers and spatial positions to be equal. The quarter surface forces versus the uniform displacement increment curves resulting from the four analyses are compared in Figure 2b) to analytical curve for the given input according to the equations presented in [5]. It can be observed that

for orders higher than 1st results are very close to the analytical one and lie on top of each other.

Conclusions

A novel implementation of the mortar contact approach for hierarchical basis functions and regularisation of the complementarity function was presented. The model results for sphere-to-sphere Hertz problem matched well analytical solution for higher orders of approximation. The promising approach is a good candidate for simulating more challenging problems with spatially heterogeneous basis functions after further development.

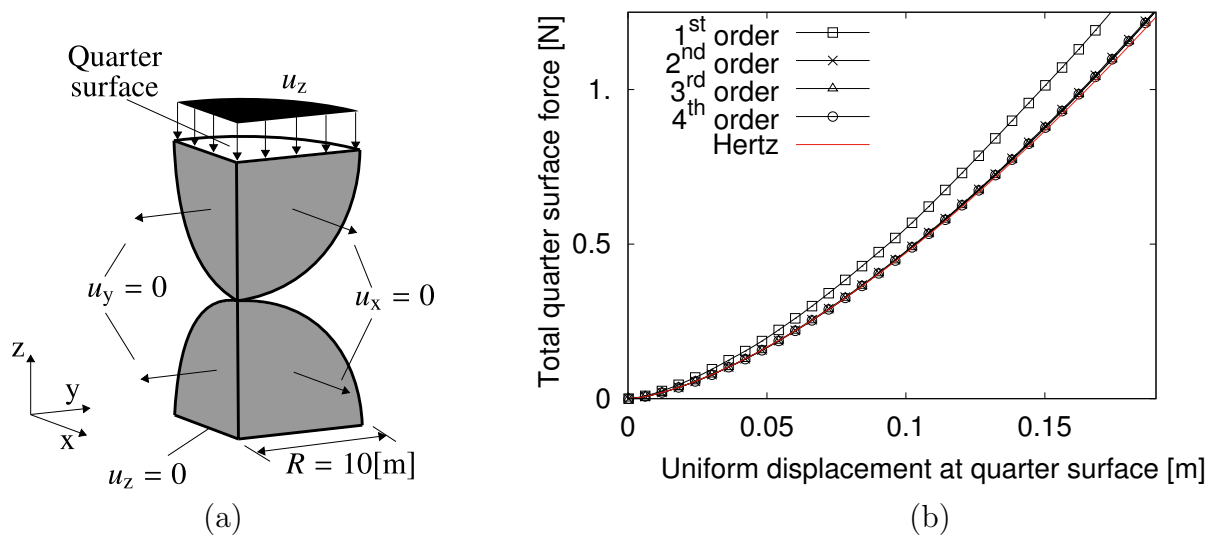


Figure 2: Sphere-to-sphere Hertz problem: (a) problem setup where only an eighth of each sphere is considered (b) comparison of model result with analytical curve for total quarter surface forces versus vertical displacements.

References

- 1 Popp, A., Gee, M.W. and Wall, W.A., A finite deformation mortar contact formulation using a primal-dual active set strategy. *International Journal for Numerical Methods in Engineering*, Vol. 79, 1354-1391, 2009.
- 2 Ainsworth M. and Coyle J., Hierarchic finite element bases on unstructured tetrahedral meshes *International Journal for Numerical Methods in Engineering.*, Vol. 58, 2103-2130, 2003.
- 3 Ullah, Z., Kaczmarczyk, Ł., and Pearce, C.J., Three-dimensional mortar contact formulation: an efficient and accurate numerical implementation. In: *25th UKACM Conference on Computational Mechanics, University of Birmingham Birmingham, United Kingdom* 4 pp.
- 4 Kaczmarczyk, Ł., Ullah, Z. and Pearce, C.J., Energy consistent framework for continuously evolving 3D crack propagation. *Computer Methods in Applied Mechanics and Engineering*, Vol. 324, pp. 54-73, 2017
- 5 Di Renzo, A. and Di Maio, F. P., Comparison of contact-force models for the simulation of collisions in DEM-based granular flow codes. *Chemical Engineering Science*, Vol. 59, 525-541, 2004.

ANALYSING GREENHOUSE VENTILATION USING COMPUTATIONAL FLUID DYNAMICS

Mohammad Akrami¹, *Akbar A. Javadi¹, Matt Hassanein¹, Raziye Farmani¹, Gavin Tabor¹, Abdelazim Negm², Hassan E. S. Fath³

¹ Department of Engineering, University of Exeter, Exeter, EX4 4QF, UK

² Faculty of Engineering, Zagazig University, Zagazig 44519, Egypt

³ Egypt-Japan University of Science and Technology (E-JUST), Borg El-Arab, Alexandria, Egypt

*a.a.javadi@exeter.ac.uk

Summary

Greenhouses (GH) are used to shield the crops from excessive cold or heat. They are used for growing certain types of cultivations during the year round. The aim of this study is to design a greenhouse using solar-powered technology to produce a Zero-Liquid-Discharge (ZLD) by using Solar Stills and adding condensers to dehumidify the excess vapoured water. This allows to have small-scale plants to reduce the cost of water treatment while increasing its sustainability. Computational fluid dynamics was used to find the best locations for the dehumidifiers in the GH and design the necessary ventilation. This can help to plan ahead and evaluate the optimal amount of produced water for different sizes of greenhouse before they are constructed physically.

Key Words: Greenhouse, ventilation, CFD

Introduction

In order to design a greenhouse system, it is necessary to analyse the amount of humidity and the optimal locations for the dehumidifiers. Although the technologies applied to greenhouses may vary based on the region and severity of the weather conditions, high temperatures are recorded within the greenhouses in hot climate areas such as the middle east and north African countries. Such greenhouses need to be ventilated [1] to keep the internal temperature of the greenhouse in a steady range, suitable for the plants' growth [2]. The temperature inside the greenhouses is designed in the range of 14°C-35°C, while the humidity range can be in the range of 50-90% for different types of cultivation [3]. When the temperature is raised, the vents can help to decrease it in order to have a steady internal temperature within the greenhouse. In order to analyse the optimal locations for the ventilation, a conceptual greenhouse model was designed using the Computational Fluid Dynamics (CFD) software, ANSYS Fluent v19.2., and the range of humidity, temperature, and wind velocity within the greenhouses was analysed. The wind speed was assigned to be kept as 0.1–0.3 m/s as another requirement for the plant growth [4].

Materials and methods

The general materials used in the greenhouse CFD model were glass and soil. The relevant properties of these materials are summarised in Table 1.

Table 1: Properties of glass and soil used in the model

Property	Glass	Soil
Density/ kg m ⁻³	2400	1500
Specific heat capacity/ J kg ⁻¹ K ⁻¹	753	800
Thermal conductivity/ W m ⁻¹ K ⁻¹	1	0.5

This model was designed based on a single-span, with the ridge of the greenhouse running parallel to the length of the greenhouse. The greenhouse also had roof and side vents the dimensions of which are summarised in Table 2.

Table 2: greenhouse dimensions used in the model

Dimension	Value
Length/ m	8.25
Width/ m	6.4
Eaves height/ m	2.15
Ridge height/ m	3.75
Side vent size/ m	0.5
Roof vent size/ m	0.5

In the model, the radiation heat flux in the soil was determined based on the information from the literature. The effective heat flux from the soil to the air in the greenhouse was determined based on a location close to the equator where the ground would have a strong heat flux. The calculation started with the theoretical solar irradiance on Earth, and then accounted for the effect of the absorption in the atmosphere and the zenith effect (the extra distance the radiation travels through the atmosphere as a result of the location not being on the equator). The albedo effect was also accounted for. A set of assumptions were made for these calculations as:

- The solar radiation was not affected by the solar constant – the actual solar radiation varies with time.
- The sun was assumed to be a perfect black body.
- The sun-earth distance was assumed to be constant.
- The greenhouse was assumed to be at sea level.
- The sky was assumed to have no turbidity.

Based on the above assumptions, a heat flux of $500 \text{ W}\cdot\text{m}^{-2}$ was applied in the CFD model, as a boundary condition for the floor of the greenhouse in all simulations. This is similar to values used in other literature [5]. The 2D ventilation model was used to analyse many effects of different boundary conditions on the velocity and temperature of the air in the greenhouse. The model studied the effect of ventilation perpendicular to the axis of the greenhouse ridge. The model was first set up by defining the equations to be solved, and the boundary conditions of the greenhouse. The initial model was set to a steady-state pressure solver model. The energy equation and a standard $k\text{-}\epsilon$ model were used with standard wall treatments. The material properties shown in Table 1 were used in the model. To simulate the effect of the natural convection due to the difference in air temperatures, the Boussinesq approximation was used, with air density of 1.225 kg m^{-3} , and a thermal expansion coefficient of 0.0034 K^{-1} , and $g=0.81\text{m/s}$ in the negative x direction. The boundary conditions were set as 1 ms^{-1} velocity at the inlet, with the roof inlet angled downwards at 23° , to simulate the effect of open vents. The outlets were set as pressure outlets.

Results and discussion

In order to analyse the optimal location for designing the vents, several parameters such as the inlet wind velocity, side ventilator height and roof ventilator height should be considered. In what follows, the effects of inlet wind velocity are presented (Figure 1). The analyses are based on the inlet size of 0.5m length and a height of 1m.

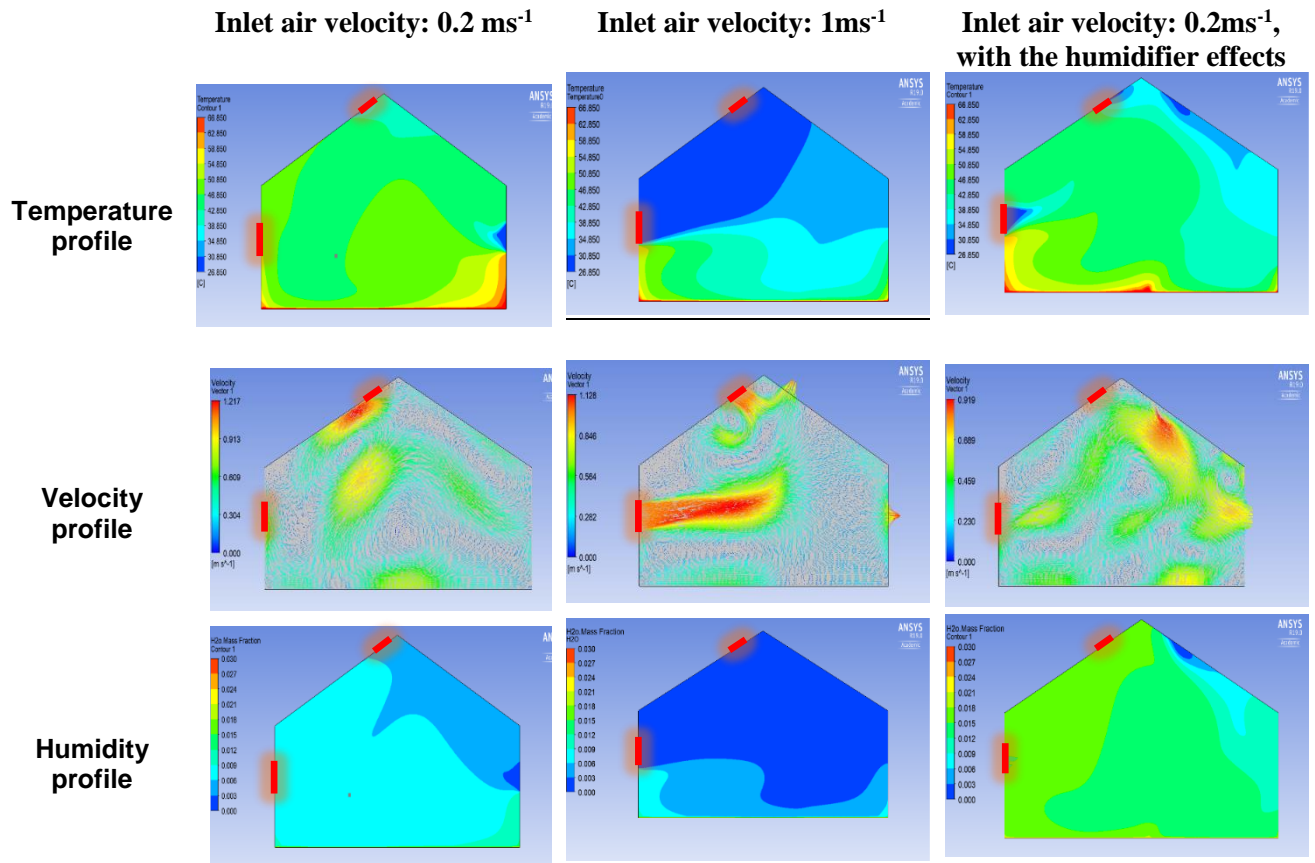


Figure 1: Inlet wind velocity effects on the temperature, velocity and humidity profiles

The preliminary results show the effects of air conditions on the humidity, velocity and temperature profiles. By using the condenser, the excess humidity can be dehumidified to keep the temperature range and air velocity suitable for the plants growth. The results show that the humidity rate is higher at the opposite corners of the inlet locations within the greenhouse which shows a suitable spot for designing the condensers. At the same time, the temperature within those regions is higher as no circulation is embedded in those regions. Therefore, assigning the outlets in those regions would be highly recommended. Based on this specific study, the velocity can be controlled by adding the humidification to the system.

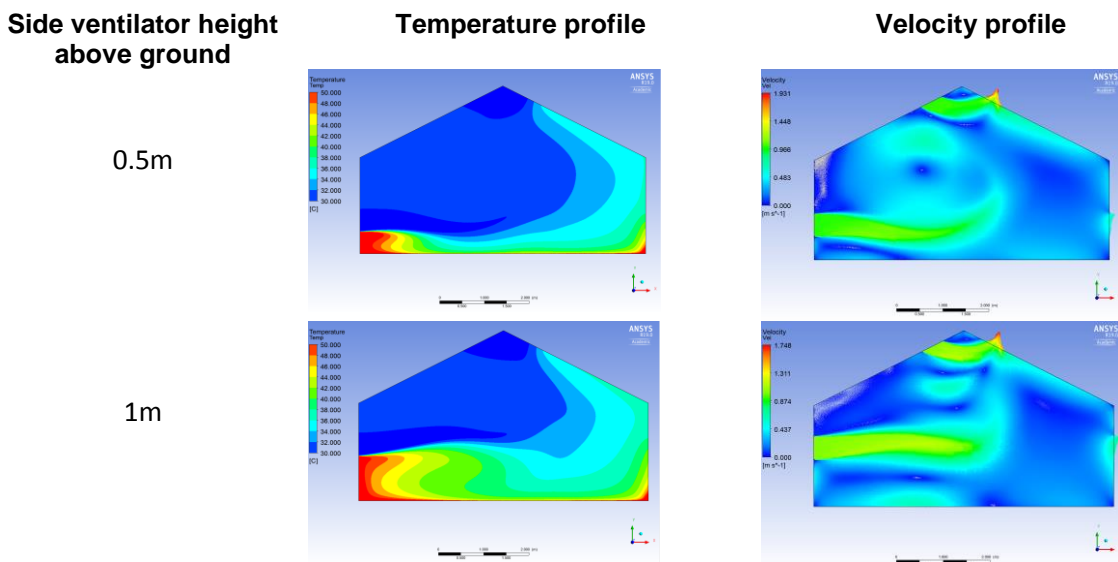


Figure 2: Effects of side ventilator height on the temperature and velocity profiles

Another influential parameter is the height of the side ventilator (Figure 2). The results show by doubling the height of the side ventilator, the regions with maximum temperature are expanded within the greenhouse cavity and it increases the importance of ventilation on the opposite sides. Also, the effects of roof ventilator height are studied (Figure 3). Based on this study, by doubling its distance from the ridge of the greenhouse, the temperature and velocity profiles are slightly changed which shows the greenhouses are not sensitive to these specific dimensions and therefore this parameter can be neglected in ventilation planning.

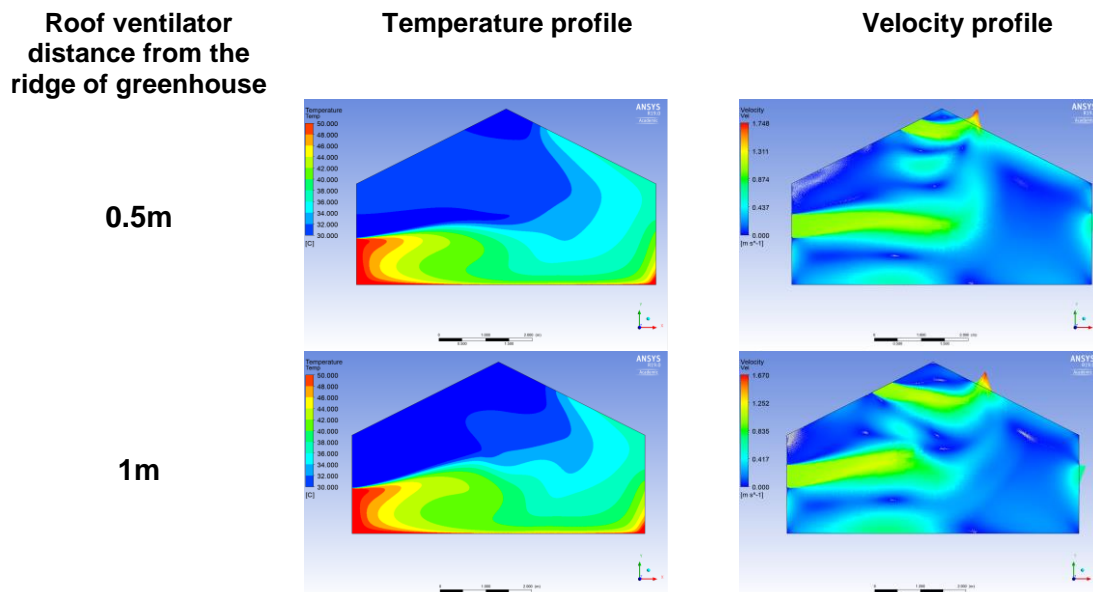


Figure 3: The effects of roof ventilator distance on the temperature and velocity profile

Acknowledgement

We acknowledge the British Council (BC) and Science & Technology Development Fund (STDF), Egypt for supporting this research paper through funding the project titled "A Novel Standalone Solar-Driven Agriculture Greenhouse - Desalination System: That Grows its Energy and Irrigation Water" via the Newton-Musharafa funding scheme (Grants ID: 332435306) from BC and ID 30771 from STDF.

References

1. Fath HE. Transient analysis of naturally ventilated greenhouse with built-in solar still and waste heat and mass recovery system. *Energy conversion and management*. 1994;35(11):955-65.
2. Mistriotis A, Bot G, Picuno P, Scarascia-Mugnozza G. Analysis of the efficiency of greenhouse ventilation using computational fluid dynamics. *Agricultural and Forest Meteorology*. 1997;85(3-4):217-28.
3. Campiotti CA, Morosinotto G, Puglisi G, Schettini E, Vox G. Performance evaluation of a solar cooling plant applied for greenhouse thermal control. *Agriculture and agricultural science procedia*. 2016;8:664-9.
4. Fernández M, Bonachela S, Orgaz F, Thompson R, López J, Granados M, et al. Measurement and estimation of plastic greenhouse reference evapotranspiration in a Mediterranean climate. *Irrigation Science*. 2010;28(6):497-509.
5. Mistriotis, A., Arcidiacono, C., Picuno, P., Bot, G.P.A. and Scarascia-Mugnozza, G., 1997. Computational analysis of ventilation in greenhouses at zero-and low-wind-speeds. *Agricultural and Forest Meteorology*, 88(1-4), pp.121-135.

AN INVESTIGATION OF STEPWISE CRACK TIP ADVANCEMENT

*Yanan Sun¹, Bin Chen², Michael G Edwards¹, and Chenfeng Li³

¹Zienkiewicz Centre for Computational Engineering, College of Engineering, Swansea University, SA1 8EN

²Department of Earth Science and Engineering, Imperial College London, SW7 2BX

³Energy Safety Research Institute and Zienkiewicz Centre for Computational Engineering, College of Engineering, Swansea University, SA1 8EN

*966781@Swansea.ac.uk

Summary

This research focuses on stepwise crack tip advancement associated with hydraulically induced fractures, which are observed both in the field and in experiments and reported in the numerical fracture modelling literature[1, 2, 3]. A numerical model of hydraulically induced fractures in porous media is presented. The finite element method is employed to solve the fully coupled equation system that includes rock deformation, fluid flow in both the fracture and rock matrix and fracture propagation. To reproduce the stepwise phenomenon, a special time stepping scheme is used, which allows for multiple incremental fracture advancement within a time step according to a cohesive stress constraint. Contributing factors to stepwise phenomenon are compared and contrasted with a numerical sensitivity analysis using the method presented.

Key Words: *hydraulic fracturing; finite element methods; porous media; stepwise phenomenon*

Mathematical Models

In order to study the stepwise phenomenon, a 2D numerical model of a hydraulic fracture in porous media is established, as shown in Fig. 1. A plane strain assumption is applied along the plane orthogonal to the vertical wellbore. The rock formation is assumed to be poroelastic and homogeneous. At the center of the model, a fluid is injected at a constant flow rate Q_0 , which can be modeled as a point source. The fluid is incompressible Newtonian fluid and is assumed to be laminar flow. For simplicity, the fracture propagates along a straight line. Then, by taking advantage of the symmetries of the model, only the one quarter of the block is considered, as shown in Fig. 2.

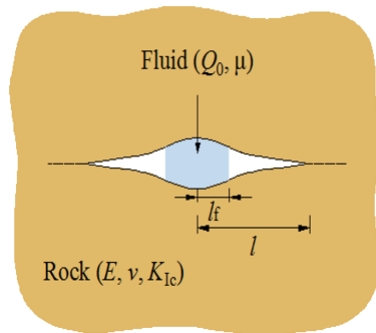


Figure 1: The ketch of the model.

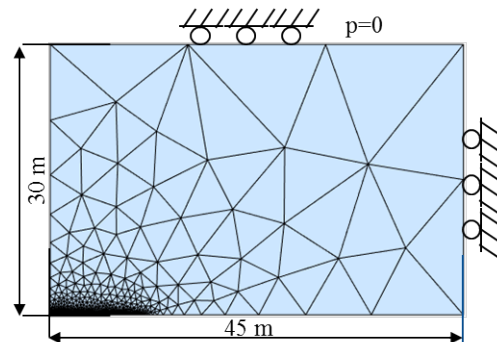


Figure 2: Numerical model.

Governing equations

To model fracture propagation in porous media, and capture the full effects of fluid-structure

interaction, four processes need to be considered: (i) rock deformation, and (ii) fluid flow in porous media, and (iii) fluid flow in the fracture, and (iv) propagation criteria. These processes reveal a strong coupling between rock deformation and fluid.

For a fully saturated porous media with a single-phase fluid, the solid deformation equation is

$$\nabla \cdot \boldsymbol{\sigma} = 0 \quad (1)$$

where $\boldsymbol{\sigma}$ is the total Cauchy stress, which can be expressed in terms of the effective stress tensor $\boldsymbol{\sigma}'$:

$$\sigma_{ij} = \sigma'_{ij} - \mathbf{I}\alpha p_w \quad (2)$$

where p_w is the fluid pressure, \mathbf{I} the identity tensor and α the Biot's coefficient, which is given by $\alpha = 1 - K_t/K_s$, with K_t the bulk modulus of the porous media and K_s the bulk modulus of the solid. α equals 1 for incompressible solids.

The equation for the fluid in the porous media is

$$\frac{\partial \zeta}{\partial t} + \nabla \cdot \mathbf{q} = 0 \quad (3)$$

where ζ is the variation of fluid volume per unit volume of the porous material, and \mathbf{q} denotes the flux which is defined by Darcy's law as

$$\mathbf{q} = -\frac{\mathbf{k}_w}{\mu}(\nabla p_w) \quad (4)$$

where μ is the fluid viscosity, and \mathbf{k}_w the permeability tensor and both gravity and acceleration terms are omitted.

The equation for fluid flow in the fracture is

$$\frac{\partial w}{\partial t} + \frac{\partial q}{\partial s} + q_l = 0 \quad (5)$$

where w is the width of the fracture, q the flow rate, s the local coordinate aligned with the tangential direction to the fracture path, and q_l the fluid rate loss in rock formation.

The cohesive zone method, first developed by Dugdale [4] and Barenblatt [5], is adopted here as the propagation criterion. It assumes a process zone ahead of the real crack tip, where the stress varies with deformation. In this way, the singularity at the crack tip is avoided.

The equations above are spatially discretized with the Galerkin finite element method (FEM). In a compact matrix form, the equation system can be written as

$$\begin{aligned} \mathbf{K}\mathbf{u} - \mathbf{Q}\mathbf{p}_w &= \mathbf{f}_1 \\ \mathbf{Q}^T\dot{\mathbf{u}} + \mathbf{C}\dot{\mathbf{p}}_w + \mathbf{H}\mathbf{p}_w &= \mathbf{f}_2 \\ \mathbf{L}^T\dot{\mathbf{w}} + \mathbf{h}(\mathbf{w}, \mathbf{p}_f) &= \mathbf{f}_3 \end{aligned} \quad (6)$$

The system can be solved implicitly in time using backward Euler. To reproduce the stepwise phenomenon, the time step algorithm adopted needs to allow for more than one fracture advancement within one time step [6].

Sensitivity analysis

To evaluate the sensitivity of the stepwise phenomenon in the hydraulic fracturing model and to have a better understanding on the physical processes behind it, the effects of different parameters

are studied. According to the controlling equation and propagation criterion, all the parameters can be divided into three categories, the solid part, the fluid part and external condition. The solid part includes Young’s modulus, Poisson’s ratio, Biot’s coefficient, Biot’s modulus, rock porosity, and permeability, the fluid part includes viscosity, injection rate, and the external condition is fracture toughness. Among all the factors, Young’s modulus, permeability, injection flow rate, fluid viscosity and fracture toughness have a predominant influence. The difference between the velocity of the fracture tip and the fluid front needs to be considered to account for the reasons behind this phenomenon.

From Fig. 3, it is concluded that Young’s modulus is inversely proportional to the pause time. The stepwise behaviour is more obvious with smaller Youngs modulus. A likely reason for this is that the smaller the Youngs modulus, the easier the rock deforms, which leads to more time for the fluid to accumulate energy to open the fracture.

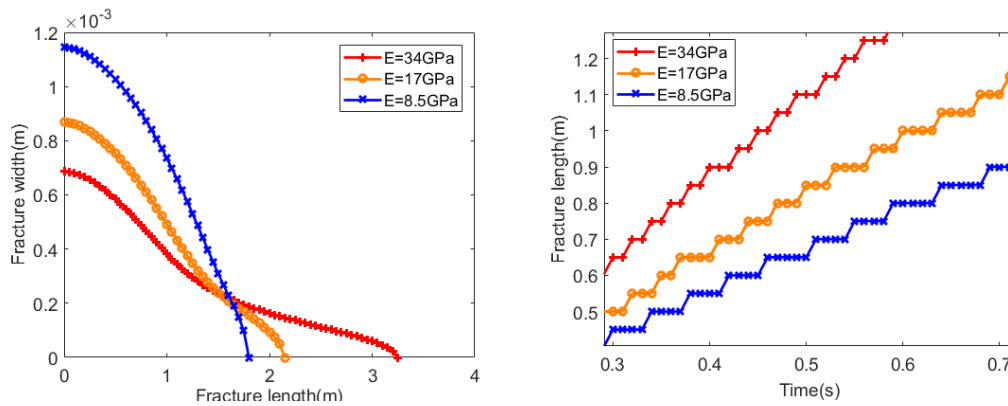


Figure 3: Comparison of fracture shape at same time with different Young’s modulus (left) and stepwise phenomenon with different Young’s modulus (right).

Fig. 4 shows that the viscosity and permeability are positively correlated with pause time, the higher the viscosity and permeability, the slower the fluid flows into the fracture, which means it needs more time for the fluid to catch up with the crack tip.

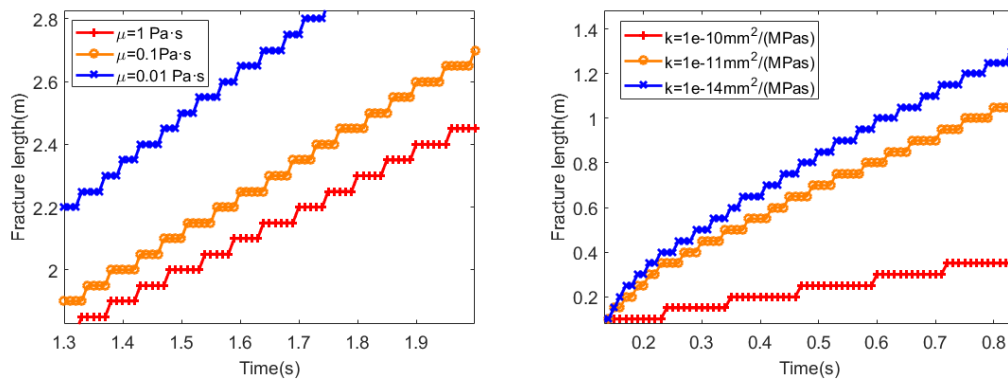


Figure 4: Stepwise phenomenon with different viscosity (left) and different permeability (right).

The injection rate and the fracture toughness both have strong effects, as shown in Fig. 5. Both of them not only influence the pause time but also the fracture jump. At the early stage of fracture propagation, a larger jump is observed for higher flow rate and reduced toughness, while at later

time step-wise phenomena occurs over a larger time interval, because the velocity of the fracture decreases with the increase of fracture volume.

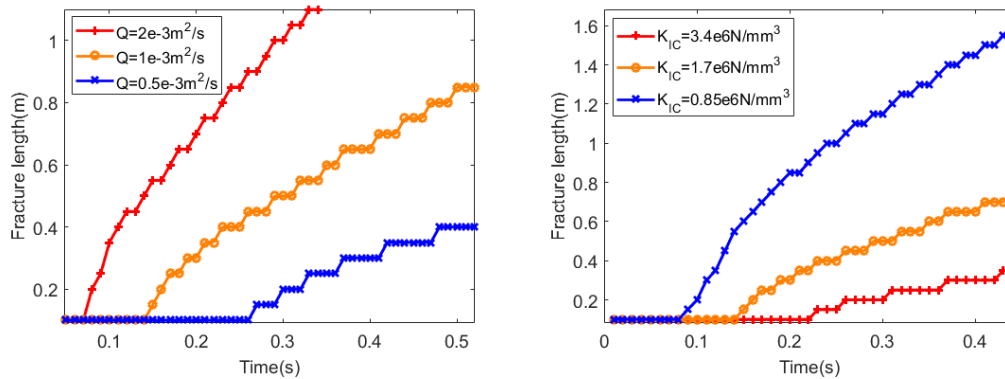


Figure 5: Stepwise phenomenon with different injection rate (left) and different fracture toughness (right).

Conclusions

A fully coupled model of a hydraulic fracture is developed and exhibits stepwise crack tip advancement. The sensitivity of the stepwise phenomenon under different factors has been studied and forces behind the phenomenon have been explored. Young's modulus, permeability, injection flow rate, fluid viscosity and fracture toughness are found to be predominant. A further key contributing factor is that the velocity of solid deformation is much faster than fluid deformation.

References

- [1] F Pizzocolo, JM Huyghe, and K Ito. Mode I crack propagation in hydrogels is step wise. *Engineering Fracture Mechanics*, 97:72–79, 2013.
- [2] Stefano Secchi and Bernhard A Schrefler. Hydraulic fracturing and its peculiarities. *Asia Pacific Journal on Computational Engineering*, 1(1):8, 2014.
- [3] Yongcun Feng and KE Gray. Parameters controlling pressure and fracture behaviors in field injectivity tests: a numerical investigation using coupled flow and geomechanics model. *Computers and Geotechnics*, 87:49–61, 2017.
- [4] Donald S Dugdale. Yielding of steel sheets containing slits. *Journal of the Mechanics and Physics of Solids*, 8(2):100–104, 1960.
- [5] Grigory Isaakovich Barenblatt. *The mathematical theory of equilibrium cracks in brittle fracture*, volume 7, pages 55–129. Elsevier, 1962.
- [6] Toan Duc Cao, Enrico Milanese, Ernst W Remij, Paolo Rizzato, Joris JC Remmers, Luciano Simoni, Jacques M Huyghe, Fazle Hussain, and Bernhard A Schrefler. Interaction between crack tip advancement and fluid flow in fracturing saturated porous media. *Mechanics Research Communications*, 80:24–37, 2017.

UNIFIED ONE-FLUID FORMULATION FOR MULTIBODY DYNAMICS AND MULTIPHASE FLOW INTERACTION

***Liang Yang**^{1,2}, **Antonio J. Gil**³ and **Christopher Pain**¹

¹Department of Earth Science and Engineering, Imperial College London, SW7 2BP

²Department of Energy and Power, Cranfield University, MK43 0AL

³Zienkiewicz Centre for Computational Engineering, Swansea University, SA1 8EN

*liang.yang@imperial.ac.uk

Summary

Within the group of immersed computational methodologies [1;2;3] which can be employed for the numerical simulation of fluid-structure interaction (FSI) problems, the multi-phase one-fluid formulation was recently introduced [4;5] to enable the modelling of immersed rigid bodies as an additional physical phase of the coupled fluid-structure system. The new methodology does not require the direct solution of the Newton-Euler equations for rigid bodies but instead introduces a weighted least square projection algorithm to account for the rigid body motion [6]. In this work, this FSI simulation is further extended to the case of articulated rigid-body systems, where multiple rigid bodies are interconnected via joints. Several types of joints can be used, limiting the number of degrees of freedom to the allowed relative motions, and leading to different cases within the linear least square approach. The key ingredients of this methodology are: 1) the solution of the underlying Navier-Stokes equations and 2) the consideration of distributed Lagrange multipliers to enforce rigid body constraints. The dynamics of a double pendulum interaction immersed within a fluid will be presented in order to demonstrate the capability of the methodology.

Key Words: *rigid multibody system, one-fluid formulation, fluid-structure interaction, distributed Lagrange multipliers*

Methodology

The interaction of a fluid with a Multibody dynamics (MBD) system is a prototypical problem often encountered in complex coupled engineering systems such as wind or tidal turbines, wave energy converters or underwater robotics. Such systems often involve multiphase flows, flexible structures and rigid bodies, that are all connected via joints that restrict their relative motions. The ‘one-fluid’ formulation has been recently exploited for fluid-structure interaction problems by modelling immersed solids as an additional phase of the underlying fluid. In this way, deformable structures and fluids are treated in an identical manner, except for the deviatoric part of the stress [4,5] which is phase-dependent. Similarly, immersed rigid bodies are considered as an incompressible non-viscous continuum with motion constraints resulting in a Lagrange multiplier type stress. Following this ‘one-fluid’ methodology, immersed rigid bodies have been investigated [6;7] with application to water impact problems in [8;9] and wave energy converters in [10]. We consider an incompressible continuum domain $\Omega \subset \mathbb{R}^n$, $n = 2, 3$ and a partition into disjoint sets Ω_i that represent each of the possible phases, i.e. $\Omega = \cup_i \Omega_i$, $\Omega_i \cap \Omega_j = \emptyset$, $i \neq j$. A phase-dependent regularised Heaviside function H_i is computed at each phase Ω_i , satisfying that $\sum_i H_i = 1$. This allows us to consider the linear momentum conservation equation and the mass conservation equation in an Eulerian setting as

$$\begin{aligned} \rho(\mathbf{H}) \left[\frac{\partial \mathbf{u}}{\partial t} + (\nabla \mathbf{u}) \mathbf{u} \right] &= -\nabla p + \mathbf{f}(\mathbf{H}) + \rho(\mathbf{H}) \mathbf{g}; \\ \nabla \cdot \mathbf{u} &= 0, \end{aligned} \tag{1}$$

where \mathbf{u} is the velocity field, p is the pressure, \mathbf{g} is the gravity acceleration, $\rho(\mathbf{H})$ is the density (dependent upon the Heaviside vector valued function) and $\mathbf{f}(\mathbf{H})$ is a vector representing the (phase-dependent) divergence of the stress tensor. For an articulated rigid structure occupying a domain $\Omega_i^{RB} \subset \Omega$, the following additional constraint on the velocity field has to be fulfilled

$$\mathbf{u} = \boldsymbol{\omega}_i \times \mathbf{x} + \mathbf{b}_i \quad (2)$$

where $\boldsymbol{\omega}_i$ represents an angular velocity vector, \mathbf{b}_i a translation velocity vector and \mathbf{x} the spatial position, with additional kinematic constraints imposed for the links of the system and collected as $g_i(\mathbf{u}) = 0$. For a simple relative motion, the kinematic equations describing the system are formulated using a reduced set of variables and the solution for above equations can be achieved via an implicit distributed Lagrange multiplier method [3]. In this work, we apply the weighted least square projection similar to [6]. Finally, the rigid structure is ‘tracked’ in a Lagrangian way. From the spatial discretisation point of view, we employ a Cartesian staggered Finite Volume scheme (Marker-and-Cell (MAC) grid) and a level set methodology to describe the evolution of the various interacting phases.

Numerical example: double pendulum

In this example, we consider a simple open-loop mechanism, namely, the dynamics of a double pendulum in a viscous fluid, with the framework presented above. The physical domain is defined by the rectangle 12 m \times 10 m, discretised with a (h-refinement) series of Cartesian meshes, the finest of which is comprised of 2080 \times 1760 cells, filled with a Newtonian viscous fluid of viscosity $\mu = 10^{-5}$ Pa s, density $\rho = 1$ kg/m³ and gravity acceleration 9.8 m/s². Two cylinders of radius $r = 0.125$ m with density $\rho_s = 1000$ kg/m³ are suspended from a pivot so that they can swing around it. The first cylinder is placed with an angle of 90° with respect to the vertical axis and the massless rod has a length of 2.9 m, the second cylinder is placed an angle of 0° with respect to the vertical axis with a massless rod length 1.45 m. The location of the fixed point is at position (6,6) with respect to bottom left corner of the fluid domain, as shown Fig. 1(a). The total run-time for the case with the finest mesh is 12 h using a 3.0 GHz Intel Core CPU. Fig. 1 (b) shows the h-convergence of the evolution of the path of the centre of the second cylinder. In Fig. 2, a series of snapshots of the solution are displayed, where it can be observed how as the double pendulum moves it creates vortices in its wake represented with contour lines of vorticity ($-200 < \omega < 200$).

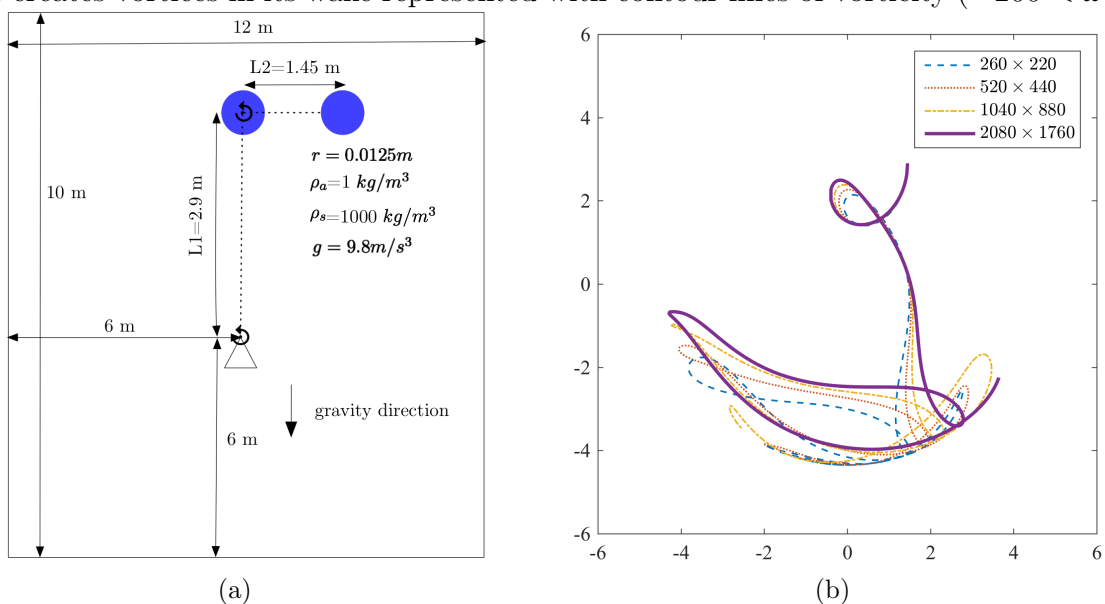


Figure 1: (a) Problem description; (b) Path trajectory.

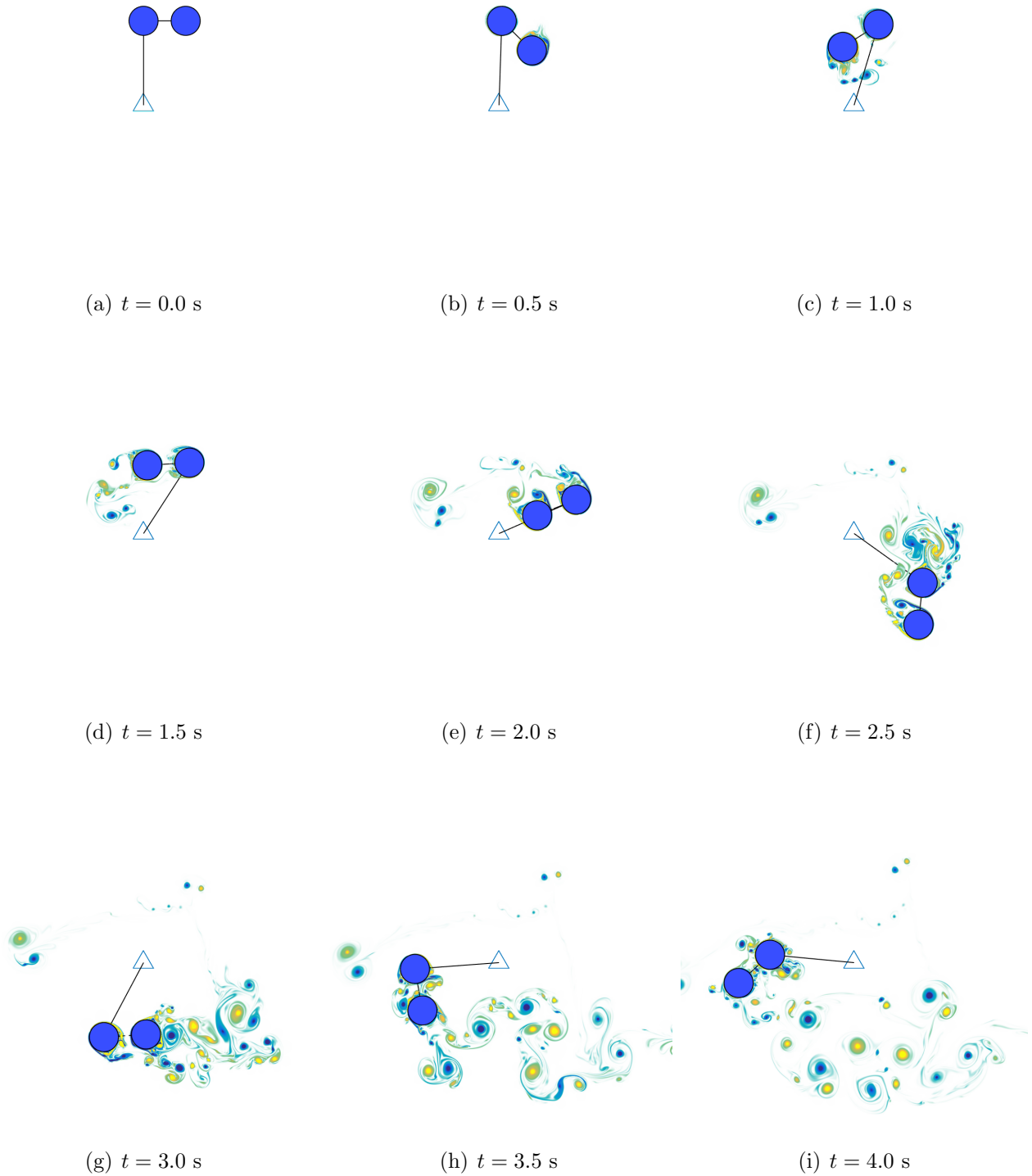


Figure 2: Double pendulum: vorticity contours ($-200 < \omega < 200$).

Conclusions

This work has presented a ‘one-fluid’ computational framework for the the interaction of fluids with Multibody Dynamics systems. The proposed method builds on the existing ‘one-fluid’ formulation for solving flexible structure and a single rigid body previously introduced by some of the authors. The proposed enhanced ‘one-fluid’ formulation solves implicitly the Navier-Stokes equations along with a least square motion projection. A double pendulum example is presented in order to demonstrate the capabilities of the enhanced methodology.

Acknowledgements

The first author acknowledges the financial support provided by the Engineering and Physical Sciences Research Council through the grant EPSRC grant (EP/P013198/1).

References

- 1 N. A. Patankar, P. Singh, D. D. Joseph, R. Glowinski, and T. W. Pan. A new formulation of the distributed Lagrange multiplier/fictitious domain method for particulate flows. *International Journal of Multiphase Flow*, 26(9), 1509-1524, 2000.
- 2 A. J. Gil, A. A. Carreño, J. Bonet, and O. Hassan. The immersed structural potential method for haemodynamic applications. *Journal of Computational Physics*, 229(22):8613-8641, 2010.
- 3 C. Hesch, A. J. Gil, A. A. Carreño, J. Bonet, and P. Betsch. A mortar approach for fluid-structure interaction problems: Immersed strategies for deformable and rigid bodies. *Computer Methods in Applied Mechanics and Engineering*, 278:853-882, 2014.
- 4 L. Yang, A. J. Gil, A. A. Carreño, and J. Bonet. Unified one-fluid formulation for incompressible flexible solids and multiphase flows: Application to hydrodynamics using the immersed structural potential method (ISPM). *International Journal for Numerical Methods in Fluids*, 86(1):78-106, 2018.
- 5 L. Yang. *An Immersed Computational Framework for Multiphase Fluid-Structure Interaction*. PhD thesis, Swansea University, 2015
- 6 L. Yang. One-fluid formulation for fluid-structure interaction with free surface. *Computer Methods in Applied Mechanics and Engineering*. 332:102-135, 2018.
- 7 L. Yang, A. A. Carreño, A. J. Gil, and J. Bonet. An immersed structural potential method framework for incompressible flexible/rigid/multi-phase flow interactions. In *Proc. 22nd UK Conference of the Association for Computational Mechanics in Engineering*, 2014.
- 8 L. Yang, H. Yang, S. Yan, Q. Ma, and M. Bihnam. Comparative study on water impact problem. In *The 26th International Ocean and Polar Engineering Conference*, 2016
- 9 L. Yang, H. Yang, S. Yan, and Q. Ma. Numerical investigation of water-entry problems using IBM method. *International Journal of Offshore and Polar Engineering*, 27(02):152-159, 2017
- 10 L. Yang, Z. Lyu, P. Yang, D. Pavlidis, F. Fang, J. Xiang, J.-P. Latham, and C. C. Pain. Numerical Simulation of Attenuator Wave Energy Converter Using One-Fluid Formulation. In *The 28th International Ocean and Polar Engineering Conference*, 2018.

Resolution Effect: An Error Correction Model for Intrinsic Permeability of Sandstones Estimated from Lattice Boltzmann Method

*Jinlong Fu¹, Jiabin Dong^{1,2} and Chenfeng Li¹

¹ Zienkiewicz Center for Computation Engineering, College of Engineering, Swansea University, SA1 8EN.

² State Key Laboratory for Geomechanics and Deep Underground Engineering, Xuzhou, China, 221116.

*887538@swansea.ac.uk

Summary

Digital rock physics (DRP) has been applied to reveal the mechanisms how pore-scale processes govern macroscopic rock properties, such as transport, elastic, thermal and electrical properties, in a non-destructive manner [1,2]. DRP uses modern imaging techniques such as X-ray micro-computed tomography (μ -CT) to obtain high resolution 3D images of rocks. By separating the pore space from mineral matrix phases through segmentation processing on the raw images, the 3D representations of complex pore geometry are available. Subsequently, physical simulations are performed on the pore-scale microstructures to determine the effective properties of rocks (e.g. permeability, elastic moduli, thermal conductivity and electrical resistivity). In this study, we focus on one of the most important transport properties of rocks—intrinsic permeability, which is relevant to many fields: oil and gas production, geothermal energy extraction, contaminant absorption, carbon geological sequestration and others.

Currently, lattice Boltzmann method (LBM) is one of the most widely-used approaches for numerical flow simulations inside the porous media, because it can be directly applied to the 3D digital pore-scale microstructures without simplification and it has the flexibility in handling complex flow geometries. Compared to the laboratory measurements, LBM has the advantage that the velocity distribution can directly be linked to the micro-scale geometry of porous media. Intrinsic permeability of a rock sample can be computed via LBM by solving a Navier-Stokes problem, and more details about permeability computation by using LBM can be found in Ref. 3 and 4.

However, valid pore-scale analysis by using LBM relies heavily on the simulation on a large enough volume (representative elementary volume) at a high enough spatial resolution, which usually takes long time and requires high computer power to fulfill the simulating computations. Modern X-ray tomography facilities are capable to provide digital images with more than $1024 \times 1024 \times 1024$ voxels at submicron resolution, and the LBM programs have to be highly parallelized to deal with such large volumes [5]. Nevertheless, computational limitations may require the segmented images of large volumes to be downscaled, in order to make lattice Boltzmann simulation of pore scale flow computationally feasible. This is especially the case for limited memory architectures like graphics processing unit (GPU), which are unable to fit a representative elementary volume with high resolution on a single graphics card [6]. Reducing the resolution of binary image segmentations can not only improve the efficiency of lattice Boltzmann simulations of pore-scale flow significantly, but also greatly lower the requirement of computer hardware.

As shown in Figure 1, the computation times and memory requirements of lattice Boltzmann simulations to calculate intrinsic permeabilities of a group of Fontainebleau sandstones are illustrated. This group of sandstone consists of seven Fontainebleau samples with different porosities, which are 8.6%, 10.1%, 12.5%, 15.3%, 17.6%, 20.6%, and 24.5% respectively [7]. The digital μ -CT images of these samples are equally $480 \times 480 \times 480$ voxels in size, with a voxel resolution of $5.7 \mu\text{m}$, which represent equivalent physical sample dimension of 2.7 mm cubed. We numerically downscale these images to image size of $240 \times 240 \times 240$ and $120 \times 120 \times 120$, representing voxel

resolution around $11.4\mu\text{m}$ and $22.8\mu\text{m}$ respectively, as shown in Figure 2. According to Figure 1, image downscaling indeed brings great benefits for lattice Boltzmann simulations in terms of computation complexity.

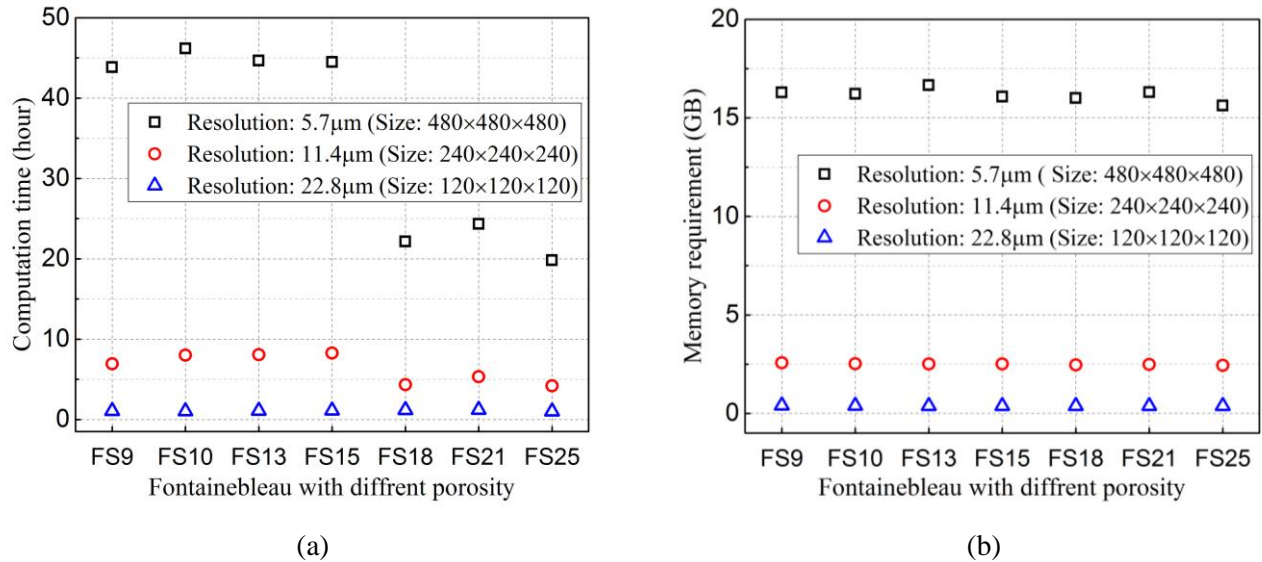


Figure 1: (a) Computation time and (b) Memory requirement of permeability calculation by using LBM.

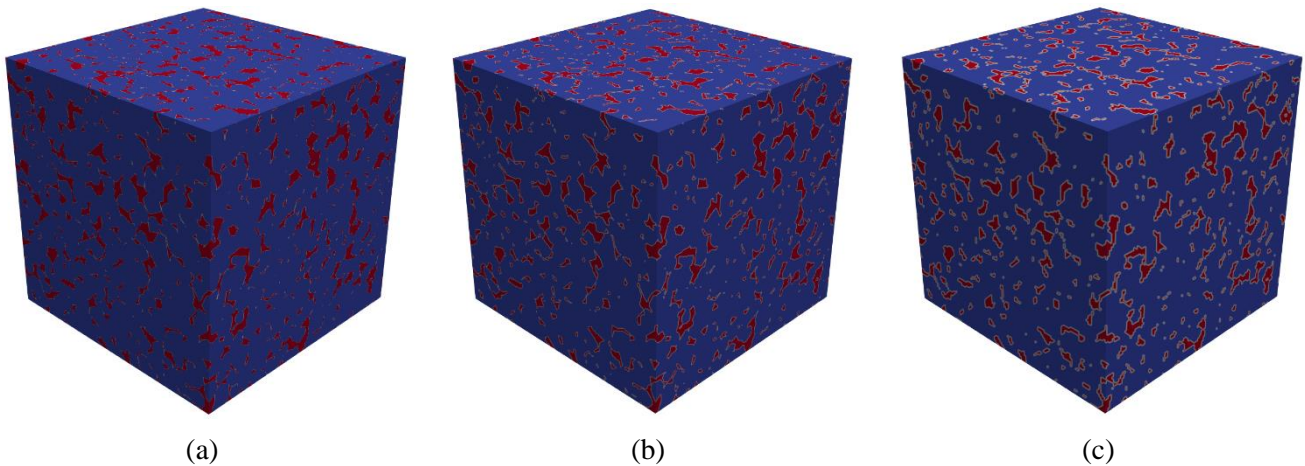


Figure 2: 3D images of the Fontainebleau sandstone with porosity equal to 15.3% at three different resolution level: (a) $5.7\mu\text{m}$, (b) $11.4\mu\text{m}$, and (c) $22.8\mu\text{m}$.

The benefits of image downscaling also have a negative role, which leads to a geometric loss for the pore-scale microstructure. Usually, the permeability results calculated from LBM cannot maintain consistency absolutely before and after image coarsening. As demonstrated in Figure 3, the intrinsic permeabilities of the Fontainebleau sandstones at three different resolution levels are calculated by using LBM. Only the permeability results from the images at highest resolution are closed to the references values, and the coarsened images of Fontainebleau sandstones tend to overestimate the permeability values. The range of errors between permeability results of original and that of coarsened images is from 16.48% to 47.37% for this group of Fontainebleau sandstones. And the permeability errors of some other sandstone samples in our study even exceed 85%. Academically, the permeability error due to resolution effect should not be ignored, even though permeability of rock is a physical property varying by orders of magnitude in practical engineering.

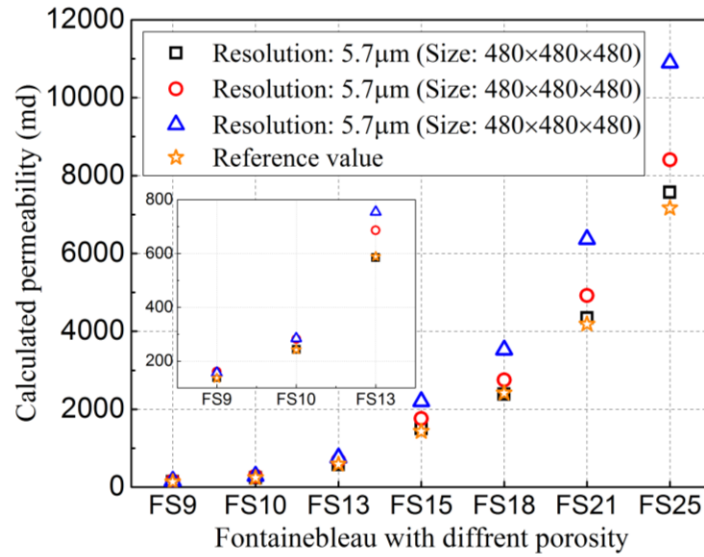


Figure 3: Permeability results calculated by LBM for images at different resolution levels.

Table 1: Corrected permeability results for different types of sandstone.

Sandstone type	Resolution (μm)	Size (voxel)	Porosity (%)	Calculated Permeability (md)	Corrected Permeability (md)
FS_9	5.7	480 ³	8.61	138.1	--
	11.4	240 ³	8.63	160.8	137.4
	22.8	120 ³	8.58	155.9	142.5
FS_10	5.7	480 ³	10.10	243.4	--
	11.4	240 ³	10.08	281.6	248.3
	22.8	120 ³	10.07	283.8	241.5
FS_13	5.7	480 ³	12.57	584.6	--
	11.4	240 ³	12.54	685.9	592.7
	22.8	120 ³	12.56	754.2	608.2
FS_15	5.7	480 ³	15.36	1506.5	--
	11.4	240 ³	15.33	1759.5	1489.8
	22.8	120 ³	15.29	2200.7	1515.1
FS_18	5.7	480 ³	17.62	2391.3	--
	11.4	240 ³	17.61	2753.0	2330.3
	22.8	120 ³	17.58	3524.0	2339.5
FS_21	5.7	480 ³	20.65	4343.5	--
	11.4	240 ³	20.63	4919.1	4233.7
	22.8	120 ³	20.65	6366.4	4235.2
FS_25	5.7	480 ³	24.50	7571.6	--
	11.4	240 ³	24.49	8404.2	7319.3
	22.8	120 ³	24.46	10899.7	7425.5
Berea Sandstone	5.345	400 ³	19.65	1871.1	--
	10.69	200 ³	19.57	2224.1	1872.3
	21.38	100 ³	19.41	2896.5	1798.5
Doddington Sandstone	5.549	400 ³	20.38	5222.3	--
	11.098	200 ³	20.33	6113.0	5248.4
	22.196	100 ³	20.24	8158.4	5178.0

In this study, we propose an error correction model for intrinsic permeability calculation by using LBM. We apply this model to different kinds of sandstones to test its performance, and the results show that the error correction model can effectively eliminate the permeability errors due to the resolution effect. As illustrated in Table 1, the permeability errors caused by resolution effect are declined to less than 5% for different sandstone samples.

References

- 1 Andr  H, Combaret N, Dvorkin J, et al. Digital rock physics benchmarks—Part I: Imaging and segmentation[J]. *Computers & Geosciences*, 2013, 50: 25-32.
- 2 Andr  H, Combaret N, Dvorkin J, et al. Digital rock physics benchmarks—Part II: Computing effective properties[J]. *Computers & Geosciences*, 2013, 50: 33-43.
- 3 Jin G, Patzek T W, Silin D B. Direct prediction of the absolute permeability of unconsolidated and consolidated reservoir rock[C]//SPE Annual Technical Conference and Exhibition. Society of Petroleum Engineers, 2004.
- 4 Kutay M E, Aydilek A H, Masad E. Laboratory validation of lattice Boltzmann method for modeling pore-scale flow in granular materials[J]. *Computers and Geotechnics*, 2006, 33(8): 381-395.
- 5 Degruyter W, Burgisser A, Bachmann O, et al. Synchrotron X-ray microtomography and lattice Boltzmann simulations of gas flow through volcanic pumices[J]. *Geosphere*, 2010, 6(5): 470-481.
- 6 Jones B D, Feng Y T. Effect of image scaling and segmentation in digital rock characterisation[J]. *Computational Particle Mechanics*, 2016, 3(2): 201-213.
- 7 Berg, C. (2016, May 18). Fontainebleau 3D models. Retrieved March 15, 2019, from www.digitalrockportal.org.

TOPOLOGY OPTIMISATION OF SOUND ABSORBING MATERIALS USING AN ISOGEOMETRIC BOUNDARY ELEMENT METHOD THROUGH SUBDIVISION SURFACES

*Zhaowei Liu¹, LeiLei Chen² and Chuang Lu²

¹Glasgow Computational Engineering Centre, University of Glasgow, UK, G12 8QQ

²College of Architecture and Civil Engineering, Xinyang Normal University, Xinyang, Henan, P.R.China, 464000

*z.liu.2@research.gla.ac.uk

Summary

A topology optimisation approach based on the boundary element method (BEM) with subdivision surfaces is proposed for the optimal distribution of sound absorbing material on structural surfaces. The proposed optimisation method aims to find a cost-efficient distribution of sound absorbing material for a given structural design.

Key Words: *Isogeometric Analysis; Topology optimisation; Boundary element method; Acoustic material*

Motivations

The sound absorbing materials used here are porous materials. The materials are passive mediums which can reduce acoustic energy by transferring it into heat. They are widely used in many manufacturing industries, e.g. automotive, electronic and electrical equipment and building industries. However, applying those material onto the surfaces will increase the weight and cost of the design structures. It is not very efficient to use a uniform distribution of these sound absorbing material on the whole surface of the object. Therefore, it is necessary to find an optimal material distribution under a given vibration and noise constraints.

Boundary element method

The boundary element method solves integral equations constructed only on the boundaries, which only requires a boundary discretisation to solve this problem. Moreover, the boundary element method automatically satisfies the Sommerfeld boundary condition[4] which has advantages over other methods in handling exterior acoustic scattering problems. Thus, the BEM is the most appropriate numerical method for this optimisation analysis. The governing equation for the time harmonic acoustic problem is the Helmholtz equation defined as:

$$\nabla^2 p(\mathbf{x}) + k^2 p(\mathbf{x}) = 0, \quad (1)$$

where ∇^2 is the Laplace operator, k is the wavenumber. p represents the acoustic pressure which is a function of a physical point \mathbf{x} . Using a collocation method, the boundary integral equation is defined as:

$$c(\mathbf{x})p(\mathbf{x}) = \int_{\Gamma} \left[G(\mathbf{x}, \mathbf{y}) \frac{\partial p}{\partial n}(\mathbf{y}) - \frac{\partial G}{\partial n}(\mathbf{x}, \mathbf{y}) p(\mathbf{y}) \right] d\Gamma + p_{inc}(\mathbf{x}), \quad (2)$$

where Γ denotes the physical domain of the problem which is the surface of the structure. \mathbf{x} and \mathbf{y} are source point and field point respectively. c is known as the jump term in the boundary element method which equals $\frac{1}{2}$ if the boundary is smooth. G is the fundamental solution of the Helmholtz equation also called Green function. $\frac{\partial G}{\partial n}$ is the normal derivative of the Green function. $p_{inc}(\mathbf{x})$ denotes the acoustic pressure of the incident wave at source point. Discretising this boundary domain into N_e Loop subdivision surfaces elements. The maxima of the subdivision basis functions (shown in figure 1), which are associated with the control vertices, are used as the collocation points to formulating the discretised boundary integral equation:

$$\begin{aligned} c(\mathbf{x}_i)p(\mathbf{x}_i) = & \sum_{j=1}^{N_e} \sum_{k=1}^{N_c} \frac{\partial p_k^j}{\partial n} \int_{\Gamma_j} N_k(\mathbf{y}(\xi, \eta)) G(\mathbf{x}_i, \mathbf{y}(\xi, \eta)) d\Gamma_j \\ & - \sum_{j=1}^{N_e} \sum_{k=1}^{N_c} p_k^j \int_{\Gamma_j} N_k(\mathbf{y}(\xi, \eta)) \frac{\partial G}{\partial n}(\mathbf{x}_i, \mathbf{y}(\xi, \eta)) d\Gamma_j + p_{inc}(\mathbf{x}_i), \end{aligned} \quad (3)$$

where i is the i^{th} collocation point. N denotes the subdivision basis function. Then the system matrix can be formulated as:

$$\mathbf{H}\mathbf{p} = \mathbf{G}\mathbf{q} + \mathbf{p}^{inc}, \quad (4)$$

where \mathbf{H} and \mathbf{G} are known as boundary element method matrices. \mathbf{p} and \mathbf{q} are the coefficient vectors of acoustic pressures and their normal derivatives. \mathbf{p}^{inc} can be applied as a boundary condition which is the vector of incident acoustic pressures at collocation points defined as

$$p_{inc}(\mathbf{x}_i) = e^{i\mathbf{k}\cdot\mathbf{x}_i}, \quad (5)$$

Also apply an impedance boundary condition as

$$\frac{\partial p}{\partial n}(\mathbf{y}) = ik\beta p(\mathbf{y}), \quad (6)$$

where β denotes the normalized acoustic admittance at the field point \mathbf{y} . The system equation can be modified as

$$[\mathbf{H} - \mathbf{G}\mathbf{B}]\mathbf{p} = \mathbf{p}^{inc}, \quad (7)$$

where \mathbf{B} is known as the admittance matrix. Then the coefficients of acoustic pressure \mathbf{p} can be solved. And the acoustic pressures on the surfaces can be interpolated using subdivision basis functions.

Loop subdivision surfaces

Subdivision surfaces begin with a coarse polygon mesh and applies a certain subdivision algorithm to recursively refine this polygon mesh until refined meshes eventually converge to a smooth limit surface. The limit surface can be evaluated using spline functions from any level of refined meshes. The polygon mesh can be locally refined and adjusted to model any arbitrary topologies. Loop[3] developed a subdivision scheme in 1987, which can generate smooth surfaces through triangular control meshes. The Loop subdivision surfaces can be evaluated using box splines basis functions. Figure 1 shows an example of the Loop subdivision surfaces. It uses a linear triangular mesh as the control mesh which is easily refined and adjusted during the recursive analysis process. The analysis method with subdivision surface discretisation can analyse a complex engineering geometry with only a single linear mesh where NURBS-based isogeometric approach[2] may need multiple patches to address the complex topologies. Cirak[1] implemented Loop subdivision surfaces for Kirchhoff-Love shell analysis in 2000.

Objective function and constrains

The objective function and constrains of this optimisation problem is defined as:

$$\begin{cases} \min \Pi = \bar{\mathbf{p}}_f \mathbf{p}_f \\ s.t. \sum_{e=1}^{N_e} \rho_e v_e - f_v \sum_e v_e \leq 0, \\ 0 \leq \rho_{min} \leq \rho_e \leq 1 \end{cases} \quad (8)$$

where $\bar{\mathbf{p}}_f$ denotes the conjugate transpose of this vector. The ρ_e and v_e denotes the density and volume of the e^{th} element and f_v is a constrain ratio of the volume. ρ_{min} is the minimum constrain of the element density. \mathbf{p}_f is the vector sound pressure of a number observation points which are computed using the boundary integral equation. Computed in the matrices form as:

$$\mathbf{p}_f = -[\mathbf{H}_f - \mathbf{G}_f \mathbf{B}]\mathbf{p} + \mathbf{p}_f^{inc}. \quad (9)$$

\mathbf{H}_f and \mathbf{G}_f are boundary element matrices for the observation points. \mathbf{p}_f^{inc} is the acoustic pressure of the incident wave at those points. As the observation points are far field points, the jump term c in the boundary integral equation 3 is zero.

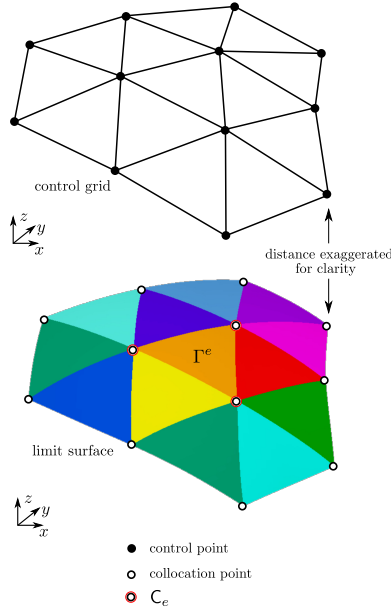


Figure 1: Loop subdivision surfaces: control grid, limit surface and collocation points.

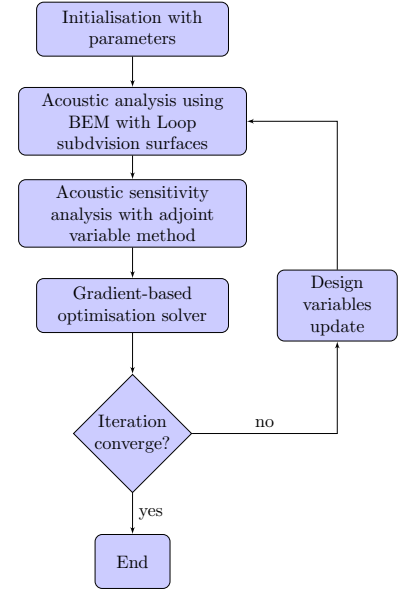


Figure 2: A workflow of topology optimisation.

Sensitivity analysis

The optimisation solver we used is a gradient-based solver, which requires a sensitivity analysis associated with those design variables. The adjoint variable method is chosen to conduct it. We first introduce two arbitrary adjoint vectors λ_1 and λ_2 associated with the two boundary element system of equations and the objective function can be expressed as:

$$\Pi = \Pi(\mathbf{p}_f) + \lambda_1^T [(\mathbf{H} - \mathbf{G}\mathbf{B})\mathbf{p} - \mathbf{p}^{inc}] + \lambda_2^T [\mathbf{p}_f + [\mathbf{H}_f - \mathbf{G}_f\mathbf{B}]\mathbf{p} - \mathbf{p}_f^{inc}]. \quad (10)$$

Take a direct differentiation of the objective function respected to design variable ρ_e . The sensitivity of the objective function can be eventually derived as

$$\frac{\partial \Pi}{\partial \rho_e} = -\Re(\lambda_1^T \mathbf{G} \frac{\partial \mathbf{B}}{\partial \rho_e} \mathbf{p} + \lambda_2^T \mathbf{G} \frac{\partial \mathbf{B}}{\partial \rho_e} \mathbf{p}). \quad (11)$$

Optimisation workflow

Figure 2 shows a workflow of the proposed topology optimisation method. The optimisation is firstly initialised by choosing the constrain parameters. Then, it solves the acoustic boundary element method and computes the value of objective functions. After that, a sensitivity analysis will be conducted using the adjoint variable method. The value of the objective function and the sensitivity solution are passed to a gradient-based optimisation solver, which compute the updated design variables. The process will repeat a number of times until the optimising results of two iterations converges.

Numerical Examples

The optimisation of the distribution of sound absorbing material on a submarine surfaces is conducted as an numerical example. We choose a incident wave with frequency equal to 200Hz. Figure 3 shows the acoustic pressure changes during a number of optimisation iterations. Figure 4 shows the final optimisation of the material density on the surfaces.

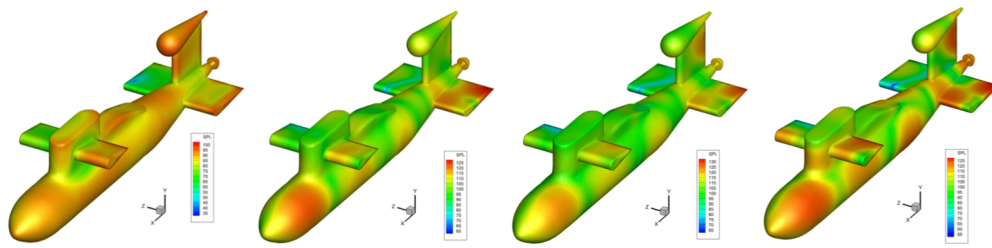


Figure 3: Acoustic pressure plots on a submarine surfaces at 4 different iterations in the material topology optimisation.

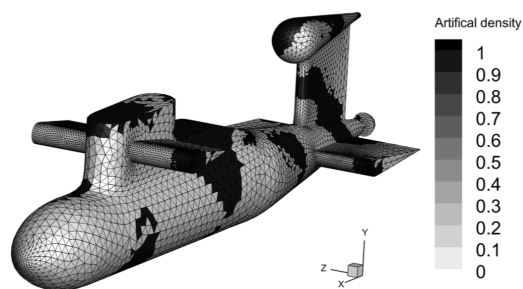


Figure 4: Optimisation results for the acoustic absorbing material of the submarine.

Conclusion

An topology optimisation of the distribution of sound absorbing materials using boundary element method with subdivision surfaces is proposed. The densities of the sound absorbing material are used as the design variables. A minimum volume of the sound absorbing material is used as the optimising constraint. The optimisation problem is solved by using the method of moving asymptotes (MMA) algorithm.

References

- 1 F. Cirak, M. Ortiz, and P. Schroder. Subdivision surfaces: a new paradigm for thin-shell finite-element analysis. *International Journal for Numerical Methods in Engineering*, 47 (12):2039–2072, 2000.
- 2 T. J. R. Hughes, J. A. Cottrell, and Y. Bazilevs. Isogeometric analysis: CAD, finite elements, NURBS, exact geometry and mesh refinement. *Computer Methods in Applied Mechanics and Engineering*, 194(39):4135–4195, 2005.
- 3 C. Loop. *Smooth subdivision surfaces based on triangles*. Master's thesis, Department of Mathematics, The University of Utah, 1987.
- 4 A. Sommerfeld. *Partial Differential Equations in Physics*, volume 1. Academic Press, 1949.

A MATERIAL POINT METHOD FOR THE ROBUST SIMULATION OF ROCKING INDUCED DAMAGE

***Savvas P. Triantafyllou¹, Emmanouil G. Kakouris¹ and Manolis N. Chatzis²**

¹Centre for Structural Engineering and Informatics, Faculty of Engineering, The University of Nottingham, NG7 2RD, UK

²Dept. of Engineering Science, Univ. of Oxford, Oxford, OXI 3PA, UK

*savvas.triantafyllou@nottingham.ac.uk

Summary

Rocking dynamics occur in systems whose connection with their support medium is achieved through a non-tensile interface where the shear forces are frictional. Examples of rocking systems can be found in a wide range of applications: from museum exhibits and hospital equipment to electrical devices and structural elements. The response of such systems when subjected to ground excitations is substantially different to the response of monolithic structures. A distinctive feature is the appearance of rigid body rotations and displacements during the motion. As a reasonable consequence, the majority of relevant literature examines rocking systems under the assumptions of rigid support medium and body, or by assuming that the rocking body is flexible only in the lateral direction. However, the decelerations of the rocking body during the occurring impacts are often of the order of tenths of g . These large forces may induce large local stresses at the points of application that may deteriorate the contact surface or lead to local failures. This mode of failure has often been ignored in the literature. This is mainly due to the computational complexity of the problem between large displacement kinematics and computational mechanics. The change of the contact surface during the rocking motion in combination with an impact and sliding contact problem pose substantial challenges for standard FE methods: they result in the need for re-meshing techniques, or very dense initial meshes. Hence, we propose a Material Point Method implementation for the robust simulation of large displacement kinematics associated with rocking fused with a phase field description of fracture to examine the resulting damage evolution.

Key Words: *Material Point Method; impact dynamics; rocking*

Governing Equations

The case of two deformable domains Ω_1 and Ω_2 shown in Figure 1 is considered for brevity. Following a discrete field approach [2], each domain is attached to a discrete field $\{\mathcal{D} \mid \mathcal{D} = 1, 2\}$.

The coupled, i.e., displacement and phase field, strong form assumes the following for for each individual discrete field \mathcal{D} , i.e.,

$$\left\{ \begin{array}{l} \nabla \cdot \boldsymbol{\sigma}_{\mathcal{D}} + \mathbf{b}_{\mathcal{D}} = \rho_{\mathcal{D}} \ddot{\mathbf{u}}_{\mathcal{D}} \quad \text{on } \Omega_{\mathcal{D}} \\ \left(\frac{4l_{0\mathcal{D}} \mathcal{H}_{\mathcal{D}}}{\bar{\mathcal{G}}_{c_{\mathcal{D}}}} + 1 \right) c_{\mathcal{D}} - 4l_{0\mathcal{D}}^2 \Delta c_{\mathcal{D}} = 1 \quad \text{on } \Omega_{\mathcal{D}}. \end{array} \right. \quad (1)$$

where $\boldsymbol{\sigma}_{\mathcal{D}}$ is the stress tensor, $\mathbf{b}_{\mathcal{D}}$ corresponds to the vector of body forces, and ρ is the material density. Furthermore, c is the phase field, l_0 is the phase field regularization length, and \mathcal{H} is the phase field history variable [3]. The strong form of Eq. (1) is supplemented by the following set of boundary

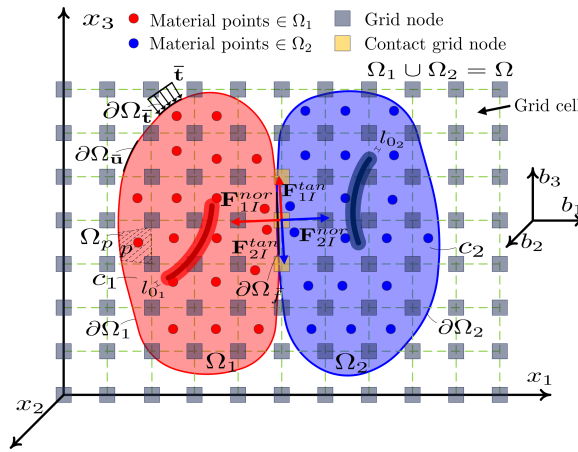


Figure 1: Phase field material point method approximation

conditions

$$\left\{ \begin{array}{ll} \boldsymbol{\sigma}_{\mathcal{D}} \cdot \mathbf{n}_{\mathcal{D}} = \bar{\mathbf{t}}_{\mathcal{D}}, & \text{on } \partial\Omega_{\bar{\mathbf{t}}_{\mathcal{D}}} \\ \mathbf{u}_{\mathcal{D}} = \bar{\mathbf{u}}_{\mathcal{D}}, & \text{on } \partial\Omega_{\bar{\mathbf{u}}_{\mathcal{D}}} \\ \mathbf{u}_{\mathcal{D}} = {}^{(0)}\mathbf{u}_{\mathcal{D}}, & \text{on } {}^{(0)}\Omega_{\mathcal{D}} \\ \dot{\mathbf{u}}_{\mathcal{D}} = {}^{(0)}\dot{\mathbf{u}}_{\mathcal{D}}, & \text{on } {}^{(0)}\Omega_{\mathcal{D}} \\ \ddot{\mathbf{u}}_{\mathcal{D}} = {}^{(0)}\ddot{\mathbf{u}}_{\mathcal{D}}, & \text{on } {}^{(0)}\Omega_{\mathcal{D}} \\ \nabla c_{\mathcal{D}} \cdot \mathbf{n} = 0, & \text{on } \partial\Omega_{\mathcal{D}} \\ c_{\mathcal{D}} = {}^{(0)}c_{\mathcal{D}}, & \text{on } {}^{(0)}\Omega_{\mathcal{D}} \\ \boldsymbol{\sigma}_{\mathcal{D}} \cdot \mathbf{n}_{\mathcal{D}}^{\text{cont}} = \bar{\mathbf{f}}_{\mathcal{D}}^{\text{cont}}, & \text{on } \partial\Omega_{\mathcal{D}\bar{\mathbf{f}}} \end{array} \right. \quad (2)$$

The last boundary condition accounts for the contact forces that are considered as being externally applied to each discrete field \mathcal{D} . Furthermore, the coupled strong form is subjected to kinematic constraints for the imposition of the non-tension and impenetrability conditions at the contact interface [4]. Coulomb friction contact constraints are imposed at the interface. The coupled strong form of Eq. (1) is re-instated in the weak sense via the Galerkin method. The resulting coupled weak form is then discretized using a material point method approach [1]. In this, each discrete field comprises a set of material points $\mathcal{N}_{\mathcal{D}}$. The resulting discrete equations of motion are solved with explicit time integration within a staggered iterative scheme.

Application

A circular arch with two buttresses is examined to ascertain the ability of the method to simulate rocking induced failure. The structure is subjected to the Chi-Chi, Taiwan ground motion record with a $\text{PGA}=3.9\text{m/s}^2$. The geometry of the structure and the material properties considered are shown in Fig. 2. The ground motion record is shown in Fig. 3a.

Quadratic B-splines are utilized for the background grid with a cell spacing equal to 0.10 m. Plane strain conditions are assumed. The circular arch with the two buttresses consists of 5886 material points whereas the ground is discretised with 12960 material points. The initial cell density of each parent cell is at least 3×3 material points. The equations of motion are integrated using explicit time integration with a step $\Delta t = 0.00005$ sec. The ground excitation is applied using D' Alembert's principle.

The time history of the angle of oscillation of the left buttress with respect to the horizontal is shown

in Fig. 3(b). The buttress undergoing small angle rocking motion (i.e. less than 2°) for the first 28sec of its response. As the ground acceleration increases, material degradation initiates until the first hinge forms on the left side of the arch at time $t = 31.75$ sec (see Fig. 4(b)). Next, two more hinges develop, one at the left haunch (see Fig. 4(c)) and another close to the right buttress 4(d) at time $t = 32$ and $t = 32.25$ sec. The collapse mechanism and the final configuration of the structure are shown in Figs. 4(e) and 4(f), respectively.

The proposed scheme accurately captures the collapse mechanism of the arch. It is of interest to note that, due to the rocking response of the buttresses, this evolves with three plastic hinges rather than the standard 4-hinge mechanism that is common in fully supported arches. Furthermore, the formulation succeeds in providing a robust estimate of the post-collapse configuration of the structure.

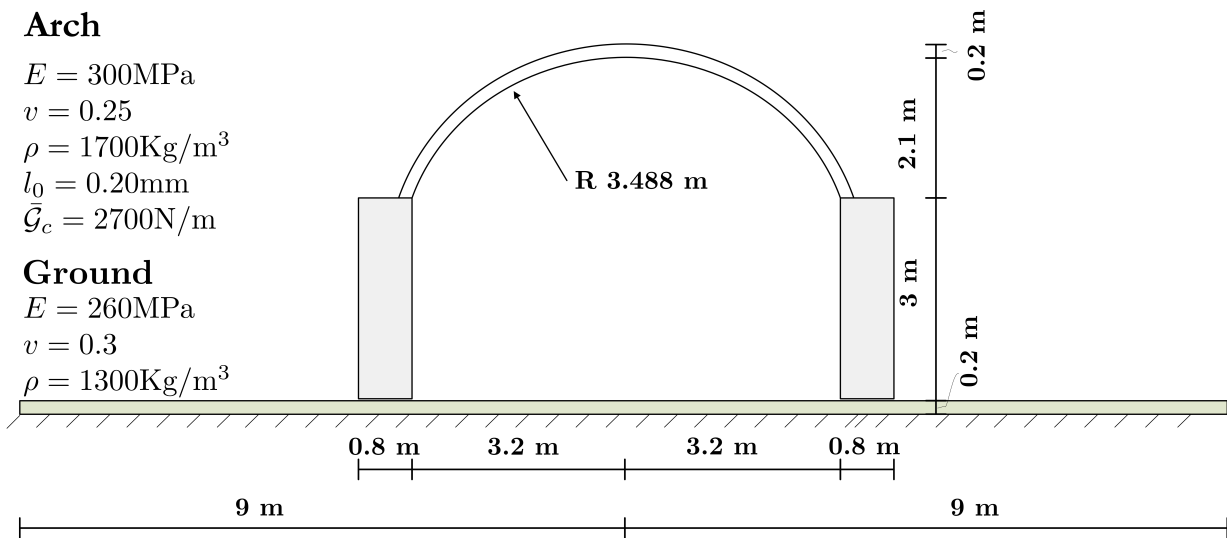


Figure 2: Geometry and boundary conditions

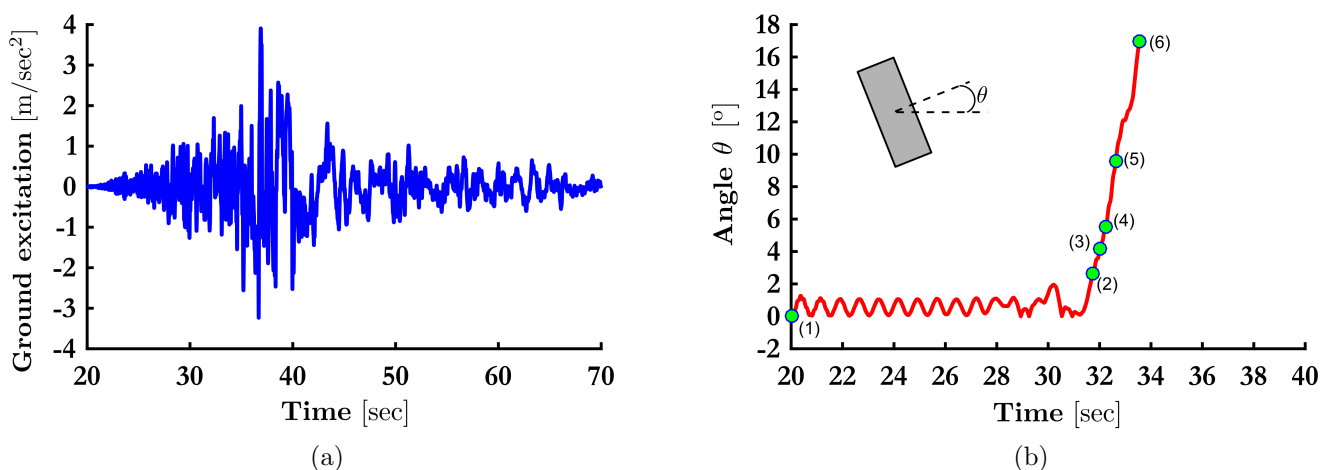


Figure 3: (a) Ground Motion Record (b) Rocking body angle with ground [labels (1) to (6) correspond to Fig. 4 sub-captions (a) to (f)].

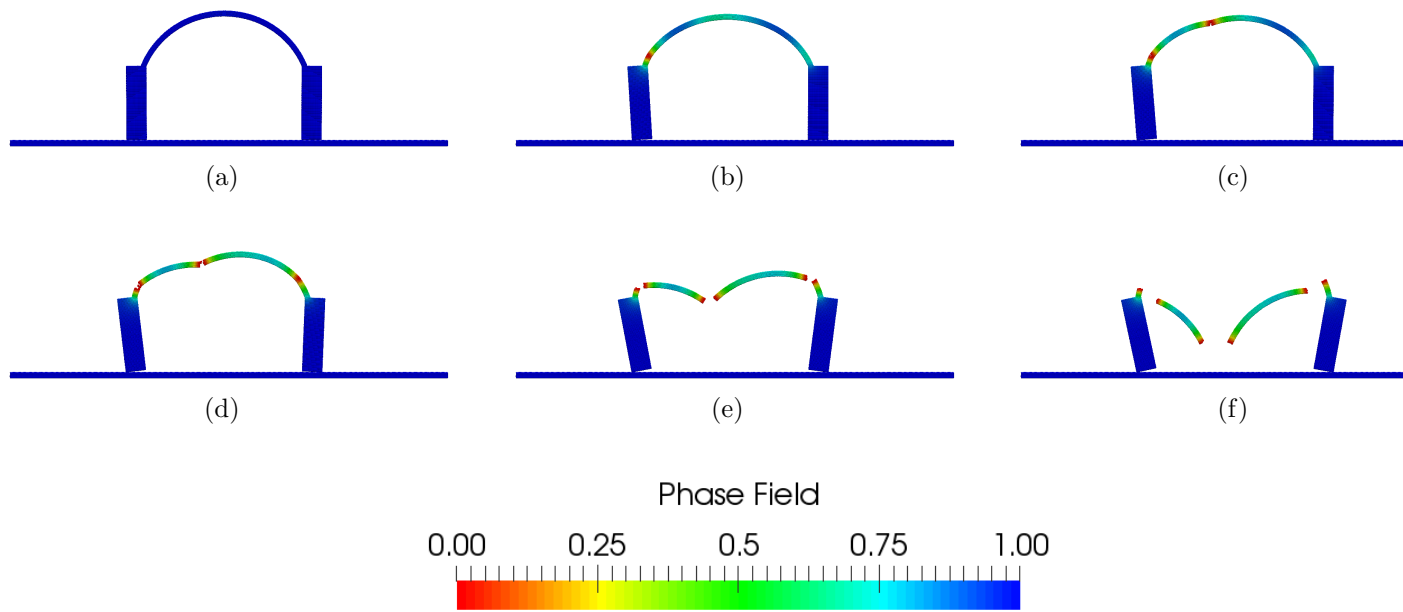


Figure 4: Circular Arch with Buttresses: Phase field for time step (a) $t = 20$ sec (initial state) (b) $t = 31.75$ sec (first hinge) (c) $t = 32$ sec (second hinge) (d) $t = 32.25$ sec (third hinge) (e) $t = 32.63$ sec (collapse) and (f) $t = 33.53$ sec (final state)

Conclusions

A material point method is presented for the simulation of rocking body dynamics. In this, the solution of the governing equations of motion is performed for each field individually while the physics describing the field interfaces are explicitly introduced into the strong form of the problem through appropriate boundary conditions. The solution of the resulting governing equations is performed via the material point method in an explicit manner. The method is shown to successfully capture the large displacement kinematics of a structure undergoing rocking vibrations and the resulting failure mechanics. Of interest is the ability of the method to also capture the post-failure kinematics of the structure.

References

- [1] SG Bardenhagen, JU Brackbill, and Deborah Sulsky. “The material-point method for granular materials”. In: *Computer methods in applied mechanics and engineering* 187.3-4 (2000), pp. 529–541.
- [2] Peng Huang et al. “Contact algorithms for the material point method in impact and penetration simulation”. In: *International journal for numerical methods in engineering* 85.4 (2011), pp. 498–517.
- [3] EG Kakouris and Savvas P Triantafyllou. “Phase-field material point method for brittle fracture”. In: *International Journal for Numerical Methods in Engineering* 112.12 (2017), pp. 1750–1776.
- [4] Olek C Zienkiewicz and Robert L Taylor. *The finite element method for solid and structural mechanics*. Elsevier, 2005.

LAYERED SHELL COUPLED NLFE FORMULATION FOR NEARLY INCOMPRESSIBLE ORTHOTROPIC MYOCARDIUM

***Yew Wong and Roger Crouch**

School of Mathematics, Computer Science & Engineering, City, University of London

*yew.wong.1@city.ac.uk

Summary

This paper reports on progress made in the development of a nonlinear Finite Element analysis capability to simulate the beating of a human heart. A layered shell approach enables the different muscle fibre directions (which significantly change their orientation through the myocardium) to be considered. The paper begins with a description of a Total Lagrangian FE code for the layered shell. It then illustrates the use of the Mean Dilation Method (MDM) to handle near incompressibility, although this approach has currently only been tested by the authors on 8-noded hexahedral elements. Cook's tapered skew cantilever problem is examined. The paper then goes on to describe the Holzapfel-Ogden [4] constitutive model which is to be used to represent the myocardium. Finally, we describe the manner in which the Electro-Mechanics are to be coupled to simulate muscle fibre contraction.

Key Words: *Finite Deformation, Layered Shell, Orthotropic Hyperelastic Myocardium*

Introduction

There are over 7 million people in the UK living with cardiovascular disease (CVD). It is the principal cause of death in the UK; claiming over 170,000 lives each year. To comprehend the various forms of CVD and determine appropriate medical treatment, cardiac surgeons would benefit greatly from having accurate simulators which can capture patient-specific features. This study contributes to the research being conducted worldwide to arrive at a high-fidelity 3-dimensional Electro-Mechanics representation of a beating heart. The novel aspect of the approach taken here is the adoption of shell Finite Elements to model the walls of the geometrically complex atria and ventricles, rather than conventional solid (tetrahedral, for example see [1], or hexahedral) Finite Elements.

Total Lagrangian Layered Shell Formulation

Multiple layers within the shell elements are formed by duplicating the integration points through the thickness direction. The through-thickness local coordinates are transformed as follows

$$\zeta = -1 + \frac{1}{T_t} (2T_i - T_l(1 - \zeta_l)) \quad (1)$$

where T_t is the total thickness, T_i is the thickness of the layers preceding the layer under consideration, T_l is the thickness of the current layer and ζ_l is the original ζ value locating the integration points in a non-layered element.

Figure 1 illustrates the deformation of just 8 shell elements (forming a cantilever beam) subjected to an increasing end moment. A comparison is given between a single layer model and a softer 3-layer representation (with through-thickness elasticities of $0.5E : E : 2E$).

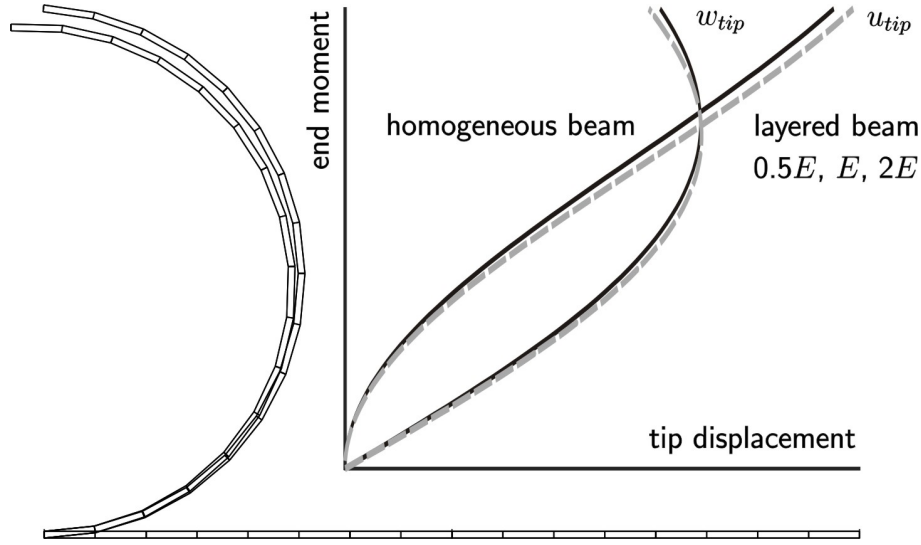


Figure 1: Finite deformation of cantilever subjected to end moment [6], showing the homogeneous shell and layered shell results.

Updated Lagrangian Stiffness Matrix (Mean Dilation Method)

The element stiffness matrix for the Updated Lagrangian formulation comprises 3 components (material, geometric and pressure). The latter is a consequence of the Mean Dilation Method which can handle the near-incompressibility of the myocardium.

$$[K] = [K_c] + [K_g] + [K_p] \quad \text{where} \quad [K_c] = \left\{ \frac{\partial N}{\partial x} \right\}^T [\bar{c}] \left\{ \frac{\partial N}{\partial x} \right\} \quad (2)$$

$$[\bar{c}] = [c] + \rho[I_4] \quad \text{where} \quad [I_4] \equiv I_{ijkl} = \delta_{ij}\delta_{kl} - \delta_{ik}\delta_{jl} - \delta_{il}\delta_{jk} \quad (3)$$

The elasticity matrix for a Neo-Hookean (near-incompressible) material, $[c]$, may be found in [2].

$$[K_g] = \begin{bmatrix} [K_{g11}] & [K_{g12}] & \cdots & [K_{g1n}] \\ [K_{g21}] & \ddots & \ddots & \vdots \\ \vdots & \ddots & \ddots & \vdots \\ [K_{gn1}] & \cdots & \cdots & [K_{gnn}] \end{bmatrix} \quad [K_{g_{ij}}] = \left\{ \frac{\partial N}{\partial x_i} \right\}^T [\sigma] \left\{ \frac{\partial N}{\partial x_j} \right\} [I] \quad (4)$$

$[\sigma]$ refers to the Cauchy stresses and the subscript n refers to the number of nodes in each element.

$$[K_p] = \begin{bmatrix} [K_{p11}] & [K_{p12}] & \cdots & [K_{p1n}] \\ [K_{p21}] & \ddots & \ddots & \vdots \\ \vdots & \ddots & \ddots & \vdots \\ [K_{pn1}] & \cdots & \cdots & [K_{pnn}] \end{bmatrix} \quad [K_{p_{ij}}] = \bar{\kappa} v_e \left\{ \frac{\partial \tilde{N}}{\partial x_i} \right\} \left\{ \frac{\partial \tilde{N}}{\partial x_j} \right\}^T \quad (5)$$

$$\left\{ \frac{\partial \tilde{N}}{\partial x} \right\} = \sum^{nGP} \det \left(\left\{ \frac{\partial N}{\partial r} \right\} \right) \left\{ \frac{\partial N}{\partial x} \right\} \quad (6)$$

$\left\{ \frac{\partial N}{\partial r} \right\}$ are the derivatives of the shape functions with respect to the local coordinates. $\bar{\kappa} = \kappa \bar{J}$ where $\bar{J} = \frac{v_e}{V_e}$, v_e is the volume of the deformed element, V_e is the initial volume of the element and $J = \det([F])$ where $[F]$ is the deformation gradient. nGP gives the number of quadrature points.

The Mean Dilation Method is used to simulate the in-plane shearing and bending of Cook's benchmark problem (Figure 2). The 8-noded hexahedral convergence plot agrees well with that obtained from published results [5].

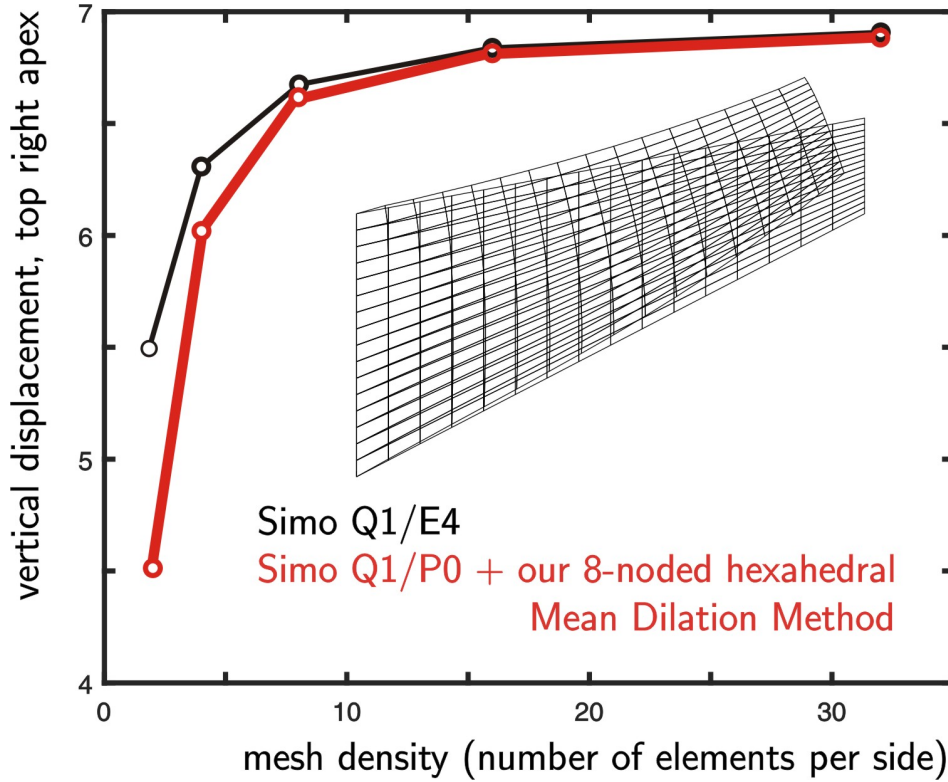


Figure 2: Convergence plot for Cook's tapered skew cantilever using a Neo-Hookean model.

Anisotropic Hyperelasticity

The Neo-Hookean model used above defines a purely isotropic response. This fails to take account of the presence of the directional myocardial fibres which have a strong influence on the finite deformation of the myocardial tissue. At any one location, the inner endocardium fibres are not parallel to the outer epicardium fibres. This difference in orientation gives rise to a twisting motion of the contracting and expanding ventricles. The following 3-component orthotropic hyperelastic Holzapfel-Ogden [4] strain energy density function is able to reproduce that material behaviour

$$\Psi = \underbrace{\frac{a}{2b} \exp(b(I_1 - 3))}_{\text{isotropic } \mathcal{F}(I_1)} + \underbrace{\frac{a_f}{2b_f} (\exp(b_f(I_{4f} - 1)^2) - 1) + \frac{a_s}{2b_s} (\exp(b_s(I_{4s} - 1)^2) - 1)}_{\text{transversely isotropic } \mathcal{G}(I_{4f}) \mathcal{G}(I_{4s})} + \underbrace{\frac{a_{fs}}{2b_{fs}} (\exp(b_{fs}(I_{8fs})^2) - 1)}_{\text{orthotropic } \mathcal{H}(I_{8fs})}$$

Eight positive material constants $a, b, a_f, a_s, b_f, b_s, a_{fs}$ and b_{fs} define the material. The first invariant of the right Cauchy-Green deformation matrix $[C] = [F]^T[F]$ is given by its trace $I_1 = \text{tr}[C]$. A right-handed orthonormal coordinate system identifies the undeformed fibre axis orientation $\{f_0\}$ and

the undeformed sheet axis orientation $\{s_0\}$. These are used in the definition of the mixed invariants I_{4f} , I_{4s} and I_{8fs} .

$$I_{4f} = \{f_0\}^T [C] \{f_0\} \quad I_{4s} = \{s_0\}^T [C] \{s_0\} \quad I_{8fs} = \{f_0\}^T [C] \{s_0\}$$

The Cauchy stress is obtained from

$$[\sigma] = [F] \frac{\partial \Psi}{\partial [F]} - p[I]$$

Coupled Electro-Mechanical Behaviour

The transmembrane current sweeping around the heart drives the change in a local Action Potential which triggers the contraction of the myocardial fibres. This evolving potential is simulated using a monodomain Aliev-Panfilov excitation model (for example, see [3] for the FE formulation). The changing potential gives rise to an active stress. A code which can replicate the transmission of the electrical signal through the shell elements has already been produced by the authors. This is now being coupled to the mechanical Total and Updated Lagrangian FE simulators; which are themselves to be extended to incorporate the Holzapfel-Ogden material model.

Conclusions

While the study is not yet complete, this paper points to some of the achievements made by the authors in the development of a Finite Element simulator of a beating human heart. The layered shell formulation is promising, and the hyperelastic constitutive model examined provides a sophisticated representation of the behaviour of the orthotropic, nearly-incompressible myocardium. It has been shown that the Total Lagrangian shell Finite Element code and nearly-incompressible Updated Lagrangian hexahedral Finite Element code offer good agreement with established published results. This provides confidence in the algorithms constructed to-date.

References

- [1] Baillargeon, B *et al.*, The Living Heart Project: A Robust and Integrative Simulator for Human Heart Function, *European J. Mech. A/Solids*, 48, 38-47, 2014.
- [2] Bonet, J, Gil, A J and Wood, R D, *Nonlinear Solid Mechanics for Finite Element Analysis: Statics*, Cambridge University Press, 2016.
- [3] Göktepe S and Kuhl E, Computational Modeling of Cardiac Electrophysiology: A Novel Finite Element Approach, *Int. J Num. Meth. Eng.*, 79, 156-178, 2009.
- [4] Holzapfel, G A and Ogden, R W, Constitutive modelling of passive myocardium: a structurally based framework for material characterization, *Phil. Trans. Royal Soc. A: Math. Phys. Eng. Sci.*, 367 (1902), 3445-3475, 2009.
- [5] Simo, J C and Armero F, Geometrically Non-Linear Enhanced Strain Mixed Methods and the Method of Incompatible Modes, *Int. J Num. Methods in Eng.*, 33, 1413-1449, 1992.
- [6] Sze, K *et al.*, Popular Benchmark Problems for Geometric Nonlinear Analysis of Shells, *Finite Elements in Analysis and Design*, 40(11), 1551-1569, 2004.

AN IMPLICIT NON-ORDINARY STATE-BASED PERIDYNAMICS FOR LARGE DEFORMATION ANALYSIS

*Nur A. Hashim¹, W. M. Coombs¹, C. E. Augarde¹ and G. Hattori²

¹Department of Engineering, Durham University, South Road, DH1 3LE, Durham, UK

²Department of Engineering, University of Cambridge, Trumpington Street, CB2 1PZ, Cambridge, UK

*nur.a.hashim@durham.ac.uk

Summary

This paper focuses on applying implicit time stepping approaches to a non-ordinary state-based peridynamics formulation for quasi-static problems. The paper is restricted to two-dimensional large deformation analysis with linear elastic material behaviour with a modified correspondence model to suppress spurious zero energy modes. Equilibrium is obtained at each quasi-static time (or load) step through a Newton-Raphson solution procedure, including the derivation of an analytical expression for the consistent Jacobian matrix to ensure optimum convergence rates. The correspondence approach, which is a subclass of the non-ordinary state-based peridynamics, permits constitutive models from local theory to be used for the modelling of long-range forces. However, previous studies show the standard correspondence model suffers from zero-energy mode instability. Hence, this study also considers the effectiveness of the use of a stabilising parameter in removing these instabilities. Computational examples validate the ability of the adopted peridynamics model to eliminate zero energy modes and quantify the impact of the particles' spacings and horizon sizes on the choice of the stabilisation parameter.

Key Words: *Peridynamics; State-based; Implicit; Finite deformation; Zero-energy mode*

Introduction

Peridynamics (PD) was proposed by Silling [1] as a particle-based continuum model that can intrinsically handle problems involving discontinuities. However, up to now, little attention has been paid to using implicit time stepping formulations with PD. As a non local theory, it becomes challenging to obtain PD solutions in a reasonable run time especially in the case of quasi-static loading with large deformation problems. In these situations, implicit methods have the potential to be more computationally efficient and accurate compared to explicit methods. PD formulations can be classified into bond-based and state-based peridynamics (SB PD). The SB PD formulations can be further categorised as ordinary state-based peridynamics and non-ordinary state-based peridynamics (NOSB PD) depending on the types of material being modelled by the method (for example NOSBPD can include arbitrary constitutive formulations).

Non-ordinary state-based peridynamics with stabilised correspondence model

Based on the principle of virtual work, the equation of motion of NOSB PD takes the following form [1]

$$\left(\sum_{j=1}^m \underline{\mathbf{T}}[\mathbf{x}_i, t] \langle \mathbf{x}_j - \mathbf{x}_i \rangle - \underline{\mathbf{T}}[\mathbf{x}_j, t] \langle \mathbf{x}_i - \mathbf{x}_j \rangle \right) V_j + \mathbf{b}(\mathbf{x}_i, t) = \rho(\mathbf{x}_i) \ddot{\mathbf{u}}(\mathbf{x}_i, t), \quad (1)$$

where ρ represents the mass density in the initial configuration, $\ddot{\mathbf{u}}$ is the second-order time derivative of displacement and \mathbf{b} is the prescribed body force at time t and j is a counter for the m particles in the horizon of particle i , in which interaction between particles occurs over a finite distance defined by a horizon, δ . V_j is the volume of particle j and $\underline{\mathbf{T}}$ is the force vector state of a bond with stabilised correspondence model defined as

$$\underline{\mathbf{T}}[\mathbf{x}, t] = \omega(\boldsymbol{\xi}) \mathbf{P}(\mathbf{x})^T \mathbf{B}(\mathbf{x}) \boldsymbol{\xi} + \underline{\mathbf{T}}_z[\mathbf{x}, t]. \quad (2)$$

The first Piola-Kirchoff stress, $\mathbf{P}(\mathbf{x})$, for each particle \mathbf{x} can be obtained from the Cauchy stress, $\boldsymbol{\sigma}$, the deformation gradient, $\mathbf{F}(\mathbf{x})$ and the determinant of the deformation gradient, J

$$\mathbf{P}(\mathbf{x}) = J\boldsymbol{\sigma}(\mathbf{x})\mathbf{F}(\mathbf{x})^{-T}. \quad (3)$$

The non-local PD deformation gradient is expressed as a non-local integration given by [2]

$$\mathbf{F}(\mathbf{x}) = \left(\int_R \omega(\boldsymbol{\xi}) (\underline{\mathbf{Y}}(\boldsymbol{\xi}) \otimes \boldsymbol{\xi}) dV_{\boldsymbol{\xi}} \right) \mathbf{B}(\mathbf{x})^{-1} \quad \text{and} \quad \mathbf{B}(\mathbf{x}) = \int_R \omega(\boldsymbol{\xi}) (\boldsymbol{\xi} \otimes \boldsymbol{\xi}) dV_{\boldsymbol{\xi}}, \quad (4)$$

where $\mathbf{B}(\mathbf{x})$ is the non-local shape tensor and $\boldsymbol{\xi}$ denotes the reference position vector state between two particles, while $\omega(\boldsymbol{\xi})$ is a dimensionless weighting function of radius δ and the dyadic product of two vectors is denoted by \otimes . An additional stabilisation term is added to the peridynamic force vector defined as

$$\underline{\mathbf{T}}_{\mathbf{z}} = \frac{GC}{\omega_0} \underline{\mathbf{z}}(\boldsymbol{\xi}), \quad \underline{\mathbf{z}}(\boldsymbol{\xi}) = \underline{\mathbf{Y}}(\boldsymbol{\xi}) - \mathbf{F}\boldsymbol{\xi}, \quad C = \frac{12k'}{\pi h \delta^4} \quad \text{and} \quad k' = \frac{E}{2(1-\nu-2\nu^2)} \quad (5)$$

for 2D plane strain problems, where $\underline{\mathbf{Y}}$ denotes the deformed state of the bond, ν is the Poisson's ratio, E is the elastic modulus, h is the out-of-plane thickness and ω_0 is the integration of the weighting function in the neighbourhood. In this paper, we utilise a full Newton-Raphson (NR) method in order to solve the non-linear system of equations and update the stiffness matrix at each iteration.

Jacobian matrix

Based on Eq. (2), the Jacobian can be expressed as

$$\mathbf{K} = \sum_i^{I_n} \sum_{j=1}^m \sum_k^{ndof} \left(\left(\omega_i(|\boldsymbol{\xi}|) \frac{\partial \underline{\mathbf{T}}[\mathbf{x}_i, t]}{\partial \mathbf{u}_k} \right) - \left(\omega_j(|\boldsymbol{\xi}|) \frac{\partial \underline{\mathbf{T}}[\mathbf{x}_j, t]}{\partial \mathbf{u}_k} \right) \right) V_j. \quad (6)$$

Note that I_n is the total number of particles, m is the total number of neighbouring particles and k is a counter for the *ndof* degree of freedom. Loads are applied in increments where force equilibrium is sought between internal resisting forces, \mathbf{f}^{int} and external forces, \mathbf{f}^{ext} . The Jacobian matrix is recomputed at each iteration thus enabling convergence at an optimum rate. The solution of this non-linear system of equations can be obtained from repeatedly solving

$$\mathbf{K} \Delta \mathbf{u}_{l+1} = \mathbf{f}_l^{oobf}, \quad (7)$$

where $l+1$ represent the current equilibrium iteration within the NR procedure and $\mathbf{f}^{oobf} = \mathbf{f}^{ext} - \mathbf{f}^{int}$ is the global residual out of balance force vector.

Numerical example

The problem considered was a beam with simply-supported ends subjected to a total pressure of $p = 276$ kPa applied in 10 loadsteps. The beam domain had length, L of 254 mm and a depth, d_0 of 5.08 mm, with material properties being Young's modulus, $E = 68.95$ GPa and Poisson's ratio, $\nu = 0.25$. Due to symmetry, only half of the beam was analysed with two different particle discretisations and three different horizon sizes. Boundary conditions (BC) were imposed through the fictitious boundary layer, in which the fictitious layer was introduced outside the beam domain at the support region where the thickness of the layer was equivalent to the horizon size, δ [4]. A uniform transverse pressure was applied to all the particles on the top surface with the same load. In this paper, a dimensionless tolerance of 1×10^{-10} was used on the global normalised out of balance force. The final normalised vertical displacements predicted by the method is compared here in Figure 2 against the analytical result, for 3×75 particles with different horizon sizes and an "optimum" stabilised parameter. It can be clearly seen that the normalised vertical displacements agree well with the analytical result. The "optimum" stabilised parameter, G is given for both particle discretisations and different horizon sizes in Table 1. It can be seen that as the horizon size increases and as the particle discretisation coarsens,

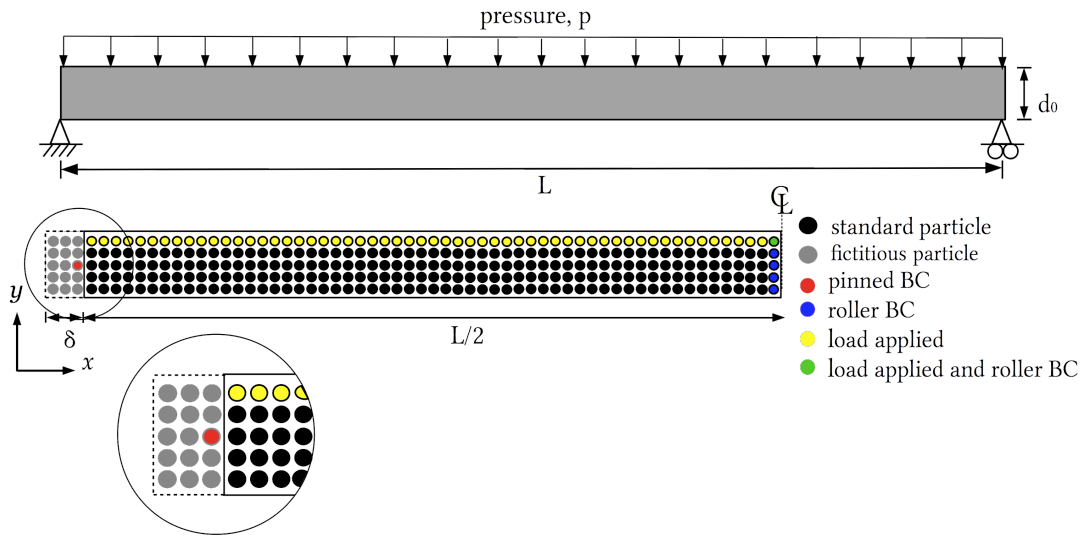


Figure 1: Simply-supported slender beam subjected to uniform transverse pressure.

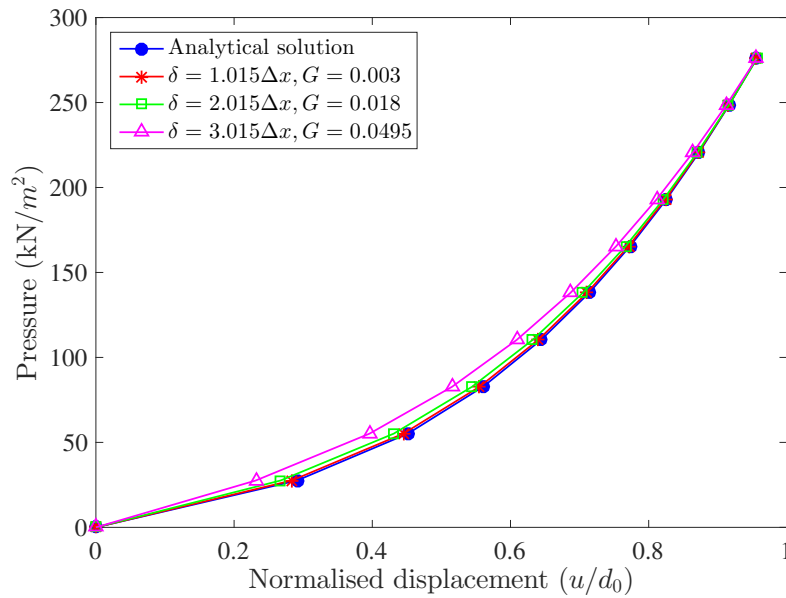
Figure 2: Simply-supported beam: normalised vertical end with 3×75 particles.

Table 1: Relative displacement error with different particle discretisations and different horizon sizes.

Particles discretisation	Horizon size, δ	"optimum" G
3×75	$1.015\Delta x$	0.0030
	$2.015\Delta x$	0.0180
	$3.015\Delta x$	0.0495
5×125	$1.015\Delta x$	0.0025
	$2.015\Delta x$	0.0115
	$3.015\Delta x$	0.0300

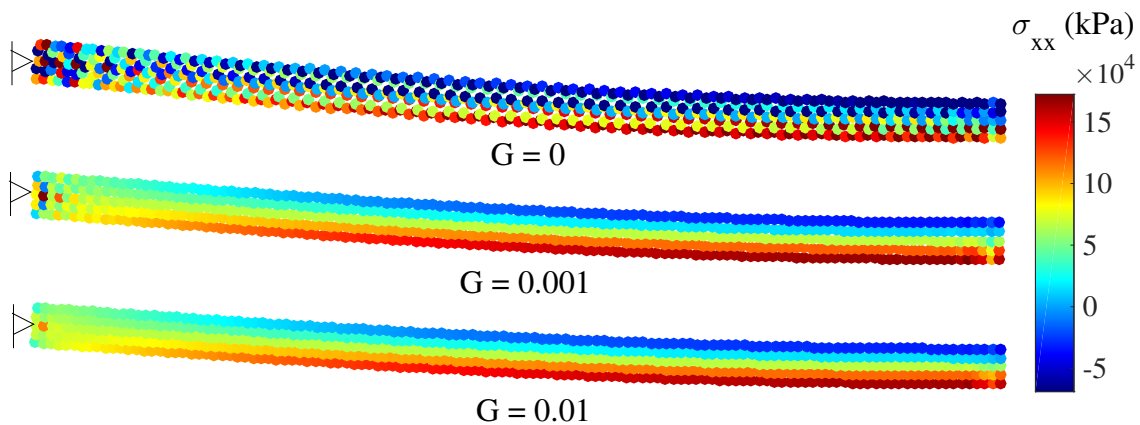


Figure 3: Simply-supported beam: stress contour, σ_{xx} , for $p = 276\text{kPa}$, $\delta = 2.015 \Delta x$, 5×125 particles with different values of G

a higher value of “optimum” stabilised parameter are needed. Therefore, G must be adjusted based on the horizon size for the optimum value of the stabilisation parameter.

Stress contours, σ_{xx} , corresponding to the external load for $p = 276\text{Pa}$, $\delta = 2.015\Delta x$ and 5×125 particles for the beam with different G value are shown in Figure 3. The plots show that non-ordinary state-based peridynamics has instabilities when $G = 0$, indicating the necessity of the zero-energy modes control. The absence of the zero-energy mode control results in significant oscillations in the stress field. The stabilisation method proposed in [3] effectively suppresses the zero-energy modes instabilities, with increasing values of G , resulting in a stabilised stress field.

Conclusions

This paper has investigate a non-ordinary state-based peridynamics method with a stabilised correspondence material model for large deformation. The proposed formulation has been demonstrated on a 2D simply-supported beam problem with large strains to validate the effectiveness of the method. One of the significant finding to emerge from this study is that NOSBN PD is capable of modelling large deformation problems, with a reasonable accuracy, provided that spurious energy modes are suppressed.

Acknowledgements

Nur A. Hashim gratefully acknowledges the financial support from Ministry of Education Malaysia and University of Malaysia Perlis.

Reference

- 1 Silling, S A and Askari, E. *A meshfree method based on the peridynamic model of solid mechanics*, Computers & Structures, 83, 17-18, 2005.
- 2 Silling, S A, Epton, M, Weckner, O, Xu, J and Askari, E. *Peridynamic States and Constitutive Modeling*, Journal of Elasticity, 2, 151-184, 2007.
- 3 Silling, S A. *Stability of peridynamic correspondence material models and their particle discretizations*, Computer Methods in Applied Mechanics and Engineering, 322, 42-57, 2017.
- 4 Yang, Z, Oterkus, E and Tien, C. *Implementation of peridynamic beam and plate formulations*, Continuum Mechanics and Thermodynamics, 31, 301-315, 1977.

Developing a Finite Element Model to Investigate Second Metatarsal Stress During Running

*M. Ellison¹, H. Rice¹, M. Akrami², A. Javadi²

¹Sport and Health Sciences, University of Exeter, Exeter, UK.

²College of Engineering, Mathematics and Physical Sciences, University of Exeter, Exeter, UK

* me351@exeter.ac.uk

Summary

Second metatarsal (2MT) stress fracture is a common and burdensome injury amongst runners, however understanding of the risk factors leading to injury is limited. Finite Element (FE) modelling represents a viable biorealistic alternative to invasive studies and simple beam theory models. This study shows the design and validation of a simple subject-specific FE model of the 2MT incorporating geometrically accurate soft tissue and loading. Results show a good comparison with both recent models and bone staple strain gauge data.

Key Words: *Biomechanics; Stress fracture; Finite element; Modelling*

Introduction

Running is an excellent method of training cardiovascular fitness, which has numerous well documented health benefits. Importantly, physical fitness is strongly linked with longevity [4, 13] with regular physical activity reducing the risks of coronary heart disease, cerebrovascular disease, hypertension, type II diabetes, various cancers, and osteoporosis [8]. A recent study has suggested that physical inactivity is responsible for 6% of coronary heart disease burden worldwide, 7% of diabetes, 10% each of colon and breast cancers [9]. It has been suggested that inactivity is responsible for 9% of premature mortality and another systematic study [11] suggests that vigorous exercise and sports shows the largest reduction in all-cause mortality with moderate activities of daily living being beneficial but to a lesser extent. Any sporting activity brings with it the risk of injury, with certain injuries associated with certain types of training. For long distance runners, there is a particularly high incidence of lower limb injuries, with one systematic review finding the incidence to range from 19.4% to 79.3% across the 17 studies it included [14]. Injury is detrimental as it diminishes the pleasure derived from exercise and limits participation, sometimes for an extended period of time or may cause a permanent withdrawal from the activity. An injury of particular burden amongst runners is stress fracture injury of the 2nd metatarsal (2MT) bone [2, 7, 10] which may take up to 12 weeks to heal resulting in reduced activity during that time. Current understanding of the factors that may predispose an athlete to this injury is limited particularly as direct measurement of the stress in the bone during running requires invasive procedures, such as the surgical implantation of a bone staple strain gauge [10], leading to altered biomechanics during gait and confounding study results. In contrast to direct measurement, mathematical modelling has been used to estimate forces acting on the metatarsals during running or walking in several studies [7, 12] but these require many assumptions regarding geometry and cannot account for interactions between tissue types. In contrast, the finite element (FE) method has been used more recently to investigate stress distributions in the metatarsals during running [5], however, biorealistic models often have prohibitively long development, construction and run times when investigating groups of participants [1] and many simplifications are needed to produce a model that can investigate groups of participants in a realistic timeframe. Therefore the purpose of this study was to develop and validate a FE model that allows estimation of the stresses acting on the 2MT during the ground contact phase of one running step. The model incorporates subject-specific geometry and soft tissue effects, whilst minimising the complexity and therefore computing cost.

Methods

Data were collected from eighteen (10 female) participants (age 24 ± 7.8 years; mass 64.8 ± 11.2 kg; height 1.68 ± 0.09 m). No participants reported any current injuries affecting their running regimen and no participants had sustained any lower limb injuries that prevented their normal training within the last year. Eligible participants were given information about the study and provided written informed consent. The study was given ethical approval by the Sport and Health Sciences Ethics Committee, University of Exeter.

To determine individual metatarsal geometry, magnetic resonance (MR) images were collected from each participant whilst lying supine within a 1.5 T superconducting whole body scanner (Gyrosan Intera, Philips, The Netherlands). The location of the second metatarsal and phalange was initially identified via palpation and a cod liver oil capsule placed on the foot at that location using micropore tape. The unloaded foot was then placed against a flat vertical barrier within a quadrature head coil to minimize

movement, and to ensure each data set was acquired with the foot in a similar position. Stacks of MR images covering the whole of the foot and centred around the second metatarsal, as identified in the images from the high intensity cod liver oil capsule, were then acquired in sagittal, coronal and axial planes. In all cases a T1 weighted (repetition time 20 ms, echo time 4.0 ms, flip angle 500) 3D gradient echo sequence was utilised with an in-plane resolution of 0.3 x 0.3 mm and a slice thickness of 0.7 mm. Depending on the imaging orientation, between 60 and 160 slices within a stack were required for full coverage.

The participant's height and mass were measured whilst participants wore their own running kit. Synchronised kinematic, kinetic and plantar pressure data were collected during running at a constant speed of 3.6 ms⁻¹ along a runway using four CX1 units (Coda CX1, Codamotion – Charnwood Dynamics Ltd., U.K.) with an integrated force plate (1000 Hz) (AMTI BP400600HF, Advanced Mechanical Technology Inc., U.S.A.). 19 active skin markers (200 Hz) were attached directly to the skin and used to mark strategic bony landmarks of the foot and shank, similar to the Oxford Foot Model [3].

A separate plantar pressure plate (RSscan 0.5 m Hi-End Footscan, RSscan – Beringen, Belgium) was placed over the force plate such that the pressure plate was entirely within the boundaries of the force plate. Pressure data were collected at 200 Hz using Footscan software (RSscan Footscan Gait v7, RSscan – Beringen, Belgium). Trials were completed barefoot. An opportunity to warm up was provided and familiarisation trials were completed until the participant was comfortable running at the desired speed on the runway surface (EVA foam). Feedback on the running speed was provided after each attempt. The experimental protocol consisted of running at a constant speed ensuring that the right foot contact was within the pressure plate boundaries. A trial was considered successful when the right foot contacted the pressure plate, speed was registered as 3.6 ms⁻¹ (±5%), markers showed good visibility during foot contact with the pressure plate and the investigator observed no unusual movement during footplate contact. Ten successful trials were recorded per participant.

Geometrically accurate 2MT and encapsulating soft tissue geometry were recreated from MR images using ScanIP software (Simpleware ScanIP, Synopsys, CA U.S.A.), separating cortical and trabecular tissues and segmenting only the soft tissue directly surrounding the 2MT. Ground reaction force data in both the vertical and anterior/posterior direction were scaled to represent the load under the 2MT using the mapped pressure data from the pressure plate. The angle between the 2MT head and the ground was calculated from the posterior and distal 2MT markers whilst the eversion angle of the foot was calculated using the markers at the first and fifth metatarsal heads.

The model was assembled in Abaqus software (Simulia Abaqus, Dassault Systemes, France). Literature values [1, 6] were used to assign material properties to parts as described in Table 1.

Part	Young's modulus (MPa)	Poisson's ratio
Cortical Bone	17000	0.3
Trabecular Bone	700	0.3
Encapsulating Soft Tissue	1.15	0.49
Ground Support	50000	0.1

Table 1: Material properties of model parts

The boundaries between tissue types were modelled as a fixed encapsulation, and the interface between the foot and the ground was modelled using contact elements with a coefficient of friction equal to 0.6 [1]. Loading was applied via a ground support structure under the soft tissue, using a total force load on the relevant faces. Final assembly can be seen in Figure 1.

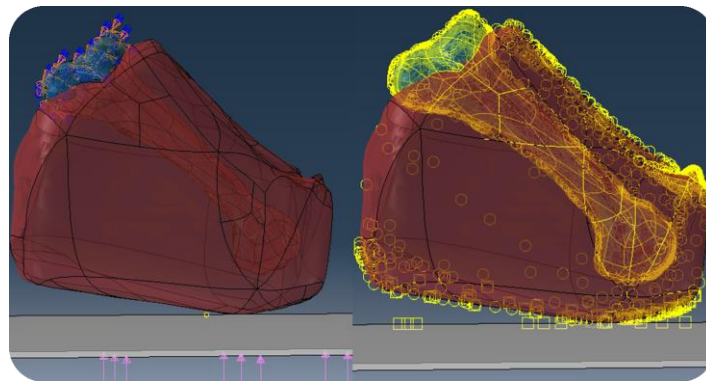


Figure 1: Wire model showing Left: boundary conditions (blue and orange arrows) and loading applied to ground support (pink arrows). Right: Soft tissue interactions (circles), floor interactions (squares)

A FE simulation was used to determine deformation of the tissues and corresponding stress patterns and magnitudes under the application of load. A mesh sensitivity analysis was conducted to ensure the stability of results and the model was validated by comparing peak contact stress between the foot and the ground to experimentally collected pressure data.

Results and Discussion

Initial sensitivity analysis results from one participant reveal the model to be sensitive to floor element number but that it does not increase computing cost more than a few minutes, therefore a relatively high number of floor elements can be used. The encapsulating soft tissues were sensitive to an increase in element number, but an increase from 33361 to 66512 elements did not change the stress seen in other parts of the model by more than 1%. However it did greatly increase computational time, therefore the lower number was chosen. The bone was found to be sensitive to changes in element number up to 10303 elements, at which point the change in stress seen was less than 1% and the computing time increased from 110 minutes to 27 hours. Peak floor pressure seen during the simulation was 0.4368 MPa compared to 0.4745 MPa seen experimentally, a difference of 8%. A maximum stress on the dorsal surface of the 2MT of 38.03 MPa (Figure 2) was seen, equivalent to 2237 $\mu\epsilon$, which compares well with both existing recent models showing median strain of 1937 $\mu\epsilon$ during overground running in minimalist shoes [5] and bone staple strain gauge data showing 1891 $\mu\epsilon$ during barefoot treadmill jogging [10]. Element sizes corresponding to this analysis were used for all other participants. Average results from all 18 participants at the time of peak ground reaction force show an average maximum stress of 29.39 MPa equivalent to 1728 $\mu\epsilon$, again comparing favourably to strain gauge experimentation.

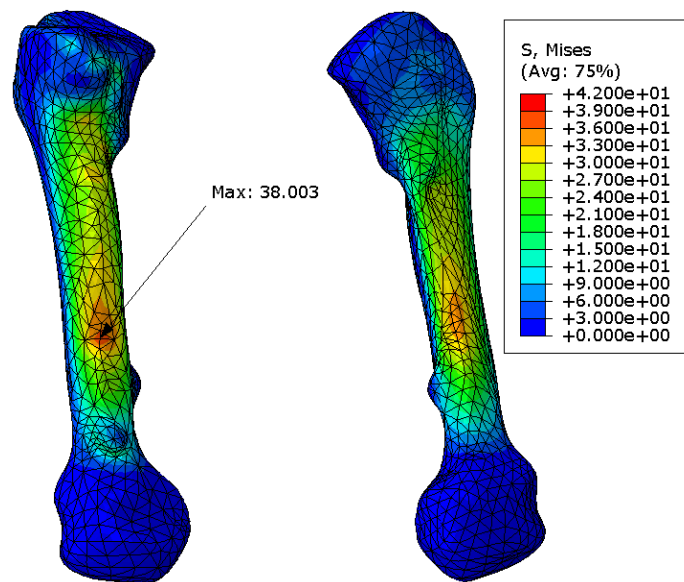


Figure 2: stress distribution (MPa) on the second metatarsal of a single participant at midstance showing maximum stress location on the dorsal surface (left) and stress distribution on the plantar surface (right).

Conclusions

A FE model of the 2MT and surrounding soft tissues has been developed and initial results show the model to be stable and providing a good match to both experimentally collected data and previous research using models and bone strain gauge experiments in vivo.

Acknowledgments

This work is part of a studentship that was funded by the Engineering and Physical Sciences Council (EPSRC) through the EPSRC Doctoral Training Partnership at the University of Exeter.

References

-
- [1] Akrami, M., Qian, Z., Zou, Z., Howard, D., Nester, C. J. & Ren, L. 2017. Subject-specific finite element modelling of the human foot complex during walking: sensitivity analysis of material properties, boundary and loading conditions. *Biomechanics and modeling in mechanobiology*, 1-18.
- [2] Bennell, K. L., Malcolm, S. A., Brukner, P. D., Green, R. M., Hopper, J. L., Wark, J. D. & Ebeling, P. R. 1998. A 12-month prospective study of the relationship between stress fractures and bone turnover in athletes. *Calcif Tissue Int*, 63, 80-5.
- [3] Carson, M. C., Harrington, M. E., Thompson, N., O'connor, J. J. & Theologis, T. N. 2001. Kinematic analysis of a multi-segment foot model for research and clinical applications: a repeatability analysis. *J Biomech*, 34, 1299-307.
- [4] Fields, K. B., Sykes, J. C., Walker, K. M. & Jackson, J. C. 2010. Prevention of Running Injuries. *Current Sports Medicine Reports*, 9, 176-182.
- [5] Firminger, C. R., Fung, A., Loundagin, L. L. & Edwards, W. B. 2017. Effects of footwear and stride length on metatarsal strains and failure in running. *Clinical Biomechanics*, 49, 8-15.
- [6] Garcia-Aznar, J. M., Bayod, J., Rosas, A., Larrainzar, R., Garcia-Bogalo, R., Doblare, M. & Llanos, L. F. 2009. Load transfer mechanism for different metatarsal geometries: a finite element study. *J Biomech Eng*, 131, 021011.
- [7] Gross, T. S. & Bunch, R. P. 1989. A mechanical model of metatarsal stress fracture during distance running. *Am J Sports Med*, 17, 669-74.
- [8] Lee, I. M., Paffenbarger, R. S. & Hennekens, C. H. 1997. Physical activity, physical fitness and longevity. *Aging Clinical and Experimental Research*, 9, 2-11.
- [9] Lee, I. M., Shiroma, E. J., Lobelo, F., Puska, P., Blair, S. N. & Katzmarzyk, P. T. 2012. Impact of Physical Inactivity on the World's Major Non-Communicable Diseases. *Lancet*, 380, 219-229.
- [10] Milgrom, C., Finestone, A., Sharkey, N., Hamel, A., Mandes, V., Burr, D., Arndt, A. & Ekenman, I. 2002. Metatarsal strains are sufficient to cause fatigue fracture during cyclic overloading. *Foot Ankle Int*, 23, 230-5.
- [11] Samitz, G., Egger, M. & Zwahlen, M. 2011. Domains of physical activity and all-cause mortality: systematic review and dose-response meta-analysis of cohort studies. *International Journal of Epidemiology*, 40, 1382-1400.
- [12] Stokes, I. A., Hutton, W. C. & Stott, J. R. 1979. Forces acting on the metatarsals during normal walking. *J Anat*, 129, 579-90.
- [13] Van Der Worp, M. P., Ten Haaf, D. S. M., Van Cingel, R., De Wijer, A., Nijhuis-Van Der Sanden, M. W. G. & Staal, J. B. 2015. Injuries in Runners; A Systematic Review on Risk Factors and Sex Differences. *PLOS ONE*, 10, e0114937.
- [14] Van Gent, R. N., Siem, D., Van Middelkoop, M., Van Os, A. G., Bierma-Zeinstra, S. M. A. & Koes, B. W. 2007. Incidence and determinants of lower extremity running injuries in long distance runners: a systematic review. *British Journal of Sports Medicine*, 41, 469-480.

ON THE USE OF SUB-STRUCTURING FOR THE FEA OF TALL SLENDER BUILDINGS

***Jovana Veletic and Roger Crouch**

School of Mathematics, Computer Science & Engineering, City, University of London

*jovana.veletic.1@city.ac.uk

Summary

This paper reports on several novel Finite Element (FE) structural analysis techniques to aid the efficient design of tall slender buildings. Detailed FE analyses of structures with over 100 floors can be computationally expensive, yet the hierarchical approach adopted here (and the mesh generator provided) offers significant time savings to the analyst.

Using an existing FE framework (based on the CALFEM `m-script` library [1]) we have introduced (i) a Master-Slave approach for 3D beam and truss elements; tying degrees of freedom (DoF) together to simulate the membrane action of the floors, (ii) MITC [3] shell elements to represent the reinforced concrete core walls and composite floors in regions where detail is necessary, (iii) a sub-structuring approach whereby only part of the building is modelled in detail, and the super-elements (sub-structures) condense-out internal DoF in the more remote zones, (iv) efficient matrix storage and solver schemes for the sparse system of equations and (v) a bespoke 3D mesh generator. This paper introduces the hierarchical *zoom-in* strategy whereby an engineer can rapidly analyse and design a local region of several (say 5) floors within the overall structure. This can reduce the size of the governing equations by an order of magnitude. Thus the method gives rise to valuable memory and computational run-time savings.

Introduction

There is a growing interest in constructing slender tall buildings in high-density urban environments. As the slenderness ratio (height to base-width) increases, so the challenges for a structural engineer increases. Consider a building with a slenderness ratio of 20:1 and $40m^2$ square floor plan. A frame comprising all structural components could result in a system with 160k+ DoF. This can reduce to just 6k when the sub-structuring approach (advocated here) is adopted.

Figure 1 illustrates the *zoom-in* strategy by which an engineer can examine different regions of the building in some detail while still capturing the response of the overall structure. 3D Euler-Bernoulli beam elements are used to model the spandrel perimeter and internal beams as well as the external columns (there are no internal columns in this example). The reinforced concrete elevator shafts (core walls) and the composite steel-concrete floors are modelled using MITC-4 quadrilateral shell elements. The compact Open Source FE code has been written in a way that encourages additional features to be incorporated relatively easily.

This paper reviews the use of Multi-Point Constraints which lead to a reduced system of equations. The paper refers to different idealisations (flexible, semi-rigid and rigid) which can be used to represent the membrane (diaphragm) action of the floor slabs. In the accompanying presentation, we illustrate the mesh-generator which has been developed specifically for these *pencil-like* buildings.

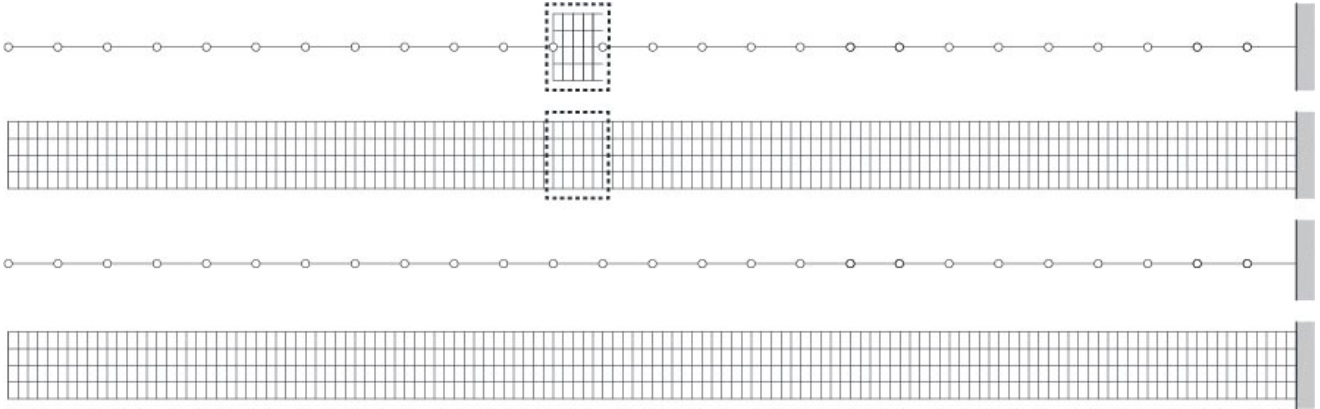


Figure 1: Rotated view of the side elevation of a slender periodic structure. The lower two images show the full structure and its beam representation while the upper two images illustrate the sub-structure approach.

A Master-Slave approach (Figure 2) enables nodes which share identical (in this case, horizontal) displacements to be eliminated from the analysis. This method can be used to simulate the various types of *diaphragm action* of the floors.

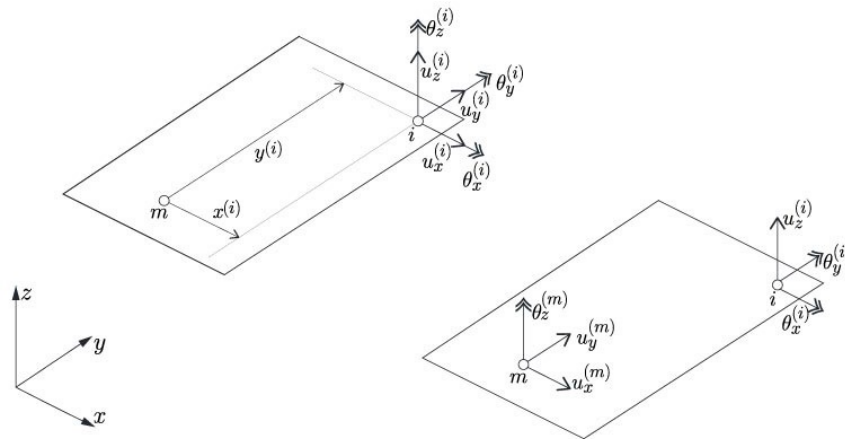


Figure 2: Master-Slave approach for the diaphragm action of a floor slab.

In this example, the following compatibility equations will be satisfied

$$\begin{aligned} u_x^{(i)} &= u_x^{(m)} - y^{(i)} u_{\theta_z} \\ u_y^{(i)} &= u_y^{(m)} - x^{(i)} u_{\theta_z} \end{aligned} \quad (1)$$

where $u_x^{(m)}$ and $u_y^{(m)}$ are the Master node in-plane displacements, and $u_x^{(i)}$ and $u_y^{(i)}$ are the Slave node in-plane displacements. The rotation $u_{\theta_z}^{(i)}$ may, or may not, be constrained depending on how the beams and columns are physically connected to the floor system [4].

In order to make use of the sub-structuring technique, the engineer first identifies a region where a detailed representation of the structural system is required. For example, a block of 5 floors could be chosen as the sub-structure. The elimination of internal nodes is undertaken hierarchically [5]. The

elimination process can be viewed as a transformation process, as described in the following section. The final stiffness matrix is further manipulated (prior to solving for the unknown displacements) so as to arrive at a form which takes account of the symmetric, banded, sparse nature of the system. This further reduces the solution time.

In order to implement both the Master-Slave method and the sub-structuring (elimination) technique, we make use of multi-point constraint (MPC) equations. These express the relationships between selected DoF. The next section outlines that approach, using matrix notation.

Example of using Multi-Point Constraint Equations

We adopt the following form of the MPC equations.

$$[A]\{d\} - \{g\} = \{0\} \quad (2)$$

The order of $[A]$ is $a \times b$ where a identifies the number of DoF that are constrained (that is, those which are tied to the *free*, or Master, DoF) whereas b identifies the total number of DoF in the system [2]. $\{d\}$ (which is equivalent to $\{u\}$ in Figure 2 above) represents the full vector of DoFs; which could be displacements and/or rotations. $\{g\}$ enables a non-zero constraint to be used. The latter is explained through the following examples. Consider an idealised 4-noded one-dimensional structure comprising three 2-noded bar Finite Elements (each node having just one DoF) as illustrated in Figure 3.

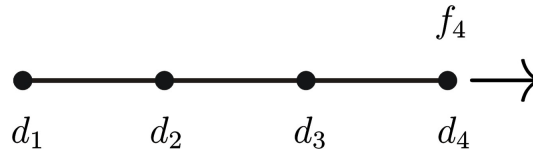


Figure 3: One dimensional bar with 3 Finite Elements.

If the left-most node were fixed (that is, $d_1 = 0$) and d_2 was constrained to equal d_3 , while d_4 had no constraint, then the following $[A]$ matrix and $\{g\}$ vector (on the left) would express the system. Whereas, if d_3 were constrained to be equal to $2d_2$ then the system would read as shown on the right

$$\begin{bmatrix} 1 & 0 & 0 & 0 \\ 0 & 1 & -1 & 0 \end{bmatrix} \begin{Bmatrix} d_1 \\ d_2 \\ d_3 \\ d_4 \end{Bmatrix} = \begin{Bmatrix} 0 \\ 0 \end{Bmatrix} \quad \begin{bmatrix} 1 & 0 & 0 & 0 \\ 0 & 2 & -1 & 0 \end{bmatrix} \begin{Bmatrix} d_1 \\ d_2 \\ d_3 \\ d_4 \end{Bmatrix} = \begin{Bmatrix} 0 \\ 0 \end{Bmatrix} \quad (3)$$

By way of a third example, if the constraint $d_2 + d_3 = 1$ were applied, then we would have

$$\begin{bmatrix} 1 & 0 & 0 & 0 \\ 0 & 1 & 1 & 0 \end{bmatrix} \begin{Bmatrix} d_1 \\ d_2 \\ d_3 \\ d_4 \end{Bmatrix} = \begin{Bmatrix} 0 \\ 1 \end{Bmatrix} \quad (4)$$

We partition (2) as follows

$$\begin{bmatrix} [A^m] & [A^i] \end{bmatrix} \begin{Bmatrix} \{d^m\} \\ \{d^i\} \end{Bmatrix} - \{g\} = \{0\} \quad (5)$$

where superscripts m and i again refer to the Master and Slave DoF respectively. Solving (5) for $\{d^i\}$, we obtain

$$\{d^i\} = -[A^i]^{-1}[A^m]\{d^m\} + [A^i]^{-1}\{g\} \quad (6)$$

We now write

$$\{d^m\} = [I]\{d^m\} + \{0\} \quad (7)$$

(where $[I]$ is the identity matrix) such that

$$\{d\} = \begin{Bmatrix} \{d^m\} \\ \{d^i\} \end{Bmatrix} = \begin{bmatrix} [I] \\ -[A^i]^{-1}[A^m] \end{bmatrix} \{d^m\} + \begin{Bmatrix} \{0\} \\ [A^i]^{-1}\{g\} \end{Bmatrix} \quad (8)$$

Making the substitutions

$$[T] = \begin{bmatrix} [I] \\ -[A^i]^{-1}[A^m] \end{bmatrix} \quad \text{and} \quad \{g^0\} = \begin{Bmatrix} \{0\} \\ [A^i]^{-1}\{g\} \end{Bmatrix} \quad (9)$$

yields

$$\{d\} = [T]\{d^m\} + \{g^0\} \quad (10)$$

so that

$$[K]\{d\} = \{f\} \rightarrow [K][T]\{d^m\} + [K]\{g^0\} = \{f\} \rightarrow [K][T]\{d^m\} = \{f\} - [K]\{g^0\} \quad (11)$$

Pre-multiplying both sides (of the final equation on the right) by $[T]^T$ gives

$$\underbrace{[T]^T[K][T]}_{[K]} \{d^m\} = \underbrace{[T]^T\{f\} - [T]^T[K]\{g^0\}}_{\{\hat{f}\}} \quad \text{or} \quad [\hat{K}]\{d^m\} = \{\hat{f}\} \quad (12)$$

Conclusions

In this brief paper it has only been possible to touch lightly on the techniques developed to enable an engineer to rapidly undertake a linear analysis of a slender tall building (for example, static drift under wind loading or modal dynamics). The Finite Element software can allow sub-structures specifically tailored for such buildings (for example, bundled tubes, outriggers or external trusses) to be incorporated into the model. The approach helps reveal optimal structural solutions when undertaking both preliminary and detailed designs of these elegant forms.

References

- [1] Austrell P E *et al.*, *CALFEM*, A Finite Element Toolbox, Version 3.4.
- [2] Ho, R J, Meguid, S and Sauve, R G, Novel Coupling Constraint Technique for Explicit Finite Element Analysis, *International Journal of Computational Methods*, 1(02), 309-328, 2004.
- [3] Ko, Y, Lee, P-S and Bathe, K-J, The MITC4+ Shell Element and its Performance, *Computers and Structures*, 169, 57-68, 2016.
- [4] Wilson E L, Three Dimensional Static and Dynamic Analysis of Structures, *Computers and Structures Inc.*, 2002.
- [5] Wilson E L, The Static Condensation Algorithm, *International Journal of Numerical Methods in Engineering*, (8), 198-203, 1978.

COMBINING COMPUTATIONAL MECHANICS AND MACHINE LEARNING TECHNIQUES TO CALCULATE FRACTIONAL FLOW RESERVE

Neeraj Kavan Chakshu¹, Jason Carson¹, Igor Sazonov¹, and Perumal Nithiarasu*¹

¹Biomedical Engineering Group, Zienkiewicz Centre for Computational Engineering, College of Engineering, Swansea University, Swansea SA2 8PP, UK

*Correspondence to Professor P. Nithiarasu, e-mail: P.Nithiarasu@swansea.ac.uk

Summary

In this work how machine learning can be combined with computational engineering to find solutions to real practical problems of clinical interest has been discussed. The potential uses of machine learning in the context of approximate solution to differential equations with the application to cardiovascular problems is discussed. The paper also discusses the use of synthetic data generated to use in the training of machine learning algorithms and parameter identification. The fractional flow reserve is used as an example to demonstrate the use of machine learning in computational bioengineering.

Key Words: *Fractional flow reserve; artificial intelligence; passive digital twin; blood flow; coronary arteries*

INTRODUCTION

Fractional flow reserve, a technique used to measure pressure difference across a coronary artery stenosis in coronary catheterization, is a decisive factor used by cardiologists to evaluate the risk of performing a percutaneous coronary intervention to treat an individual suffering from carotid artery stenosis. The conventional invasive method used to determine FFR involves insertion of a catheter, using a sheath and a guidewire, through the femoral or radial artery and guiding the wire with pressure sensor tip to the coronary arteries. Recent development of passive but non-invasive FFR measuring technique [1, 2, 4], using computational fluid dynamics, has given rise to a quick, low-cost approach for screening of patients. It has also provided a promising platform for artificial intelligence to be introduced and used as an alternative but robust tool to calculate FFR.

Passive digital twin is a concept of replicating a human digitally using obtained data, such as Computed tomography scans, and creation of an off-line model to study various aspects of the body. In the present study, discussions have been limited to replication of coronary circulation for measurement of FFR, the parameter of interest (see Fig1).

In this work, we propose a method to predict FFR value by coupling CT scan and a passive coronary digital twin model using machine learning. The method was developed primarily in three steps, 1) Development of a passive digital twin model of the cardiovascular system, capable of mimicking the coronary arterial system with geometrical and haemodynamic parameters close to that of the actual human subject, 2) Generation of a massive virtual database for FFR results, covering a wide range of various physiological and stenotic parameters, with the help of the digital twin model developed, 3) Training of a machine learning algorithm using the virtual database generated and then enhancing the prediction capability with transfer learning technique using the few actual patient FFR results.

Machine learning in fractional flow reserve

Machine learning is currently one of the most sought after technique in biomedical engineering because of its overwhelming capability to accurately predict values and categorize health conditions in problems where mathematical approximations cannot provide acceptable results. Given the wide prevalence of

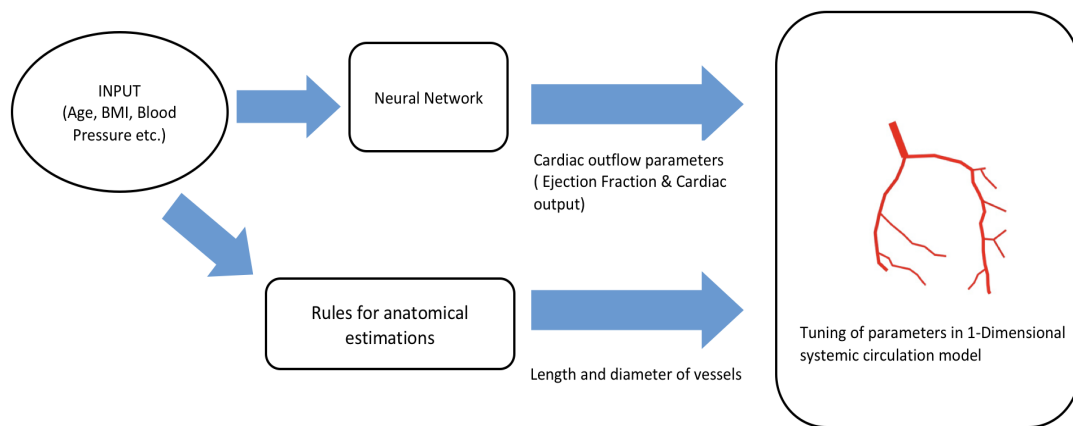


Figure 1: Passive digital twin of the coronary artery system

cardiovascular diseases and its link to 7.2 million deaths[5] in the world, an interest amongst academics and industry to use artificial intelligence in treatment can be anticipated. In the case of FFR, Itu *et al* [6] used machine learning to predict FFR values. A multilayered perceptron model, trained using a database of 12,000 virtual patients developed using a one dimensional haemodynamic model, was used in their work. A variation in anatomical parameters of the coronary arteries and the resulting haemodynamic parameters were used to train their machine learning model. The scope for using not just the anatomical parameters but also the cardiac parameters of the human subject, such as cardiac output, downstream resistance and ejection fraction, to increase the accuracy of prediction still exists. The work presented in this paper proposes a novel digital twin model that utilizes the power of machine learning to incorporate hemodynamic conditions arising not only because of the anatomy of coronary arteries but also cardiac condition of the subject.

METHODOLOGY

Passive Digital Twin

The passive digital twin proposed in this work primarily consists of two components, a one dimensional haemodynamic model and a machine learning (ML) model.

One dimensional haemodynamic model

The haemodynamic model adopted in this work, is a modified version of the model proposed by Mynard and Smolich [7]. In this work, only the coronary arterial system is of interest. The model considers major vessels in the systemic arteries as 1-D vessel segments. The inlet of the aorta is connected to a two chamber 0-D heart model, while the outlet of peripheral vessels connects to a three element Windkessel model, which accounts for the micro-circulation.

Blood flow in the 1-D vessel is governed by the non-linear set of equations, eq 1 and 2. An assumption of a flat velocity profile is used for the convective acceleration term, and a profile with boundary layer is chosen for the viscous friction term. A viscoelastic constitutive law is chosen for the walls, which consists of a power law model for the elastic term and a Voigt model for the viscous wall term (Eqs. 3, 4). The majority of vascular beds in this model are treated using three element Windkessel models, which are constructed using 1) lumped compliances on the arterial side, 2) characteristic impedances coupling any number of connecting 1-D arteries to the lumped parameter microvasculature, and 3) a constant vascular bed resistance to represent downstream resistance from the micro-circulation. These

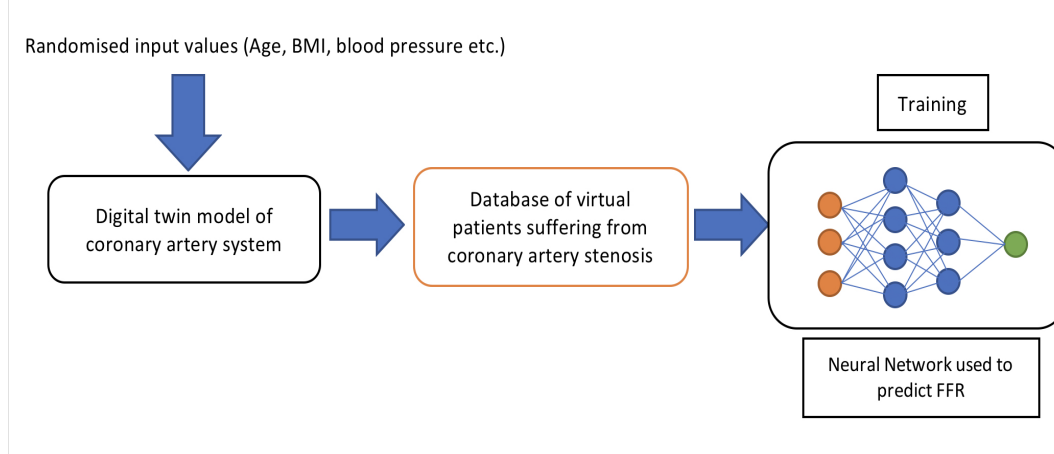


Figure 2: Method used in the present study to develop a neural network capable of predicting FFR

vascular beds have been incorporated in all microvasculature beds except the myocardium. For a detailed discussion of the vascular bed modelling of myocardium, see Mynard et al. [8].

A 0-D or lumped model of heart is used in this model. Lagrange multipliers have been used to connect 1-D vessels. The connectivity between 1-D and 0-D models is performed by sharing a pressure node. The system of equations are solved using the methodology in [3] are:

$$\frac{\partial A}{\partial P} \frac{\partial P}{\partial t} + \frac{\partial Q}{\partial x} = 0, \quad (1)$$

$$\frac{\rho}{A} \frac{\partial Q}{\partial t} + \frac{\rho}{A} \frac{\partial}{\partial x} \left(\frac{Q^2}{A} \right) + \frac{\partial P}{\partial x} = \frac{-22\mu\pi Q}{A^2}, \quad (2)$$

$$P - P_{ext} = \frac{2\rho c_0^2}{b} \left[\left(\frac{A}{A_0} \right)^{b/2} - 1 \right] + \frac{\Gamma}{A\sqrt{A}} \frac{\partial A}{\partial t} + P_0, \quad (3)$$

$$b = \frac{2\rho c_0^2}{P_0 - P_{collapse}}, \quad (4)$$

where Q is the flow rate, P is the total pressure, A is the arterial cross sectional area, t is the time, x is the coordinate axis, ρ is the density of blood, μ is the dynamic viscosity of the blood, c is the intrinsic wave speed and Γ is the viscoelastic parameter. The subscripts *ext*, 0 and *collapse* represent respectively external, stress free and collapse.

Machine learning for estimating cardiac outflow

A machine learning model is used to predict cardiac outflow parameters such as ejection fraction and cardiac output by using input parameters such as systolic and diastolic blood pressure, age, weight, height, pre-existing cardiac diseases and so on. The output from this ML model and other haemodynamic conditions is replicated in the above systemic circulation model by varying parameters such as elastance curve of the heart and resistances. Anatomy of the arteries used in the systemic circulation model is varied using relations obtained from literature to make the geometry used more patient oriented.

Virtual Database

Using the above developed passive digital twin model, a massive database of 20,000 virtual patients

was generated. The anatomical conditions, such as lengths and diameters of the coronary arteries and the aortic root, and cardiac conditions, varied using parameters such as age, weight, height and so on, were varied using random function. This led to the generation of a database having a large set of varying patient parameters.

Neural Network to predict FFR

A neural network, Multilayer Perceptron, comprising of 5 hidden layers was used to predict FFR value in a particular coronary artery. All hidden layers used 'Tanh' activation function, except for the final layer which used 'sigmoid' function. The input consisted of 45 parameters, such as cardiac output, vessel radius at the occlusion and location of occlusion (see Fig2). This network was able to predict results with levels of accuracy as high as 89%, when observed on synthetic data.

CONCLUSIONS

The proposed model has shown promising results in calculating FFR with high levels of accuracy. It now has the potential to be tested and re-calibrated in clinical environments. The levels of accuracy may come down by a marginal amount when used by clinicians, which will account for actual patient data, but a re-calibration of the machine learning model using transfer learning technique can enhance the accuracy.

REFERENCES

1. Boileau E., Nithiarasu P.. One-Dimensional Modelling of the Coronary Circulation. Application to Noninvasive Quantification of Fractional Flow Reserve (FFR). In: Tarves J.M.R.S, Jorge R.M.N., eds. *Computational and experimental biomedical sciences: Methods and Applications*, Springer 2013 (pp. 137-156).
2. Boileau Etienne, Pant Sanjay, Roobottom Carl, et al. Estimating the accuracy of a reduced-order model for the calculation of fractional flow reserve (FFR). *International Journal for Numerical Methods in Biomedical Engineering*. ;10.1002/cnm.2908:e2908.
3. Carson Jason, Van Loon Raoul. An implicit solver for 1D arterial network models. *International Journal for Numerical Methods in Biomedical Engineering*. 2017;33(e2837).
4. Carson Jason, Pant Sanjay, Roobottom Carl, et al. Non-invasive coronary CT angiography-derived fractional flow reserve: A benchmark study comparing the diagnostic performance of four different computational frameworks. *International Journal for Numerical Methods in Biomedical Engineering*. 2018;.
5. Mackay Judith, Mensah George, Mendis Shanthi, Greenlund Kurt. *The atlas of heart disease and stroke*. : WHO; 2004.
6. Itu Lucian, Rapaka Saikiran, Passerini Tiziano, et al. A machine-learning approach for computation of fractional flow reserve from coronary computed tomography. *Journal of Applied Physiology*. 2016;121(1):42-52. PMID: 27079692.
7. Mynard Jonathan P., Valen-Sendstad Kristian. A unified method for estimating pressure losses at vascular junctions. *International Journal for Numerical Methods in Biomedical Engineering*. 2015;31(DOI: 10.1002/cnm.2717).
8. Mynard J. P., Smolich J. J.. One-dimensional haemodynamic modeling and wave dynamics in the entire adult circulation. *Ann Biomed Eng*. 2015;43 (6)(DOI: 10.1007/s10439-015-1313-8):1443-60.

MIXED FORMULATION WITH STRESSES IN H-DIV SPACE FOR LARGE STRAINS

*Ł. Kaczmarczyk¹, Christophe-Alexandre Chalons-Mouriesse¹ and Chris J. Pearce¹¹Glasgow Computational Engineering Centre, School of Engineering, University of Glasgow

*lukasz.kaczmarczyk@glasgow.ac.uk

Summary

A mixed formulation for large strain-elasticity is presented. The paper extends previous developments for small strain [1,2]. In this contribution, we approximate stresses in H-div space, with displacements, stretches and rotations in L2 spaces. The implementation uses hierarchical approximation bases of arbitrary order. The work is supplemented with a solution scheme that exploits the sparsity of the tangent matrix by using a block Schur-complement solver. Two formulations are briefly described: (1) total Lagrangian and (2) updated Lagrangian formulation for mixed elements and show that solutions are equivalent. The paper will present numerical examples that demonstrate the accuracy of the implementation. The work was implemented in MoFEM (<http://mofem.eng.gla.ac.uk>) [3].

Key Words: *Mixed formulation; H-div; Large deformations; nearly incompressible; polyconvex*

Introduction

A family of mixed finite elements, with stresses approximated in h-div space, has been developed over the past few decades. The formulation of these elements promises optimal convergence for all the approximated variables, i.e. the error reduces at a rate equal to the order of the polynomial approximation field. Weakly enforced symmetry, i.e. where conservation of angular momentum and linear momentum is enforced in a strong integral sense is a particularly attractive feature. This family of elements is characterised by kinematic natural boundary conditions and static essential boundary conditions. Moreover, the displacement field is approximated in L2 space. However, these elements were only developed for linear elastic problems. Here we show a successful mixed element formulation for nearly incompressible materials subjected to large strains.

Furthermore, the lower regularity of the displacement field, i.e. derivatives are not needed and so displacements can be in L2 space (non-conforming elements) will enable us to have material displacements which are caused by plastic flow, thereby providing an opportunity to unify the theory for plasticity and configuration (Eshelbian) mechanics. However, this will form the basis of future work, which will build on the large strain framework described in this paper.

Element formulation*Kinematics*

The spatial gradient of deformation is decomposed as follows

$$h_{iJ} = (\Delta r_{i\alpha} \Delta u_{\alpha\beta}) h_{\beta J}^{\mathcal{I}} \quad (1)$$

where $\mathbf{h}^{\mathcal{I}}$ is the spatial gradient of deformation at the intermediate configuration, $\Delta \mathbf{u}$ is finite increment of the spatial stretch tensor and $\Delta \mathbf{r}$ is the increment of spatial rotation. An intermediate configuration is introduced for generality, that enables a total-Lagrangian formulation when $\mathbf{h}^{\mathcal{I}}$ is fixed, and an updated-Lagrangian when $\mathbf{h}^{\mathcal{I}}$ follows the deformation. In this paper for simplicity we use cartesian coordinate system. Indices in large latin letters $(\cdot)_{IJ}$ indicate tensor coefficients in the reference material configuration, small Latin letters $(\cdot)_{ij}$ indicate tensor coefficients in the current spatial configuration, and greek letters $(\cdot)_{\alpha\beta}$ indicate tensor coefficients in the intermediate configuration.

The stretch tensor $\Delta \mathbf{u}$ is symmetric, whereas the rotation $\Delta \mathbf{r}$ is orthonormal and can be expressed using an exponential map, as follows

$$\Delta \mathbf{r} = e^{\mathbf{A}} = \exp(\mathbf{A}), \quad \omega = \|\boldsymbol{\omega}\|, \quad \bar{\boldsymbol{\omega}} = \frac{\boldsymbol{\omega}}{\omega}, \quad \mathbf{A} = \boldsymbol{\varepsilon} \cdot \bar{\boldsymbol{\omega}} \quad (2)$$

where $\boldsymbol{\varepsilon}$ is the Levi-Civita tensor and $\boldsymbol{\omega}$ is a pseudovector representing the axis of rotation. In this formulation, the axis of rotation is approximated on the mesh.

Consistency

With the above decomposition at hand, starting with the consistency equation between the gradient of deformation and the gradient of displacement, we get

$$(\delta P_{i\beta}^{\mathcal{J}}, \Delta r_{i\alpha} \Delta u_{\alpha\beta} - \delta_{i\beta})_{\Omega_t^{\mathcal{J}}} - \left(\delta P_{i\beta}^{\mathcal{J}}, \frac{\partial \Delta w_i}{\partial y_\beta} \right)_{\Omega_t^{\mathcal{J}}} = 0 \quad (3)$$

where Δw_i displacements in the intermediate configuration and first Piola stress $P_{i\alpha}^{\mathcal{J}}$ in intermediate configuration is

$$P_{i\alpha}^{\mathcal{J}} = \frac{1}{J^{\mathcal{J}}} h_{\alpha J}^{\mathcal{J}} \delta P_{iJ}. \quad (4)$$

where P_{iJ} is stress in reference configuration and $J^{\mathcal{J}} = \det(\mathbf{h}^{\mathcal{J}})$, y_β are coordinates in intermediate configuration. Applying differentiation by parts to the first term in square brackets we get

$$(\delta P_{i\beta}^{\mathcal{J}}, \Delta r_{i\alpha} \Delta u_{\alpha\beta} - \delta_{i\beta})_{\Omega_t^{\mathcal{J}}} + (\delta P_{i\beta, \beta}^{\mathcal{J}}, \Delta w_i)_{\Omega_t^{\mathcal{J}}} - (n_\beta^{\mathcal{J}} \delta P_{i\beta}^{\mathcal{J}}, \Delta \bar{w}_i)_{\partial \Omega_t^{\mathcal{J}}} = 0 \quad (5)$$

Note that kinematic constraints are enforced in a weak sense, i.e. constraints on the displacement field are natural boundary conditions.

Physical equation

The physical equations are enforced in an integral, strong sense as follows

$$(\delta u_{\alpha\beta}, \Delta r_{i\alpha} P_{i\alpha}^{\mathcal{J}} - \frac{1}{J^{\mathcal{J}}} h_{\beta J}^{\mathcal{J}} \hat{P}_{\alpha J} (\Delta u_{\alpha\beta} h_{\beta J}^{\mathcal{J}}))_{\Omega_t^{\mathcal{J}}} = 0 \quad (6)$$

It should be noted that the above equation is tested (i.e. weighted) by the variation of the stretch tensor.

Angular momentum equation

The conservation of linear momentum is enforced (weakly) in the strong integral sense as follows

$$(\varepsilon_{ij\gamma} \delta \omega_\gamma, P_{i\alpha}^{\mathcal{J}} \Delta h_{j\alpha})_{\Omega_t^{\mathcal{J}}} = 0 \quad (7)$$

Linear momentum equation

Finally, the linear conservation equation is enforced as follow

$$(\delta w_i, P_{i\alpha, \alpha}^{\mathcal{J}} - b_i)_{\Omega_t^{\mathcal{J}}} = 0, \quad (8)$$

where b_i are coefficients of body force vector field.

Element equations

$$\left\{ \begin{array}{l} (\delta P_{i\beta}^{\mathcal{J}}, \Delta r_{i\alpha} \Delta u_{\alpha\beta} - \delta_{i\beta})_{\Omega_i^{\mathcal{J}}} + (\delta P_{i\beta,\beta}^{\mathcal{J}}, \Delta w_i)_{\Omega_i^{\mathcal{J}}} - (n_{\beta}^{\mathcal{J}} \delta P_{i\beta}^{\mathcal{J}}, \Delta \bar{w}_i)_{\partial\Omega_i^{\mathcal{J}}} = 0 \\ (\delta u_{\alpha\beta}, \Delta r_{i\alpha} (P_{i\alpha}^{\mathcal{J}} - \frac{1}{J_{\mathcal{J}}} h_{\beta J}^{\mathcal{J}} \hat{P}_{iJ}(\mathbf{h})))_{\Omega_i^{\mathcal{J}}} = 0 \\ (\varepsilon_{ij\gamma} \Delta h_{j\alpha} \delta \omega_{\gamma}, P_{i\alpha}^{\mathcal{J}})_{\Omega_i^{\mathcal{J}}} = 0 \\ (\delta w_i, P_{i\alpha,\alpha}^{\mathcal{J}})_{\Omega_i^{\mathcal{J}}} = 0. \end{array} \right. \quad (9)$$

Approximation Spaces

With the above equations at hand, the approximation spaces are chosen as follows

$$\left\{ \begin{array}{l} \delta \mathbf{P} \in \mathbf{V}_0^h(\mathcal{K}) \subset H_0^{\text{div}}(\mathcal{B}_0^h) := \{\delta \mathbf{P} \in H_0^{\text{div}}(\mathcal{B}_0^h) : N_j \delta P_{ij} = 0 \text{ on } \partial\mathcal{B}_0^{h,\sigma}\} \\ \tilde{\mathbf{P}} + \mathbf{P} \in \mathbf{V}^h(\mathcal{K}) \subset H^{\text{div}}(\mathcal{B}_0^h) := \{\tilde{\mathbf{P}} + \mathbf{P} \in H^{\text{div}}(\mathcal{B}_0^h) : N_j \delta P_{ij} = \bar{\mathbf{t}} \text{ on } \partial\mathcal{B}_0^{h,\sigma}\} \\ \mathbf{w}, \delta \mathbf{w} \in \mathcal{P}^{k-1}(\mathcal{K}) \subset L^2(\mathcal{B}_0^h) \\ \boldsymbol{\omega}, \delta \boldsymbol{\omega} \in \mathcal{P}^k(\mathcal{K}) \subset L^2(\mathcal{B}_0^h) \\ \mathbf{u}, \delta \mathbf{u} \in \mathbf{S}^h \subset \mathbf{S}^{k+1} := \{u_{ij} \in \mathcal{P}^{k+1}(\mathcal{K}) \subset L^2(\mathcal{B}_0^h) : u_{ij} = u_{ij}^T\} \end{array} \right. \quad (10)$$

where \mathcal{K} are non-overlapping tetrahedra covering \mathcal{B}_0^h , and $\mathcal{P}^k(\mathcal{K})$ is the space of polynomials of degree k . H^{div} indicates an H-div conforming space, i.e. vectorial approximation space for which the normal component on element faces is continuous. In this paper, finite element space for stress, after [1], is defined as follows

$$\mathbf{V}(\mathcal{K}) = \mathcal{P}^k(\mathcal{K}) + \text{curl}((\text{curl} \tilde{\mathbf{A}}^k(\mathcal{K})) \mathbf{b}_K) \quad (11)$$

where \mathbf{b}_K is "matrix bubble", and $\tilde{\mathbf{A}}^k(\mathcal{K})$ is an antisymmetric matrix of homogenous polynomials of degree k . This space can be considered as an extension of the Brezzi-Douglas-Marini element using a bubble in H-div space. Note that, as a consequence of the properties of the matrix bubble (see details in [1]), the space added to $\mathcal{P}^k(\mathcal{K})$ is a space of "normal bubbles", in the sense that they have zero normal stress components. Moreover, one can note that the divergence of the bubble in the volume is zero.

Linearised system of equations

Linearising the element equations (9), and applying finite element discretisation (10), the system of equations takes the form:

$$\begin{bmatrix} \mathbf{0} & \mathbf{0} & \overline{\mathbf{P}\mathbf{u}} & \overline{\mathbf{P}\boldsymbol{\omega}} & \overline{\mathbf{P}\mathbf{w}} \\ \mathbf{0} & \mathbf{0} & \overline{\mathbf{B}\mathbf{u}} & \overline{\mathbf{B}\boldsymbol{\omega}} & \mathbf{0} \\ \overline{\mathbf{u}\mathbf{P}} & \overline{\mathbf{u}\mathbf{B}} & \overline{\mathbf{u}\mathbf{u}} & \overline{\mathbf{u}\boldsymbol{\omega}} & \mathbf{0} \\ \overline{\boldsymbol{\omega}\mathbf{P}} & \overline{\boldsymbol{\omega}\mathbf{B}} & \overline{\boldsymbol{\omega}\mathbf{u}} & \overline{\boldsymbol{\omega}\boldsymbol{\omega}} & \mathbf{0} \\ \overline{\mathbf{w}\mathbf{P}} & \mathbf{0} & \mathbf{0} & \mathbf{0} & \mathbf{0} \end{bmatrix} \begin{Bmatrix} \delta \overline{\mathbf{P}} \\ \delta \overline{\mathbf{B}} \\ \delta \overline{\mathbf{u}} \\ \delta \overline{\boldsymbol{\omega}} \\ \delta \overline{\mathbf{w}} \end{Bmatrix} = \begin{Bmatrix} \overline{\mathbf{r}_P} \\ \overline{\mathbf{r}_B} \\ \overline{\mathbf{r}_u} \\ \overline{\mathbf{r}_\omega} \\ \overline{\mathbf{r}_w} \end{Bmatrix} \quad (12)$$

where $\delta \overline{\mathbf{P}}$, $\delta \overline{\mathbf{B}}$, $\delta \overline{\mathbf{u}}$, $\delta \overline{\boldsymbol{\omega}}$, $\delta \overline{\mathbf{w}}$ are degrees of freedom for, stresses, bubble of stresses, stretches, axis of rotations and displacements, respectively. To solve this system of equations, one can apply the process of hybridisation, i.e. introduce another displacement field on the skeleton and "break" the H-div space for stresses. This will lead to a Discontinuous Petrov-Galerkin (DPG) formulation. However, since MoFEM [3] has H-div spaces available, it is possible to use the Schur complement, to eliminate fields one by one, starting from stretches, and then bubbles, to solve the system of equations effectively.

Numerical example

In this section, after [4], we analyse Cook type cantilever problem, with a polyconvex, nearly incompressible Mooney-Rivlin material defined as

$$W_q(\mathbf{h}, \mathbf{h}, j) = \alpha_q (\mathbf{h} : \mathbf{h})^2 + \beta_q (\mathbf{y} : \mathbf{y})^2 + f_q(j) \quad (13)$$

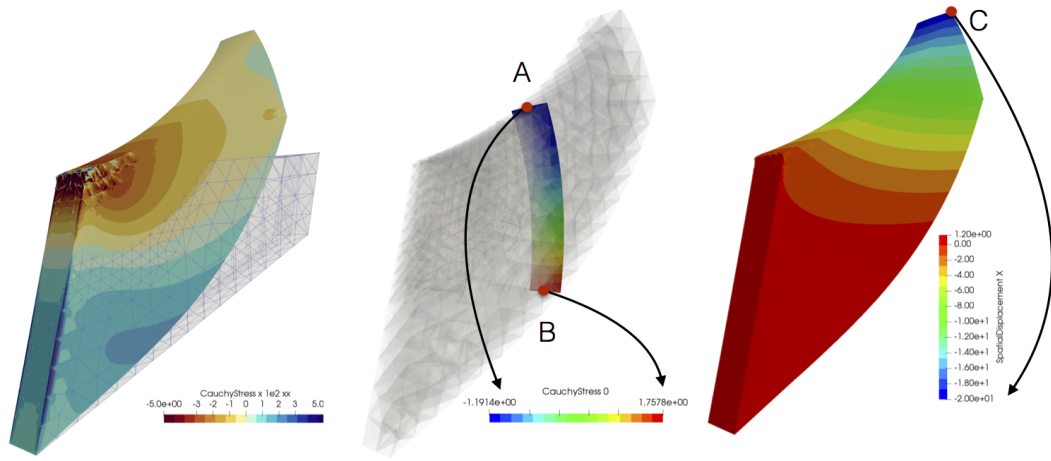


Figure 1: From the left; Cauchy stress σ_{xx} distribution, σ_{xx} on cut (to compare see [4]), displacement u_x (to compare see [4]).

where \mathbf{y} is cofactor $\mathbf{y} = \mathbf{J}\mathbf{h}^{-T}$, j is Jacobian of \mathbf{h} , and f is defined as follows

$$f_q(j) = -24\beta \ln(j) - 12\alpha \ln(j) + \frac{\lambda}{2\varepsilon^2}(j^\varepsilon + j^{-\varepsilon}) \quad (14)$$

Results are presented on figure 1. The model has 1,575,600 DOFs; stresses and rotations are approximated with 3rd order polynomials, and displacements 2nd order. The DOFs for stretches and bubble functions were solved using the Schur complement, one-by-one at element level.

The geometrical nonlinearities were linearised analytically, and the physical relation, as a function of stretches, is linearised using automatic differentiation with ADOL-C, starting from the strain energy function.

Conclusions

The proposed finite element formulation has excellent potential. It enables separation of nonlinearities that allows for robust solution schemes, good quality solution of stresses, and overall low-regularity. This will enable the unification of configurational mechanics and plasticity in the future.

References

- 1 Gopalakrishnan, Jayadeep, and Johnny Guzmán. "A second elasticity element using the matrix bubble." *IMA Journal of Numerical Analysis* 32.1 (2012): 352-372.
- 2 Arnold, Douglas, Richard Falk, and Ragnar Winther. "Mixed finite element methods for linear elasticity with weakly imposed symmetry." *Mathematics of Computation* 76.260 (2007): 1699-1723.
- 3 Kaczmarczyk, Lukasz, Ullah, Zahur, Lewandowski, Karol, Meng, Xuan, Zhou, Xiao-Yi, Pearce, Chris, Miur, Euan. (2018, November 18). MoFEM-v0.8.16. <http://doi.org/10.5281/zenodo.1490890>
- 4 Bonet, Javier, Antonio J. Gil, and Rogelio Ortigosa. "A computational framework for polyconvex large strain elasticity." *Computer Methods in Applied Mechanics and Engineering* 283 (2015): 1061-1094.

SOME EFFECTS OF PARTICLE SHAPE ON THE MECHANICAL BEHAVIOUR OF GRANULAR MATERIALS

John Harkness¹ and *Antonis Zervos¹

¹Department of Civil, Maritime and Environmental Engineering, University of Southampton, SO17 1BJ, U.K.

*az@soton.ac.uk

Summary

The behaviour of a granular material depends on the shape, material properties and packing of the grains. Starting with a particle characterization, the ability to make predictions of the macroscopic behaviour of an assembly of particles without recourse to laboratory or numerical experiments would be very useful. With this ultimate goal in mind, this work presents some first findings of an investigation into the effects on macroscopic behaviour of two key measures of particle shape: form and angularity. The form of a particle is quantified using the Longest (L), Intermediate (I) and Shortest (S) dimensions of an equivalent scalene ellipsoid; A sum of the local volumetric deviations of the particle from that ellipsoid as a ratio of the ellipsoid volume is used as a measure of angularity. Discrete element, periodic cell simulations of ellipsoidal and realistic particle shapes sampled from railway ballast are used to investigate mechanical behaviour in terms of critical state friction angle. Characterization of the observed behaviour in terms of a single shape parameter is explored. It is found that deviation of particle form from that of a sphere together with increases in angularity both lead to higher angles of friction at critical state. It is argued that, at least to some extent, the higher critical state strength exhibited by non-spherical particles is due to their form and/or angularity suppressing particle rotation and leading to increased interparticle sliding, a mechanism that in comparison expends more energy.

Key Words: *granular materials; railway ballast; DEM analysis; particle shape*

Introduction

Particle shape is a fundamental property of a granular material. It is quantified by considering three different aspects of shape, which generally correspond to different scales of observation and are assumed independent: particle *form*, *angularity* and *roughness*. Form quantifies the overall shape, angularity is usually considered to describe the number and sharpness of angles on the particle's surface, and roughness relates to the microscopic variations of the particle surface that are to some extent responsible for interparticle friction. Form in particular is generally quantified using the longest (L), intermediate (I) and shortest (S) dimensions of the particle along orthogonal axes. Whilst different measures of form have been proposed, no consensus exists on whether one has an advantage over the others [2]. Following the idea first presented in [3], we describe form on the basis of an equivalent scalene ellipsoid, here considered to be the ellipsoid that best fits, in the least squares sense, the shape of the particle. Its axes are taken to represent the dimensions S , I and L . We adopt the framework of [6, 7, 8], where particle form is uniquely defined by two parameters: *platyness* $\alpha = 2(I - S)/(L + I + S)$ and *elongation* $\zeta = (L - I)/(L + I + S)$, with $0 \leq \alpha \leq 1$ and $0 \leq \zeta \leq 1$. All possible ellipsoids plot in $\alpha - \zeta$ space within the triangle of Figure 1. In a further departure from customary practice, we define as *angularity* the sum of the local volumetric deviations of the particle's shape from its equivalent scalene ellipsoid, divided by the ellipsoid's volume [5].

To investigate the effect of these three measures, we perform DEM simulations of triaxial compression (employing periodic boundaries) on granular assemblies representative of ballast particles. We use the method of potential particles [4], which allows modelling of (almost) arbitrary shapes.

Method

Models were created, each using particles of a single form and angularity. The particle size distribution

(PSD) was representative of railway ballast; to determine the PSD, 5 different sizes between the maximum and minimum gradation curves for railway ballast as defined in [1] were created for each model, keeping I equal to the respective sieve size. The total volume contained within each model was kept as close to $0.2m^3$ as possible, although obtaining a meaningful number of particles meant larger volumes were needed for the very elongated particles. The number of particles contained within each model varied with particle shape, however this is also the case with specimens of fixed dimensions used in physical tests. To create a model, a number of particles were randomly dispersed within 3D space to a target initial void ratio of 2.0. The particles themselves were given random orientation to remove any bias in the initial conditions. The model was then subjected to isotropic compression using zero gravity and zero inter-particle friction. Once a void ratio of 0.65 were reached, isotropic stress of $100kPa$ was applied to the boundaries and the model was allowed to reach equilibrium. At that point inter-particle friction was reintroduced and the model was subjected to triaxial loading, where the lateral boundaries were stress controlled at $100kPa$. The top boundary moved downwards at a constant axial strain rate. Table 1 shows the different model parameters that were used.

Properties	Value
Particle Density	$2700Kg/m^3$
Interparticle Friction Angle	30 degrees
Particle Young's Modulus	40 GPa
Particle Poisson's Ratio	0.3

Table 1: Material Properties

Two sets of simulations were carried out: the first with a wide range of forms using ellipsoidal particles (zero angularity); the second with constant form, but varying angularity. For the latter set, four particles, spanning the range of forms for a measured railway ballast, were selected and, for each, a range of new numerical particles was then created, interpolating between the scanned particle and its equivalent scalene ellipsoid. The new particles were modelled using overlapping clumps of between 100 and 1000 spheres.

Results

Figure 2 presents a plot of friction angle at critical state ϕ'_{crit} as a function of particle platyness and angularity. Each point represents the result of a model consisting of ellipsoids with the corresponding form. The results can be fitted reasonably accurately by a plane, which is also plotted, showing that ϕ'_{crit} varies linearly with α and ζ . Evidently ϕ'_{crit} depends on a single parameter, corresponding to the distance along the direction of the maximum gradient of this plane. This parameter is equal to $F' = (1.0166 \cdot L - 0.0333 \cdot I - 0.9834 \cdot S)/(L + I + S)$ or, acknowledging that the contribution of I is very small compared to the contributions of L and S , which are practically equal:

$$F = \frac{L - S}{L + I + S} \quad (1)$$

We call the parameter defined by Equation 1 the *effective form* of a particle, in the sense that it suffices to predict (at least for ellipsoidal particles) the strength of the aggregate. Figure 2 shows a plot of ϕ'_{crit} vs F , along with the linear best fit and the 95% confidence intervals, demonstrating a tight correlation. Figure 3 shows the friction angle at critical state plotted against the angularity and the effective form, F , for the clumped-sphere particles together with the ellipsoid data from Figure 2. Once again, a plane can be fitted reasonably well to the data and a further parameter can be defined as $F_a = F + 1.21 \times \text{angularity} \approx F + (6/5) \times \text{angularity}$, corresponding to the distance along the maximum gradient of the plane. Figure 3 shows a plot of ϕ'_{crit} vs the angularity-augmented effective form,

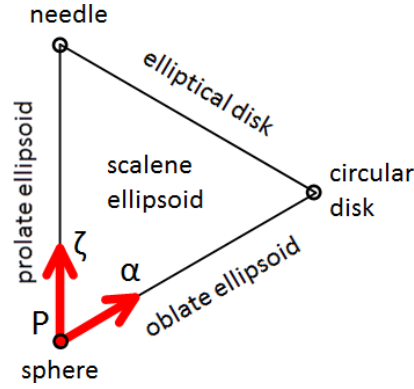


Figure 1: The platyness $\alpha = 2(I - S)/(L + I + S)$ vs. elongation $\zeta = (L - I)/(L + I + S)$ space, with a description of the corresponding forms.

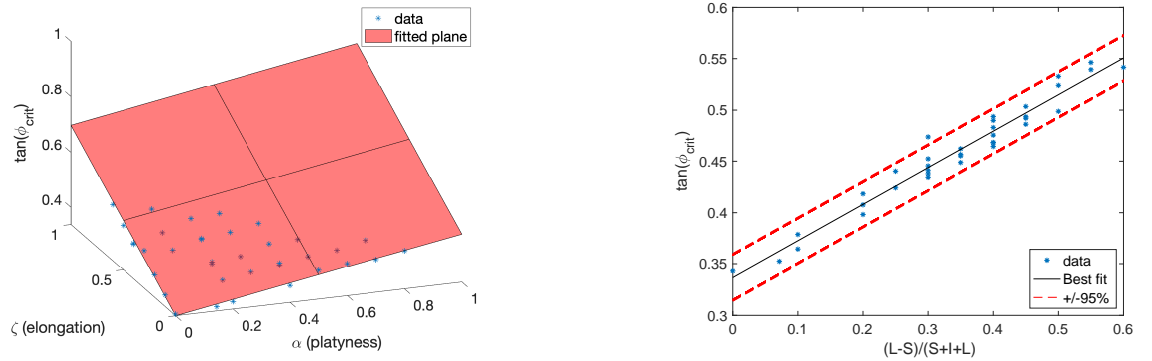


Figure 2: Friction angle at critical state for ellipsoidal particles, as a function of: particle platyness α and elongation ζ (left); effective form F (right).

F_a , along with the linear best fit and the 95% confidence intervals, demonstrating a similarly tight correlation between strength and F_a .

As already shown in [6, 7, 8] for some of the models also presented here, the higher ϕ'_{crit} exhibited by non-spherical and/or angular particles is due to their form and/or angularity suppressing particle rotation and leading to increased interparticle sliding, a mechanism that in comparison expends more energy. Although the relevant micro-mechanical analyses are pending for the angular particles used here, it is expected that the same mechanism is responsible for the observed behaviour.

Conclusions

Discrete element simulations were used to investigate the dependence of the friction angle at critical state, ϕ_{crit} , on the form and angularity of particles. Simulations with ellipsoids showed a very strong correlation between ϕ_{crit} and a single parameter of effective form, approximated by $(L - I)/(S + I + L)$ (in which S, I and L are the shortest, intermediate and longest dimensions of the ellipsoid). A second set of simulations added increasing angularity to particles of constant form (modelled with clumps of overlapping spheres). The results demonstrated a reasonably linear dependence of ϕ_{crit} with both angularity and effective form, enabling the definition of a single augmented-form parameter, with a strong correlation to ϕ_{crit} .

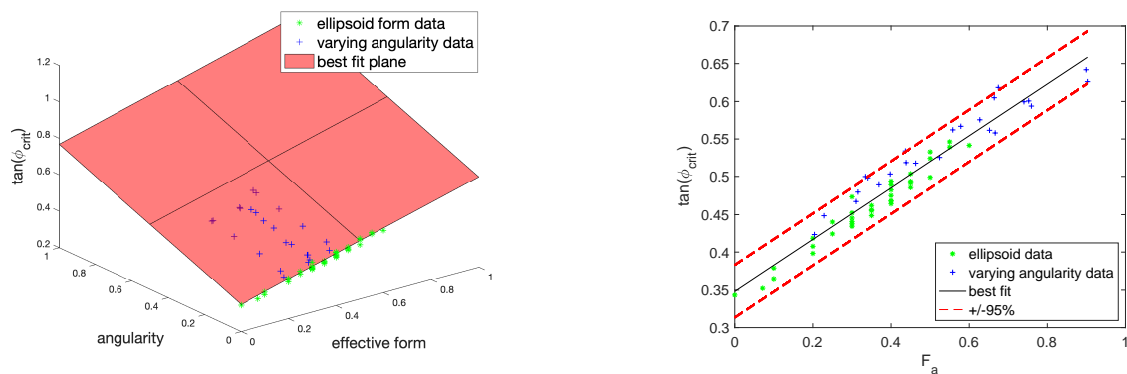


Figure 3: Friction angle at critical state for both sets of particles, as a function of: angularity and effective form (left); angularity-augmented effective form F_a (right).

Acknowledgements

We gratefully acknowledge support from Network Rail through its Strategic Partnership with the University of Southampton, and from the E.P.S.R.C. Track21 (EP/H044949/1) and Track2Future (EP/M025276/1) Programme Grants. Use of the IRIDIS High Performance Computing Facility and associated support services at Southampton are also acknowledged. Some of the models using ellipsoidal particles presented here were developed by M. Potticary and were first presented in [5, 6, 7, 8].

References

- [1] *BSI Standards Publication Aggregates for railway ballast BS EN 13450:2013* BSI. BSI Standards Limited 2013, 2013.
- [2] S.J. Blott and K. Pye. Particle shape: a review and new methods of characterization and classification. *Sedimentology*, pages 31–63, September 2007.
- [3] C.R.I. Clayton, C.O.R. Abbireddy, and R. Schiebel. A method of estimating the form of coarse particulates. *Géotechnique*, 59(6):493–501, 2009.
- [4] J Harkness. Potential particles for the modelling of interlocking media in three dimensions. *International Journal for Numerical Methods in Engineering*, 80:1573–1594 (June):1573–1594, 2009.
- [5] M. Potticary. *A Numerical Investigation of the Effect of Particle Shape on the Strength of Coarse Granular Materials*. PhD Thesis, University of Southampton, 2018.
- [6] M. Potticary, A. Zervos, and J. Harkness. A numerical investigation into the effect of particle form on the strength of granular materials. In A. Javadi and M. S. Hussain, editors, *Proceedings of the 22nd UK National Conference of the Association for Computational Mechanics in Engineering*, pages 61–64, 2014.
- [7] M. Potticary, A. Zervos, and J. Harkness. An investigation into the effect of particle platyness on the strength of granular materials using the discrete element method. In E. Oñate, M. Bischoff, D.R.J. Owen, and Wriggers P., editors, *IV International Conference on Particle-based Methods. Fundamentals and Applications (PARTICLES 2015)*, 2015.
- [8] M. Potticary, A. Zervos, and J. Harkness. The effect of particle elongation on the strength of granular materials. In *Proceedings of the 24th UK National Conference of the Association for Computational Mechanics in Engineering*, pages 239–242, 2016.

ESTABLISHMENT AND APPLICATION OF THE QUANTIFIED RELATIONSHIP BETWEEN CONCRETE PROPERTIES AND WORKABILITY TESTS

Sizeng YOU¹, Ashutosh Bhokare¹ and *Chenfeng Li¹

¹ College of Engineering, Swansea University, SA2 8PP

*Corresponding author: c.f.li@swansea.ac.uk

Summary

Self-compacting concrete, known as SCC, has been continuously growing since its invention. Due to its massive production and wide application, a more accurate and quantified understanding on SCC rheology is highly required. It's known that flow behavior of fresh concrete can be described by Bingham Model. But, a reliable way to obtain relative parameters (yield stress and viscosity) is still absent, despite of the various proposed solutions. As a result, the industry chooses to rely on the indicative measures of some robust workability tests.

Based on this knowledge, a systematic study was carried on by numerical simulation to investigate the relationship between SCC rheology and workability test performance. The former covers the commonly used concrete, where yield stress varies from 10 to 500 Pa and the plastic viscosity from 10 to 100 Pa·s. The latter tests includes slump flow test and modified-cone outflow test. This study confirms that the workability tests of fresh concrete are monotonically related to the rheological properties of concrete. In addition, an easy-to-use chart is established to accurately quantify concrete rheology from workability tests.

At last, as an example to apply this chart, construction process of a 6-meter high diaphragm wall is simulated, where the rheological parameters of placed concrete are determined according to workability test results by referring this chart. To shown construction process, 9 representative parameter combination are chosen, and the simulation result shows the distribution of those different concretes.

Key Words: *SCC; concrete flow; workability test; numerical modeling; Bingham fluid; computational fluid dynamics*

1. Background

Self-compacting concrete (SCC), invented in Japan during 1980s, has the ability to flow freely under its own weight. So it's usually applied in the situations where external compaction is not available. Nowadays, the increasing importance of this type concrete has been demanding deeper understanding on its flow behavior to serve for variety of complicated practices. It's already accepted that the flow performance of fresh SCC can be captured by Bingham model (Figure 1), which contains two parameters yield stress (τ_0) and viscosity (μ). In the past decades, researchers have proposed various solutions to measure these two values.

Rheometers such as BML viscometer^[1] and ICAR^[2] are equipments invented to measure τ_0 and μ of SCC directly. But their disadvantage is that readings from different rheometers vary greatly^[3]. Besides, for practical usage, rheometer is expensive and hard to perform on site. Because of that, various empirical, theoretical or numerical solutions were developed to measure τ_0 and μ . Kokado^[4], Roussel^[5] and Bouvet^[6] proposed different equations to quantify the relation between τ_0 and spread diameter of slump flow test, while introducing different factors respectively. Roussel and Le Roy^[7] also established another equation to link discharge time of Marsh cone with τ_0 , μ and cone shape. There are also some researchers^[8] treating the concrete as a homogeneous particle-fluid suspension, and proposed several formulas to predict viscosity according to concrete components. At last, numerical simulations^[6,9,10] of different workability tests also have been performed in various ways to match the real test and propose the suitable rheological parameters. Despite the various research works summarized above, no general agreement has been reached on how to determine μ and τ_0 for fresh concrete. The analytical approaches are based on various assumptions and simplifications, limiting their applicability to specific conditions. Moreover, the analytic predictions provide only rough approximations to the concrete rheology, and not suitable for accurate quantification. There have been some interesting numerical works, but

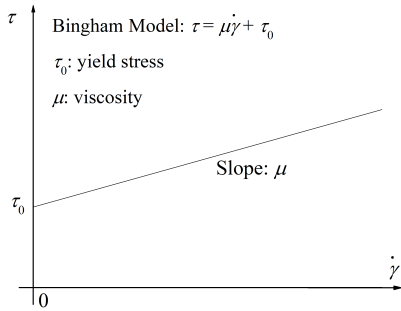


Figure 1: Concept of Bingham Model

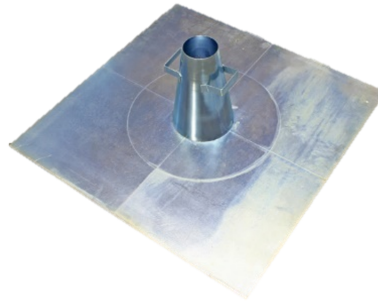


Figure 2: Apparatus of Slump Flow Test



Figure 3: Apparatus of Modified-cone Outflow Test

they are mainly feasibility studies focusing on modeling methodology instead of the quantification of concrete rheology.

2. Methodology

In view of above knowledge, this study systematically investigated in a quantified manner the relationship between rheological properties of fresh SCC and their performance in workability tests including slump flow tests and modified-cone outflow test (Figure 2 and 3). The modified-cone outflow test is a newly introduced equipment trying to replace V-funnel test as it's not adequate for high yield stress concrete. This investigation involves a series of numerical simulation on both tests, and the methodology can be concluded into 4 steps

The first step is numerical modeling. Balancing between effectiveness and accuracy of current CFD solutions, FVM approach is adopted. In addition, the volume of fluid (VOF) model is chosen for multiphase flow. Before starting the massive simulation, resolution requirement and suitable mesh size should be carefully calibrated. The accuracy for slump flow test simulation is determined to 1 cm, while for the other it's 0.1 s, which are both in accordance with workability test specifications. What's more, to minimize the influence of mesh size on simulation, mesh convergence check should be performed for each test to find the best structured mesh. When above requirements are all satisfied, the models are ready for simulation.

The second step is massive simulation. To cover all the commonly used concrete, 11 levels of yield stress and 10 levels of viscosity are chosen for each test simulation, which counts 220 cases in total. The former values include 10, 50, 100, 150, 300, 350, 400, 450, 500 Pa, and the latter includes 10, 20, 30, 40, 50, 60, 70, 80, 90, 100 Pa-s. To record the whole flow process, data of every time step is recorded.

The third step is data processing. Simulation result from second step could provide various indices, but only the simplest one of either test is extracted for analysis, which are spread diameter (D) for slump flow test, discharge time (t'_n) for modified-cone outflow test. As there are only 2 parameters in Bingham model, theoretically, results given by two different tests should be enough to determine SCC properties. Therefore, an easy-to-use graph could be generated to quantify this corresponding relationship.

The fourth step is to simulate a diaphragm wall as an example to apply the graph proposed in third step. Knowing testing result of slump flow test and modified-cone outflow test, the rheological properties of SCC can be obtained by referring to the graph. Then, choose 9 representative combination of (τ_0 , μ) to simulate the variation of commonly used SCC, and place them into the diaphragm wall at different simulation time. The simulation will output the final distribution of all these concretes.

3. Result

The influence of yield stress and viscosity on 2 workability tests are plotted in Figure 4 to 7. It shows, for slump flow test, D is mostly determined by τ_0 , but when τ_0 is small, μ also cannot be neglected. For modified-cone outflow test, both τ_0 and μ have significant influence on t'_n . Now, considering that, for both workability tests,

they share the same set of parameter input (τ_0, μ), and output a corresponding set of (D, t'_n). Based on this idea, Figure 8 can be plotted. In it, there are two groups of curves on which the cases share either the same τ_0 or μ ("YS" means yield stress, "VIS" means viscosity). Referring to this graph, rheology properties of certain SCC can be easily obtained once their workability tests were done.

According to the testing result of commonly used SCC, 9 pairs of representative values are chosen for (τ_0, μ). Referring Figure 8, the corresponding rheological properties are decided. Then, the construction process of a 6-meter high diaphragm wall (geometry in Figure 9) is simulated. Its dimension is 6.2 m×1m×6 m, and the rebar diameter in rebar cage is 30 mm. The concrete is placed through its two tremies, which are modeled in square shape to reduce meshing work. The final distribution of 9 type SCC in the cross sections of left half diaphragm wall is shown in Fig. 10. The number on top of each section is the distance from this position to the left surface, and different color means different type of SCC.

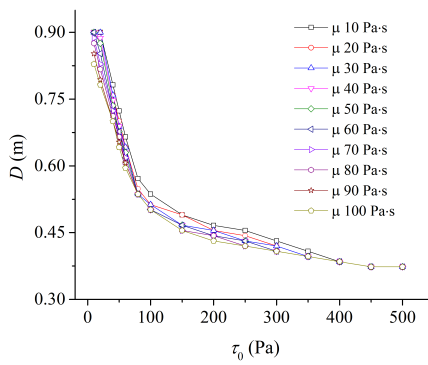


Figure 4: Impact of μ respecting to D

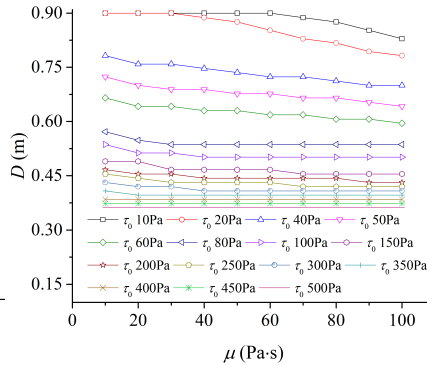


Figure 5: Impact of τ_0 respecting to D

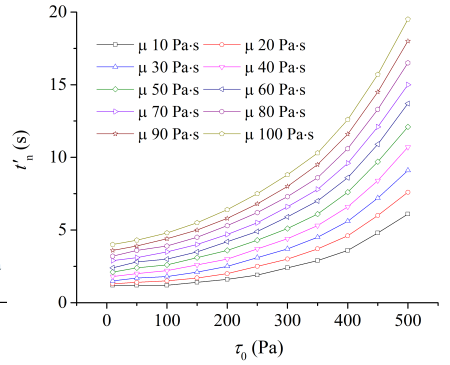


Figure 6: Impact of τ_0 respecting to t'_n

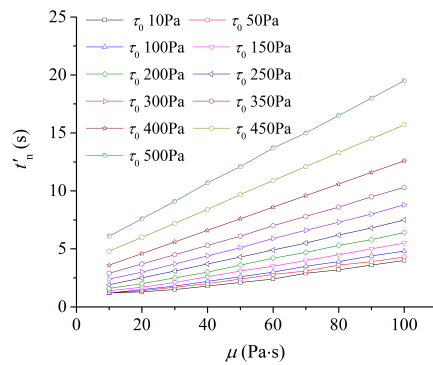


Figure 7: Impact of μ respecting to t'_n

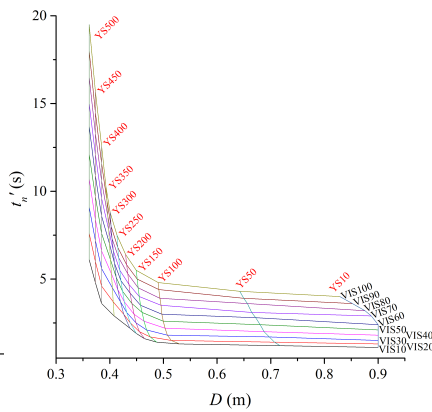


Figure 8: Relationship between (D, t'_n) and (τ_0, μ)

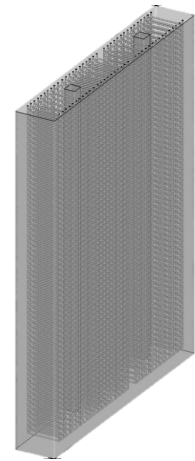


Figure 9: Geometry of Diaphragm Wall

3. Conclusions

The key aim of this study is to quantify the relationship between the flow behaviour of SCC and its rheological properties. Comparing with previous work, method of this study has the following advantages. Comparing with solution by experiments, the unpredictable variation of concrete mixture can be avoided by numerical method; comparing with theoretical solution based on different kinds of assumptions, this method is more realistic; comparing with previous various numerical work, this study gives a systematic and practical result.

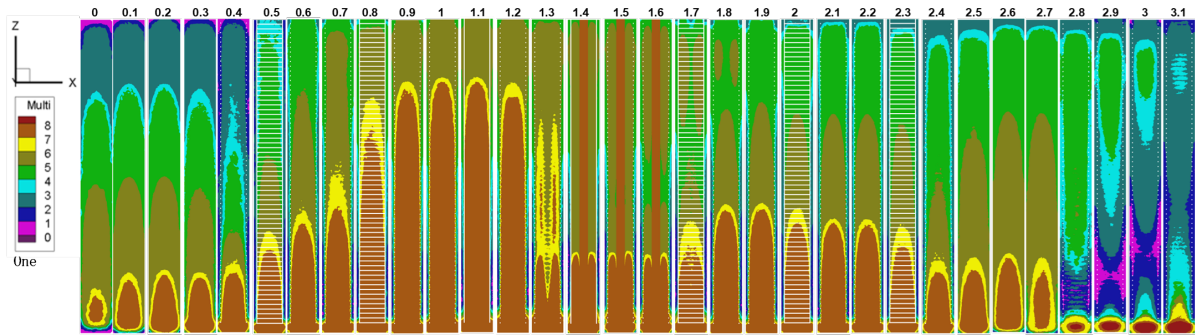


Figure 10: Distribution of 9 types of SCC in Cross Sections of left-half Diaphragm Wall

The following are main conclusions of our study. (1) For both tests, the influence of yield stress in nonlinear, while the viscosity is linear. (2) In space formed by orthogonal D and t'_n , two groups of curves can be plotted, and they form a closed net. They represent the test performance of concrete with constant yield stress or viscosity respectively. This figure can be used to determine concrete properties based on test result of slump flow test and modified-cone outflow test. (3) The proposed figure can be used to determine concrete properties which can be used to simulate the pile simulation.

References

- 1 Tattersall, G. Howarth. Workability and quality control of concrete. *CRC Press*, 2014
- 2 E. P. Koehler and D. W. Fowler. Development of a portable rheometer for fresh Portland cement concrete. *Technical Report*, 2004.
- 3 L.E. Brower and C. F. Ferraris. Comparison of concrete rheometers. *Concrete International*, 25(8), 41-47, 2003.
- 4 T. Kokado, T. Hosoda, T. Miyagawa, and M. Fujii. Study on a method of evaluating a yield value of fresh concrete with a slump flow value. *Doboku Gakkai Ronbunshu*, 1997(578): 19-29, 1997.
- 5 N. Roussel and P. Coussot. Fifty-cent rheometer for yield stress measurements: from slump to spreading flow. *Journal of rheology*, 49(3):705-718, 2005.
- 6 A. Bouvet, E. Ghorbel and R. Bennacer. The mini-conical slump flow test: Analysis and numerical study. *Cement and concrete research*, 40(10), 1517-1523, 2010.
- 7 N. Roussel and R., Le Roy. The marsh cone: a test or a rheological apparatus? *Cement and Concrete Research*, 35(5):823-830, 2005.
- 8 C. F. Ferraris and F. DeLarrard. Testing and modeling of fresh concrete rheology. *Technical report*, 1998.
- 9 H. Lashkarbolouk, A. M. Halabian, and Chamani, M. R. Simulation of concrete flow in V-funnel test and the proper range of viscosity and yield stress for SCC. *Materials and structures*, 47(10): 1729-1743, 2014.
- 10 F. Badry, S. Kulasegaram and B. L. Karihaloo. Estimation of the yield stress and distribution of large aggregates from slump flow test of self-compacting concrete mixes using smooth particle hydrodynamics simulation. *Journal of Sustainable Cement-Based Materials*, 5(3): 117-134, 2016.

PHASE FIELD MODELLING OF HYDROGEN ASSISTED CRACKING

Emilio Martínez-Pañeda

Department of Engineering, University of Cambridge, CB2 1PZ

mail@empaneda.com

Summary

Hydrogen is ubiquitous, diffuses rapidly through the crystal lattice, and drastically reduces the ductility and fracture toughness of metals. The sensitivity to hydrogen damage increases with material strength and hydrogen related failures are now pervasive in the energy, defence, transport, and construction sectors. The prevention and modelling of hydrogen-induced fracture requires capturing multiple micro-mechanical and chemical phenomena across a wide range of scales. We aim at this elusive challenge by developing a coupled deformation-diffusion-fracture multiphysics finite element framework. The model builds upon (i) a variational phase field description of crack nucleation and growth; (ii) a stress-driven mass diffusion law for hydrogen transport; (iii) an enriched characterization of crack tip fields through higher order strain gradient plasticity; and (iv) a first principles based fracture energy dependence on hydrogen concentration. The coupled problem is solved in an implicit time integration scheme, where displacements, plastic strains, phase field order parameter and hydrogen concentration are the primary variables. Crack initiation and growth is computed in a number of configurations as a function of the material properties, the loading conditions and the environment. Computations reveal a good agreement with experiments, highlighting the predictive capabilities of the model. In addition, we showcase the capabilities of the model by addressing engineering case studies with complex loading conditions and crack trajectories. The finite element code developed can be downloaded from www.empaneda.com/codes

Key Words: *Phase field; Hydrogen embrittlement; Fracture; Finite element analysis; Strain gradient plasticity*

A phase field formulation for hydrogen embrittlement

Alan Arnold Griffith's energy-based analysis of cracks in 1920 is considered to be the birth of the field of fracture mechanics [1]. Consider a cracked solid with strain energy density $\Psi(\boldsymbol{\varepsilon})$, which is a function of the strain tensor $\boldsymbol{\varepsilon}$. In the absence of external forces, the variation of the total energy Π due to an incremental increase in the crack area dA is given by

$$\frac{d\Pi}{dA} = \frac{d\Psi(\boldsymbol{\varepsilon})}{dA} + \frac{dW_c}{dA} = 0 \quad (1)$$

where W_c is the work required to create new surfaces. The last term is the so-called critical energy release rate $G_c = dW_c/dA$, a material property that characterizes the fracture resistance. Accordingly, Griffith's energy balance can be formulated in a variational form as

$$\Pi = \int_{\Omega} \Psi(\boldsymbol{\varepsilon}) dV + \int_{\Gamma} G_c d\Gamma \quad (2)$$

with V denoting the volume of the solid and Γ being the crack surface. The latter is unknown, hindering minimization of (2). A phase field order parameter ϕ can be used to track the crack interface, see Fig. 1. This phase field parameter ϕ is a damage variable that takes the values of 0 in an intact material point, and of 1 in a fully cracked material point. As in continuum damage mechanics, a degradation

function $g(\phi) = (1 - \phi)^2$ is defined that diminishes the stiffness of the material with evolving damage [2]. Accordingly, the total potential energy functional can be formulated as

$$\Pi_\ell = \int_{\Omega} \left\{ (1 - \phi)^2 \Psi(\boldsymbol{\varepsilon}) + G_c \left(\frac{1}{2\ell} + \frac{\ell}{2} |\nabla \phi|^2 \right) \right\} dV \quad (3)$$

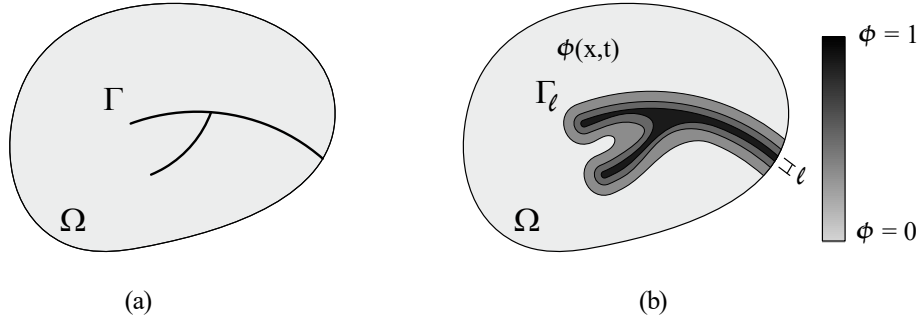


Figure 1: Schematic representation of a solid body with (a) internal discontinuity boundaries, and (b) a phase field approximation of the discrete discontinuities.

The work required to create a cracked surface, Γ , is now expressed as a volume integral, making the problem computationally tractable. As shown by Γ -convergence, the regularized functional Π_ℓ approaches the functional of the discrete crack problem Π for $\ell \rightarrow 0$ [3]. We follow Martínez-Pañeda et al. [4] and define the fracture energy as a function of the concentration of hydrogen, $G_c(c)$, with

$$G_c(c) = (1 - \chi) G_c(0) \quad (4)$$

where χ is a damage coefficient that characterizes the degradation of bonding strength due to the presence of hydrogen atoms. The value of χ can be inferred from atomistic calculations of surface energy degradation with hydrogen occupancy.

Stress-assisted diffusion of hydrogen

Mass conservation requirements relate the rate of change of the hydrogen concentration c with the hydrogen flux \mathbf{J} as

$$\frac{dc}{dt} + \nabla \cdot \mathbf{J} = 0 \quad (5)$$

where t denotes time. Hydrogen diffusion is driven by the gradient of the chemical potential $\nabla \mu$, with the mass flux following a linear Onsager relationship

$$\mathbf{J} = -\frac{Dc}{RT} \nabla \mu. \quad (6)$$

Here, D is the diffusion coefficient, R is the universal gas constant, and T is the temperature. The chemical potential depends on the hydrostatic stress σ_h , the partial molar volume of hydrogen \bar{V}_h , and the occupancy of lattice sites θ_L as

$$\mu = \mu^0 + RT \ln \frac{\theta_L}{1 - \theta_L} - \bar{V}_h \sigma_h \quad (7)$$

with μ^0 denoting the chemical potential in the standard case. Consider the relation between the occupancy and the number of sites $\theta_L = c/N$, and assume low occupancy ($\theta_L \ll 1$) and constant interstitial sites concentration ($\nabla N = 0$) [5]; Eq. (6) can be reformulated as

$$\mathbf{J} = -D \nabla c + \frac{Dc}{RT} \bar{V}_h \nabla \sigma_h \quad (8)$$

Thus, hydrogen atoms diffuse from regions of high chemical potential to regions of low chemical potential, and hydrostatic stresses increase hydrogen solubility by lowering the chemical potential. The role of hydrogen trapping is accounted for by means of the Langmuir-McLean isotherm.

An implicitly multiscale description of plastic deformation

Crack tip stresses are key, as cleavage fracture is stress-controlled and σ_h governs diffusion towards the fracture process zone [6]. We make use of strain gradient plasticity theory to accurately estimate the stress levels at the small scales involved in crack tip deformation, see Ref. [7] for details. Adopting a small strain formulation, the total strain ε is the symmetric part of the spatial gradient of the displacement rate $\varepsilon = \text{sym} \nabla \mathbf{u}$, and decomposes additively into an elastic part, ε^e , and a plastic part, ε^p . Write $\boldsymbol{\sigma}$ as the Cauchy stress, \mathbf{q} as the so-called micro-stress tensor and $\boldsymbol{\tau}$ as the higher order stress tensor. For a solid of volume V and surface S , the principle of virtual work reads,

$$\int_V (\boldsymbol{\sigma} \cdot \delta \boldsymbol{\varepsilon}^e + \mathbf{q} \cdot \delta \boldsymbol{\varepsilon}^p + \boldsymbol{\tau} \cdot \nabla \delta \boldsymbol{\varepsilon}^p) dV = \int_S (\mathbf{T} \cdot \delta \mathbf{u} + \mathbf{t} \cdot \delta \boldsymbol{\varepsilon}^p) dS \quad (9)$$

Write $\boldsymbol{\sigma}'$ as the deviatoric part of $\boldsymbol{\sigma}$, and write \mathbf{n} as the unit outward normal to the surface S . Then, upon making use of the Gauss divergence theorem, equilibrium within V reads

$$\begin{aligned} \nabla \cdot \boldsymbol{\sigma} &= \mathbf{0} \\ \nabla \cdot \boldsymbol{\tau} + \boldsymbol{\sigma}' - \mathbf{q} &= \mathbf{0} \end{aligned} \quad (10)$$

for, respectively, the primal kinematic variables \mathbf{u} and $\boldsymbol{\varepsilon}^p$. Accordingly, the corresponding conventional and higher order tractions respectively read $\mathbf{T} = \boldsymbol{\sigma} \mathbf{n}$ and $\mathbf{t} = \boldsymbol{\tau} \mathbf{n}$.

Coupled finite element implementation

The coupled problem is solved in an implicit time integration scheme, with the nodal unknowns being the displacements \mathbf{u} , the plastic strains $\boldsymbol{\varepsilon}^p$, the phase field parameter ϕ and the hydrogen concentration c . The residuals and the associated components of the consistent stiffness matrix are obtained by discretising the weak forms of the fracture, diffusion and mechanical laws. The hydrostatic stresses drive hydrogen diffusion, which in turn degrades the fracture resistance. A penalty approach is employed to model *moving* chemical boundary conditions that capture how the environment (hydrogen gas or the liquid electrolyte) promptly enters into contact with the new surfaces created with crack advance.

Representative results

We mimic the experiments by Olden et al. [8], and compute the time for crack initiation in single-edged notched specimens immersed in sea water and subjected to different constant net stresses σ_{net} . The samples are made of duplex stainless steel, with the material properties described in Ref. [8], and we characterize the environmental conditions by prescribing a hydrogen concentration of 1 wppm at the outer surfaces. The mechanical load is insufficient to trigger fracture at the beginning of the test but as hydrogen accumulates in the fracture process zone, G_c is reduced and cracking initiates. The crack is shown in Fig. 2a, where blue and red colors correspond to the completely intact and the fully broken state of the material, respectively. See Ref. [4] for other examples involving complex crack paths. As shown in Fig. 2b, the numerical predictions accurately capture the increase in time to failure with diminishing σ_{net} . Furthermore, predictions can be obtained for large time scales, unattainable in laboratory testing, enabling to identify the net stress level below which cracking will not occur.

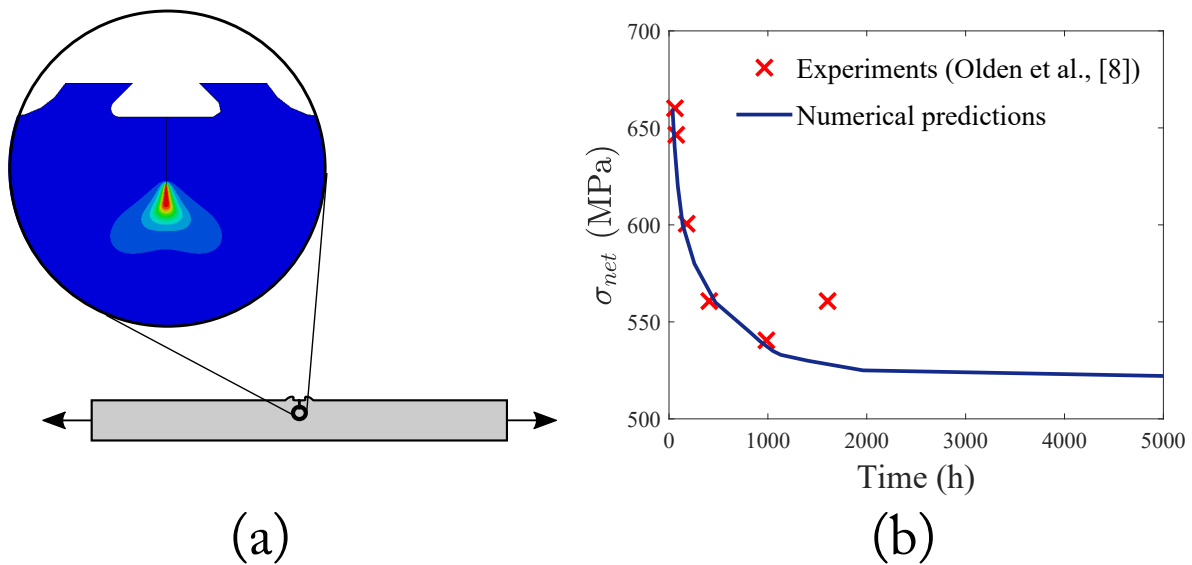


Figure 2: Cracking of single-edged specimens immersed in sea water and subjected to a constant load: (a) crack trajectory, and (b) net section stress versus time to crack initiation.

Conclusions

We present a mechanistic deformation-diffusion-fracture modelling framework for predicting hydrogen assisted cracking. The model captures the ductile-to-brittle transition observed when metals are exposed to hydrogen and enables large scale multiphysics predictions in complex scenarios resembling those inherent to engineering practice.

References

- 1 A.A. Griffith. The Phenomena of Rupture and Flow in Solids. *Philosophical Transactions A*, 221, 163-198, 1920.
- 2 B. Bourdin, G.A. Francfort, J.J. Marigo. Numerical experiments in revisited brittle fracture. *Journal of the Mechanics and Physics of Solids*, 48, 797-826, 2000.
- 3 T. Linse, P. Hennig, M. Kästner, R. de Borst. A convergence study of phase-field models for brittle fracture. *Engineering Fracture Mechanics*, 184, 307-318, 2017.
- 4 E. Martínez-Pañeda, A. Golahmar, C.F. Niordson. A phase field formulation for hydrogen assisted cracking. *Computer Methods in Applied Mechanics and Engineering*, 342, 742-761, 2018.
- 5 S. del Busto, C. Betegón, E. Martínez-Pañeda. A cohesive zone framework for environmentally assisted fatigue. *Engineering Fracture Mechanics*, 185, 210-226, 2017.
- 6 E. Martínez-Pañeda, C.F. Niordson, R.P. Gangloff. Strain gradient plasticity-based modeling of hydrogen environment assisted cracking. *Acta Materialia*, 117, 321-332, 2016.
- 7 E. Martínez-Pañeda, V.S. Deshpande, C.F. Niordson, N.A. Fleck. The role of plastic strain gradients in the crack growth resistance of metals. *Journal of the Mechanics and Physics of Solids*, 126, 136-150, 2019.
- 8 V. Olden, C. Thaulow, R. Johnsen, E. Østby, T. Berstad. Influence of hydrogen from cathodic protection on the fracture susceptibility of 25%Cr duplex stainless steel. *Engineering Fracture Mechanics*, 76, 827-844, 2009.

IMMERSED B-SPLINE FINITE ELEMENTS FOR COMPLEX GEOMETRIES

*Eky Febrianto¹ and Fehmi Cirak¹¹Department of Engineering, University of Cambridge, Trumpington Street, Cambridge CB2 1PZ, UK

Email: {evf27, fc286}@cam.ac.uk

Summary

We present a higher-order immersed b-spline finite element technique suitable for parametrically described complex solid geometries. Prevalent parametric representations in industry include the trimmed NURBS from CAD and the STL meshes from polygonal modelling. For discretisation we use non-boundary-conforming tensor-product b-splines and enforce the Dirichlet boundary conditions with the Nitsche technique. The cells intersected by the parametric bounding surface are first tessellated using a marching tetrahedra algorithm, and the linear tetrahedra are subsequently degree elevated and fitted to the curved bounding surface. This process relies on repeated and efficient interrogation of the parametric surface, i.e. ray-surface intersection computations. To this end, we consider two complementary robust interrogation approaches. In the first, for STL meshes a ray-triangle intersection algorithm and for NURBS novel non-iterative interrogation techniques from CAD are employed for computing the intersection in one shot. In the second approach, the finely tessellated parametric solid is first implicitised on an auxiliary tensor-product grid with a similar resolution (up to 2000³ cells). The subsequent interrogation of the implicit geometry on the auxiliary grid becomes straightforward. In this second approach the boundary approximation errors are controlled by the ratio of the cell sizes of the auxiliary and computational simulation grids. The robustness and accuracy of the developed approach are demonstrated with a number of benchmark examples and industrial geometries.

Key Words: *immersed finite elements; b-splines; parametric solids; NURBS; STL*

Introduction

In industrial settings, geometry is commonly represented using parametric CAD boundary descriptions e.g. trimmed NURBS and the STL meshes. The analysis of such geometry requires the generation of a good quality boundary-fitted meshes through an error-prone meshing procedure. The difficulty of the meshing process is the primary motivation behind an emerging class of numerical methods that work without boundary-conforming discretisations. Immersed, or embedded, method describes the domain boundary as the zero-contour of an implicit signed-distance function. The implementation of immersed method in the context of finite element is extensively demonstrated in, for example [1, 2]. The introduced method uses a logically Cartesian embedding grid to facilitate the use of tensor product b-spline basis functions for approximation. This construction allows the physical domain boundary to intersect the Cartesian grid cells and the basis functions in an arbitrary way. It is therefore obvious that the recovery of the geometry in the cut-cells becomes a crucial step in the computation of the integrals appearing in the weak form. The recovery process greatly relies on a repeated interrogation of the enclosing boundary. This paper will discuss our implementation of efficient interrogation techniques suitable for the parametric bounding surface.

Immersed b-spline finite elements

We consider the weak formulation of the Poisson equation as: Find $u \in H^1(\Omega)$ such that

$$\int_{\Omega} \nabla u \cdot \nabla v \, d\Omega + \gamma \int_{\Gamma_D} (u - \bar{u}) v \, d\Gamma = \int_{\Omega} f v \, d\Omega + \int_{\Gamma_N} \bar{g} v \, d\Gamma + \int_{\Gamma_D} \left((u - \bar{u}) \mathbf{n} \cdot \nabla v + (\mathbf{n} \cdot \nabla u) v \right) d\Gamma \quad (1)$$

for all $v \in H^1(\Omega)$. In the present work the solution field and the test functions are discretised using uniform b-splines that are defined on a regular tensor-product grid. The approximation of the solution u and test functions v with the b-splines of degree μ reads

$$u^h(\mathbf{x}) = \sum_i B_i^\mu(\mathbf{x})u_i \quad \text{and} \quad v^h(\mathbf{x}) = \sum_i B_i^\mu(\mathbf{x})v_i, \quad (2)$$

where d-tuple $\mathbf{i} = \{i_1, \dots, i_d\}$ is a multi-index for numbering the knots. The problem domain $\Omega \in \mathbb{R}^d$ is contained within a sufficiently large tensor-product grid domain $\Omega_\square \in \mathbb{R}^d$, i.e. $\Omega \subset \Omega_\square$. In the above formulation, the Dirichlet boundary condition is enforced using the Nitsche method [3].

The grid cells are categorised into active, inactive, and cut depending whether the cell is fully inside, outside or being intersected by the enclosing boundary surface. While integration over active cells is straightforward, the integral evaluation over the cut-cells requires special treatment. We firstly indicate whether the cut-cell is a non-standard cut-cell. A cut-cell is classified as non-standard when it contains sharp crease/corner based on the criteria in [4] or when its edges are intersected more than once by the boundary. A standard cut cell is simply tessellated using marching tetrahedra and subsequently degree elevated and fitted to the curved bounding surface. The non-standard cut-cell is reconstructed using a novel bottom-up octree with refinement up to $2^5 \times 2^5 \times 2^5$ cells. Small cut-cells lead to the system matrix conditioning problems and is robustly handled using an extrapolation scheme introduced in [5].

Extention to complex parametric geometry

We firstly define a scalar-valued implicit signed-distance function as

$$\phi(\mathbf{x}) = \begin{cases} \text{dist}(\mathbf{x}, \Gamma) & \text{if } \mathbf{x} \in \Omega \\ 0 & \text{if } \mathbf{x} \in \Gamma \\ -\text{dist}(\mathbf{x}, \Gamma) & \text{otherwise,} \end{cases} \quad (3)$$

where $\text{dist}(\mathbf{x}, \Gamma) = \min_{\mathbf{y} \in \Gamma} |\mathbf{x} - \mathbf{y}|$ is the shortest distance between the point \mathbf{x} and the surface Γ . We refer the process of obtaining scalar field $\phi(\mathbf{x})$ from a parametric geometry description as implicitisation. When the surface is represented with low-order triangular facets, such as STL meshes, the implicitisation comprises of simple interrogation for each surface facet based on a ray-triangle intersection algorithm. However, the signed distance function may contain large numerical error when the triangular facets are slivers. A more robust approach is the scan conversion algorithm explained in [6]. The algorithm creates a closest point transform (CPT) and is able to avoid ambiguous sign identification when the closest surface feature is an edge or a vertex of the faceted surface representation.

When the enclosing boundary surface is represented with spline, such as NURBS, we consider two approaches for surface interrogation. The first approach is a novel non-iterative interrogation technique as elaborated in [7] and more recently in [8]. The process requires a computation of an implicit matrix of the Bézier representation of the surface. This therefore eliminates the use of an iterative root finding such as Newton's method where convergence is not guaranteed. The second approach is to refine the boundary representation and subsequently implicitise it on a fine auxiliary tensor product grid with resolution up to 3000^3 cells. In this approach, the boundary approximation error depends highly on the ratio of the cell sizes of the auxiliary and computational simulation grids.

Figure 1 depicts the application of the algorithm for a complex engineering problem. The geometry of the turbine rotor is given as STL meshes exported from a parametric CAD system. The

immersed b-spline finite element analysis of the turbine is performed on a tensor product grid with size $180 \times 90 \times 180$ cells. A finer auxiliary grid with resolution $2880 \times 1440 \times 2880$ is utilised for computing the signed-distance function. The auxiliary grid is then efficiently represented as a sparse grid with the highest accuracy within a narrow band of 20 voxel size from the surface. The turbine is subjected to an initial tangential loading with variation along its radial axis. The result of the analysis shows that the largest displacement occurs at the tip of the blades.

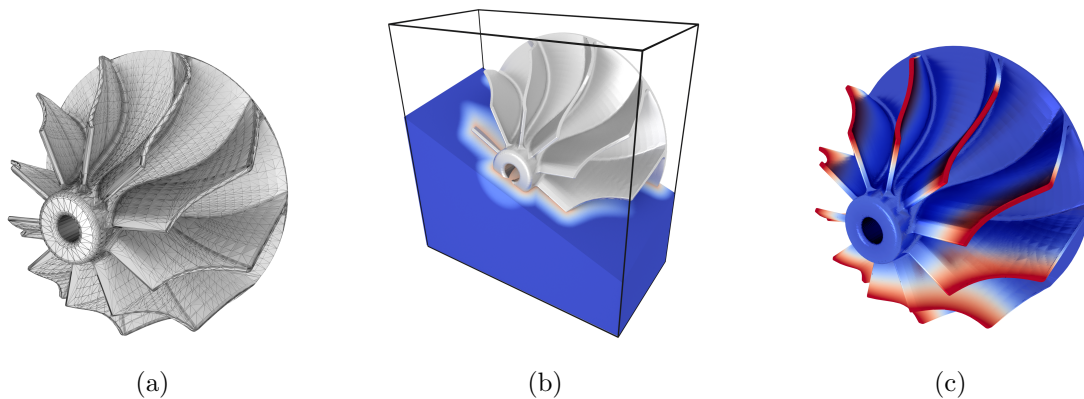


Figure 1: Representative application of the proposed immersed finite element approach. (a) The initial geometry of the turbine is given as a STL mesh that has been exported from a CAD system. The resolution of the STL mesh has been chosen relatively coarse so that the mesh is discernible. (b) Implicit representation of geometry computed on a $2880 \times 1440 \times 2880$ sparse uniform grid as a narrow band level set. (c) Reconstructed higher order finite element representation and computation results on a $180 \times 90 \times 180$ uniform grid.

Conclusion

The introduced extension of the immersed b-spline finite element includes two complementary interrogation techniques for parametric geometry. The first is based on ray-triangle intersection and closest point transform algorithm which is more suitable for a faceted representation. The second, aimed for spline surface, exploits a non-iterative interrogation technique and a geometry refinement implicitised on a much finer auxiliary grid. The proposed approach is robust for a complex engineering geometry with sharp creases and corners represented with poor quality STL meshes.

References

- [1] Bandara, K, Rüberg, T. and Cirak, F. Shape optimisation with multiresolution subdivision surfaces and immersed finite elements. *Computer Methods in Applied Mechanics and Engineering* (2016) **300**:510–539.
- [2] Rüberg, T. and Cirak, F. A fixed-grid b-spline finite element technique for fluid–structure interaction. *International Journal for Numerical Methods in Fluids* (2014) **74**:623–660.
- [3] J. Nitsche, Über ein Variationsprinzip zur Lösung von Dirichlet-Problemen bei Verwendung von Teilräumen, die keinen Randbedingungen unterworfen sind, *Abh. Math. Sem. Univ. Hamburg* (1971)**36**:915.
- [4] Kobbelt, L., Botsch, M., Schwaner, U., and Seidel, H. Feature Sensitive Surface Extraction from Volume Data. *Proceedings of the 28th Annual Conference on Computer Graphics and Interactive Techniques* (2001) **10**:57–66

- [5] Rberg, T. and Cirak, F. Subdivision-stabilised immersed b-spline finite elements for moving boundary flows. *Computer Methods in Applied Mechanics and Engineering* (2012) **209212**:266283.
- [6] Mauch, S. A Fast Algorithm for Computing the Closest Point and Distance Transform. *Technical report: California Institute of Technology* (2000).
- [7] Laurent, B. Implicit matrix representations of rational Bzier curves and surfaces. *Computer Aided Design* (2014) **46**:14-24
- [8] Xiao, X., Sabin, M., and Cirak, F. Interrogation of spline surfaces with application to isogeometric design and analysis of lattice-skin structures. Pre-print (2018).

RESOLUTION OF DISCONTINUITY IN SHELL MODELS OF FOLDED PLATES

*Qili Fang¹, Bassam A. Izzuddin¹¹Department of Civil and Environmental Engineering, Imperial College London, SW74HA

*qili.fang14@imperial.ac.uk

Summary

The modelling of folded plates with displacement-based shell elements introduces an incompatibility that leads to inaccuracy compared to high fidelity models based on 3D continuum finite elements. This issue arises regardless of whether drilling rotational degrees of freedom are used, though the focus of this paper is on shell finite elements that exclude drilling DoF. In this paper, the dominant factor causing inaccuracy in the conventional-shell-based models of folded plates is recognised as the incompatible rotations of the normal on the two sides of the intersection. Towards resolving this uncoupling issue, a 3-noded coupling element utilising an augmented continuous Lagrangian multiplier approach is introduced to impose a continuous constraint on the product of the corresponding tangential rotations and the thickness of shells on the two sides of the intersection. Several numerical studies comparing shell-based models to high fidelity solid-based models are performed, through which the significance of the discontinuity in the shell-based folded structure is demonstrated, and the effectiveness of the proposed coupling element is verified.

Key Words: *folded plates; conventional shells; augmented continuous Lagrangian multiplier method; coupling elements*

Introduction

Conventional shell theory based on two rotational parameters has been extensively studied and generally applied to smooth plate problems. However, when the smoothness assumption no longer holds and three independent rotations have to be included at one node, conventional shell theory fails to accurately capture the true kinematic configuration along the intersection. The modelling of folded plates was considered previously by introducing a drilling DoF [1], though such DoFs are not generally necessary or meaningful for modelling the smooth regions. In this paper, the most significant source of inaccuracy is identified as the incompatibility of longitudinal displacement within the intersection, which exists regardless of the consideration of the drilling DoF.

This incompatibility of longitudinal displacement is illustrated in Figure 1a, where a folded plate is represented by 4-noded shell elements that are directly connected along the mid-plane intersection. The initial and deformed configurations of two nodal strips orthogonal to the intersection are shown in Figures 1b-1c, respectively. A clear discontinuity can be observed for the overlapping region over the re-entrant corner due to the uncoupled tangential rotations, such discontinuity becoming more significant for plates with a greater thickness.

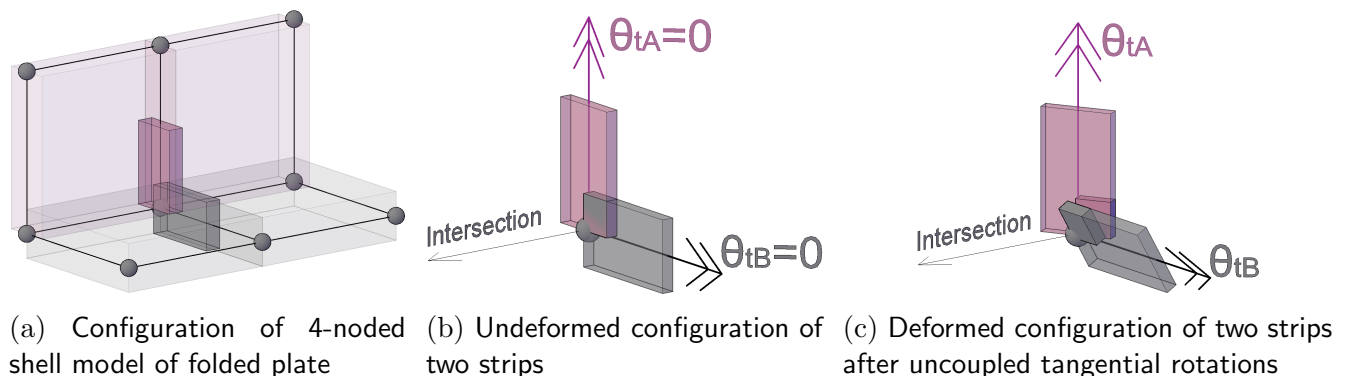


Figure 1: Discontinuity in folded plate model with uncoupled tangential rotations on the intersection

A 3-noded coupling element imposing a constraint on the product of the corresponding tangential rotations and the thickness of shells is introduced to resolve this longitudinal displacement discontinuity. This coupling element is to be employed along the intersection of two non-smoothly connected shell elements, as shown in Figure 2. The discrepancy within the intersection is determined by utilising the orientation vectors along the intersection, the mid-surface normal vectors of shells and the thickness of shells on the two sides of the intersection. A constraint is subsequently applied to eliminate the discrepancy by employing a continuous augmented Lagrangian multiplier approach. Details of the kinematic relationship of the involved vectors and the weak form of the constraint are presented in the following sections.

Kinematics of Coupling Element

For consistency, in all the equations below the i subscript refers to the i^{th} shell and the j subscript refers to the j^{th} node. The unit orientation vector \mathbf{c}_j in the longitudinal direction at each node is obtained by the derivative of the interpolated translational displacement field with respect to the local natural coordinate:

$$\mathbf{c}_j = \left. \frac{\bar{\mathbf{X}}_{,\xi}}{\|\bar{\mathbf{X}}_{,\xi}\|} \right|_{\xi=\xi_j} \quad (j = 1, 2, 3) \quad (1)$$

where $\bar{\mathbf{X}}$ is the continuous displacement field interpolated with the translational DoFs on the coupling element in the current configuration, and ξ is the natural coordinate axis on the 1D system.

The normal vectors employed by the coupling element are intrinsic mid-surface normal vectors on both sides of the folded plate, which are generated by the conventional displacement-based 9-noded shell elements [2]. A standard approach based on the incremental rotation method is employed for the update of the normal vectors [3]. At the start of nonlinear analysis, the mid-surface normal vector \mathbf{n}^0 at each node of the shell element is obtained based on the initial configuration of the shell element. In subsequent incremental steps, the current normal vector is updated by the multiplication of a transformation matrix and the normal vector at the end of the previous step:

$${}_i\mathbf{n}_j = {}_{\text{ir}}\mathbf{T} \cdot {}_i\mathbf{n}_j^o \quad (i = 1, 2; j = 1, 2, 3) \quad (2)$$

where ${}_i\mathbf{n}_j$ and ${}_i\mathbf{n}_j^o$ are the current and previous normal vectors on the shell elements, as shown in Figure 3, and ${}_{\text{ir}}\mathbf{T}$ is a second-order orthogonal rotation matrix defined by incremental rotational DoFs, as proposed in [3].

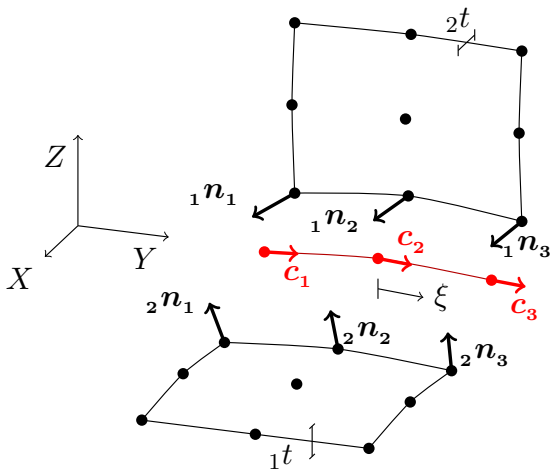


Figure 2: Deformed configuration of a coupling element with two connected shell elements

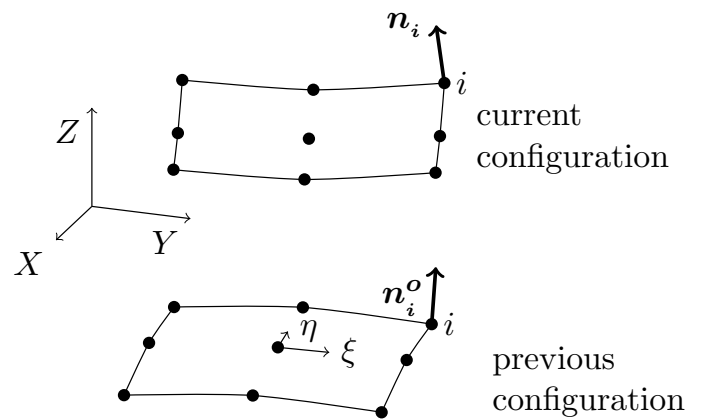


Figure 3: Previous and current deformed configurations of a 9-noded shell element

Constraint Function and Weak Form

The longitudinal displacement at the outer fibre of a plate can be obtained by projecting the vector along the normal \mathbf{n}_j with a magnitude of $(t/2)$ along the longitudinal orientation vector \mathbf{c}_j . Hence, a nodal constraint function at node j is given as below to eliminate the discontinuity in the longitudinal displacement over the re-entrant corner between the two shells on either side of the intersection:

$$g_j = {}_1t \cdot \mathbf{c}_j^T \cdot {}_1\mathbf{n}_j - {}_2t \cdot \mathbf{c}_j^T \cdot {}_2\mathbf{n}_j \quad (j = 1, 2, 3) \quad (3)$$

where ${}_1t$ and ${}_2t$ are the thickness of shells. Note that the factor of $(1/2)$ in $(t/2)$ is omitted for convenience, given that the objective constraint value is zero.

The constraint in Eq. (3) is introduced in the weak form of the global boundary value problem by constructing an augmented Lagrange multiplier formulation [4]:

$$\Pi_{ALM} = \int_L \lambda \cdot g + \frac{1}{2} \cdot \epsilon \cdot g^2 ds^0 = \int_{-1}^1 \left(\lambda \cdot g + \frac{1}{2} \cdot \epsilon \cdot g^2 \right) \cdot \|\bar{\mathbf{X}}_{,\xi}^0\| d\xi \quad (4)$$

where g and λ are the continuous constraint function and continuous Lagrangian multiplier field interpolated by the nodal values based on a second-order shape function, $\epsilon > 0$ is the penalty parameter, $\bar{\mathbf{X}}^0$ is the interpolated continuous displacement field in the previous configuration.

The global stiffness matrix and global nodal force are subsequently obtained by the first and second partial derivatives of Eq. (4) with respect to the corresponding DoFs and the Lagrangian multipliers.

Numerical Examples

Three multi-folded roof-like structures subject to torsional action in the intersection are simulated in ADAPTIC [5], including a 50mm thick 4-fold plate, a 100mm thick 4-fold plate and a 100mm thick 6-fold plate, as shown in Figure 4. These structures are clamped supported on one edge and subject to point loads at corners on opposite edge, as depicted in Figure 4a. For each structure, three models are considered: A) conventional model with displacement-based 9-noded shell elements [2]; B) a similar model with 9-noded shell elements but employing 3-noded coupling constraint elements along the folds; and C) a high-fidelity model with 20-noded 3D brick elements.

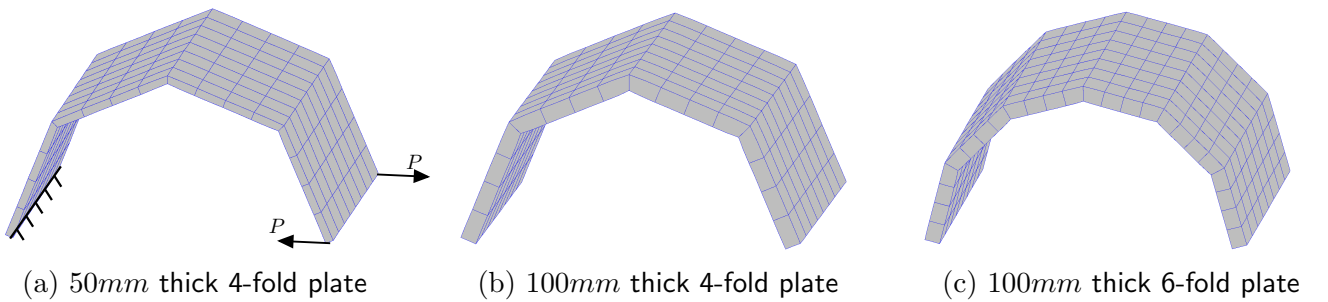


Figure 4: Configuration of three models by solid elements

The convergence of strain energy for models of the 50mm thick 4-fold plate and the error of strain energy in the converged shell-based models compared to the high-fidelity solid based models are depicted in Figures 5-6, respectively. From Figure 5, it can be observed that a tangible reduction in stiffness is incurred by the conventional shell model in comparison with the high-fidelity model, as manifested by a greater strain energy. On the other hand, the proposed approach based on coupling the tangential rotations in shell models achieves a significant improvement, as demonstrated by a substantial reduction of the error in the strain energy. Comparing the converged results obtained from the different models in

Figure 6, proportional increases in error of the conventional shell-based models are observed when the thickness is doubled or the number of folds is increased. In contrast, the proposed coupling approach effectively maintains an error below 1.5% for all folded structures.

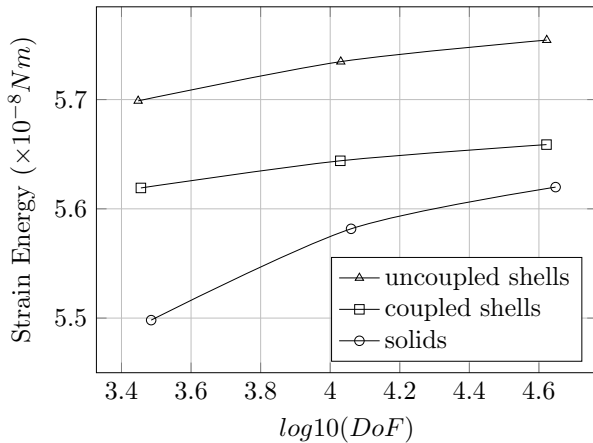


Figure 5: Convergence of strain energy of the 50mm thick 4-fold plate

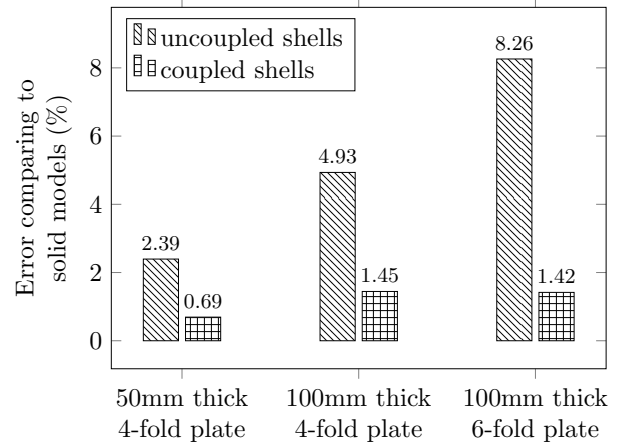


Figure 6: Error of strain energy in shell-based models compared to high-fidelity 3D continuum models

Conclusions

This paper identifies the longitudinal displacement discontinuity induced by the uncoupled tangential rotations as the main source of inaccuracy in conventional displacement-based shells model of folded plates, and proposes an effective method for the alleviation of displacement discontinuity. The proposed method involves applying a continuous constraint on the discrepancy of longitudinal displacement along the intersection utilising a 1D 3-noded coupling element, whose effectiveness is demonstrated in terms of providing an excellent comparison of strain energy in comparison to high-fidelity 3D continuum models. With the proposed approach, a simplified and effective treatment of the kinematics in the fold region is achieved with conventional displacement-based shell models.

References

- [1] J Chróścielewski, J Makowski, and H Stumpf. Finite element analysis of smooth, folded and multi-shell structures. *Computer Methods in Applied Mechanics and Engineering*, 141(1-2):1–46, 1997. ISSN 0045-7825.
- [2] BA Izzuddin and Y Liang. A hierarchic optimisation approach towards locking-free shell finite elements. *Computers & Structures*, 2017. ISSN 0045-7949.
- [3] BA Izzuddin. Conceptual issues in geometrically nonlinear analysis of 3d framed structures. *Computer methods in applied mechanics and engineering*, 191(8-10):1029–1053, 2001.
- [4] P Papadopoulos and RL Taylor. A mixed formulation for the finite element solution of contact problems. *Computer Methods in Applied Mechanics and Engineering*, 94(3):373–389, 1992. ISSN 0045-7825.
- [5] BA Izzuddin. *Nonlinear dynamic analysis of framed structures*. PhD thesis, Imperial College, University of London, 1991.

THE LOCAL MAXIMUM ENTROPY POINT COLLOCATION APPROACH FOR MEMBRANE ANALYSES

*Lei Fan¹, Charles E. Augarde¹ and William M. Coombs¹

¹Department of Engineering, Durham University, DH1 3LE

*lei.fan@durham.ac.uk

Summary

In this paper, the development is described of a strong form-based local maximum entropy point collocation approach to analyse simple membrane problems. Point collocation methods work with discretised strong forms, presenting some attractive features, e.g. no background mesh. In this analysis, three configurations including the reference, prestressed and current configurations are introduced. A Total Lagrangian description with respect to the reference configuration is adopted to describe the motion. Rubber-like hyperelastic materials are used where the constitutive models are derived from the stored strain energy. The arc-length Newton-Raphson method is used to solve the non-linear system. A numerical example is presented to validate the performance of this proposed framework.

Key Words: *membrane; large deformation; hyperelasticity; point collocation*

1. Introduction

Membrane structures are appealing in a wide range of areas, for instance as they can make attractive roof structures with much lower weight than most traditional structures, possessing high performance in resisting external loads and reducing the cost and environmental impact of structures. Membrane theory which is used to make some specific requirements for the realistic description of the mechanical behaviour of membranes, in principle, is extracted from classical shell theory, however, the bending stiffness is completely neglected in membrane theory. It remains computationally challenging to analyse these structures due to their structural characteristics and the need for large deformation mechanics. The mechanical response of membrane structures is usually described by in-plane strains rather than full three dimensional constitutive theory and the membranes modelled here are assumed to be non-compression structures, which makes their equilibrium physically unstable. Finite strain hyperelastic materials are particularly appropriate for the analyses of rubber-like solids often employed in real membrane structures, which brings computational complexity [1]. Many weak form-based numerical methods have been employed to analyse the membrane inflation problem, which can however lead to severe mesh distortion using those methods [2]. In this work, the strong form-based local maximum entropy point collocation method (MEPCM), proposed and explained in detail by the present authors in [3], is adapted to membrane analyses.

2. Membrane theory

Kinematics for inflated membrane problems starts with a description of three successive configurations, reference (undeformed), initial (prestressed) and current (deformed) configuration as shown in Figure 1. The governing PDEs for the geometrically non-linear membranes are given with respect to the reference configuration as [3]

$$\frac{\partial N_{xx}}{\partial X} + \frac{\partial N_{xy}}{\partial Y} = p_x \quad (1a)$$

$$\frac{\partial N_{xy}}{\partial X} + \frac{\partial N_{yy}}{\partial Y} = p_y \quad (1b)$$

$$\frac{\partial}{\partial X} \left(N_{xx} \frac{\partial u_z}{\partial X} + N_{xy} \frac{\partial u_z}{\partial Y} \right) + \frac{\partial}{\partial Y} \left(N_{yy} \frac{\partial u_z}{\partial Y} + N_{xy} \frac{\partial u_z}{\partial X} \right) = p_z \quad (1c)$$

where u_z is the displacement in the out-of-plane direction and N_{xx} , N_{yy} and N_{xy} are the resultant forces (integrated forces or membrane forces). p_x , p_y and p_z are the external pressure vector components. Dirichlet and Neumann boundary conditions are given as

$$\{u\} = \{\bar{u}^0\} \quad \text{and} \quad [n]^T \{N\} = \{\bar{t}^0\} \quad (2)$$

where $\{u\}$ is the vector of unknown field variables (i.e. displacement in this case), $\{\bar{u}^0\}$ and $\{\bar{t}^0\}$ are the prescribed displacements and tractions and $[n]$ is a matrix of the outer normals of a point lying on the boundary. In the MEPCM, a linear system is assembled from collocation points in the domain and

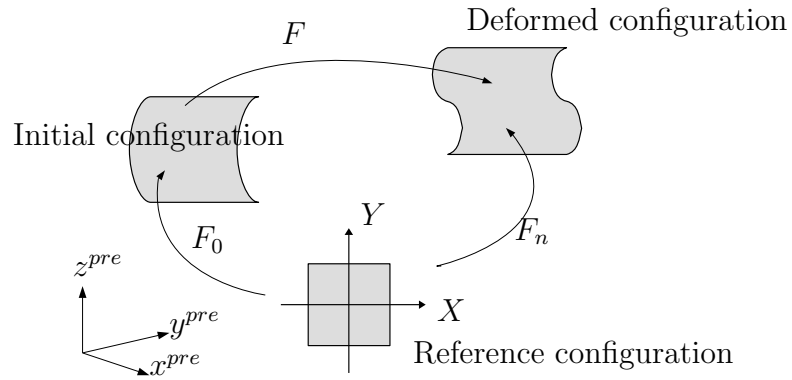


Figure 1: Reference, initial and current membrane configurations.

on two types of boundaries satisfy the governing equations in Eqs. (1) and boundaries conditions in Eq. (2). The non-linear system of equations includes three different components to match these three types of collocation point as

$$\{G\} = \{\{G_1\}, \{G_2\}, \{G_3\}\}^T. \quad (3)$$

Then the field variables at discrete source points can be obtained by solving the non-linear system of equations in Eqs. (3).

An appropriate constitutive model is required to describe the relationship between stresses and stains. In this paper, the hyperelastic Ogden model with finite strain is used. An expression of a specific free energy function ψ in terms of the principal stretch λ_i with respect to the prestressed configuration given by Ogden takes the form [4, 5]

$$\psi = \hat{\psi}(\lambda_1, \lambda_2, \lambda_3) = \sum_{p=1}^N \frac{\mu}{\alpha_p} (\lambda_1^{\alpha_p} + \lambda_2^{\alpha_p} + \lambda_3^{\alpha_p} - 3) \quad (4)$$

where α_p and μ are constants obtained from experiments. The second Piola-Kirchhoff stress referred to the reference configuration $[S_n]$ for hyperelastic materials is

$$[S_n] = \frac{\partial \psi}{\partial [E_n]} = 2 \frac{\partial \hat{\psi}}{\partial [C_n]} \quad (5)$$

where E_n and C_n refer to the reference configuration. As the equilibrium for a hyperelastic membrane is unstable, a problem cannot be solved by the load or displacement controlled Newton method. Therefore the arc-length method provides an efficient way to trace the equilibrium path with snap-back or snap-through phenomena.

3. Numerical examples

In this example, the inflation of a square thin rubber sheet under uniform internal pressure is simulated. The side length of the square membrane is $L = 20$ cm and $\delta l = 0.05$ cm is the in-plane prestretch. $h_0 = 0.1$ cm is the initial thickness of the membrane. The initially applied external pressure is $p_z = 0.01$ kg/cm² and increments in the following steps are determined by the non-linear solver. Figure 2 depicts

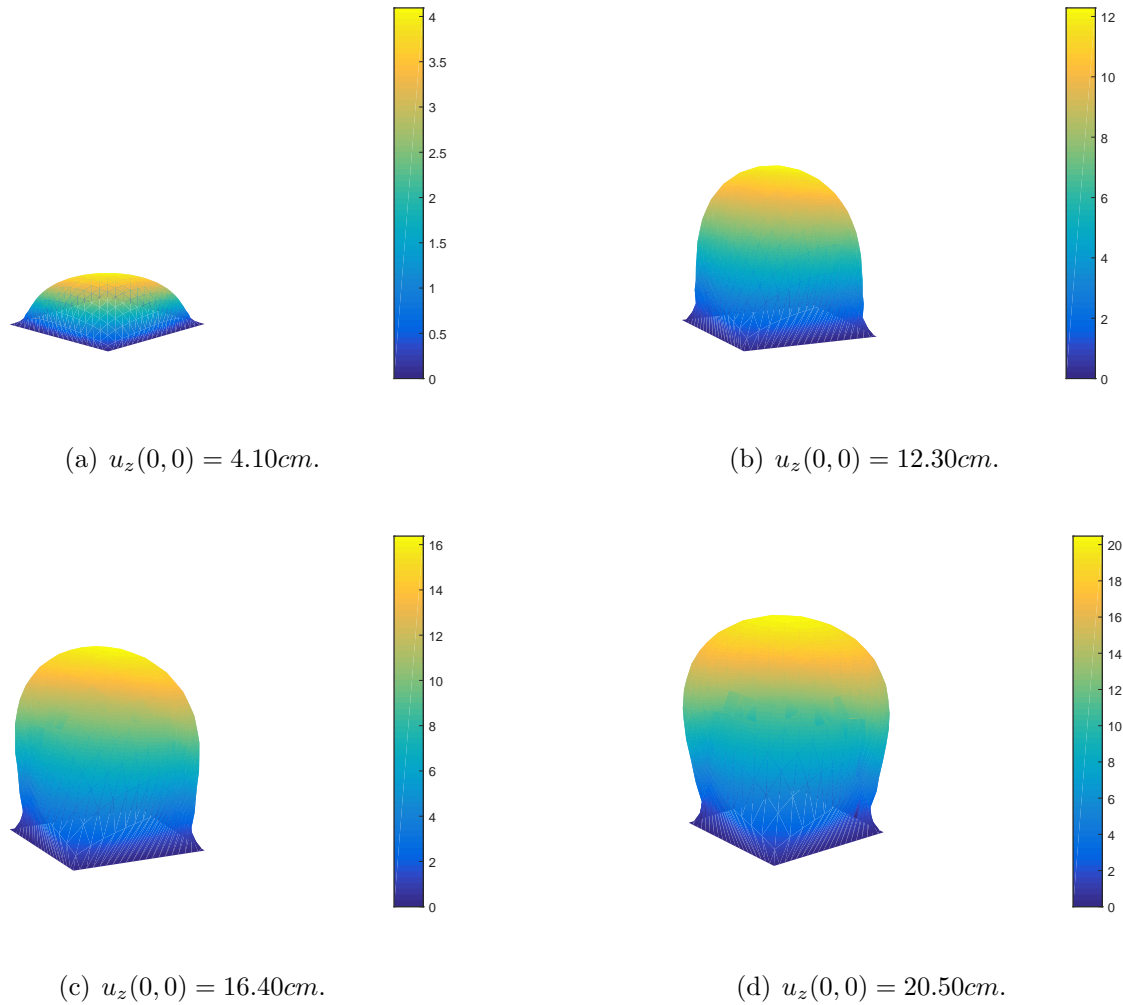


Figure 2: The deformed configurations of square membrane.

the evolution of the deformed geometry of the square membrane at different stages predicted by the MEPCM. The initially flat membrane evolves into a spherical shape with increasing out-of-plane and in-plane deformations. In Figure 2, it can be seen that the deformation leads to tension in the membrane and the edges have zero displacements. With an increasing pressure, the in-plane tension and out-of-plane inflation gradually become significant. It should be noted that the deformation is that predicted after the initial prestretch configuration under the externally applied pressure. The pressure is plotted against the deflection at the middle point with different prestretch values using the arc-length Newton method in Figure 3, where a snap through behaviour can be seen. At the beginning of the inflation, pressure goes up with an increasing out-of-plane deflection until the pressure reaches a limit point. It is also observed that different values of prestretch have an effect on the deformation profile.

4. Conclusions

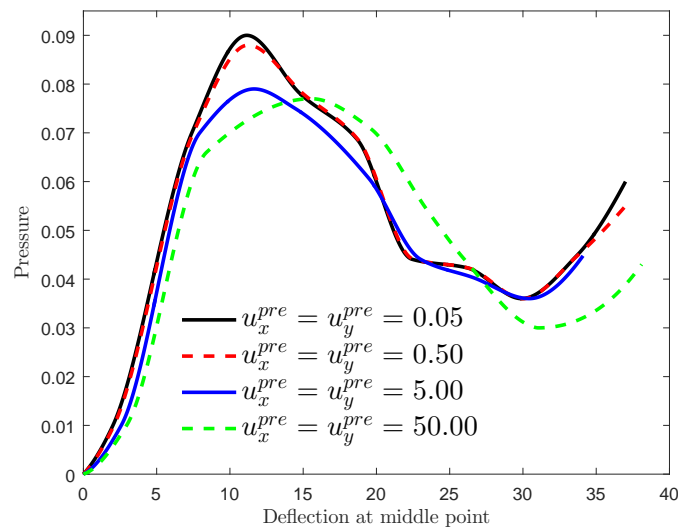


Figure 3: Pressure-deflection at the middle collocation point.

Numerical modelling for membrane structures has been successfully demonstrated using a new meshless method, the geometrical non-linear MEPCM based on the total Lagrangian formulation. The proposed model can accommodate hyperelastic materials and here the arc-length method has been employed to work with standard Newton-Raphson method, searching for the equilibrium path in the face of instability. A numerical example using the hyperelastic Ogden model with large strain for membrane inflation has been presented to validate the capabilities of the newly proposed framework.

Acknowledgements

This work has been sponsored by the China Scholarship Council (CSC) and the Department of Engineering, Durham University.

References

- 1 E. A. de Souza Neto, D. Peric and D. R. Owen. *Computational methods for plasticity: theory and applications*, John Wiley & Sons, 2011.
- 2 J. Bonet, R. D. Wood, J. Mahaney and P. Heywood. Finite element analysis of air supported membrane structures, *Comput. Methods Appl. Mech. Engrg.*, Volume 190, 579-595, 2000.
- 3 L. Fan, W. Coombs and C. Augarde. The point collocation method with a local maximum entropy approach. *Comput. & Struct.*, 201(C), 1-14, 2018.
- 4 K. F. Kolsti and D. L. Kunz. A point collocation method for geometrically non-linear membranes. *Int. J. Solids. Struct.*, 50, 288-296, 2013.
- 5 R. Ogden, G. Saccomandi and I. Sgura, Fitting hyperelastic models to experimental data. *Computat. Mech.*, 34, 484-502, 2004.
- 6 M. Crisfield, A fast incremental/iterative solution procedure that handles snapthrough. *Comput. Methods Non-linear Struct. Solid. Mech.* 55-62, 1981.

A COMPLEMENTARY LOW AND HIGH ORDER SCHEME FOR UNSTEADY FLOW SIMULATIONS IN COARSE MESHES

***Sanjay Komala Sheshachala, Ruben Sevilla and Oubay Hassan**

Zienkiewicz Centre for Computational Engineering,
College of Engineering, Swansea University SA1 8EN, Wales, UK

*835537@swansea.ac.uk

Summary

Industry-standard, second-order Finite Volume (FV) [1] schemes offer robust solution framework for steady flows but suffer high dissipation and dispersion effects for transient simulations and require excessively refined meshes to accurately capture flow features. In contrast, high-order schemes such as Hybridisable Discontinuous Galerkin (HDG) [2, 3] offer high-fidelity, low dissipation and dispersion solutions at a reasonable cost but lack robust meshing techniques to produce high-quality curvilinear meshes for complex configurations in industrially relevant problems.

The proposed novel FV-HDG combination scheme for transient flows uses the same meshes employed to simulate steady flows, which are partitioned based on element size, wherein, FV is used in elements small enough to provide the desired accuracy and HDG scheme elsewhere. Interface conditions to ensure stability and conservation of the proposed scheme are highlighted. Simulation of the wind gust around aerodynamic objects [4] will be shown to demonstrate the optimal approximation properties of the method and the advantages with respect to standard FV.

Key Words: *Hybridisable Discontinuous Galerkin; Finite Volume; gust flow*

1 Problem statement

Let the computational domain, $\Omega \in \mathbb{R}^{n_{sd}}$, be an open bounded domain with boundary $\partial\Omega$ and n_{sd} be the number of spatial dimensions. It is then partitioned into disjoint domains, Ω^1 for FV and Ω^2 for HDG, such that $\Omega = \Omega^1 \cup \Omega^2$, $\Omega^1 \cap \Omega^2 = \emptyset$, resulting in the FV-HDG interface Γ^{1-2} defined as $\Gamma^{1-2} = \partial\Omega^1 \cap \partial\Omega^2$. With governing compressible Euler equations, the problem can be stated as: Find \mathbf{U} such that,

$$\left\{ \begin{array}{l} \frac{\partial \mathbf{U}}{\partial t} + \frac{\partial \mathbf{F}_l(\mathbf{U})}{\partial x_l} = \mathbf{s}(\mathbf{x}, t) \quad \text{in } \Omega^1 \times [t^0, T] \text{ and } \Omega^2 \times [t^0, T], \\ \llbracket \mathbf{U} \rrbracket = \mathbf{0} \quad \text{on } \Gamma^{1-2} \\ \llbracket \mathbf{F}_l n_l \rrbracket = \mathbf{0} \quad \text{on } \Gamma^{1-2}, \end{array} \right. \quad (1)$$

where $\mathbf{U} = [\rho, \rho \mathbf{v}, \rho E]$ is the vector of conserved variables, $\mathbf{F}_l(\mathbf{U}) = [\rho v_l, \rho v_l \mathbf{v} + p \mathbf{e}_l, (\rho E + p) v_l]$ is the vector of inviscid convective flux along x_l direction and $\mathbf{s}(\mathbf{x}, t)$ is the vector of sources, ρ is the density, \mathbf{v} the velocity, E the specific total energy, p is the thermodynamic pressure of the gas, \mathbf{e}_l is an unitary vector in x_l direction and \mathbf{n} is the outward unit normal vector. Jump conditions denoted by $\llbracket \cdot \rrbracket$, express the *transmission conditions* which requires continuity of variable \mathbf{U} and normal flux $\mathbf{F}_l n_l$ across Γ^{1-2} . Appropriate initial and boundary conditions are applied. Ideal gas equation assumed for the fluid closes the system of equations.

1.1 Hybridisable Discontinuous Galerkin scheme

We assume that Ω^2 is partitioned into n_{e1} subdomains Ω_e^2 with internal interface Γ^2 defined as $\Gamma^2 = [\bigcup_{e=1}^{n_{e1}} \partial\Omega_e^2] \setminus \partial\Omega^2$. HDG defines \mathbf{U}^2 in-terms of its trace $\hat{\mathbf{U}}^2$ defined on the skeleton which includes element faces/edges that lie in the interior and on the boundary of the discretized domain. The problem in (1) for Ω^2 is split into two smaller problems. A local element-by-element problem: Find \mathbf{U}_e^2 in Ω_e^2 for $e = 1, \dots, n_{e1}$ such that

$$\begin{cases} \frac{\partial \mathbf{U}_e^2}{\partial t} + \frac{\partial \mathbf{F}_l(\mathbf{U}_e^2)}{\partial x_l} = \mathbf{s}(\mathbf{x}, t) & \text{in } \Omega_e^2 \times [t^0, T], \\ \mathbf{U}_e^2 = \hat{\mathbf{U}}^2 & \text{on } \partial\Omega_e^2 \end{cases} \quad (2)$$

with supplied initial condition.

The global problem is defined to determine $\hat{\mathbf{U}}^2$ and corresponds to the imposition of the continuity of \mathbf{U} across Γ^{1-2} from (1) and transmission conditions on Γ^2 . Since $\hat{\mathbf{U}}^2$ is unique between adjacent elements, continuity of \mathbf{U}^2 along Γ^2 is automatically satisfied in the local problem. The global problem reads: Find $\hat{\mathbf{U}}^2$ on Γ^2 such that,

$$\begin{cases} \llbracket \mathbf{F}_l n_l^2 \rrbracket = \mathbf{0} & \text{on } \partial\Gamma^2 \\ \boldsymbol{\tau}(\hat{\mathbf{U}}^2, \mathbf{n}^2) (\hat{\mathbf{U}}^2 - \mathbf{U}^1) = \mathbf{0} & \text{on } \partial\Gamma^{1-2} \end{cases} \quad (3)$$

along with incorporating appropriate boundary conditions, where \mathbf{n}^2 is the unit outward normal with respect to $\partial\Omega^2$ and $\boldsymbol{\tau}(\hat{\mathbf{U}}^2, \mathbf{n}^2)$ is the stabilization term defined in the numerical normal flux, whose choice impacts the stability and accuracy of the solution. Numerical normal flux is defined as shown below:

$$\hat{\mathbf{F}}_l n_l^2 = \mathbf{F}_l(\hat{\mathbf{U}}^2) n_l^2 + \boldsymbol{\tau}(\hat{\mathbf{U}}^2, \mathbf{n}^2) (\mathbf{U}^2 - \hat{\mathbf{U}}^2) \quad (4)$$

1.2 Vertex-centred Finite Volume scheme

We begin with the partition of Ω^1 into control volumes V_i^1 generated by median dual approach for n_{mn} mesh nodes. Integral form of the conservation equation in (1) after application of the divergence theorem results in the following volume and surface integrals. The problem reads: Find \mathbf{U}^1 in V_i^1 , for $i = 1, \dots, n_{mn}$,

$$\int_{V_i^1} \frac{\partial \mathbf{U}^1}{\partial t} dV + \int_{\partial V_i^1} \mathbf{F}_l(\mathbf{U}^1) n_l^1 dS = \int_{V_i^1} \mathbf{s}(\mathbf{x}, t) dV, \quad (5)$$

where \mathbf{n}^1 is the unit outward normal with respect to $\partial\Omega^1$. The surface integral in (5) can now be modified to include the continuity of normal flux across Γ^{1-2} from (1) as shown below:

$$\int_{\partial V_i^1} \mathbf{F}_l(\mathbf{U}^1) n_l^1 dS = \int_{\partial V_i^1 \setminus \Gamma^{1-2}} \mathbf{F}_l(\mathbf{U}^1) n_l^1 dS + \int_{\partial V_i^1 \cap \Gamma^{1-2}} \mathbf{F}_l(\hat{\mathbf{U}}^2) n_l^1 + \boldsymbol{\tau}(\hat{\mathbf{U}}^2, \mathbf{n}^1) (\hat{\mathbf{U}}^2 - \mathbf{U}^2) dS \quad (6)$$

1.3 Algebraic system of equations

The discretisation of the weak forms of (2) and (3) and the integral form in (5) results in an algebraic system of equations as shown below

$$\begin{pmatrix} \mathbf{A}^{U^1, U^1} & \mathbf{A}^{U^1, U^2} & \mathbf{A}^{U^1, \hat{U}^2} \\ \mathbf{0} & \mathbf{A}^{U^2, U^2} & \mathbf{A}^{U^2, \hat{U}^2} \\ \mathbf{A}^{\hat{U}^2, U^1} & \mathbf{A}^{\hat{U}^2, U^2} & \mathbf{A}^{\hat{U}^2, \hat{U}^2} \end{pmatrix} \begin{bmatrix} \mathbf{U}^1 \\ \mathbf{U}^2 \\ \hat{\mathbf{U}}^2 \end{bmatrix} = \begin{bmatrix} \mathbf{R}^{U^1} \\ \mathbf{R}^{U^2} \\ \mathbf{R}^{\hat{U}^2} \end{bmatrix} \quad (7)$$

The two schemes are solved in a monolithic fashion after performing the static condensation as indicated below:

$$\begin{pmatrix} \mathbf{A}^{U^1, U^1} & \left(\mathbf{A}^{U^1, \hat{U}^2} - \mathbf{A}^{U^1, U^2} \mathbf{Z}^{U^2, \hat{U}^2} \right) \\ \mathbf{A}^{\hat{U}^2, U^1} & \left(\mathbf{A}^{\hat{U}^2, \hat{U}^2} - \mathbf{A}^{\hat{U}^2, U^2} \mathbf{Z}^{U^2, \hat{U}^2} \right) \end{pmatrix} \begin{bmatrix} \mathbf{U}^1 \\ \hat{\mathbf{U}}^2 \end{bmatrix} = \begin{bmatrix} \mathbf{R}^{U^1} - \mathbf{A}^{U^1, U^2} \mathbf{F}^{U^2} \\ \mathbf{R}^{\hat{U}^2} - \mathbf{A}^{\hat{U}^2, U^2} \mathbf{F}^{U^2} \end{bmatrix} \quad (8)$$

where, $\mathbf{Z}^{U^2, \hat{U}^2} = \mathbf{A}^{U^2, U^2} \mathbf{A}^{U^2, \hat{U}^2}$ and $\mathbf{F}^{U^2} = \mathbf{A}^{U^2, U^2} \mathbf{R}^{U^2}$.

2 Numerical example

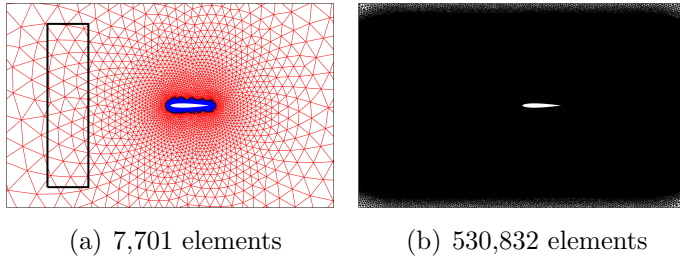


Figure 1: Meshes employed in the gust study.

Comparison of FV and FV-HDG scheme for gust flow over NACA0012 airfoil is performed. Mesh suited for steady-state solution (without gust) in Figure. 1(a) is used for gust simulation with proposed FV-HDG scheme. The black rectangle shows the region of the sinusoidal gust generation using source terms in (1). The figure also shows segregation based on element size, Ω^1 in blue, Ω^2 in red and Γ^{1-2} in black. Figure. 1(b) shows mesh refinement in the gust path required for the FV scheme. Vorticity of flow field is plotted in Figure. 2 and variation in lift coefficient is shown in Figure. 3 for the different cases listed in Table 1. FV scheme is highly dissipative and dispersive in coarse meshes and require fine elements. On the other hand, FV-HDG scheme offers high-fidelity solution in coarse elements with significantly reduced memory and CPU requirement.

Case	Mesh	Scheme	DOF	CPU time (hh:mm:ss)	Dissipation (%)	Dispersion (%)
1	Figure. 1(a)	Implicit FV	15,760	00:07:12	86.21	18.75
2	Figure. 1(b)	Implicit FV	530,832	43:39:51	0.13	-0.36
3	Figure. 1(a)	FV-HDG $k = 1$	67,240	00:28:38	14.35	3.13
4	Figure. 1(a)	FV-HDG $k = 2$	93,716	01:24:44	2.17	3.13

Table 1: Comparison of schemes for gust flow problem

3 Conclusions

The paper proposed a novel combination of high order HDG and low order FV schemes to solve transient flow problems. The details of interface treatment was highlighted. The advantages and efficacy of

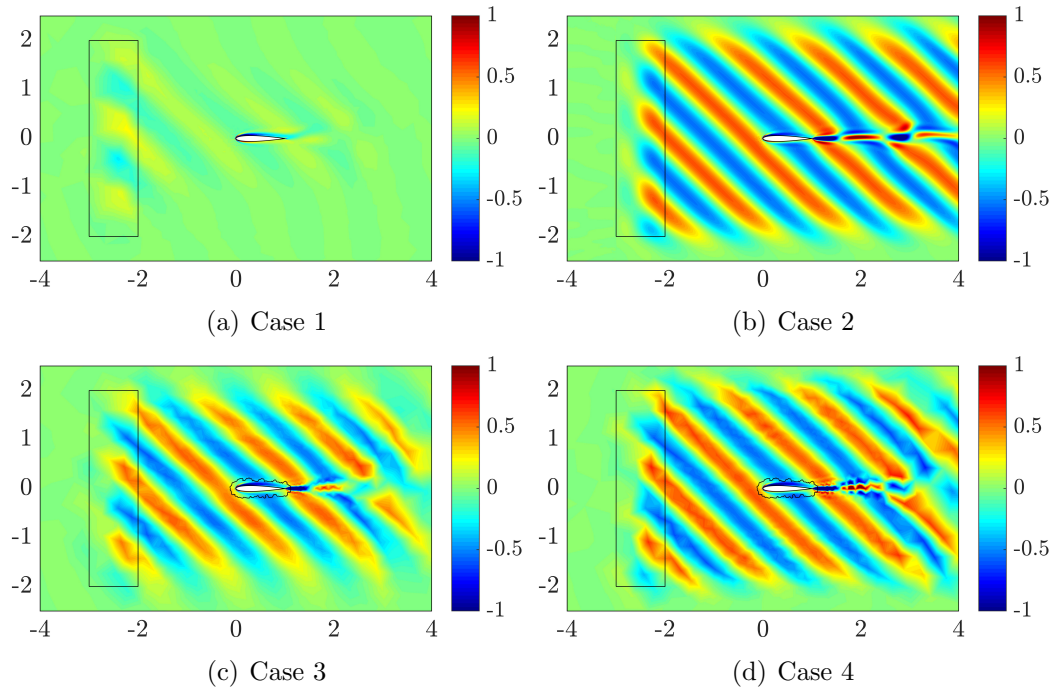


Figure 2: Vorticity plots for various cases shown in Table 1

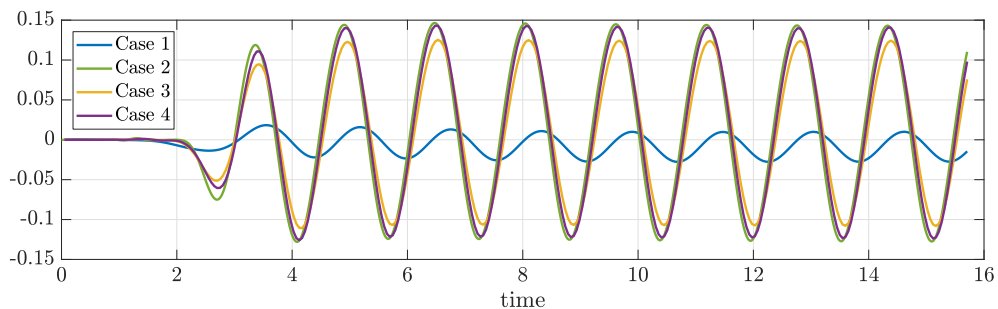


Figure 3: Variation in lift coefficient (normalised with respect to steady state value) for various cases shown in Table 1

the combined scheme with respect to existing second order FV scheme was shown in terms of reduced memory and computational costs for the transient wind gust simulations.

References

- [1] K. A. Sørensen and O. Hassan and K. Morgan and N. P. Weatherill, A multigrid accelerated hybrid unstructured mesh method for 3D compressible turbulent flow *Computational Mechanics*, Vol. **31**(1-2), pp. 101–114, 2003.
- [2] J. Peraire and N.C. Nguyen and B. Cockburn, A Hybridizable Discontinuous Galerkin method for the compressible Euler and Navier-Stokes equations, *AIAA*, 2010-363, 2010.
- [3] R. Sevilla and A. Huerta, *Advanced Finite Element Technologies*. Tutorial on Hybridizable Discontinuous Galerkin (HDG) for second-order elliptic problems, Springer International Publishing, 2016.
- [4] V. Golubev, B. Dreyer, T. Hollenshade M. Visbal, High-Accuracy Viscous Simulation of Gust-Airfoil Nonlinear Aeroelastic Interaction, *39th AIAA Fluid Dynamics Conference*, 2009-4200, 2009

MODELLING OF CRACK PROPAGATION IN HETEROGENEOUS MATERIALS LIKE BONES

*Karol Lewandowski¹, Łukasz Kaczmarczyk¹, John F. Marshall² and Chris J. Pearce¹

¹School of Engineering, The University of Glasgow, Glasgow, UK, G12 8LT

²School of Veterinary Medicine, The University of Glasgow, Glasgow, UK, G61 1QH

*k.lewandowski.1@research.gla.ac.uk

Abstract

Fractures of the metacarpal condyle are a common orthopaedic injury in Thoroughbred racehorses [1]. A large proportion of injuries occur in the absence of a specific traumatic event and show typical characteristics of stress fractures. The purpose of this work is to develop a combined remodelling and fracture finite element based framework allowing for integrated simulation of equine 3rd metacarpal remodelling under specific exercise regime (boundary conditions), followed by crack propagation analysis. Such an approach may help to better understand the correlation between high exercise intensity, bone adaptation and fracture risk, ultimately improving the welfare of the racehorse. The authors' bone remodelling model, presented in [2], provides the prediction of bone material distribution. Assessment of the fracture risk is conducted by evaluating the strain release energy rate within the context of configurational mechanics [3]. The implemented framework provides a robust, accurate and energy consistent method for quantifying the influence of bone adaptation on the fracture propensity. Performance of the presented method is demonstrated by the numerical example of crack propagation in a heterogeneous plate in 3D. The proposed approach is fully implemented in open-source finite element library MoFEM [4]. The promising results of this study offer a novel framework to simulate crack propagation in bones, followed by bone adaptation, potentially providing better insight into quantifying propensity for fracture.

Key Words: *crack propagation; configurational mechanics; heterogeneity; racehorse; bone;*

1 Introduction

Fractures of the third metacarpal bone are one of the main reasons for euthanasia of Thoroughbred racehorses on racecourses in the UK [1]. Most of these fractures occur due to the accumulation of tissue fatigue as a result of repetitive loading rather than a specific traumatic event. The bone repair is overwhelmed by load-induced bone densification that also increases brittleness which ultimately results in fatal injury. An efficient and accurate method to predict the fracture risk and prevent these types of injuries would significantly improve horse welfare. Therefore, the development of computational tools with the capability to estimate bone resistance to fracture is potentially viable and robust solution. The goal of this study is to explore the potential of a computational framework based on the Finite Element Method to quantify fracture resistance of heterogeneous bodies (like bones) using linear fracture mechanics for brittle materials.

Although the crack propagation in heterogeneous materials has been widely investigated in continuum mechanics, this remains a challenging topic. In the proposed approach the physical and mathematical descriptions makes it possible to determine whether the crack will propagate and how far will it move for particular loadings and local material properties. It can be achieved by solving the conservation of momentum in both the spatial and material domains. Furthermore, the equilibrium of the crack front is established in a thermodynamically consistent manner. The configurational forces, driving the crack

growth, are hereby balanced with the material resistance arising from Griffith's criterion for brittle fracture. The approach is based on the principle of maximum dissipation for elastic solids with a restriction that energy is released only for the creation of new crack surfaces. This approach has been successfully adopted by many researchers in the context of homogeneous materials, e.g. [5]. For the numerical implementation, the Finite Element Method is solved within an Arbitrary Lagrangian-Eulerian (ALE) formulation in order to describe the movement of the nodes independently from the material, thus preserving the mesh quality.

2 Kinematics of crack propagation

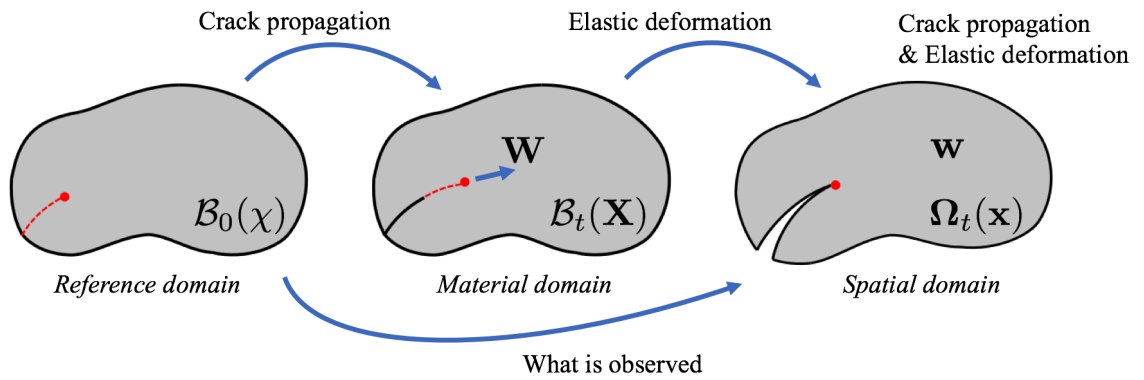


Figure 1: Elastic deformation and configurational change of a body due to crack propagation.

In the context of configurational mechanics, an elastic body with an initial crack, as visualised in Figure 1, is considered. To independently observe the deformation of the material in physical space Ω_t and the evolution of the crack surface in material space \mathcal{B}_t , it is convenient to decompose the problem into separate configurations. The physical, material and spatial displacements are expressed as follows:

$$\mathbf{u} = \mathbf{x} - \mathbf{X}, \quad \mathbf{W} = \mathbf{X} - \chi \quad \text{and} \quad \mathbf{w} = \mathbf{x} - \chi \quad (1)$$

3 Implementation

In the context of the finite element method, fields are approximated in the current material and current spatial spaces. Three-dimensional domains are discretised with tetrahedral finite elements with hierarchical basis functions of arbitrary polynomial order, following the work of Ainsworth and Coyle [6]. Moreover, the density field (derived for example from CT scanning) is approximated by meshless Moving Weighted Least Squares. It should be also noted that MWLS shape functions are evaluated at current material points \mathbf{X} ; therefore such an approximation is independent of changes in the material configuration (changing mesh). The resulting residuals in the spatial and material domain, that represent the two primary nonlinear equations that need to be solved, are expressed as follows:

$$\mathbf{r}^x = \lambda \mathbf{f}^{\text{s,ext}} - \mathbf{f}^{\text{s,int}}, \quad \mathbf{r}^X = \mathbf{f}^{\text{m,res}} - \mathbf{f}^{\text{m,driv}} - \mathbf{f}^{\text{m,inh}} \quad (2)$$

where λ is the load factor of the external load ($\mathbf{f}^{\text{s,ext}}$), vector $\mathbf{f}^{\text{s,int}}$ represents internal forces, $\mathbf{f}^{\text{m,res}}$ is the material resistance, $\mathbf{f}^{\text{m,driv}}$ is the crack driving force vector and finally, the main novelty of the

presented work, $\mathbf{f}^{\text{m,inh}}$ is a fictitious force, directed from the denser part of the material to the less dense part. Above equations are linearised and solved using the Newton-Raphson method. Furthermore, an arc-length method is adopted to control the dissipative load path for fracture propagation, using the crack surface area as a control. The spatial internal force vector is expressed as:

$$\mathbf{f}^{\text{s,int}} = \int_{\mathcal{B}_t^h} \nabla_{\mathbf{X}} \Phi^T \mathbf{P}^h(\mathbf{F}^h, \rho^h) dV \quad (3)$$

Note that the approximated Piola-Kirchhoff stress tensor \mathbf{P}^h , depends on both deformation gradient \mathbf{F}^h and density ρ^h . Moving on, the material driving force takes the following form:

$$\mathbf{f}^{\text{m,driv}} = \int_{\mathcal{B}_t^h} \nabla_{\mathbf{X}} \Phi^T \Sigma^h dV \quad (4)$$

The vector of additional configurational forces arising from material defects and inhomogeneities can be expressed as:

$$\mathbf{f}^{\text{m,inh}} = \int_{\mathcal{B}_t^h} \Phi^T \frac{\partial \Psi^h}{\partial \rho^h} \left(\frac{\partial \rho^h}{\partial \mathbf{X}} \right) dV \quad (5)$$

where Σ^h and Ψ^h is the Eshelby stress tensor and elastic strain energy, respectively. Lastly, the vector of nodal material resistance forces is given as:

$$\mathbf{f}^{\text{m,res}} = \frac{1}{2} (\tilde{\mathbf{A}}_{\Gamma}^h)^T \mathbf{g}_c \quad (6)$$

where \mathbf{g}_c is a vector of size equal to the number of nodes in the mesh, with zero for all components except those associated with nodes on the crack front, where the value is g_c (Griffith energy). The matrix $(\tilde{\mathbf{A}}_{\Gamma}^h)^T$ defined in [5], has dimensions of length and describes the current orientation of the crack surface. It is worth to emphasise that configurational forces and resistance forces are evaluated at the crack front nodes only.

4 Numerical example

To demonstrate the performance of the model for quasi-static loading, a numerical example is presented which considers a thin plate subjected to the 3-point loading. The model is spatially discretised using 2nd order tetrahedrons. The analysis is conducted for three different meshes consisting of 1340, 5145 and 10341 elements. The force is applied in the middle top of the plate. The material density is prescribed by function of model coordinates: $\rho(x,y,z) = 2x + 1$. Similar to bones, Young's modulus depends on the density in a power law model of the form: $E = a\rho^n$, where coefficients a and n are chosen to be 1 and 2, respectively. The crack is initialised in the middle bottom of the plate.

Figure 2a) shows that configurational forces are driving the crack in the direction opposite to the density gradient. It should be noted that the crack path is smooth even for a coarse mesh thanks to the state of the art mesh cutting algorithm implemented in MoFEM [4]. The load-displacement curves in Figure 2b) demonstrate that the results for the consecutive refinements are converging. These preliminary results indicate the ability of the formulation to accurately and robustly predict crack paths for heterogeneous bodies without bias from the original mesh.

5 Conclusions

In this study, the basis for crack propagation in heterogeneous bodies such as bones using configurational mechanics has been presented. The highly nonlinear system of equations are implemented in and solved

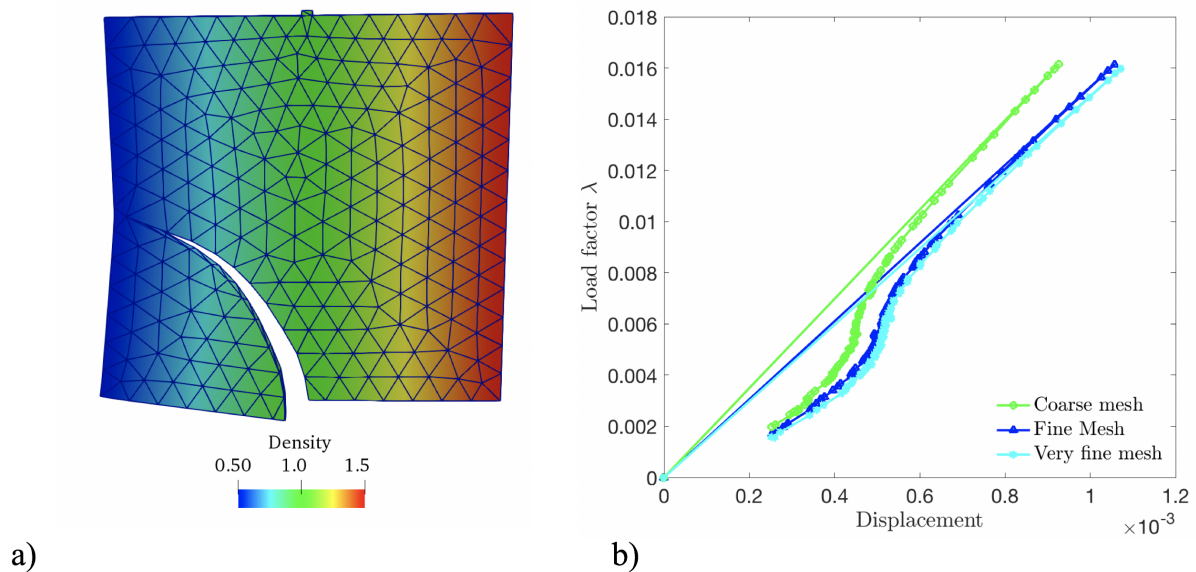


Figure 2: Heterogeneous 3D plate. a) model geometry with predicted crack, material distribution and coarse discretisation with 1340 tetrahedral elements. b) load-displacement response for three consecutive h-refinements.

using MoFEM. Performance of the model is demonstrated for an example problem comprising a plate with non-uniform material distribution. The developed framework has proved to be robust and fully capable of simulating crack propagation in heterogeneous bodies like bones, which will be the scope of authors' future studies.

References

- [1] TD Parkin, PD Clegg, NP French, CJ Proudman, CM Riggs, ER Singer, PM Webbon, and KL Morgan. Risk of fatal distal limb fractures among Thoroughbreds involved in the five types of racing in the United Kingdom. *The Veterinary Record*, 154(16):493–497, 2004.
- [2] Karol Lewandowski, Łukasz Kaczmarczyk, John F. Marshall, and Chris J. Pearce. Numerical analysis of bone remodelling for equine 3rd metacarpal. In *Proceedings of the 25th UKACM Conference on Computational Mechanics*, United Kingdom, 2017. University of Birmingham.
- [3] Łukasz Kaczmarczyk, Zahur Ullah, and Chris J Pearce. Energy consistent framework for continuously evolving 3d crack propagation. *Computer Methods in Applied Mechanics and Engineering*, 324:54–73, 2017.
- [4] Lukasz Kaczmarczyk, Zahur Ullah, Karol Lewandowski, Xuan Meng, Xiao-Yi Zhou, Chris Pearce, Athanasiadis. Ignatios, Hoang Nguyen, Christophe-Alexandre Chalons-Mouriesse, Euan Miur, and et al. Mofem-v0.8.16. Nov 2018. <http://mofem.eng.gla.ac.uk>.
- [5] Łukasz Kaczmarczyk, Mohaddeseh Mousavi Nezhad, and Chris Pearce. Three-dimensional brittle fracture: configurational-force-driven crack propagation. *International Journal for Numerical Methods in Engineering*, 97(7):531–550, 2014.
- [6] Mark Ainsworth and Joe Coyle. Hierarchic finite element bases on unstructured tetrahedral meshes. *International journal for numerical methods in engineering*, 58(14):2103–2130, 2003.

A STUDY ON FIBRE KINKING CRITERIA FOR UNIDIRECTIONAL CFRPs UNDER OFF-AXIS COMPRESSION AT QUASI-STATIC AND DYNAMIC LOADING RATES

*Daniel M. Thomson¹, Gustavo Quino¹, Hao Cui², Borja Erice³ and Nik Petrinic¹

¹Department of Engineering Science, University of Oxford, OX1 3PJ, United Kingdom

²School of Aerospace, Transport and Manufacturing, Cranfield University, MK43 0AL, United Kingdom

³Department of Structural Engineering, Norwegian University of Science and Technology, NO-7491, Norway

*daniel.thomson@eng.ox.ac.uk

Summary

The failure mechanisms of fibre kinking in fibre reinforced polymers (FRPs) have been a topic of interest for many years. Starting with Rosen and Argon's work in 1965 and 1972 [1,2], the prediction of fibre kinking failure has typically been treated as a buckling instability problem of the reinforcing fibres in a polymeric matrix. Since then, theories based on this idea have grown increasingly elaborate, with the addition of initial waviness in the fibres and non-linear stress-strain behaviour in the matrix due to yielding and damage [3,4]. However, while these theories have been proven accurate for the prediction of uniaxial compression failure, confidence in their ability to predict more complex loading cases has not been so firmly established.

In this work, new experimental data from a series of off-axis compression tests at quasi-static [5] and dynamic loading rates is used to study the effects of shear and strain-rate on fibre kinking failure. These results are compared against predictions from leading failure criteria to comment on their accuracy outside of the quasi-static uniaxial compression case, for which they have been thoroughly validated in the past, and identify potential areas for improvement.

Key Words: *CFRP; Fibre kinking; Failure criteria; Rate-dependency.*

Introduction

Longitudinal compression failure in CFRP laminates has long been associated with micro-scale buckling of the fibres, also known as fibre kinking, which is strongly dependent on the properties of the matrix material. For the case of uniaxial compression, beam buckling theories for thin columns in an elastic or elasto-plastic medium have been used to accurately predict the material strength in the past [1-4]. However, few models have been expanded beyond quasi-static uniaxial compression and a lack of experimental data for more complex loading cases has made these models difficult to validate.

Recent experimental work in [5] investigated the effect of shear on the fibre compression strength in CFRP laminates at quasi-static strain rates. Since then, an additional series of high strain-rate tests has been carried out using a Split-Hopkinson Pressure Bar (SHPB) system to study how the previous results change under dynamic loading conditions. With this new data, advanced fibre kinking theories can be more adequately evaluated than what was previously possible. In particular, their ability to predict the effects of combined loads and different strain-rates will be investigated.

Fibre kinking failure criteria

As mentioned, most advanced fibre kinking theories are based on the original work by Rosen [1], where failure was predicted as elastic micro-buckling using a beam buckling model for parallel, perfectly aligned columns in an elastic medium. This gave a compressive strength of the from:

$$\sigma_c = \frac{G_b}{(1 - \nu_f)} = G \quad (1)$$

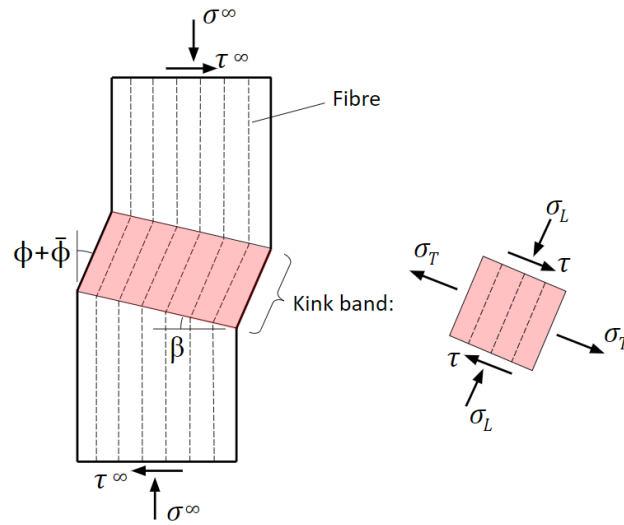


Figure 1: Kink band geometry and notation.

Where G_b is the shear modulus of the matrix and v_f the fibre volume fraction, resulting in a compressive strength equivalent to the shear modulus of the composite G , which severely over-predicted the strength of the material.

In 1972, Argon [2] argued that composites undergo plastic rather than elastic microbuckling, with kinking originating at misaligned fibres. This paved the way for the work by Budiansky and Fleck [3], who built on these theories to include the effects of fibre rotation and nonlinear shear behaviour in the matrix by solving the equilibrium of the assumed kink-band geometry (Figure 1), giving:

$$\sigma_c - 2\tau^\infty \tan\beta = \max \left(\frac{\tau - \tau^\infty + \sigma_T \tan\beta}{\phi + \bar{\phi}} \right) \xrightarrow{\tau^\infty=0} \sigma_c \approx \frac{G^*}{1 + nk^{1/n} \left(\frac{\bar{\phi}/\gamma_Y^*}{n-1} \right)^{(n-1)/n}} \quad (2)$$

With $G^* = \alpha^2 G$, $\gamma_Y^* = \frac{\tau_Y}{\alpha}$, and $\alpha = \sqrt{1 + \left(\frac{\sigma_{TY}}{\tau_Y} \right)^2 \tan^2 \beta}$. Where G is the shear modulus of the composite, $\bar{\phi}$ is the initial fibre misalignment and β the kink band angle; σ_{TY} and τ_Y are yield stresses in transverse tension and shear; and n , k and γ_Y are nonlinear shear parameters for a Ramberg-Osgood relation that fits the material response.

For off-axis compression, however, the solution becomes much more complicated and cannot be found analytically (an iterative approach is described in [3]).

On the other hand, Pinho [4] proposed an alternative numerical criterion for more general loading cases based on the same principles. In his model, a three-dimensional stress state can be rotated onto the fibre misalignment frame, where stability and matrix failure criteria are evaluated through iteration. Shear stresses in the rotated frame contribute to additional fibre rotation, which, in turn, may increase the shear stress in the misalignment frame. If a stable solution can be found, potential failure of the matrix is then evaluated using an Inter-Fibre Fracture (IFF) criterion:

$$\begin{cases} f_{kink} = \left(\frac{\tau_T}{S_T - \mu_T \sigma_n} \right)^2 + \left(\frac{\tau_L}{S_L - \mu_L \sigma_n} \right)^2 = 1 & \text{for } \sigma_b \leq 0 \\ f_{kink} = \left(\frac{\sigma_n}{Y_T} \right)^2 + \left(\frac{\tau_T}{S_T} \right)^2 + \left(\frac{\tau_L}{S_L} \right)^2 = 1 & \text{for } \sigma_b > 0 \end{cases} \quad (3)$$

Where σ_b is the transverse stress on the misalignment frame; σ_n , τ_T and τ_L are normal and shear

stresses on the IFF plane; and Y_T , S_T and S_L are the normal and shear strength properties of the composite, with frictional parameters μ_T and μ_L .

Strain-rate effects

While none of the above failure criteria were developed with rate-dependency in mind, they can be adapted for dynamic loading relatively easily. These models all have in common that they predict fibre kinking failure based on the initial fibre misalignment and the nonlinear shear stress-strain response of the composite. If the nonlinear shear properties are made rate-dependent, the same criteria should be able to predict the dynamic compressive strength with no further modifications. Following the approach described in [6], the quasi-static shear stress-strain properties can be scaled by a function $f(\dot{\epsilon})$ to obtain the dynamic value for a given strain-rate, $\dot{\epsilon}$:

$$f(\dot{\epsilon}) = 1 + \sqrt{K\dot{\epsilon}} \quad (4)$$

Experimental results

The experimental data for this work was obtained from the quasi-static tests in [5] and a subsequent series of high-rate tests using a SHPB system. A Hexcel[®] IM7-8552 cross-ply laminate with $[90^\circ, 0^\circ]_{4s}$ stacking sequence and 60% volume fraction was used to manufacture dogbone compression specimens (Figure 2), which were machined with a water jet cutter at 4 orientations ($\alpha = 0^\circ, 3^\circ, 6^\circ$ and 10°) to produce different combinations of longitudinal compression and shear.

Quasi-static compression tests were performed using a Zwick Z250 screw-driven machine at $0.001s^{-1}$. The load history was obtained from the 20kN load cell mounted on the testing rig, while the deformations were obtained from digital image correlation (DIC) of the test footage.

The dynamic compression tests were carried out on a Split Hopkinson Pressure Bar system at approximately $100s^{-1}$. The load on the specimen was calculated from strain gauge signals along the bars using one-dimensional wave theory. The strains were obtained from DIC on photos acquired at a rate of 500000fps using a Kirana high-speed camera from Specialised Imaging.

In both cases, the stress state in the longitudinal plies was extracted using classical laminate theory as described in [5] in order to produce the failure envelopes in Figure 2.

In addition, in-house data on the in-plane shear response of the material at strain rates from quasi-static to around $300s^{-1}$ was used to calibrate the rate-dependency of the different failure criteria.

Analysis and discussion

Both Budiansky and Fleck's [3] and Pinho's [4] failure criteria were evaluated for different combinations of longitudinal compression (σ_{11}) and shear (τ_{12}) using the rate-dependent nonlinear shear data for IM7-8552 and an initial misalignment angle of 1.85° (calibrated from the quasi-static uniaxial compression case). The results are shown against the experimental data in Figure 2 where it can be seen that both scale well with the strain-rate. However, Pinho's model, where the kinking strength appears to decrease linearly towards the in-plane shear strength, severely overpredicts the effects of shear. The model by Budiansky and fleck, on the other hand, shows a much closer match with the experimental results and may be improved even further by considering the effects of transverse compression, which increases with the off-axis angle α and was neglected in this study.

However, Budiansky and Fleck's only considers fibre kinking caused by plastic micro-buckling instability and can follow the shear stress-strain relation even beyond the matrix strength limit, whereas Pinho's model includes the consideration for matrix failure (IFF), which would seem to make physical sense but causes an under-prediction of the kinking strength.

Conclusions

Leading failure criteria for fibre kinking under combined loads have been compared against new quasi-

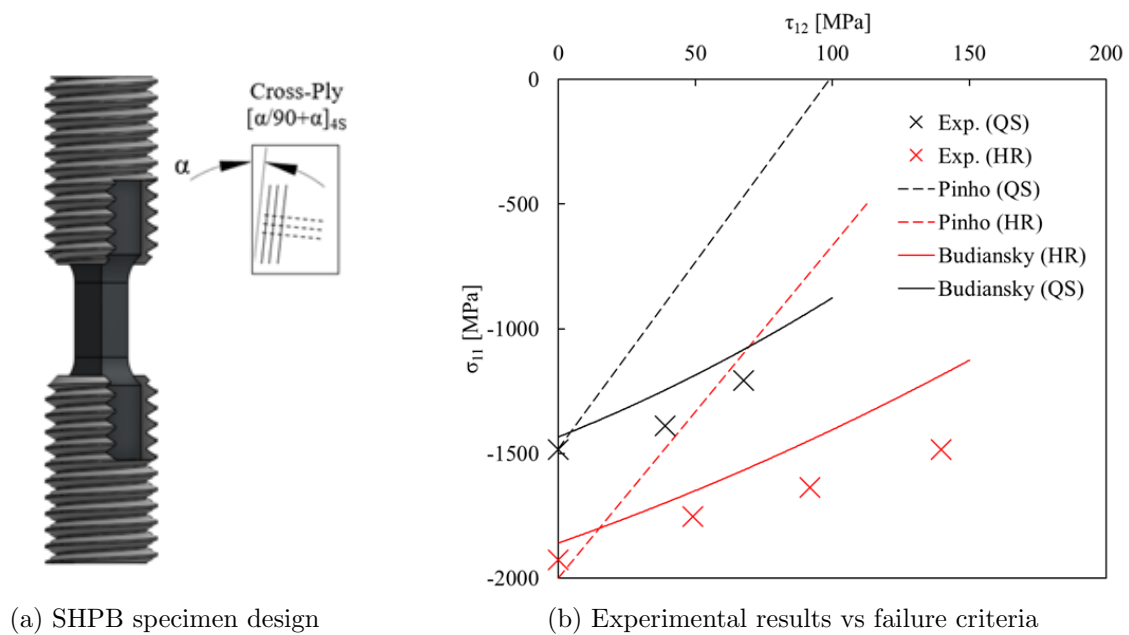


Figure 2: Summary of experimental data obtained for Hexcel[®] IM7-8552 CFRP at quasi-static and high strain-rates for different combinations of longitudinal compression (σ_{11}) and shear (τ_{12}) using off-axis cross-ply compression specimens ($\alpha = 0, 3, 6$ and 10°).

static and high-rate off-axis compression data to evaluate their performance in the prediction of more complex loading outside of the typical case of uniaxial compression. These new results highlight the limitations of available fibre kinking theories and may point to potential improvements in this area.

Acknowledgements

The authors would like to acknowledge Rolls-Royce plc, for their continuing support through the Solid Mechanics University Technology Centre at the University of Oxford.

References

- 1 B. W. Rosen. Mechanics of composite strengthening. *Fiber Composite Materials, Seminar of the American Society for Metals*, 37-75, 1965.
- 2 A. S. Argon. Fracture of composites. *Treatise of Materials Science and Technology*, Vol. 1, 79-114, 1972.
- 3 B. Budiansky and N. A. Fleck. Compressive failure of fibre composites. *Journal of the Mechanics and Physics of Solids*, 41, no. 1, 183-211, 1993.
- 4 S. T. Pinho, L. Iannucci, and P. Robinson. Physically-based failure models and criteria for laminated fibre-reinforced composites. Part I: Development. *Composites Part A: Applied Science and Manufacturing*, 37, 63-73, 2006.
- 5 D. M. Thomson, H. Cui, B. Erice and N. Petrinic. A study on the longitudinal compression strength of fibre reinforced composites under uniaxial and off-axis loads using cross-ply laminate specimens. *Composites Part A: Applied Science and Manufacturing*, (in press).
- 6 J. Wiegand. Constitutive modelling of composite materials under impact loading. PhD thesis, Department of Engineering Science, University of Oxford, 2008.

On improving the accuracy of the material point method with simplex elements

L. Wang^{1*}, W.M. Coombs^{1*}, C.E. Augarde¹, M. Brown², J. Knappett², A. Brennan², C. Davidson², D. Richards³, A. Blake³

1) Department of Engineering, Durham University, Durham, UK

* lei.wang@durham.ac.uk, w.m.coombs@durham.ac.uk

2) School of Science & Engineering, University of Dundee, Dundee, UK

3) Faculty of Engineering and the Environment, University of Southampton, Southampton, UK

Abstract

The material point method (MPM) is a relatively new numerical tool that is ideally suited to model problems involving very large deformations. It achieves this by decoupling the background mesh, which is used for computation, from the material points that represent the deforming body; removing the issues associated with mesh distortion/entanglement in the finite element method. However, the method only robust when using low order (linear) background elements due to extreme cell-crossing instabilities that occur with higher order elements. These low order elements are susceptible to volumetric locking when modelling near incompressible materials. This paper presents an $\bar{\mathbf{F}}$ -patch MPM for simplex elements (linear triangles and tetrahedra) that not only removes the locking issue but also reduces the stress oscillations seen in the standard MPM.

1 Introduction

The Material Point Method (MPM) is a promising method for modelling problems involving large deformations, which are seen in different areas of engineering, e.g. the biological soft tissue, rubber and soil. One difficulty when modelling these types of materials is volumetric locking, which is associated with material incompressibility. This issue will lead to overly stiff global force-displacement predictions and severe stress oscillations through the domain. In order to solve this issue in the Finite Element Method (FEM), several approaches [1, 2] have been proposed. With quadrilateral elements, the $\bar{\mathbf{F}}$ method [1] is recognised as an effective method to overcome volumetric locking whilst being relatively simple to implement. This method has recently been extended to the MPM [3]. However, tetrahedral meshes are preferred for some problems, due to being able to discretise complex geometries and also allow for local refinement. For simplex elements (linear tetrahedra/triangles) the $\bar{\mathbf{F}}$ -patch method [2] has been proposed to avoid volumetric locking in the FEM. This paper extends the $\bar{\mathbf{F}}$ -patch method such that it can be applied to the MPM. As part of this extension, we propose a systematic method to form the patch and demonstrate that the $\bar{\mathbf{F}}$ -patch MPM avoids the volumetric locking issue via several examples. We also find that the $\bar{\mathbf{F}}$ -patch MPM reduces stress oscillations, which are often attributed to cell-crossing.

2 $\bar{\mathbf{F}}$ -patch formulation

Following [2], the essential idea of the $\bar{\mathbf{F}}$ -patch method is to modify the deformation gradient for an element with consideration of all elements in a surrounding “patch”. For example, for the element e in a patch \mathcal{P} , the deformation gradient is modified into the following form

$$\bar{\mathbf{F}}_e = \left[\frac{v_{patch}}{V_{patch}(\det \mathbf{F}_e)} \right]^{1/3} \mathbf{F}_e, \quad (1)$$

where \mathbf{F}_e is the deformation gradient obtained from the standard displacement interpolation and v_{patch} and V_{patch} denote, respectively, the deformed and undeformed volume of the patch. As a result, the computation of the internal force and element tangent stiffness are also modified. For the internal force calculation, it is necessary to replace \mathbf{F}_e by $\bar{\mathbf{F}}_e$ when calculating the appropriate stress measure. The tangent stiffness of an element e also has contributions from all elements in its patch.

The method for formation of a patch is arbitrary in [2]. This paper proposes a systematic method to forming a patch. In this method, a quadratic mesh is generated firstly, and then each quadratic element

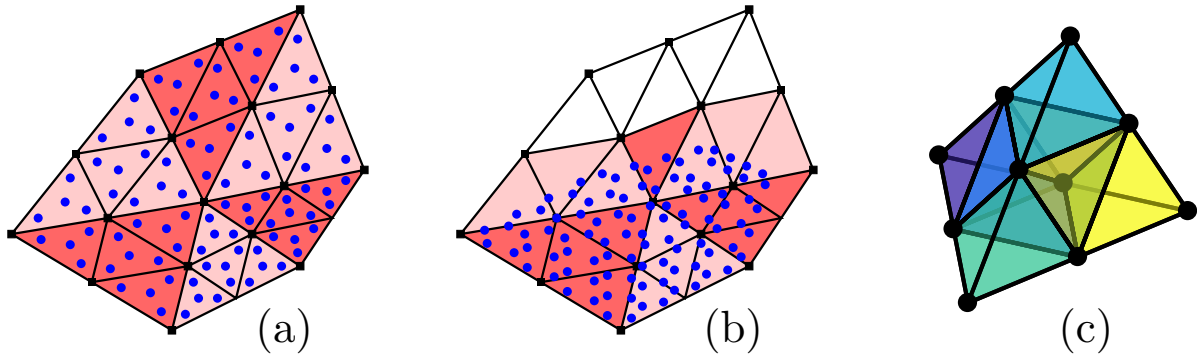


Figure 1: The patches and material points: (a) a 6-node triangle is decomposed to 4 linear triangular elements with the same colour, forming a patch in 2D, (b) the patches are updated as material points move, and (c) a 10-node tetrahedron is decomposed to 8 linear tetrahedral elements, forming a patch in 3D.

is subdivided to linear elements, forming a patch. As shown in Figure 1 (a), the 6-node triangular mesh is firstly generated in 2D, and then each element is subdivided to 4 linear triangular elements. In 3D, the 10-node tetrahedral mesh is firstly generated, and then each element is subdivided to 8 linear tetrahedral elements, as seen in Figure 1 (c). In the MPM, these patches need to be updated with the movement of material points. Only elements enclosing material points in the initial patch forms a new patch. As shown in Figure 1 (b), the patch at the top right includes three elements and the patch at the top middle includes one element after the positions of material points are updated.

3 Numerical examples

The section presents two numerical examples to show that the performance of the $\bar{\mathbf{F}}$ -patch MPM. All of the examples use a linear-elastic, perfectly plastic associated flow constitutive model with a von Mises yield function. The von Mises yield function has the following form

$$f = \varrho - \varrho_y = 0, \quad (2)$$

where ϱ_y is the yield strength of the material and $\varrho = \sqrt{2J_2}$, J_2 is the second principal invariant of the stress deviator tensor.

3.1 Footing

The first example is a 3D footing problem. Because of symmetry, only a quarter of the model is considered. As shown in Figure 2 (a), a cuboid domain with edge length, $L=5$ m and the footing area is a square with edge length, $l=0.5$ m. The material parameters are $E=10$ GPa, $\nu=0.48$, and $\varrho_y=0.85$ MPa. The bottom and all of the vertical forces are constrained by roller boundary conditions, and the footing area is subjected to a displacement of $u=2$ mm in 20 load steps. The physical domain is discretised to 921 nodes and 4176 elements, with local refinement in the region under the footing area, as shown in Figure 2 (b). There are 11 material points per element in the initial mesh. The magnitude of reaction force against displacement in Figure 2 (c) shows that the force erroneously increases with the standard MPM after the material has been yielded. This error is due to the volumetric locking, and it is avoided by the $\bar{\mathbf{F}}$ -patch MPM. In addition, we find that the stress oscillation is reduced with the $\bar{\mathbf{F}}$ -patch MPM, as shown in Figure 3.

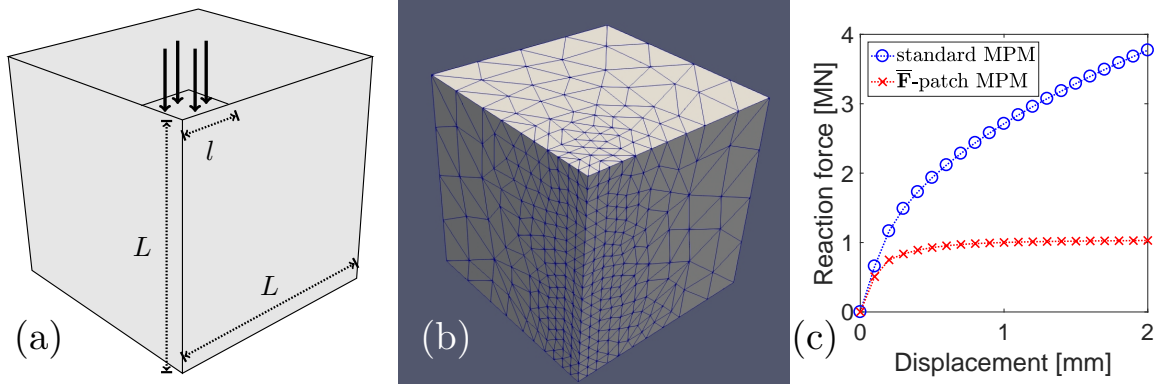


Figure 2: 3D footing problem: (a) roller on bottom, left and right surfaces; displacement is applied on the footing square; (b) computational mesh; (c) reaction force against displacement.

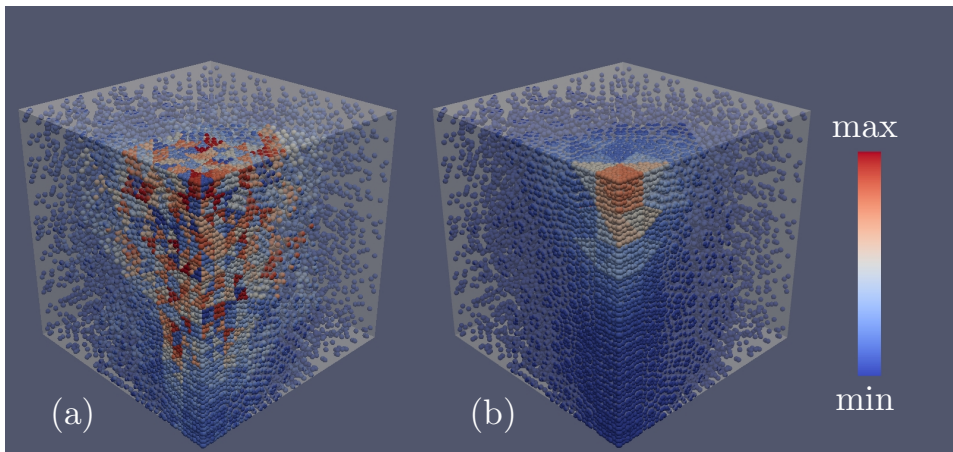


Figure 3: The magnitude of Cauchy stress tensor, $\|\boldsymbol{\sigma}\|_2$, with the (a) standard MPM and (b) $\bar{\mathbf{F}}$ -patch MPM.

3.2 Simple stretch

In order to further confirm the observation that the $\bar{\mathbf{F}}$ -patch MPM can reduce stress oscillation, this section presents a very simple example – the uniaxial stretch of a cube. The initial edge length is set to 2, and the material parameters are $E = 10^3$, $\nu = 0.0$, $\varrho_y = 400$ with consistent units. Roller boundary conditions were applied on three surfaces, $x = 0, y = 0, z = 0$, and an incremental displacement of $\Delta u = 0.4$ was applied on the surface, $y = 2$, per load step.

The cube was discretised into five 10-noded tetrahedral elements, i.e. five patches for the $\bar{\mathbf{F}}$ -patch computation, which were then subdivided into forty linear tetrahedra (eight per initial 10-noded tetrahedron as seen in Figure 1 (c)). There were eleven material points per element.

The mesh and material point distribution at the 17th load step is shown in Figure 4. The Kirchhoff stress component τ_{yy} at all material points against the load step is plotted in Figure 5. The average value agrees with the analytical solution but there is oscillation as indicated, more pronounced in the results from the standard MPM. It is clear that the oscillations in stress have been reduced by using the $\bar{\mathbf{F}}$ -patch approach. This effect seen with the $\bar{\mathbf{F}}$ -patch MPM occurs because the stiffness and internal force for an element receives contributions from other elements in the same patch. This reduces the sudden transfer of internal force between nodes as a material point crosses from one background element to another (provided that they are in the same patch).

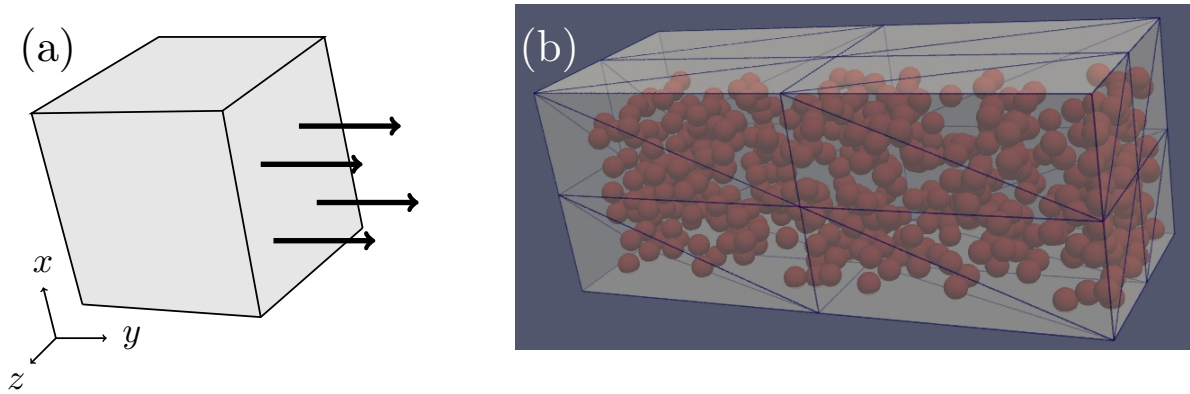


Figure 4: The geometry and discretisation (a) before and (b) after deformation in the simple stretch problem.

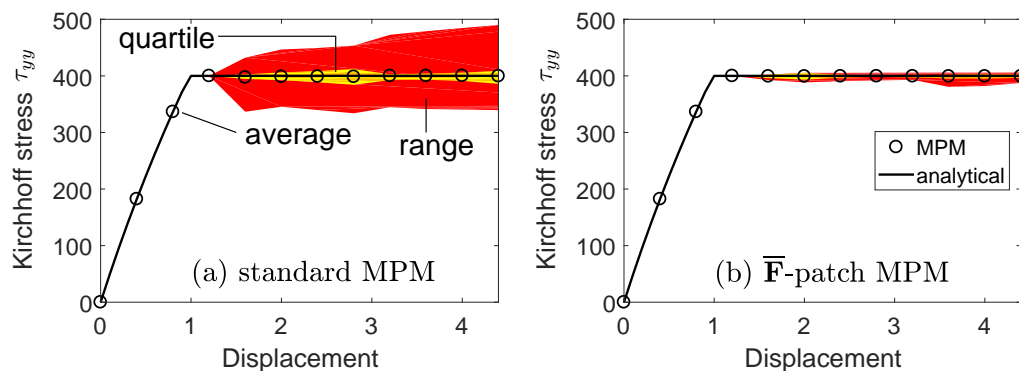


Figure 5: Kirchhoff stress component τ_{yy} at all material points with average, range and quartile.

4 Conclusions

This paper has presented the $\bar{\mathbf{F}}$ -patch MPM, which improves the accuracy of simulations for the large deformation of elasto-plastic materials. In particular, the volumetric locking problem due to the material incompressibility in the phase of plastic deformation is avoided. We also found that the $\bar{\mathbf{F}}$ -patch MPM can reduce the stress oscillation, which was commonly attributed to cell-crossing instabilities.

References

- [1] EA de Souza Neto, D Peric, M Dutko and DRJ Owen. Design of simple low order finite elements for large strain analysis of nearly incompressible solids. *International Journal of Solids and Structures*, 33:3277-3296, 1996.
- [2] EA De Souza Neto, FM Andrade Pires, and DRJ Owen. F-bar-based linear triangles and tetrahedra for finite strain analysis of nearly incompressible solids. part i: formulation and benchmarking. *International Journal for Numerical Methods in Engineering*, 62(3):353–383, 2005.
- [3] WM Coombs, TJ Charlton, M Cortis, and CE Augarde. Overcoming volumetric locking in material point methods. *Computer Methods in Applied Mechanics and Engineering*, 333:1-21, 2018.

VIBRATIONAL BEHAVIOURS OF SMALL-SCALE STRUCTURES USING GRADIENT ELASTICITY

Hoang Nguyen^{1,a} and *Thuc Vo²

¹School of Engineering, University of Glasgow, G12 8QQ

²Department of Mechanical and Construction Engineering, Northumbria University, NE1 8ST

*thuc.vo@northumbria.ac.uk

Summary

This study aims to investigate the free vibration responses of cracked small-scale plates using the strain-gradient theory and the extended isogeometric analysis (XIGA). While the strain-gradient elasticity is employed to account for the size-dependent effects, the displacement fields of plate structures are described based on the refined plate theory (RPT). The simple strain-gradient theory with one additional length scale parameter, apart from Lamé's constants, is capable of effectively capturing the small-scale effects in nano/micro structures. The RPT with four unknowns not only is able to improve the accuracy of the results for both thin and thick plates but also helps to describe the nonlinear distribution of the shear stress through the plate's thickness without using shear correction factor. The combination of SGE and RPT ends up requiring C^2 elements, which causes difficulty if traditional finite element is involved to solve for approximate solutions. The isogeometric analysis (IGA) is employed as a prominent numerical method to solve the problems that require higher-order elements. This recently developed method utilises the non-uniform rational B-splines (NURBS) functions to establish approximation functions and describe geometry domains simultaneously. In order to model the discontinuity at the cracks within the plates, the extended IGA with enrichment functions for crack path and crack tip is involved. The primary results for the free vibration of plates show that the proposed approach is able to predict both the fracture behaviours and size-dependent effects well. It yields appropriate and reliable results in which the stiffness of the structures, consequently the fundamental frequency, is increased as the length scale ratio becomes larger. It also demonstrates that strain-gradient theory plays a significant role in prediction of size-dependent effects of nano/micro structures which classical continuum theory could fail to capture.

Key Words: *Free vibration; Strain gradient elasticity; Extended isogeometric analysis*

Introduction

Classical continuum plays a crucial role in establishing mathematical models to predict structural responses in different engineering fields. However, it is well-known that the classical continuum fails to capture the size-dependent effects which normally appear in small-scale structures. The effects become significant when the size of the structure being considered is comparable to the material length scales. Generalised continuum theories which take into account length scale parameters are able to capture the size effect efficiently. The generalised strain gradient theory of Mindlin [2] considers material particle as a deformable medium. There are additional material constants apart from Lamé's ones and the strain gradients are included in the strain energy density. In addition, a micro-inertia term which is associated with the material microstructure is included in the kinetic energy density. Those inclusions of additional material constants and a micro inertia term allow better prediction in the behaviours small-scale structure. In this study, the vibration analysis of small-scale plates are investigated taking advantages of the strain gradient theory.

^aThis work was completed while at the previous affiliation Northumbria University and was extracted from the recent study [1].

Strain gradient and extended isogeometric analysis for cracked plates

The kinematic of plate structures is described following the refined plate theory suggested by Senthilnathan et al. [3] as follows

$$u(x, y, z) = u_0(x, y) - zw_{b,x}(x, y) + g(z)w_{s,x}(x, y), \quad (1a)$$

$$v(x, y, z) = v_0(x, y) - zw_{b,y}(x, y) + g(z)w_{s,y}(x, y), \quad (1b)$$

$$w(x, y, z) = w_b(x, y) + w_s(x, y), \quad (1c)$$

where u_0 and v_0 are in-plane displacement at the mid-plane and w_b and w_s represent the bending and shear transverse displacements, respectively.

Meanwhile, a simplified version of the strain gradient theory is derived from the Mindlin's Form II will be used. The strain energy density is expressed with seven material constants including two Lamé's constants (λ, μ) as follows [2, 4]

$$U_0(\varepsilon, \kappa) = \frac{1}{2}\lambda\varepsilon_{ii}\varepsilon_{jj} + \mu\varepsilon_{ij}\varepsilon_{ij} + a_1\kappa_{iik}\kappa_{kjj} + a_2\kappa_{kii}\kappa_{kjj} + a_3\kappa_{iij}\kappa_{jjk} + a_4\kappa_{kij}\kappa_{kij} + a_5\kappa_{kij}\kappa_{jik}, \quad (2)$$

where the classical strain tensor is defined as the first gradient of the macroscopic displacement, $\varepsilon_{ij} = \frac{1}{2}(u_{j,i} + u_{i,j}) = \varepsilon_{ji}$, and the microscopic deformation gradient (strain gradient tensor) are expressed in terms of the first gradient of the macroscopic strain, $\kappa_{ijk} = \varepsilon_{jk,i} = \frac{1}{2}(u_{k,ji} + u_{j,ki}) = \kappa_{ikj}$. The above complex formulation of the strain gradient density with five additional parameters can be simplified by making assumptions $a_2 = \frac{1}{2}\lambda\ell^2, a_4 = \mu\ell^2, a_1 = a_3 = a_5 = 0$, where ℓ is the characteristic length or material length scale parameter.

The kinetic energy density with the inclusion of the micro-inertia term is given as follow

$$K_0 = \frac{1}{2}\rho\dot{u}_i\dot{u}_i + \frac{1}{6}\rho d^2\frac{\partial\dot{u}_j}{\partial x_i}\frac{\partial\dot{u}_j}{\partial x_i} \quad (3)$$

By using extended isogeometric analysis, the displacements of a plate with cracks are predicted by enriching the standard approximation as follows

$$\mathbf{u}^h(\mathbf{x}) = \sum_{I \in \mathcal{N}} R_I(\mathbf{x}) \mathbf{q}_I + \sum_{J \in \mathcal{N}_{cr}} R_J(\mathbf{x}) (H(\mathbf{x}) - H(\mathbf{x}_J)) \mathbf{a}_J + \sum_{K \in \mathcal{N}_{tip}} R_K(\mathbf{x}) \sum_{\alpha=1}^{n_\alpha} (B_\alpha(\mathbf{x}) - B_\alpha(\mathbf{x}_K)) \mathbf{b}_{\alpha K}, \quad (4)$$

where the R_I, R_J , and R_K are NURBS basis functions, $H(\mathbf{x})$ and $B_\alpha(\mathbf{x})$ are Heaviside and crack-tip enrichment functions, respectively. Fig. 1 illustrates a simple representation of the Heaviside function and its effects on the basis functions in approximation of fields in which a crack at $\xi = 0.5$ is considered. The crack-tip enrichment functions are derived to improve the accuracy of the solution of singular stress field around the crack tip. They are defined in the local polar coordinates associated with the crack tip as follows

$$\mathbf{B} \equiv \begin{cases} \left[r^{3/2}\sin\frac{\theta}{2}, r^{3/2}\cos\frac{\theta}{2}, r^{3/2}\sin\frac{3\theta}{2}, r^{3/2}\cos\frac{3\theta}{2}, r^{3/2}\sin\frac{5\theta}{2}, r^{3/2}\cos\frac{5\theta}{2} \right] & \text{for } u_0, v_0, \\ \left[r^{3/2}\sin\frac{\theta}{2}, r^{3/2}\sin\frac{3\theta}{2}, r^{5/2}\sin\frac{\theta}{2}, r^{5/2}\cos\frac{\theta}{2}, r^{5/2}\sin\frac{3\theta}{2}, r^{5/2}\cos\frac{3\theta}{2}, r^{5/2}\sin\frac{5\theta}{2}, r^{5/2}\cos\frac{5\theta}{2} \right] & \text{for } w_b, w_s. \end{cases} \quad (5)$$

And the discretised systems of equations for the free vibration analysis is generally written as follows

$$\left[\mathbf{K}_c + \mathbf{K}_{gx} + \mathbf{K}_{gy} + \mathbf{K}_{gz} - \omega^2 (\mathbf{M}_c + \mathbf{M}_{gx} + \mathbf{M}_{gy} + \mathbf{M}_{gz}) \right] \mathbf{q} = \mathbf{0} \quad (6)$$

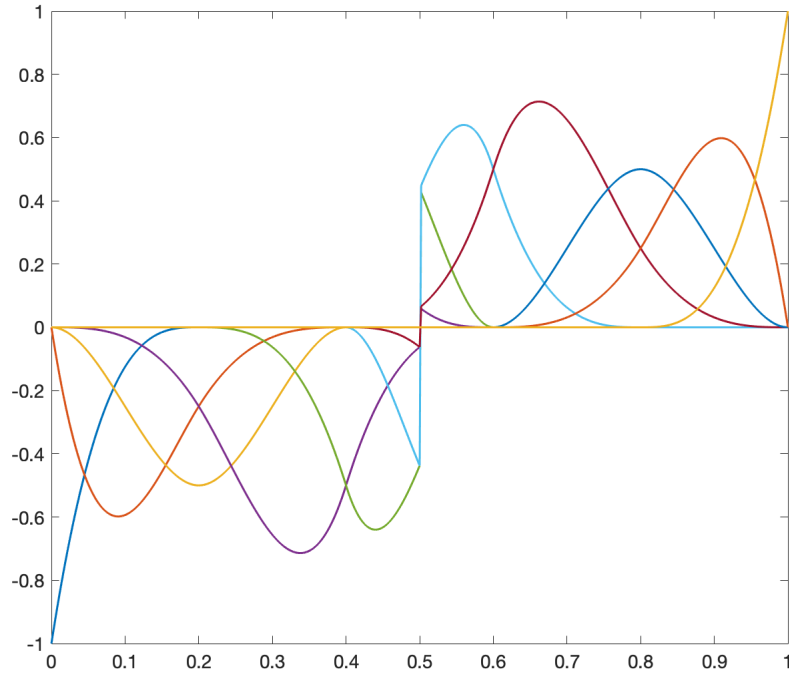


Figure 1: Product of the Heaviside function at $\xi = 0.5$ with the B-spline basis functions, knot vector $\Xi = \{0, 0, 0, 0, 1/5, 2/5, 2/5, 3/5, 3/5, 4/5, 1, 1, 1, 1\}$.

where the subscript c indicates the matrices are associated with the classical terms while the remains are with the strain gradient terms. It should be noted that above derivation of the plates with strain gradient theory requires C^2 continuity. This requirement is naturally satisfied using NURBS-based isogeometric approach.

Numerical examples

The effects of crack ratio c/a and the material length scale ratio ℓ/h on the fundamental frequencies of small-scale plates are presented in Fig. 2. As can be seen, the inclusion of material length scale to account for size-dependent effects results in the increase of the frequencies. On the other hand, as the crack expands its length, the frequencies are generally decreased as a result of the reduction in stiffness for crack opening modes (mode 2 and 4). However, this is not the case for mode 1 and 3 where cracks are closed.

Conclusions

In this study, the strain gradient theory and extended isogeometric analysis are employed to investigate the vibration behaviours of small-scale plates. While the inclusion of strain gradient terms effectively accounts for the size-dependent effects, the use of NURBS-based isogeometric approach enables efficient way to deal with high continuity requirement, in this case C^2 .

Acknowledgements

The authors gratefully acknowledge the financial support from the Northumbria University via the Researcher Development Framework to finish this work.

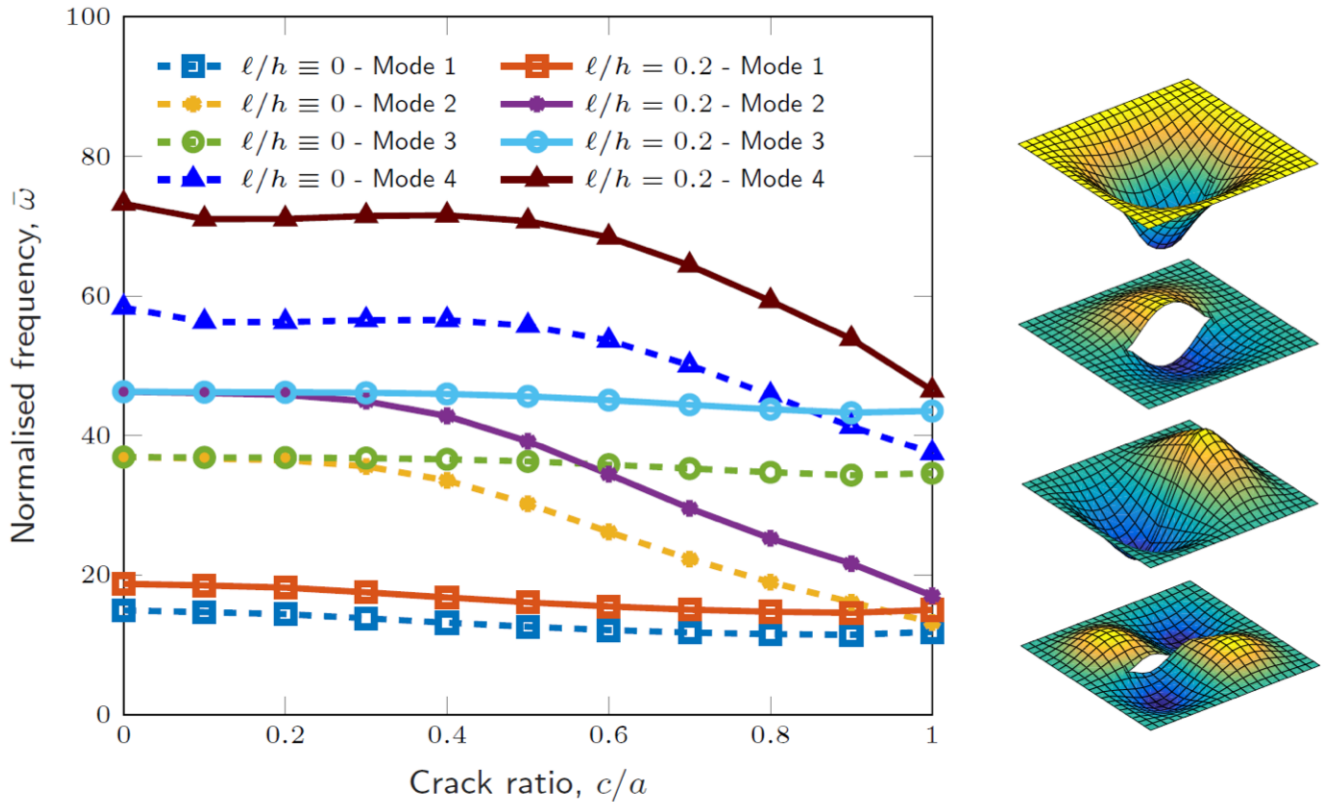


Figure 2: Fundamental frequencies of a simply-supported square plate with different crack ratio.

References

- 1 H. X. Nguyen, E. Atroshchenko, T. Ngo, H. Nguyen-Xuan, T. P. Vo. Vibration of cracked functionally graded microplates by the strain gradient theory and extended isogeometric analysis. *Engineering Structures*, 187, 251-266, 2019.
- 2 R. D. Mindlin, Micro-structure in linear elasticity, *Archive for Rational Mechanics and Analysis*, 16, 51-78, 1964.
- 3 N. R. Senthilnathan, S. P. Lim, K. H. Lee, S. T. Chow, Buckling of shear-deformable plates, *AIAA Journal*, 25, 1268-1271, 1987.
- 4 P. A. Gourgiotis, H. G. Georgiadis, Torsional and SH surface waves in an isotropic and homogeneous elastic half-space characterized by the Toupin-Mindlin gradient theory, *International Journal of Solids and Structures* 62, 217-228, 2015.

MATHEMATICAL AND NUMERICAL MODELLING OF A WATER PURIFICATION SYSTEM

*Antonios Parasyris¹, Marco Discacciati¹ and Diganta B. Das²

¹Department of Mathematical Sciences, Loughborough University, Loughborough, LE11 3TU, UK

²Chemical Engineering Department, Loughborough University, Loughborough, LE11 3TU, UK

*a.parasyris@lboro.ac.uk

Summary

We present a computational framework to study the hydrodynamic behaviour of a membrane-based water purification system for potable use. The membrane is represented as a porous medium which separates the feed and the permeate domains and the water filtration process is modelled by multi-physics problems involving both incompressible fluid flows and porous media flows. We numerically compare two modelling approaches: one based on a coupled system formed by the Navier-Stokes equations and by Darcy's law with ad-hoc coupling conditions, the other involving Brinkman's equation. Finite element simulations permit to characterize the fluid behaviour especially inside the feed domain and close to the membrane surface, where engineers are particularly interested in assessing mixing properties and possible membrane fouling. Flow instabilities in the form of Dean vortices are identified and their possible impact on filtration performance is discussed also in the light of experimental evidence. This work constitutes a first step towards the optimal design of the water filtration system.

Key Words: *Navier-Stokes equations; Porous-media flows; Brinkman model; Finite elements; Membrane filtration.*

Introduction

The design and optimisation of membrane filtration systems generally heavily relies on experimental work. However, the development of numerical simulation techniques and computer power have made computational modelling a valuable tool to support laboratory work and to reduce the amount and cost of experimental testing. In this work, we use mathematical and numerical modelling to study the behaviour of an incompressible fluid in a hybrid membrane filtration system proposed and tested experimentally in [8]. This system combines crossflow filtration (i.e., filtration where the fluid flow is mostly tangential to the membrane surface) with dead-end filtration (i.e., filtration with flow mostly perpendicular to the membrane) to increase the permeation flux while reducing membrane fouling due to suspended particles. The specific system we are considering also incorporates microchannels in the shape of a spiral (see Fig. 4) to favour mixing by creating flow instabilities (Dean vortices) [6] in the fluid domain close to the membrane surface. Characterising the hydrodynamic behaviour of the system is a first step towards its optimisation that we will address at a later stage.

Simplifying modelling approaches studied in the literature for membrane filtration devices cannot unfortunately be applied in our context. Indeed, they rely on strong assumptions either on the flow direction (see, e.g., [7]) or on the geometrical setting (see, e.g., [5]) that do not hold here. The fact that the flow pattern inside our device is quite complex and that the characteristic sizes of both the flow channels and of the membrane are comparable requires setting up a full 3D computational model. A schematic representation of the geometrical setting we study is shown in Fig. 1 where we highlight the spiral channels sitting on top of a circular membrane layer.

Mathematical models

The membrane is assumed to be an isotropic porous medium and, at this stage, we assume that there are

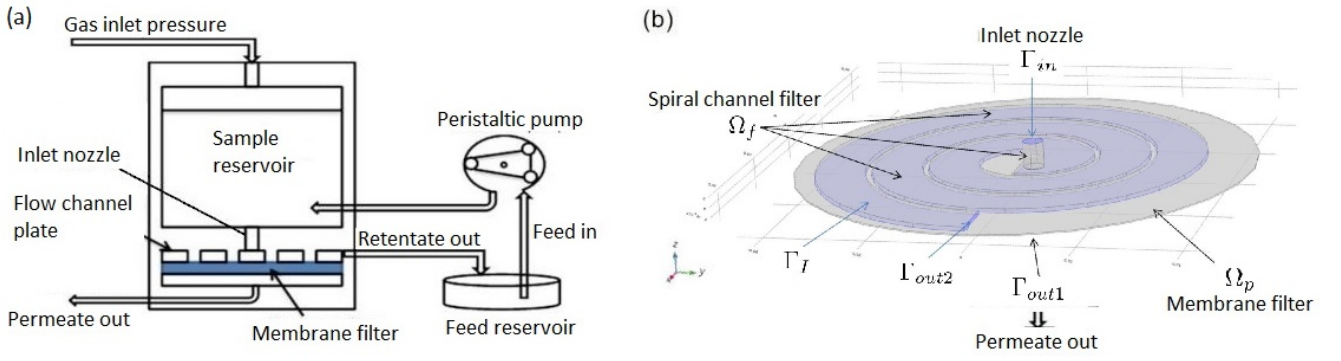


Figure 1: (a): Schematic representation of the device (b): 3D geometry reconstruction of the spiral channel filter and the membrane below it.

no impurities in the feed. To describe the flow behaviour both inside the free flow channel and through we introduce a system of partial differential equations while we represent the remaining components of the device (e.g., inflow pumps, permeate outflow) by suitable boundary conditions. To formulate the models, we denote Ω_f as the free flow domain where the fluid flows above the membrane Ω_p . These two regions are non-intersecting and separated by a common surface (interface) Γ_I : $\Omega_f \cap \Omega_p = \emptyset$, $\Gamma_I = \overline{\Omega_f} \cap \overline{\Omega_p}$. The fluid in Ω_f is characterized by its density ρ (e.g., for water $\rho = 10^3 \text{ kg/m}^3$) and dynamic viscosity (for water, $\mu = 10^{-3} \text{ Pa}\cdot\text{s}$). We indicate by \mathbf{u} and p the velocity and pressure of the fluid, respectively, and we use the subscripts f or p to denote if a variable is considered either in Ω_f or Ω_p . Variables without any subscript are understood to be defined in both domains.

Heterogeneous model A possible approach to describe filtration consists of adopting different sets of equations in Ω_f and Ω_p to account for the different physics occurring in these two regions. More precisely, in Ω_f , we consider the incompressible Navier-Stokes equations: find \mathbf{u}_f and p_f such that

$$\rho(\mathbf{u}_f \cdot \nabla) \mathbf{u}_f = \nabla \cdot T(\mu; \mathbf{u}_f, p_f) + \rho \mathbf{g} \quad \text{and} \quad \nabla \cdot \mathbf{u}_f = 0 \quad \text{in } \Omega_f, \quad (1)$$

where \mathbf{g} is gravitational acceleration, while $T(\mu; \mathbf{u}_f, p_f) = -p_f I + \mu(\nabla \mathbf{u}_f + (\nabla \mathbf{u}_f)^T)$ is the Cauchy stress tensor. (Notice that for our application the velocity regime is laminar.)

Darcy's law provides the simplest linear relation between velocity and pressure of an incompressible fluid in a saturated porous medium:

$$\mathbf{u}_p = -\frac{K}{\mu}(\nabla p_p - \rho \mathbf{g}) \quad \text{and} \quad \nabla \cdot \mathbf{u}_p = 0 \quad \text{in } \Omega_p, \quad (2)$$

where K is the permeability of the membrane which is a constant in our case.

The Navier-Stokes equations (1) and Darcy's law (2) must be coupled by suitable conditions across Γ_I to correctly represent the filtration process. A classical set of conditions (see, e.g., [1, 3]) prescribes the continuity of the normal velocity across Γ_I (as a consequence of the incompressibility of the fluid): $\mathbf{u}_f \cdot \mathbf{n} = \mathbf{u}_p \cdot \mathbf{n}$ on Γ_I ; the balance of the normal stresses across Γ_I : $p_p + \rho g z = -\mathbf{n} \cdot T(\mu; \mathbf{u}_f, p_f) \cdot \mathbf{n}$ on Γ_I , where z is the elevation with respect to a reference level, and the Beavers-Joseph-Saffman (BJS) condition on the Navier-Stokes tangential velocity: $\mathbf{t} \cdot T(\mu; \mathbf{u}_f, p_f) \cdot \mathbf{n} = -\alpha \mu K^{-1/2} \mathbf{t} \cdot \mathbf{u}_f$ on Γ_I . Here, \mathbf{n} and \mathbf{t} are the normal and tangential unit vectors on Γ_I with \mathbf{n} pointing outwards of Ω_f , and α is the non-dimensional BJS slip coefficient that depends on the characteristics of the porous medium and is roughly estimated between 0.1 and 4 [1].

One-domain approach The difficulty of solving different types of equations in two sub-regions of the domain and of handling coupling conditions is avoided by using the one-domain approach [4].

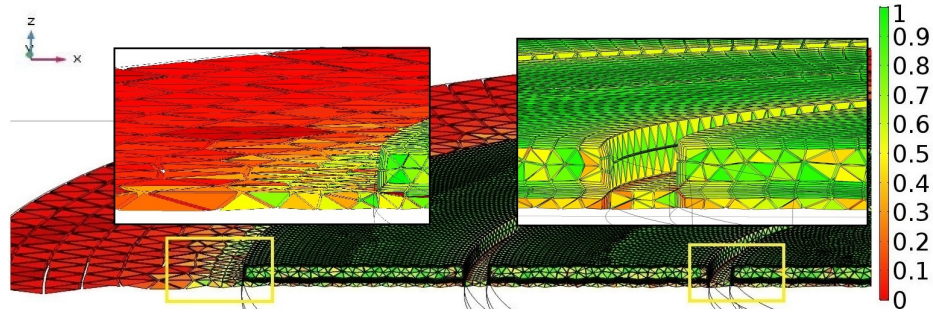


Figure 2: Mesh created in COMSOL with 659,139 elements. Boundary layers were added on the interface and on channel walls, while coarser elements were used inside the membrane where small velocity gradients are expected.

This technique, commonly implemented in commercial finite element software, considers a unified momentum equation in $\Omega = \Omega_f \cup \Omega_p$ with generalised porosity and permeability that depend on space. More precisely, the momentum equation (see, e.g., [4]) reads: find \mathbf{u} and p in Ω such that

$$\rho(\epsilon_p^{-1} \mathbf{u} \cdot \nabla) \epsilon_p^{-1} \mathbf{u} = \nabla \cdot T(\mu \epsilon_p^{-1}; \mathbf{u}, p) - \mu \tilde{K} \mathbf{u} + \rho \mathbf{g} \quad \text{and} \quad \nabla \cdot \mathbf{u} = 0 \quad \text{in } \Omega, \quad (3)$$

where the porosity ϵ_p is set equal to 1 in Ω_f , \tilde{K} vanishes in Ω_f but $\tilde{K} = K^{-1}$ in Ω_p .

Numerical results and discussion

The Navier-Stokes/Darcy (NSD) and the one-domain models were solved using the finite element software COMSOL Multiphysics [2]. We generated anisotropic computational meshes as shown in Fig. 2 with smaller elements and boundary layers introduced, e.g., in the neighbourhood of the membrane surface to correctly describe the filtration of the fluid.

In Fig. 3 we plot the computed pressure on a cross section of the channel for a given inflow pressure. We remark that, while the one-domain model gives a continuous pressure across the interface, a pressure jump is present for the NSD case. Moreover, a pressure gradient is generated between convex and concave walls due to the centrifugal force produced by the curved shape of the fluid channels.

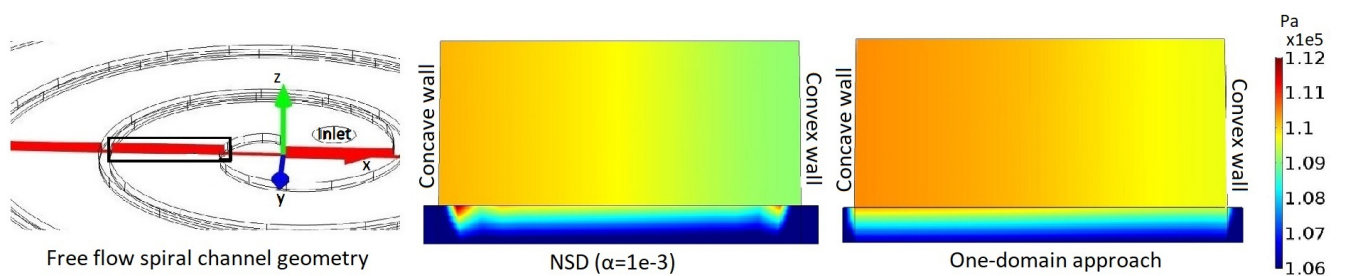


Figure 3: 3D spiral channel geometry with highlighted cross section where the results are plotted (left). Pressure computed by the NSD (centre) and the one-domain (right) models.

As expected, this gives rise to flow instabilities in the form of Dean vortices that are clearly visible in Fig. 4 where we plot the velocity magnitude in the cross section indicated in Fig. 3. Velocity vectors and streamlines highlight the vortices near the membrane surface and at the top of the channel. We can also see that the velocity magnitude is discontinuous across the interface Γ_I in the NSD model

because none of the coupling conditions prescribe the continuity of the tangential velocity component. This is not the case for the one-domain model where the velocity is continuous.

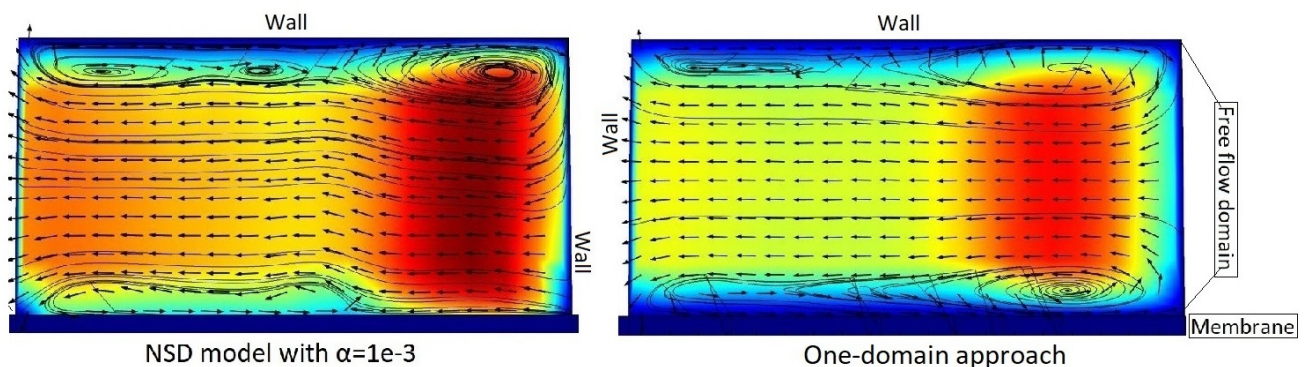


Figure 4: Velocity magnitude on the cross section of Fig. 3. Dean vortices are visible for both models.

Conclusions

The two modelling approaches we presented represent accurately and realistically any membrane filtration device without any a priori assumptions either on the geometrical setup or on the flow direction. Finite element simulations show the flow pattern both in the feed domain and through the membrane and permit to identify flow instabilities. The modelling framework we developed is a first step towards the optimal design of the water filtration system.

Acknowledgements

The first author acknowledges the support of the EPSRC Doctoral Training Programme.

References

- [1] G. S. Beavers and D. D. Joseph. Boundary conditions at a naturally permeable wall. *J. Fluid Mech.*, 30:197–207, 1967.
- [2] COMSOL Inc. COMSOL Multiphysics Reference Manual, Version 5.3a. <https://www.comsol.com>.
- [3] W. Jäger and A. Mikelić. On the boundary conditions at the contact interface between a porous medium and a free fluid. *Ann. Scuola Norm. Sup. Pisa Cl. Sci.*, 23:403–465, 1996.
- [4] M. Le Bars and M. Grae Worster. Interfacial conditions between a pure fluid and a porous medium: implications for binary alloy solidification. *J. Fluid Mech.*, 550:149–173, 2006.
- [5] V. Nassehi. Modelling of combined Navier-Stokes and Darcy flows in crossflow membrane filtration. *Chem. Eng. Sci.*, 53(6):1253 – 1265, 1998.
- [6] N. Nivedita, P. Ligrani, and I. Papautsky. Dean flow dynamics in low-aspect ratio spiral microchannels. *Scientific Reports*, 7:44072, 2017.
- [7] P. Schmitz and M. Prat. 3-D laminar stationary flow over a porous surface with suction: Description at pore level. *AIChE Journal*, 41(10):2212–2226, 1995.
- [8] N. Shamsuddin, D. B. Das, and V. M. Starov. Membrane-based point-of-use water treatment (PoUWT) system in emergency situations. *Separation & Purification Reviews*, 45(1):50–67, 2016.

A MULTIGRID APPROACH THAT IS ROBUST WITH RESPECT TO MESH QUALITY

Yuxuan Chen¹, Garth N. Wells¹¹Department of Engineering, University of Cambridge

yc397@cam.ac.uk

Summary

A multigrid smoother is proposed to overcome the degraded performance when a small number of low quality cells are present in a mesh. The smoother includes a standard smoother on the whole domain, and a local correction on the low cell quality regions. We demonstrate the performance of the method for the Poisson equation and linear elasticity.

Key Words: *multigrid; domain decomposition; mesh quality; large scale linear algebra*

Introduction

The multigrid method has theoretical algorithmic complexity of $O(N)$ for linear systems with N unknowns. However, its performance degrades with poor quality finite element meshes, possibly leading to a failure to converge [1]. We propose a smoother that can overcome the poor performance of multigrid when a small number of low quality cells are present. The smoother combines a standard smoother applied on the whole domain, followed by a local residual correction applied on the local poor quality regions. The combined smoother is in the form of an additive Schwarz-type domain decomposition solver. Numerical tests on meshes with low quality regions indicate that with the local correction smoother, multigrid convergence rate observed for high quality meshes is recovered.

Multigrid method

Let Ω_1 be the fine grid, and Ω_2 be the coarse grid. The prolongation operator $P : \Omega_2 \rightarrow \Omega_1$ projects the coarse grid information to the fine grid. The resulting restriction operator $R : \Omega_1 \rightarrow \Omega_2$ is then given by $R = P^T$. A smoother S is applied on the with $u = S(A, b, u)$. Typical smoothers could be Jacobi or Gauss-Seidel. Another common smoother is the Chebyshev method which is natural to implement in parallel. For the coarsest grid, a direct solver is employed. The coarse grid operator is obtained by the Galerkin approximation,

$$A_2 = RA_1P.$$

A two level multigrid V-cycle to solve the system $A_1u = b_1$ is illustrated as follows:

1. pre-smoothing and restriction: $u = S(A_1, b_1, u)$, $r_1 = b_1 - A_1u$, and $b_2 = Rr_1$
2. coarse grid solver: $e_2 = A_2^{-1}b_2$
3. prolongation and post-smoothing: $u \leftarrow u + Pe_2$ and $u = S(A_1, b_1, u)$

General multigrid is a recursive version of the two-grid case. We focus on the geometric multigrid (GMG) which is based on the geometric hierarchy grids. Non-nested and unstructured meshes can be freely employed in GMG via the Galerkin approach.

Smoother failure on low quality meshes

The performance of a smoother on the low quality meshes is investigated here. Consider the homogeneous Poisson equation on a unit square mesh $\Omega = (0, 1)^2$ containing 158 nodes with one low quality

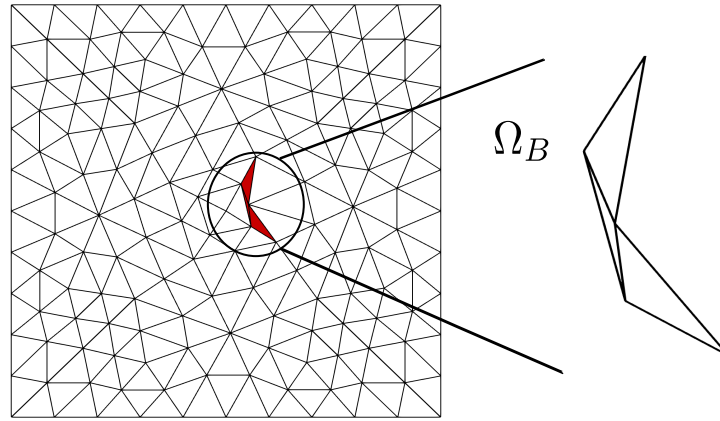


Figure 1: A unit square mesh with one poor quality cell at the centre.

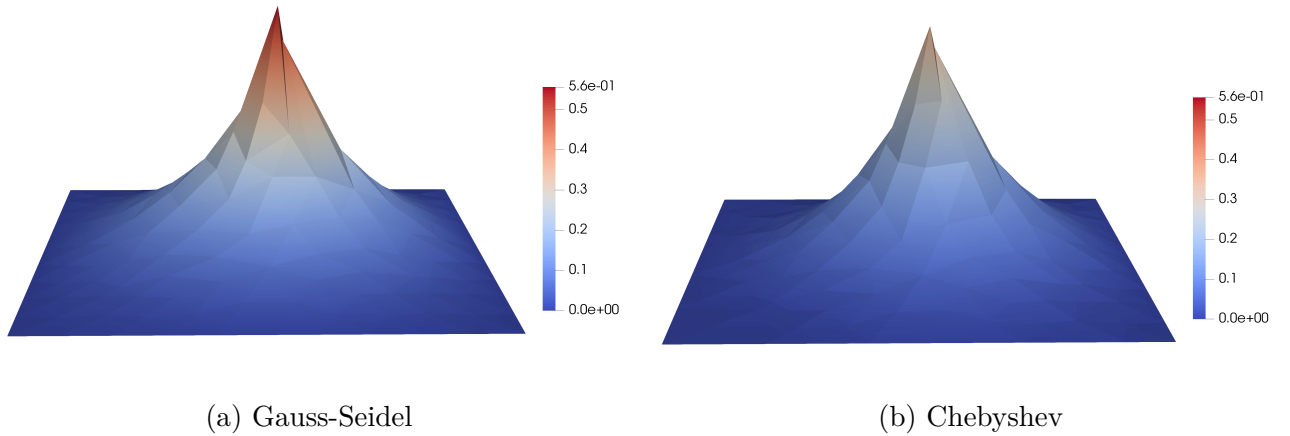


Figure 2: Absolute value of error on each vertex after ten iterations of different smoothers.

region at the centre, which is shown in fig. 1. A Gauss-Seidel and a Jacobi preconditioned Chebyshev smoothers are tested. The absolute value of the error on each vertex after ten applications of the smoother are shown in fig. 2. In both cases, the error persists in the region of low quality cells. The normal smoothing property fails locally to eliminate the high frequency error in regions of low cell quality. The restriction of multigrid misses this error and it persists throughout iterations, leading to poor convergence or a failure to converge.

Local correction smoother

Let Ω_B be the low quality region which can be found by setting a cell quality threshold on the whole domain. Suppose there are N_d subdomains containing poor quality cells, and denote them by Ω_B^d , $d = 1, 2, \dots, N_d$. It is required that Ω_B^d is a closed region. Let B_d be the set consisting of all indices b_s in Ω_B^d , i.e., $B_d = \{b_s : s = 1, 2, \dots, N_B^d\}$. We assume that these local subdomains do not intersect each other, namely, $\bigcap_d \Omega_B^d = \emptyset$, and $\bigcap_d B_d = \emptyset$. Let the natural inclusion I_d map the low quality region Ω_B^d to the whole domain Ω , which is a $N \times N_B^d$ matrix given by

$$I_d[i][j] = \begin{cases} 1 & i = b_j, \quad b_j \in B_d, \\ 0 & \text{Otherwise.} \end{cases}$$

Then the local correction system and the corresponding local residual can be generated by extracting the submatrix from the finite element system,

$$\begin{aligned} A_c^d &= I_d^T A I_d, \\ r_c^d &= I_d^T r. \end{aligned}$$

The local correction solves the local residual equation on the subdomain Ω_B^d by a direct method, and via the inclusion, the local error can be mapped to the global domain,

$$e_c^d = I_d (I_d^T A I_d)^{-1} I_d^T r.$$

The solution u is updated by adding the error calculated on all of local systems,

$$u_{k+1} = u_k + \sum_{d=1}^{N_B} e_c^d.$$

This procedure can be written in terms of a preconditioner form, which is stationary,

$$u_{k+1} = u_k + S_c (b - Au),$$

where

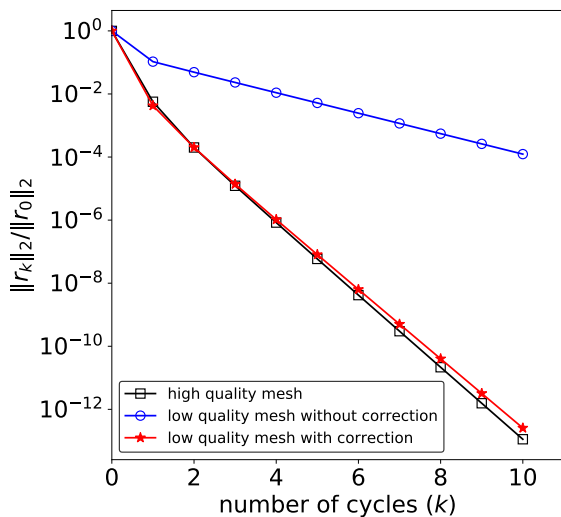
$$S_c = \sum_{d=1}^{N_B} I_d (I_d^T A I_d)^{-1} I_d^T. \quad (1)$$

The local correction is then equivalent to applying the subspace correction [2] on the local poor quality area. We propose a combined smoother which involves a regular smoother, e.g., Gauss Seidel, applied on the whole domain, and the local correction smoother applied on the local poor quality regions. The regular smoother eliminates most high frequency components of the error on the high quality regions, whereas the local correction removes the error persisting on the low quality regions which are not eliminated by the regular smoother. The combined smoother can be written in the form of $\sum_{d=0}^{N_B} I_d S_d I_d^T$, where I_0 is the identity map and S_0 is the normal smoother. Thus, it is in the form of an overlapping additive Schwarz-type domain decomposition solver.

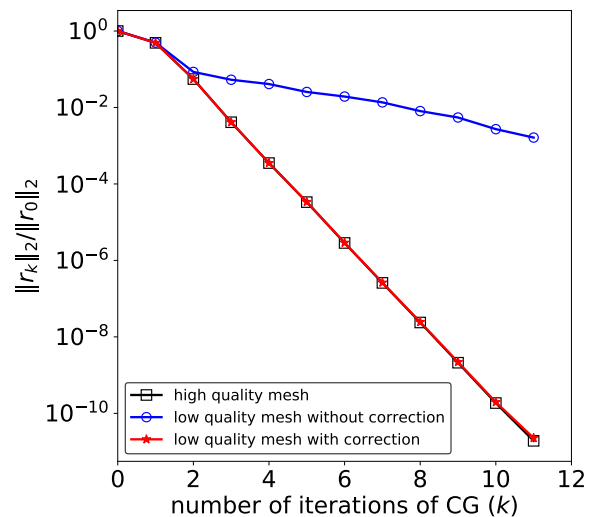
Numerical examples

The performance of the proposed smoother is tested for both scalar and vector valued equations. Gauss-Seidel is taken as the regular smoother and is applied twice in terms of pre- and post-smoothing. We return to the Poisson equation on the unit square in fig. 1. The relative residual obtained by a two-level V cycle with and without local correction is shown in fig. 3a. It is observed that the convergence improves dramatically with the local correction smoother. The recovery of the convergence rate is the result of eliminating the high frequency error in low quality region by the local correction.

The second example solves the linear elasticity equation on a lattice structure, shown in fig. 4a. The problem contains around 3 million DOFs on the finest grid. Four geometric grid levels are generated, on each level, there are four regions of low quality cells. Multigrid preconditioned conjugate gradient method is applied with one V cycle to approximate A^{-1} in each iteration of the conjugate gradient algorithm. Figure 3b shows the convergence rate, which demonstrates good performance of the local correction scheme. The convergence rate on low quality mesh is restored to the level observed for high quality mesh. To gain insights, the positions on the finest grid where the residual is large are shown in fig. 4b. Clearly, the residual is large in regions where the cell quality is low. It means that high frequency error produced by standard smoother also persists through conjugate gradient iterations and can be eliminated by the local correction.

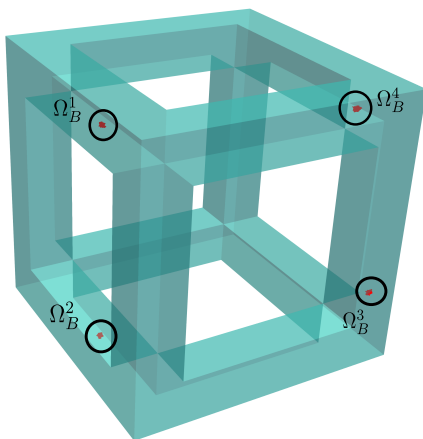


(a) Poisson equation on the square.

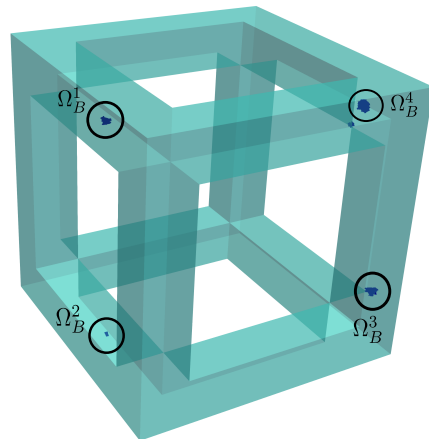


(b) Linear elasticity on the lattice.

Figure 3: Relative residual computed with and without local correction.



(a) Positions with low quality cells.



(b) Positions with large value of residual.

Figure 4: The lattice structure used for linear elasticity tests.

Conclusions

The application of the robust smoothers for meshes with regions of low quality opens new possibilities for geometric multigrid applied to complex engineering geometries, where coarse grid meshes will inevitably contain some low quality cells. Geometric multigrid approaches are particularly of great value in extreme scale due to the well understood theory and suitability for extreme parallelisation.

References

- [1] C. N. Richardson, N. Sime, and G. N. Wells. Scalable computation of thermomechanical turbomachinery problems. *Finite Elements in Analysis and Design*, 155:32–42, 2019.
- [2] J. Xu. The method of subspace corrections. *Journal of Computational and Applied Mathematics*, 128(1):335 – 362, 2001.

SIMULATING A LARGE DEFORMATION FORMING PROCESSES USING A MESHFREE METHOD BASED ON A TOTAL-LAGRANGIAN KERNEL

Stephen P. Smith¹, *Brian G. Falzon¹ and Gary H. Menary¹

¹Department of Mechanical And Aerospace Engineering, Queen's University Belfast,

*b.falzon@qub.ac.uk

Summary

In this work a meshfree method based on a total-Lagrangian kernel is used to simulate the stretch blow moulding process; the primary manufacturing technique used to produce polymer bottles for the water and soft drink industries. The use of a total-Lagrangian kernel is attractive as the shape functions are only calculated in the preprocessing stage, which provides a computational benefit. Results of the simulation justified the use of a fixed reference as good stability was displayed, despite the very large deformation experienced.

Key Words: *Meshfree methods; Material forming; Large deformation.*

Introduction

Stretch blow moulding is the primary manufacturing technique used to produce polymer bottles for the water and soft drink industries; an industry estimated to grow to \$46 billion by 2021. The process, Fig (1), features three primary stages: (i) a preform, typically composed of polyethylene terephthalate (PET), is heated above its glass transition temperature T_g , (ii) the preform is stretched by means of a stretch rod and an internally acting pressure, and (iii) the final bottle is cooled and ejected from the mould.

Traditionally, industry approached bottle design using a trial and error based method, however

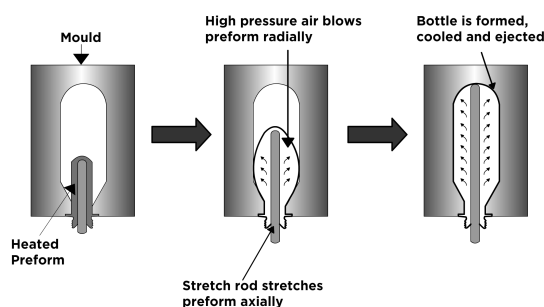


Figure 1: Stretch Blow Moulding Process

with the substantial growth in the availability of computational power it has become possible simulate this process, leading to potential optimisation. Traditionally this process has been simulated using the finite element method, however this leads to a number of mesh-related issues. In order to avoid these issues, meshfree methods have been proposed.

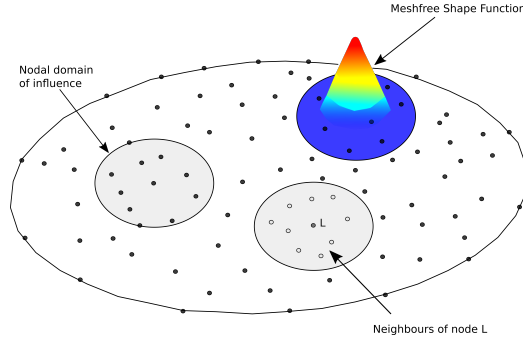


Figure 2: Meshfree discretisation

Meshfree Methods

In meshfree methods the domain $\Omega \in \mathbb{R}^d$ is discretised by a set of nodes x_I , Fig. (2), each with an arbitrary domain of influence ω_I such that $\Omega \subset \cup \omega_I$. At each point $x \in \mathbb{R}^d$ in the domain, the approximation of the displacement $u(x)$ is posed a polynomial $u(x) = p(x)^T a(x)$, where $p(x)$ is a polynomial basis, and $a(x)$ the unknown coefficients. In this work a meshfree method based off the moving least squares approximation [1] is used, where the coefficients, $a(x)$, are found by minimising the discrete norm:

$$\min \sum_I^{N_p} w(x - x_I) [p(x_I)^T a(x) - u_I]^2 \quad (1)$$

where $w(x)$, is a weight, or kernel function, which is non-zero for points within the domain of influence of x_I , i.e a set of N_p neighbours is assigned to each point $\mathcal{N}_x = \{x_I \mid w(x - x_I) > 0\}$. Solution of (1) yields the moving least squares shape functions ϕ_I , which can be used to interpolate the displacement field $u(x)$, yielding the well known approximation: $u(x) = \sum_I^{N_p} \phi_I(x) u_I$. For this study a total-Lagrangian kernel function is used, where the set \mathcal{N}_x is invariant to time, and covers the same set of neighbours throughout the simulation, this provides a computational benefit as shape functions are only calculated in the preprocessing stage.

Galerkin Weak Form

To generate a discrete system of equations suitable for computer implementation a Galerkin method, which is cast in reference configuration $\Omega_{t=0}$ is used, expressed by the following equation:

$$\int_{\Omega_0} P_{ij} \delta F_{ij} d\Omega - \int_{\Gamma_0} \delta u \cdot T = \int_{\Omega_0} \rho \delta u \cdot \ddot{u} d\Omega \quad (2)$$

where P is the first Piola-Kirchhoff stress, δF the variation in the deformation gradient, T the surface traction, and ρ the material density. As custom in a Galerkin method the displacement $u(x)$ (and variation) are expressed using the shape functions (2), and the deformation gradient as:

$$F = \mathbb{1} + \sum_I^{N_p} u_I \otimes \nabla \phi_I(x) \quad (3)$$

Domain integrals are approximated using nodal integration, with a stabilised deformation gradient [2], to remove instabilities resulting from strain sampling at nodes. Time integration is performed using forward (explicit) integration.

Simulation

The primary inputs to the stretch-blow moulding simulation are the geometry, and the material model used to approximate the behaviour of PET.

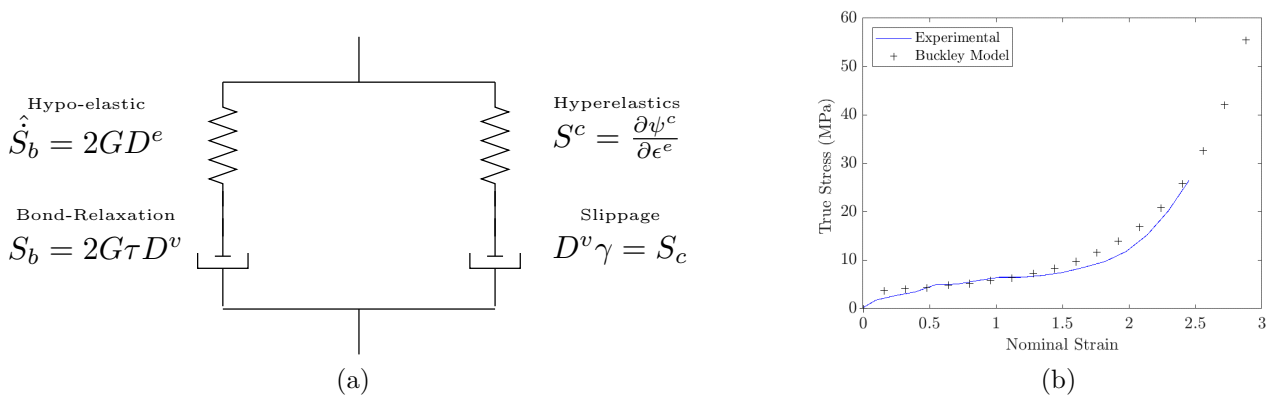


Figure 3: (a) Buckley material model and (b) Experimental validation of fitted material model under biaxial loading at a temperature of 105°C and a strain rate of 16s^{-1} .

Material Model

In this work a viscoelastic material model, known as the Buckley material model is used. This model has been adapted for stretch blow moulding by [3], and has been shown to provide good predictions of the strain and temperature history experienced by the material in blow moulding [4]. The model features two branches, Fig 3(a), which leads to an additive decomposition of the Cauchy stress σ :

$$\sigma = S^b + S^c + k^B \ln(\det(F)) \quad (4)$$

where k^B is the bulk modulus. The capability of this material model is evident in the predictions it produces, Fig 3(b), for a biaxial state of deformation at strain rate of 16s^{-1} and a temperature of 105°C , a condition which is a good representation of blow moulding. For the sake of brevity the full details of this model are not included here, but can be found in [3].

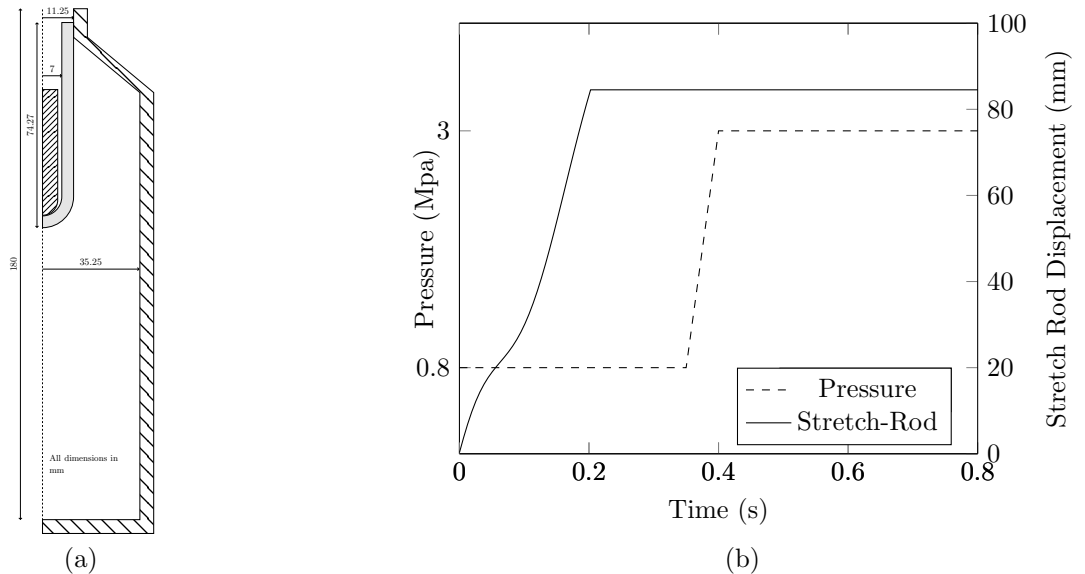


Figure 4: Geometry and Loading Conditions

Geometry & Loading

The geometry of the model is shown in Fig 4(a). The preform is discretised by 563 nodes, and the stretch-rod and mould are treated as rigid bodies. Due to the symmetry of the preform an axisymmetric formulation was employed. The displacement profile is described in terms of a 7th order polynomial,

fitted to experimental observations [4]. The pressure is supplied in two stages: (i) an initial pressure to initiate blowing of the preform, followed by (ii) a final pressure to fill the mould, Fig. 4(b).

Results

The results of the simulation are shown in Fig. (5), showing the deformation at 0.25 and 0.8 seconds, with a final volume of 620mL . Promisingly, despite the use of a fixed reference state the meshfree method was capable of simulating this large deformation process while remaining stable. This characteristic of meshfree simulations has often been attributed to the large number of nodes that contribute to the solution at each point, a behaviour experienced within this work, where small nodal domain sizes resulted in poor stability in the simulation.

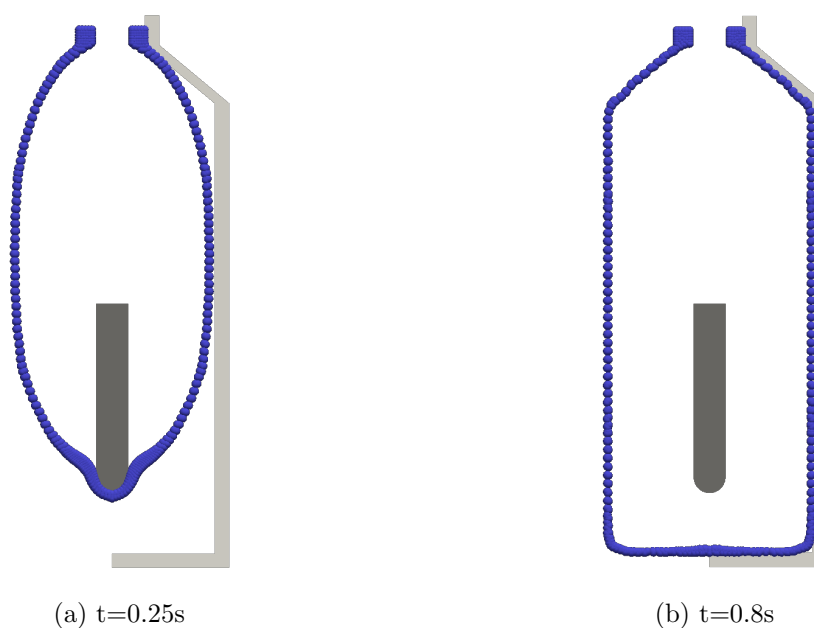


Figure 5: Deformation of the preform at two time frames.

Conclusions

In this work a meshfree method has been applied to simulate the stretch-blow moulding process. Results have highlighted the ability of meshfree methods in very large deformation applications. Experimental validation of this simulation is currently being conducted, and will be presented in a forthcoming work.

References

- 1 T. Belytschko, Y.Y. Lu and L. Gu. Element-free Galerkin Methods. *International Journal for Numerical Methods In Engineering*, 37, 229-256, 1994.
- 2 J.S Chen, et. al. A stabilized conforming nodal integration for Galerkin meshfree methods. *International Journal for Numerical Methods In Engineering*, 50, 435-466, 2001.
- 3 Yan S (2013) Modelling the Constitutive behaviour of Poly(ethylene terephthalate) for the Stretch Blow Moulding Process. PhD Thesis, Queens University Belfast
- 4 Nixon, J., Menary, G., & Yan, S. (2017). Finite Element Simulations of stretch-blow moulding with experimental validation over a broad process window. *International Journal of Material Forming*, 10(5), 793-809.

DEVELOPMENT OF A CONSTITUTIVE MODEL FOR MODELLING WIND TURBINE FOUNDATIONS IN UNSATURATED SOILS

*T.J. Charlton¹, A.S. Osman¹, W.M. Coombs¹ and C.E. Augarde¹

¹Department of Engineering, Durham University, DH13LE

*t.j.charlton@durham.ac.uk

Summary

The WindAfrica project aims to accelerate the deployment of wind turbines in Africa. It is estimated that about 50% of the Africa's population lacks access to electricity despite the fact that 35% of the world resources for wind energy are located in African countries. In some countries, such as Sudan, areas suitable for harnessing wind energy resource lie on large areas of unsaturated expansive clays which traditionally would not be chosen to build on. The WindAfrica project aims to deliver guidelines on building wind turbine foundations on these soils. These guidelines will be drawn from both physical and numerical models.

This paper will focus on the development of an advanced constitutive model which is capable of capturing the basic behaviour of these clayey soils. The constitutive model is based on an extended version of Barcelona basic model (BBM) [1] where a yield surface similar to the Modified Cam Clay (MCC) is dependent also on the suction. Results obtained using the current development of the model will be presented as well as details on the numerical implementation such as the correct calculation of the consistent tangent required for use in a finite element code.

Key Words: *elasto-plasticity;unsaturated soil;constitutive model*

Model implementation

This paper outlines a simplified version of the model to take a constant value of suction at each step which dictates the shape of the yield surface. This value of suction (rather than increment of suction) is chosen as it is available to the user in Abaqus without additional modifications. Beginning with existing stress state $\{\sigma_0\}$, increment in strain $\{\Delta\varepsilon\}$ and elastic strain from the previous step $\{\varepsilon_n^e\}$ (the sum of which gives a trial strain $\{\varepsilon^{tr}\}$), an updated stress can be calculated based on the current size of yield surface at zero suction p_{cn0} and the current suction u . A trial stress can be calculated as

$$\sigma_{tr} = p_0 \exp\left(\frac{\Delta\varepsilon_v}{\kappa}\right) \{1\} + 2G \left(\left\{ \varepsilon_1^{tr} \ \varepsilon_2^{tr} \ \varepsilon_3^{tr} \ \frac{\varepsilon_4^{tr}}{2} \ \frac{\varepsilon_5^{tr}}{2} \ \frac{\varepsilon_6^{tr}}{2} \right\} - \frac{\varepsilon_v^{tr}}{3} \{1\} \right) \quad (1)$$

where κ is the elastic compressibility index, G is the shear modulus and $\{1\} = \{1 \ 1 \ 1 \ 0 \ 0 \ 0\}^T$. A variable bulk modulus K can be calculated from

$$K = \frac{P_0}{\kappa} \exp\left(\frac{\Delta\varepsilon_v}{\kappa}\right), \quad (2)$$

and this can be used to form $[D^e]$ the elastic stiffness matrix

$$[D^e] = \begin{bmatrix} K + \frac{4}{3}G & K - \frac{2}{3}G & K - \frac{2}{3}G & 0 & 0 & 0 \\ K - \frac{2}{3}G & K + \frac{4}{3}G & K - \frac{2}{3}G & 0 & 0 & 0 \\ K - \frac{2}{3}G & K - \frac{2}{3}G & K + \frac{4}{3}G & 0 & 0 & 0 \\ 0 & 0 & 0 & G & 0 & 0 \\ 0 & 0 & 0 & 0 & G & 0 \\ 0 & 0 & 0 & 0 & 0 & G \end{bmatrix}. \quad (3)$$

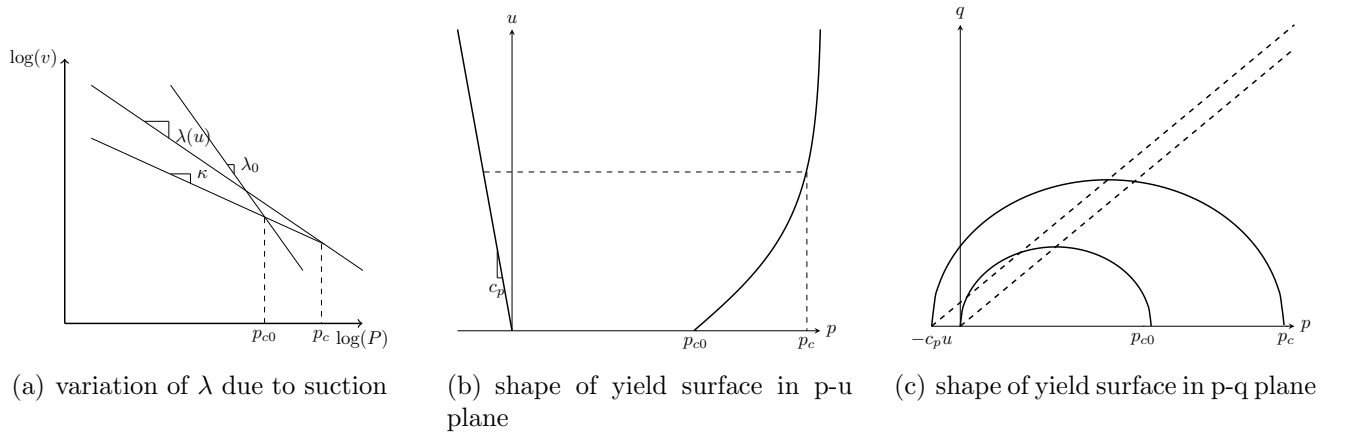


Figure 1: Influence of suction on model parameters and shape of the yield surface.

To determine whether elastic or plastic behaviour occurs a yield function f (and plastic potential g) can now be defined as

$$f = q^2 + M^2(p + c_p u)(p - p_c) \quad \text{and} \quad g = \alpha q^2 + M^2(p + c_p u)(p - p_c), \quad (4)$$

where q , p and M are the deviatoric stress invariant, mean pressure and slope of critical state line respectively - the same as in the MCC. The differences arise in the size of the yield surface. The parameter c_p determines the increase of cohesion with suction and serves to shift the yield surface based on the value of suction. The hardening law for the updated size of the yield surface at zero suction p_{c0} is given as

$$p_{c0} = p_{c0n} \exp\left(\frac{\varepsilon_v^p}{\lambda_0 - \kappa}\right) \quad (5)$$

where λ_0 is the plastic compressibility index at zero suction, however the size of the yield surface p_c is also dependent on suction and can be calculated as

$$p_c = p_{ref} \left(\frac{p_{c0}}{p_{ref}}\right)^{\frac{\lambda_0 - \kappa}{\lambda - \kappa}} \quad (6)$$

where p_{ref} is a reference mean stress [1] and λ is also dependent on suction as well as BBM parameters β and r and calculated as

$$\lambda = \lambda_0((1 - r) \exp(-\beta u) + r). \quad (7)$$

Figure 1 shows how the suction influences the values of (a) λ , (b) p_c and (c) the shape of the yield surface.

Model implementation

A backward Euler stress update procedure is carried out to calculate updated plastic and elastic strains which satisfy the yield function and update the associated hardening parameters accordingly. The following equations can be constructed and solved using a Newton Raphson process

$$b = \left\{ \begin{array}{l} \{\varepsilon^e\} - \{\varepsilon_{tr}^e\} + \Delta\gamma\{g_{,\sigma}\} \\ f \\ p_{c0} - \tilde{p}_{c0} \end{array} \right\} \quad (8)$$

with unknowns

$$x = \{\varepsilon^e \quad \Delta\gamma \quad p_{c0}\}. \quad (9)$$

The increment in these unknowns are then calculated by

$$\Delta x = [C]^{-1}\{b\} \quad (10)$$

until the residuals of (8) reach a preset tolerance, where $[C]$ contains derivatives of each of the residuals with respect to each of the unknowns

$$[C] = \begin{bmatrix} [I] + \Delta\gamma \left[\frac{\partial^2 g}{\partial \sigma^2} \right] [D^e] & \left\{ \frac{\partial g}{\partial \sigma} \right\} & \Delta\gamma \left\{ \frac{\partial^2 g}{\partial \sigma \partial p_c} \right\} \frac{\partial p_c}{\partial p_{c0}} \\ \left\{ \frac{\partial f}{\partial \sigma} \right\}^T [D^e] & 0 & \frac{\partial f}{\partial P_c} \frac{\partial p_c}{\partial p_{c0}} \\ \frac{\partial \tilde{p}_c}{\partial \{\varepsilon_v^p\}} \left\{ \frac{\partial \{\varepsilon_v^p\}}{\partial \sigma} \right\}^T [D^e] & -\frac{\partial \tilde{p}_c}{\partial \{\varepsilon_v^p\}} \left\{ \frac{\partial g}{\partial \sigma} \right\} \{1\}^T & 1 - \Delta\gamma \frac{\partial \tilde{P}_c}{\partial \{\varepsilon_v^p\}} \left\{ \frac{\partial^2 g}{\partial \sigma \partial p_c} \right\} \frac{\partial p_c}{\partial p_{c0}} \{1\}^T \end{bmatrix}. \quad (11)$$

Consistent tangent

In order to achieve an optimum rate of convergence for a global Newton Raphson loop in a finite element code it is essential to ensure that the tangent matrix passed back from the constitutive model is consistent with the stress update procedure within it. This is obtained by linearising the residuals (8) with respect to the trial strain which gives

$$[A^{alg}]^{-1} \{ \{d\sigma\} \ d\Delta\gamma \ dp_{c0} \}^T = \{ \{d\varepsilon^{tr}\} \ 0 \ 0 \}^T. \quad (12)$$

$[A^{alg}]^{-1}$ can be constructed in a very similar format to (11):

$$[A^{alg}]^{-1} = \begin{bmatrix} [C^e] + \Delta\gamma \left[\frac{\partial^2 g}{\partial \sigma^2} \right] & \left\{ \frac{\partial g}{\partial \sigma} \right\} & \Delta\gamma \left\{ \frac{\partial^2 g}{\partial \sigma \partial p_c} \right\} \frac{\partial p_c}{\partial p_{c0}} \\ \left\{ \frac{\partial f}{\partial \sigma} \right\}^T & 0 & \frac{\partial f}{\partial P_c} \frac{\partial p_c}{\partial p_{c0}} \\ \frac{\partial \tilde{p}_c}{\partial \{\varepsilon_v^p\}} \left\{ \frac{\partial \{\varepsilon_v^p\}}{\partial \sigma} \right\}^T & -\frac{\partial \tilde{p}_c}{\partial \{\varepsilon_v^p\}} \left\{ \frac{\partial g}{\partial \sigma} \right\} \{1\}^T & 1 - \Delta\gamma \frac{\partial \tilde{P}_c}{\partial \{\varepsilon_v^p\}} \left\{ \frac{\partial^2 g}{\partial \sigma \partial p_c} \right\} \frac{\partial p_c}{\partial p_{c0}} \{1\}^T \end{bmatrix}. \quad (13)$$

where

$$[C^e] = [D^e]^{-1}. \quad (14)$$

Taking the inverse of (13) gives

$$[A^{alg}] = \begin{bmatrix} [D^{alg}] & \{A_{12}^{alg}\} & \{A_{13}^{alg}\} \\ \{A_{21}^{alg}\}^T & A_{22}^{alg} & A_{23}^{alg} \\ \{A_{31}^{alg}\}^T & A_{32}^{alg} & A_{33}^{alg} \end{bmatrix} \quad (15)$$

where $[D^{alg}]$ is the consistent tangent required.

Verificaiton with single point stress paths

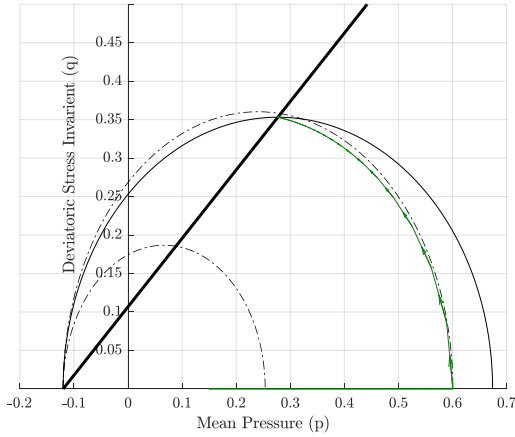
To verify the behaviour of the model at a single material point, a stress path was tested of an isotropic increase of mean net stress followed by compression under constant volume to critical state for varying values of constant suction. The parameters used for these tests can be seen in Table 1. An initial

Table 1: BBM parameters used

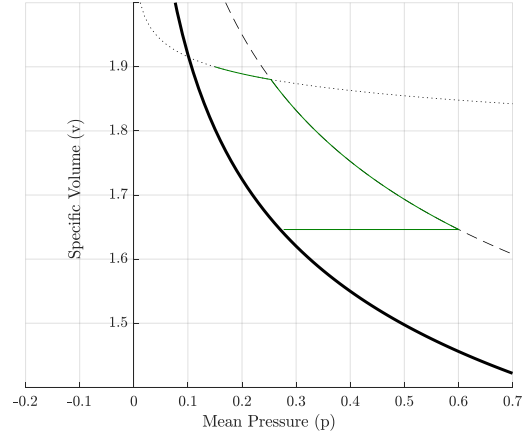
κ	λ	G	κ_s	λ_s	p_c	r	θ	ϕ	p_{ref}	c_p	α
0.02	0.02	10	0.008	0.08	0.2	0.75	12.5	0.549	0.1	0.6	1

stress was set to be

$$\sigma_0 = \{0.15 \ 0.15 \ 0.15 \ 0 \ 0 \ 0\}^T \quad (16)$$



(a) Suction=0.2. Initial void ratio=0.9.



(b) Suction=0.2. Initial void ratio=0.9.

Figure 2: Stress paths for isotropic increase of mean net stress followed by compression under constant volume for varying values of constant suction.

and a strain increment of

$$\Delta \varepsilon = \{-0.0001 \quad -0.0001 \quad -0.0001 \quad 0 \quad 0 \quad 0\}^T \quad (17)$$

was applied until the mean pressure was equal to 0.6 at which point the applied strain was

$$\Delta \varepsilon = \{-0.0015 \quad 0.003 \quad -0.0015 \quad 0 \quad 0 \quad 0\}^T. \quad (18)$$

The resulting behaviour in the p - q and p - v planes can be seen in Figure 2 along with plots of the yield surface and critical state lines.

Future work

The model described above is the simplest case designed to be able to get usable results before introducing further developments. The model has been programmed as a user element in the commercial software Abaqus which allows a vast array of tools for tackling more complex problems such as including a relationship between suction and degree of saturation. Other developments in progress include using the increment of suction as an input to the constitutive model and a second yield surface relating to the suction as in the standard BBM [2], as well as an extension to capture cyclic loading.

Conclusions

This paper has outlined a simplified version of a constitutive model for unsaturated soils currently being developed for the purpose of modelling wind turbine foundations. The implementation including a backward Euler stress update and calculation of consistent tangent was presented in addition to an example stress path at constant suction. The model has been implemented as an Abaqus user material so that it will be able to be used in more complex boundary value problems in the future.

References

- [1] E.E. Alonso, A. Gens and A. Josa, *A constitutive model for partially saturated soils*. Geotechnique (1990) 3:405–430.
- [2] J. Vaunat, J.C. cante, A. Ledesma and A. Gens *A stress point algorithm for an elastoplastic model in unsaturated soils*. International journal of plasticity (2000) 16:121-141.

Matlab m-script

The below 'interesting' MATLAB script takes coordinates, element topology, external forces and material properties and performs a simple linear elastic finite element analysis of the geometry representing 'UKACM' and plots the resulting geometry. The nodal displacements are then converted to ASCII characters and evaluated to direct the user to additional 'interesting' reading.

```
%A linear elastic finite element model of 'UKACM'
%Specify nodal coordinates
ctr=0;coord=[];
for i=1000:-200:0
    for j=0:200:3200
        ctr=ctr+1;coord(ctr,:)= [j i];
    end
end
coord([6 18 19 20 21 22 23 46 47 48 49 50 51 52 53 74 82 83 84 85 91],:)=[];
%Specify element topology
etpl=[28 1 2 29;30 3 4 31;31 4 5 32;32 6 17 33;17 6 7 18;18 7 8 19;
19 8 9 20;20 9 10 21;21 10 11 22;22 11 12 23;23 12 13 24;24 13 14 25;
25 14 15 26;26 15 16 27;34 17 18 35;36 19 20 37;37 20 21 38;48 22 23 49;
50 24 25 51;52 26 27 53;54 28 29 55;39 30 31 40;40 31 32 41;41 32 33 42;
43 34 35 44;44 35 36 45;45 36 37 46;46 37 38 47;56 39 40 57;57 40 41 58;
71 41 42 59;59 43 44 60;61 45 46 62;62 46 47 63;64 48 49 65;78 50 51 79;
80 52 53 81;66 54 55 67;67 55 56 68;68 56 57 69;69 57 58 70;71 59 60 72;
73 61 62 74;74 62 63 75;75 63 64 76;76 64 65 77];
%Specify applied external forces at nodes
fext=1E3*[-3125;22500;-3125;7250;-14750;27500;-8250;-45500;6500;-2000;
-10336.5384615385;46980.7692307692;10000;20500;-1500;5500;-8500;20250;
-13500;53500;-8375;9750;-1750;-750;6750;-250;8250;52000;625;62500;-625;
28250;14048.0769230769;-113211.538461538;-1500;-1750;250;-1750;0;-23000;
6250;-87000;7375;-19500;750;-3250;-6375;-15500;-7875;-39500;-2125;-56750;
-875;-30000;1625;-4500;1625;-20750;5000;30500;-1500;-83750;
-9288.46153846153;76769.2307692308;11576.9230769231;36211.5384615385;-8000;
45500;-6875;78500;1375;67000;7500;91500;7250;53000;14125;43250;9500;35000;
-17317.3076923077;-114096.153846154;19384.6153846154;10192.3076923077;625;
-64750;-500;-96000;-3000;-86000;0;-131000;1875;-63250;375;9500;375;500;
-375;11750;-375;12500;-125;20250;-125;1000;875;22500;1625;34000;3000;13500;
8875;105750;6625;77750;23490.3846153846;176557.692307692;-125;94750;1125;
89750;875;153250;-9625;147500;-8500;33750;875;16250;625;0;-125;0;-7375;0;
-8625;0;-2000;0;-35307.6923076923;0;-1000;0;1750;0;125;0;7750;0;9125;0;
-250;0;0;0;0;0;1625;0;0;0];
%Specify material properties and boundary conditions
E=1E6; v=0; bc=zeros(17,2); bc(:,1)=[2*66:2:2*80 161 162];
%Calculate array sizes and initialise
ngp=4; [nels,nen]=size(etpl); [nodes,nD]=size(coord); nDoF=nodes*nD;
B=zeros(3,nen*nD); Kt=zeros(nDoF); gp=zeros(ngp,nD); dNr=zeros(ngp*nD,nen);
%Calculate derivative of 2D linear shape functions
g2=1/sqrt(3); gp(:,1)=[-1 1 -1 1]'*g2; gp(:,2)=[-1 -1 1 1]'*g2;
xsi=gp(:,1);eta=gp(:,2);r2=ngp*2; wp=ones(4,1);
dNr(1:2:r2, 1)=-1/4*(1-eta);dNr(1:2:r2, 2)=-1/4*(1+eta);
dNr(1:2:r2, 3)= 1/4*(1+eta);dNr(1:2:r2, 4)= 1/4*(1-eta);
dNr(2:2:r2, 1)=-1/4*(1-xsi);dNr(2:2:r2, 2)= 1/4*(1-xsi);
dNr(2:2:r2, 3)= 1/4*(1+xsi);dNr(2:2:r2, 4)=-1/4*(1+xsi);
bml=[1 1 1 0 0 0].'; I6=[eye(3) zeros(3); zeros(3) eye(3)/2];
%Construct plane strain stiffness matrix
D=E/((1+v)*(1-2*v))*((1-2*v)*I6+v*(bml*bml.')); D=D([1 2 4],[1 2 4]);
%Calculate element stiffness matrices and assemble global stiffness matrix
```

```

for nel=1:nels
    ed=ones(nD,1)*etpl(nel,:)*nD-(nD-1:-1:0) .* ones(1,nen);
    ed=reshape(ed,1,nen*nD); JT=dNr*coord(etpl(nel,:),:); ke=zeros(nen*nD);
    for gp=1:ngp
        indx=(nD*gp-(nD-1:-1:0)); detJ=det(JT(indx,:)); dNx=JT(indx,:)\dNr(indx,:);
        B([1 3],1:nD:end)=dNx;B([3 2],2:nD:end)=dNx; ke=ke+B.*D*B*detJ*wp(gp);
    end
    Kt(ed,ed)=Kt(ed,ed)+ke;
end
%Solve linear system to obtain displacements
uvw=zeros(nDoF,1); uvw(bc(:,1))=bc(:,2); fd=(1:nDoF); fd(bc(:,1))=[];
uvw(fd)=Kt(fd,fd)\(fext(fd)-Kt(fd,bc(:,1))*bc(:,2));
xydisp=reshape(uvw,[2,81]); coord2=coord+xydisp';
%Plot original and deformed elements & colour letters
for nels=1:46
    if coord(etpl(nels,4),1)<601
        C='b';
    elseif coord(etpl(nels,4),1)<1201
        C='c';
    elseif coord(etpl(nels,4),1)<1801
        C='r';
    elseif coord(etpl(nels,4),1)<2201
        C='m';
    else
        C='y';
    end
    fill(coord(etpl(nels,:),1),coord(etpl(nels,:),2),'k'); hold on;
    fill(coord2(etpl(nels,:),1),coord2(etpl(nels,:),2),C); hold on;
end
axis equal;
%Bonus feature by evaluating the text equivalent of the vertical displacement
eval(char(round(xydisp(2,:))));

```

COMPUTATIONALLY-DERIVED DESIGN GUIDELINES AND CRACK HEALING MODELS FOR SELF-HEALING MATERIALS

Sathiskumar A Ponnusami

Department of Mechanical Engineering and Aeronautics, City, University of London, Northampton Square,
London EC1V 0HB, United Kingdom

sathiskumar.ponnusami@city.ac.uk

Summary

Research in the field of self-healing materials gained significant attention in the last decade owing to its promise of enhanced durability of the material components in engineering applications. Though the research has led to several successful demonstrations, extensive experimental tests will be required for a successful demonstration. Further, for real-time engineering applications with self-healing materials, arriving at an optimal design of the self-healing system is crucial. In this context, modelling techniques in combination with a limited number of experimental tests are potentially more efficient than a design process based on extensive experimental campaigns. With this motivation, the research aims to develop a modelling framework to analyse and understand the fracture mechanisms and the healing behaviour of self-healing material systems using finite element modelling approach. In particular, cohesive zone-based fracture mechanics in combination with cohesive elements is utilised in this work as the computational framework. The overall objective is to provide certain guidelines and suggestions for material scientists in terms of selection and design of healing particles and a computational tool to understand and quantify the cracking and healing behaviour of self-healing material systems.

Key Words: *Self-healing materials; Fracture mechanics; Finite element modelling; Crack healing model; Crack-particle interaction*

Self-healing Materials: Challenges and Requirements

A classical example of a self-healing mechanism is based on healing capsules (particles) dispersed within the base (or matrix) material as shown in Fig. 1. Upon loading the material, microcracks emanate which then interact with the healing particles, thereby activating the self-healing mechanism [1]. In the context of such capsule (or fiber)-based self-healing materials, there are two critical aspects that need to be addressed in order to achieve a robust self-healing system. Firstly, a crack initiated in the host (or matrix) material should be attracted towards the healing particle and further should break the particle for healing to occur. The second critical aspect in a self-healing system is centered on how the material recovers its mechanical properties once the healing mechanism is activated in or near the fracture surfaces. The extended abstract summarises some contributions towards the above two requirements, ultimately offering design guidelines and tools for successful realisation of self-healing materials.

Fracture Mechanisms and Design Maps

This section aims to determine the fracture mechanism in a particulate system, given the properties of the constituent material phases. Using cohesive-element based finite element fracture simulations on a single particle-matrix system Fig. 2, the effect of mismatch in elastic and fracture properties between the matrix and the particle are analysed. The results of the simulations in terms of crack path for few selected mismatch ratios are shown in left of Fig. 3. From the results, one can clearly observe the effect of mismatch in fracture properties (σ_c^p/σ_c^m) on the fracture mechanism, which is hardly dealt in the literature when compared with the mismatch in elastic properties (E^p/E^m). For example, on the

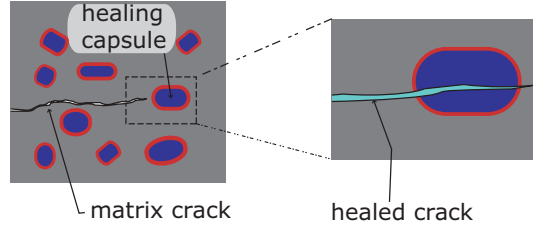


Figure 1: Schematic of healing mechanism in a particulate self-healing material.

reported crack paths, it can be seen that even for same elastic mismatch, different crack paths are reported if the particle strength is different (lower in this case) from that of the matrix. The design map shown in the right of Fig. 3 summarises an extensive set of simulations and distinguishes the two fracture mechanisms, namely particle fracture and crack deflection. This map can serve as a handy reference guide for the selection of healing particles for a given matrix system.

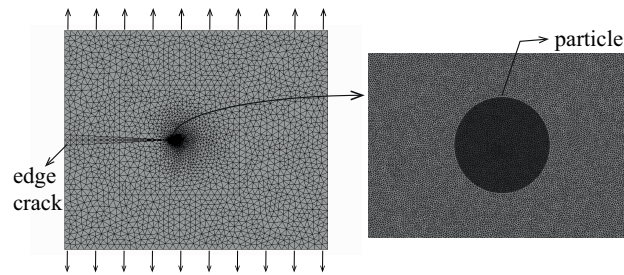


Figure 2: Finite element mesh of the model with a single particle embedded in a large matrix.

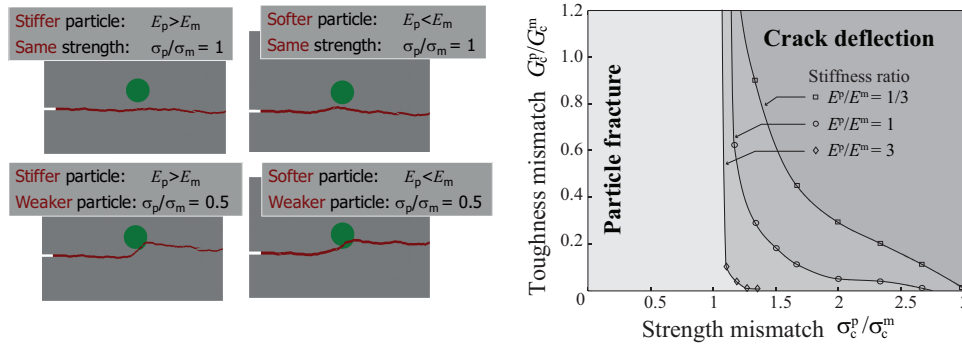


Figure 3: Crack paths for selected elastic and fracture mismatch values. The center of the particle is located at an offset of $3d/4$ with respect to the initial crack path (left). d is the particle diameter. Fracture map for various mismatch ratios distinguishing two different fracture mechanisms (right).

Cohesive Crack Healing Model

The proposed crack healing model is a composite-based constitutive model for simulating the recovery of fracture properties upon activation of crack healing and is schematically explained in Fig. 4. The traction components of the composite response, \tilde{t}_n and \tilde{t}_s , are expressed as a weighted sum of the traction contributions from the original material, $t_n^{(0)}$ and $t_s^{(0)}$, and the healing material $t_n^{(1)}$ and $t_s^{(1)}$, as follows:

$$\tilde{t}_n = w^{(0)}t_n^{(0)} + w^{(1)}t_n^{(1)} \quad \tilde{t}_s = w^{(0)}t_s^{(0)} + w^{(1)}t_s^{(1)} \quad (1)$$

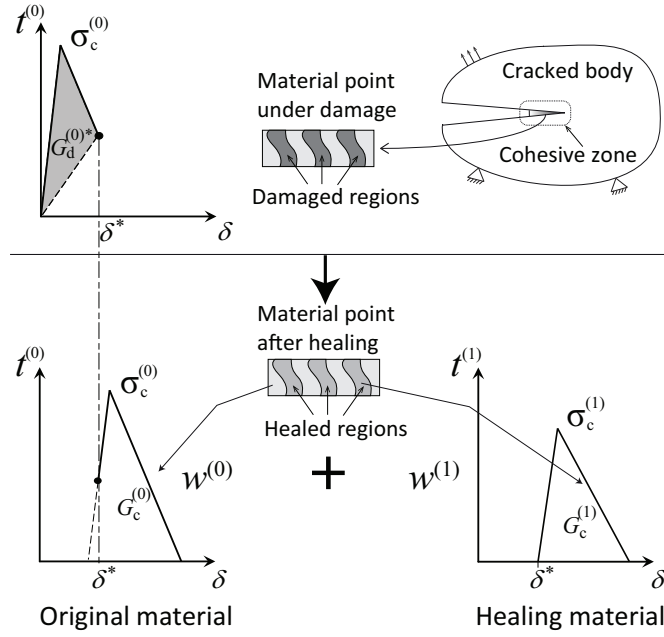


Figure 4: Traction-separation laws of original and healing material, which upon weighted addition, results in a composite cohesive relation for the crack-healing model.

where the superscripts (0) and (1) represent the original and healing materials, respectively. The weighting factors $w^{(0)}$ and $w^{(1)}$ introduced in (1), which can take values between 0 and 1, are the primary parameters in the model and can be interpreted as the surface-based volume fractions of the original and healing material respectively at the instance of healing activation.

If a single healing event occurs at a time $t = t^*$, the proposed constitutive model assumes that the factor $w^{(1)}$ is given by the value of the energy-based damage parameter at the instance of healing activation, $D^{(0)*}$, i.e.,

$$w^{(1)} = D^{(0)*} := \frac{G_d^{(0)*}}{G_c^{(0)}}. \quad (2)$$

$D^{(0)}$ represents the ratio between the energy dissipated $G_d^{(0)}(t)$ during decohesion of the original material up to time t and the fracture energy $G_c^{(0)}$ (work required for complete decohesion of the original material). In (2), $D^{(0)*}$ corresponds to the value of $D^{(0)}$ at $t = t^*$.

In accordance with (1) and (2), the effective fracture energy \tilde{G}_c of the composite material after healing becomes the weighted sum of the fracture energies of the original and healing materials, given as

$$\tilde{G}_c = w^{(0)}G_c^{(0)} + w^{(1)}G_c^{(1)}. \quad (3)$$

Another key step in the model development is the introduction of displacement shifts into the crack opening displacements in order to simulate healing process, which make the nominal crack opening zero upon complete healing [2]. The model is applied to a particulate self-healing system represented by an unit cell (single particle-matrix) and is subjected to a loading and healing sequence as indicated in Fig. 5a. Under this loading, the specimen is partially fractured and then unloaded. Healing is allowed to occur in the unloaded condition, which is then followed by reloading of the healed specimen. The response of the unit cell in terms of the applied vertical displacement and the corresponding reaction force is shown in Fig. 5b for various fracture properties of the healing material, namely $\sigma_c^{(1)}/\sigma_c^{(0)}$, $G_c^{(1)}/G_c^{(0)} = 0.25, 0.5, 0.75$ and 1, where the superscript 1 refers to the healing material. As shown in Fig. 5b, the curve corresponding to equal properties of the healing and original material predicts a recovery of

the response after healing similar to that of the original material. The next three curves correspond to lower values of the fracture properties of the healing material and hence the load-displacement curves fall below that of the original material after healing.

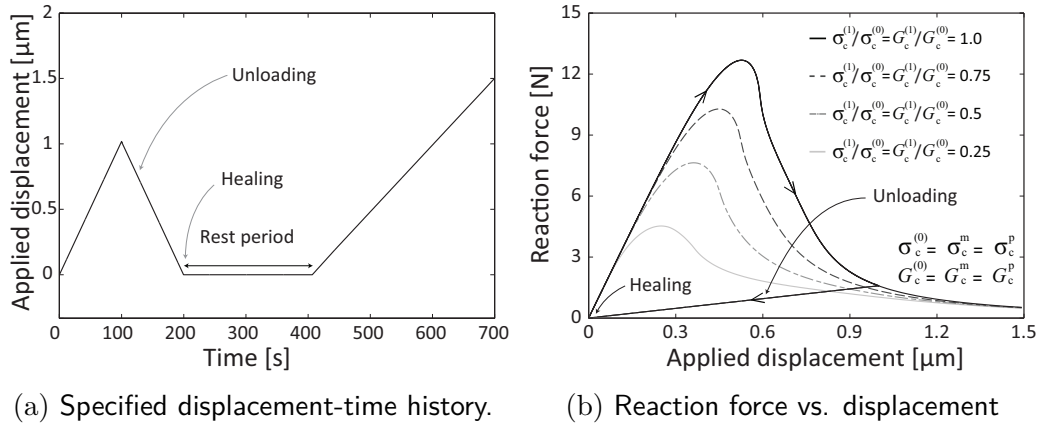


Figure 5: Application of the model to a healing scenario under unloaded condition: (a) applied loading to unit cell and (b) reaction force as a function of applied displacement for various values of the fracture properties of the healed material.

Conclusions

In the context of self-healing materials design, two different aspects were addressed using a computational fracture mechanics framework. Firstly, design maps were generated distinguishing relevant fracture mechanisms in a particulate system and it was shown the mismatch in fracture properties is more important than the elastic mismatch in deciding the crack path. This was then followed by development and numerical implementation of a crack healing model to simulate recovery of mechanical property using a modified composite traction-separation relation. From the perspective of materials scientists, the above guidelines and healing modelling technique can serve as a design and optimisation tool for successful development of self-healing materials.

Acknowledgements

This research was conducted with contributions from Dr. Sergio Turteltaub, Mr. Jayaprakash Krishnasamy and Prof. Sybrand van der Zwaag at TU Delft, Netherlands. The author acknowledges the support from IOP Self Healing Materials (Agentschap NL) and European Union Seventh Framework Programme (FP7/2007-2013, grant agreement no 309849) for their financial support of the research.

References

- 1 S. van der Zwaag and E Brinkman. eds. *Self Healing Materials: Pioneering Research in the Netherlands*, IOS Press, Netherlands, 2015.
- 2 S. A. Ponnusami, J. Krishnasamy, S. Turteltaub and S. van der Zwaag. A cohesive-zone crack healing model for self-healing materials. *International Journal of Solids and Structures*, 134, 249-263, 2018.

NOVEL UNIFIED FINITE ELEMENT SCHEMES FOR COMPUTATIONAL SOLID MECHANICS BASED ON BÉZIER ELEMENTS

***Chennakesava Kadapa**

Swansea Academy of Advanced Computing, Swansea University, Swansea SA1 8EN, United Kingdom.

*c.kadapa@swansea.ac.uk

Summary

This work introduces a novel unified finite element framework for computational solid mechanics based on quadratic Bézier triangular and tetrahedral elements that can be readily generated by exploiting the existing mesh generators for quadratic Lagrange elements. New $\bar{\mathbf{B}}$ and $\bar{\mathbf{F}}$ elements and two new mixed elements, BT2/BT0 and BT2/BT1, are introduced for dealing with the issues associated with volumetric and shear locking as well as for performing computationally efficient explicit elastodynamics simulations of problems modelled with nearly incompressible elastic and elastoplastic material models. By successfully simulating challenging benchmark examples, it is shown that the proposed work offers a simple unified finite element framework that is robust, accurate and computationally very efficient for performing the simulations of a wide variety of challenging problems in solid mechanics.

Key Words: *Bézier elements; Hyperelasticity; Elastoplasticity; Explicit scheme; Elastodynamics*

Introduction

Explicit dynamic simulations find many applications in the simulation of solid mechanics problems subjected to higher stress or strain rates and impact or blast loads. Despite numerous developments in the field of computational solid mechanics over the past couple of decades, robust and computationally efficient numerical schemes that can effectively perform explicit dynamic simulations of solid mechanics problems consisting of elastoplastic and incompressible hyperelastic materials over triangular/tetrahedral meshes are still lacking. This lack of developments is primarily due to the fundamental disadvantages of Lagrange family of elements for explicit schemes: (i) linear triangular and tetrahedral elements require very fine meshes in addition to the sophisticated formulations for overcoming the issues of volumetric and shear locking and oscillatory pressure fields, and (ii) higher-order Lagrange elements are completely useless for explicit schemes using the row-sum-lumped mass matrices.

To overcome the above issues, the author has recently proposed a novel unified finite element framework based on quadratic Bézier elements [3, 4]. The key advantage of the proposed framework lies in its ability to perform computationally efficient explicit elastodynamics simulations of nearly incompressible hyperelastic and elastoplastic material models using a finite element formulation that is also applicable for elastostatic and implicit elastodynamic simulations; the proposed framework is free from ad-hoc stabilisations and also does not require transformation of pressure equation into rate-form.

Formulations

In this paper, equations for only the explicit schemes are presented for the sake of brevity. For the details on the schemes for elastostatics and implicit elastodynamics, the reader is referred to [3, 4, 5].

Explicit scheme for the displacement, $\bar{\mathbf{B}}$ and $\bar{\mathbf{F}}$ formulations

The fully discrete system of equations for the displacement, $\bar{\mathbf{B}}$ and $\bar{\mathbf{F}}$ formulations using the explicit

scheme of [1] can be written as

$$\mathbf{M}_{uu} \mathbf{a}_{n+1} = \mathbf{F}_n^{\text{ext}} - \mathbf{F}_n^{\text{int}} \quad (1)$$

$$\mathbf{u}_{n+1} = \mathbf{u}_n + \Delta t \mathbf{v}_n + \Delta t^2 \left[\left(\frac{1}{2} - \beta \right) \mathbf{a}_n + \beta \mathbf{a}_{n+1} \right] \quad (2)$$

$$\mathbf{v}_{n+1} = \mathbf{v}_n + \Delta t [(1 - \gamma) \mathbf{a}_n + \gamma \mathbf{a}_{n+1}] \quad (3)$$

$$\text{where } \mathbf{F}_n^{\text{ext}} = \int_{\Omega} \mathbf{N}_u^T \mathbf{f}_{0n} \, d\Omega + \int_{\Gamma} \mathbf{N}_u^T \mathbf{t}_{0n} \, d\Gamma \quad (4)$$

$$\mathbf{F}_n^{\text{int}} = \int_{\Omega} \mathbf{B}_{\Omega}^T \boldsymbol{\sigma}_n \, d\Omega \quad - \quad \text{Displacement formulation - Small strains} \quad (5)$$

$$\mathbf{F}_n^{\text{int}} = \int_{\omega} \mathbf{B}_{\omega}^T \boldsymbol{\sigma}_n \, d\omega \quad - \quad \text{Displacement formulation - Finite strains} \quad (6)$$

$$\mathbf{F}_n^{\text{int}} = \int_{\Omega} \bar{\mathbf{B}}_{\Omega}^T \bar{\boldsymbol{\sigma}}_n \, d\Omega \quad - \quad \bar{\mathbf{B}}\text{- formulation} \quad (7)$$

$$\mathbf{F}_n^{\text{int}} = \int_{\omega} \bar{\mathbf{B}}_{\omega}^T \bar{\boldsymbol{\sigma}}_n \, d\omega \quad - \quad \bar{\mathbf{F}}\text{- formulation} \quad (8)$$

where \mathbf{B}_{Ω} and \mathbf{B}_{ω} are the original strain-displacement matrices, respectively, with respect to configurations Ω and ω ; $\bar{\mathbf{B}}_{\Omega}$ is the modified strain-displacement matrix for $\bar{\mathbf{B}}$ -bar formulation; $\boldsymbol{\sigma}$ is the original Cauchy stress; and $\bar{\boldsymbol{\sigma}}$ is the modified Cauchy stress tensor for $\bar{\mathbf{B}}$ -bar and $\bar{\mathbf{F}}$ -bar formulations. For third-accuracy in time, $\gamma = 3/2$ and $\beta = 13/12$.

Explicit scheme for mixed displacement-pressure formulation

With $\hat{\boldsymbol{\sigma}} = \bar{\boldsymbol{\sigma}}_{\text{dev}} + \mathbf{m}p$ as the modified Cauchy stress tensor, the fully discrete system of equations for the explicit scheme for the mixed displacement-pressure formulation can be written as

$$\mathbf{M}_{uu} \mathbf{a}_{n+1} = \mathbf{F}_n^{\text{ext}} - \mathbf{F}_n^{\text{int}} \quad (9)$$

$$\mathbf{u}_{n+1} = \mathbf{u}_n + \Delta t \mathbf{v}_n + \Delta t^2 \left[\left(\frac{1}{2} - \beta \right) \mathbf{a}_n + \beta \mathbf{a}_{n+1} \right] \quad (10)$$

$$\mathbf{v}_{n+1} = \mathbf{v}_n + \Delta t [(1 - \gamma) \mathbf{a}_n + \gamma \mathbf{a}_{n+1}] \quad (11)$$

$$\mathbf{M}_{pp} \mathbf{p}_{n+1} = \int_{\Omega} \mathbf{N}_p^T \kappa \boldsymbol{\varepsilon}_{n+1} \, d\Omega \quad - \quad \text{Small strains} \quad (12)$$

$$\mathbf{M}_{pp} \mathbf{p}_{n+1} = \int_{\Omega} \mathbf{N}_p^T \left. \frac{\partial U}{\partial J} \right|_{\mathbf{u}_{n+1}} \, d\Omega \quad - \quad \text{Finite strains} \quad (13)$$

$$\text{where } \mathbf{F}_n^{\text{int}} = \int_{\Omega} \mathbf{B}_{\Omega}^T \hat{\boldsymbol{\sigma}}_n \, d\Omega \quad - \quad \text{Small strains} \quad (14)$$

$$\mathbf{F}_n^{\text{int}} = \int_{\omega} \mathbf{B}_{\omega}^T \hat{\boldsymbol{\sigma}}_n \, d\omega \quad - \quad \text{Finite strains} \quad (15)$$

Example - Twisting of a column

The performance of the proposed scheme under extremely large deformations is assessed in this example by studying the problem of twisting of a column. The column is of size $1 \times 6 \times 1 \, \text{m}^3$; it is clamped at its bottom face and excited with an initial velocity, $\mathbf{v} = (z, 0, -x) 100.0 \sin(\pi y/12) \, \text{m/s}$. The material properties are: Young's modulus, $E = 17 \, \text{MPa}$; Poisson's ratio, $\nu = 0.499$; and density, $\rho_0 = 1100 \, \text{kg/m}^3$; the material model is assumed to be a nearly incompressible Neo-Hookean material model with the strain energy density given by

$$W(J, \bar{\mathbf{C}}) = \frac{1}{2} \mu (\text{I}_{\bar{\mathbf{C}}} - 3) + \frac{1}{2} \kappa \left(\frac{1}{2} (J^2 - 1) - \ln J \right) \quad (16)$$

where $\kappa = E/3(1 - 2\nu)$ is the Bulk modulus and $\mu = E/2(1 + \nu)$ is the shear modulus.

The evolution of Y-displacement of point A shown in Figure 1a demonstrates the apparent convergence of the proposed scheme and excellent agreement with the reference solution. Contour plots of pressure in Figure 1b show that the pressure field obtained with the proposed explicit scheme and the mixed elements is completely free from spurious oscillations and also that the pressure field obtained with the proposed scheme is in excellent agreement with the reference solution obtained with the implicit scheme.

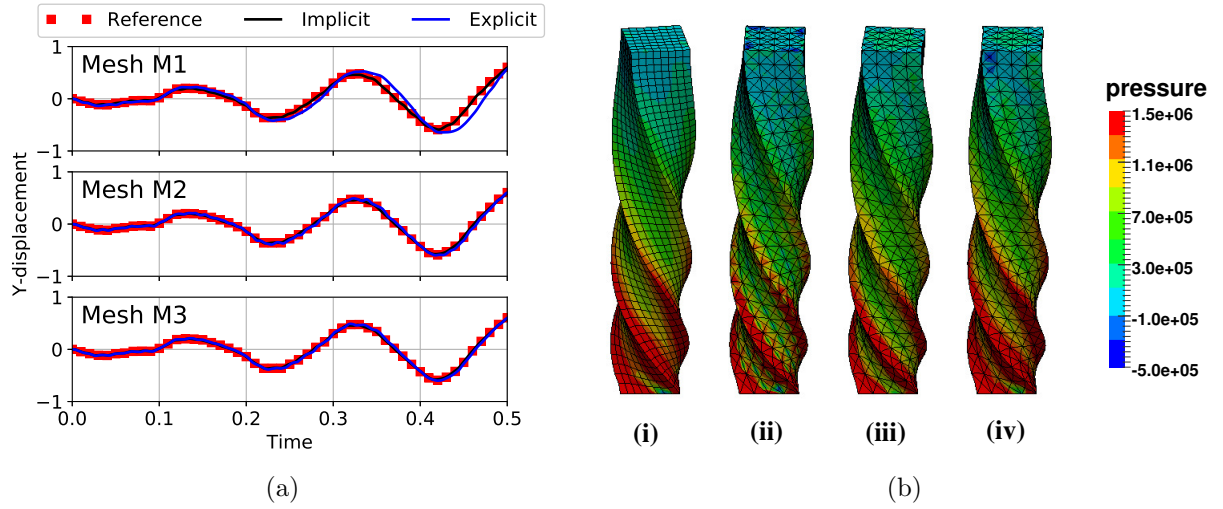


Figure 1: Twisting column: (a) evolution of Y-displacement of point A using implicit and explicit schemes. The reference solution is obtained with the mesh in (b)(i) using Q_2/Q_2 -SD elements [] and the implicit scheme; (b) contour plots of pressure at $t = 0.3$ obtained with M2 mesh and the explicit scheme - (i) Q_2/Q_2 -SD implicit scheme, (ii) BT2, (iii) BT2/BT0 and (iv) BT2/BT1.

Example - Taylor impact test

In this example, the proposed scheme is applied to simulate the well-known Taylor impact test benchmark in computational solid mechanics. In this test, a cylindrical bar of length 0.0324 m and diameter 0.0032 m impacts against a rigid frictionless wall at the speed of 227 m/s. Simulations are performed using the two meshes. The material model is elastoplastic with Young's modulus, $E = 117$ GPa; Poisson's ratio, $\nu = 0.35$; yield stress, $\sigma_y = \sigma_\infty = 0.4$ GPa; hardening modulus, $H = 0.1$ GPa; and density, $\rho_0 = 8930$ kg/m³. As shown in Figure 2, the results obtained with the proposed framework match very well with the reference solution. The results obtained with the coarse mesh with all the formulations are also not completely far off from the reference solution. The contour of the pressure field indicate that the pressure field obtained with the explicit scheme and the mixed formulation is free from spurious oscillations.

Conclusions

New \bar{B} and \bar{F} elements for quadratic Bézier triangular/tetrahedral elements (BT2) and new mixed elements, BT2/BT0 and BT2/BT1, are introduced for addressing the long-standing issues associated with performing explicit simulations of problems modelled with nearly incompressible material models. The ability of the proposed finite element framework to compute accurate numerical results using coarse triangular/tetrahedral meshes that can be generated using existing mesh generators is illustrated by studying the examples of twisting of a column and Taylor bar impact.

These results showcase the real potential of the present work in making a genuinely significant impact in performing the simulations of complex industrial problems. In particular, the present work has the

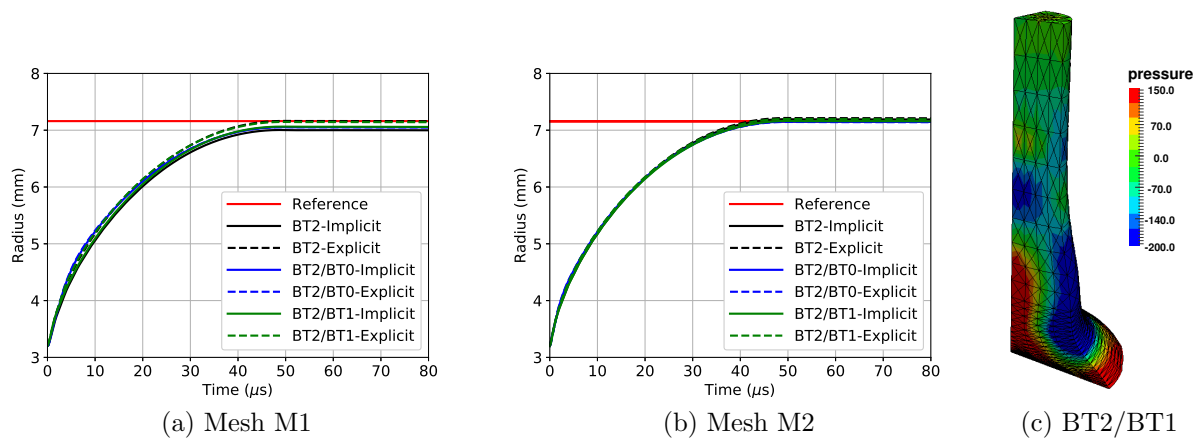


Figure 2: Taylor impact test: (a) evolution of radius of the bar for the coarse mesh (M1) (b) evolution of radius of the bar for the fine mesh (M2) (b) pressure contour plot for M2 mesh obtained with the explicit scheme and BT2/BT1 element. Reference solution is from [6].

potential to extend the capability of today's finite element codes to performing computationally efficient explicit simulations of challenging large-scale nonlinear elastodynamic problems.

Acknowledgements

The author acknowledges the support of the Supercomputing Wales project, which is part-funded by the European Regional Development Fund (ERDF) via the Welsh Government.

References

- [1] Chung J., Lee J. M.. A new family of explicit time integration methods for linear and non-linear structural dynamics. *International Journal for Numerical Methods in Engineering*. 1994;37:3961-3976.
- [2] de Souza Neto E. A., Perić D., Owen D. R. J.. *Computational Methods for Plasticity, Theory and Applications*. United Kingdom: John Wiley and Sons; 2008.
- [3] Kadapa C.. Novel quadratic Bézier triangular and tetrahedral elements using existing mesh generators: Applications to linear nearly incompressible elastostatics and implicit and explicit elastodynamics. *International Journal for Numerical Methods in Engineering*. 2019;117:543-573.
- [4] Kadapa C.. Novel quadratic Bézier triangular and tetrahedral elements using existing mesh generators: Extension to nearly incompressible implicit and explicit elastodynamics in finite strains. Accepted for publication in *International Journal for Numerical Methods in Engineering*. DOI: 10.1002/nme.6042
- [5] Kadapa C., Dettmer W. G., Perić D.. Subdivision based mixed methods for isogeometric analysis of linear and nonlinear nearly incompressible materials. *Computer Methods in Applied Mechanics and Engineering*. 2016;305:241-270.
- [6] Zienkiewicz O. C., Rojek J., Taylor R. L., Pastor M.. Triangles and Tetrahedra in explicit dynamic codes for solids. *International Journal for Numerical Methods in Engineering*. 1998;43:565-583.

PARAMETRIC STUDY OF HONEYCOMB COMPOSITE STRUCTURE USING OPEN SOURCE FINITE ELEMENT SOFTWARE

*Ahmed H. Abdulaziz^{1,2}, Mohammed Hedaya¹, John P. McCrory², Karen M. Holford², Adel Elsabbagh¹

¹Design and Production Engineering Department, Faculty of Engineering, Ain Shams University, Abbaseya, Cairo, Egypt, 11517

²School of Engineering, Cardiff University, Wales, United Kingdom, CF24 3AA

* ahesham@eng.asu.edu.eg

Summary

This paper deals with the parametric optimisation of a simply supported sandwich panel made of honeycomb composite structure using sequential quadratic programming SQP. The panel consists of aluminum honeycomb sandwiched between two orthotropic fibre glass faces. The parameters studied are fibreglass thickness, t_f , honeycomb height, h , and honeycomb wall thickness, t_c . The objective was to minimise weight to bending stiffness ratio by using the nonlinear MATLAB function *fmincon*, considering the maximum central displacement and intercellular buckling as the constraints. Following this, a static structural analysis was conducted on the optimised structure using the open source finite element solver CalculiX and Salome Platform software for preprocessing. The maximum displacement of the honeycomb panel was found less than the displacement serviceability limit state. Preliminary results show that composite honeycomb structures can be optimised yielding low weight to bending stiffness ratio using SQP method and CalculiX for design evaluation.

Keywords: *Parametric optimisation; Sequential quadratic programming; CalculiX; Salome Platform; Honeycomb composites*

Introduction

In the wind turbines industry, blade materials must have a low weight to bending stiffness ratio for optimal aerodynamics. Aluminum honeycomb can play a vital role in manufacturing longer wind turbine blades with fibre glass as outer skin due to the cost benefit when compared with using carbon fibre composites alone. This study proposes a parametric optimisation using Sequential Quadratic Programming algorithm SQP, which can be used in MATLAB's *fmincon* function to minimise weight to bending stiffness. This function deals with nonlinear constrained convex objective functions with linear/nonlinear equalities and inequalities. To evaluate the optimum values, structural analysis using finite element method was carried out using the open source finite element solver CalculiX. CalculiX has many interesting features such as wide compatibility with open source CAD modelling and mesh generating softwares such as Salome platform, FreeCad and GMSH. Further, it is extremely versatile as it can be modified using Python programming on Linux platform. For instance, recently Genao et al [1] have proposed a framework to merge Calculix FE solver with NASA's Micromechanics Analysis Code MAC to promote multiscale analysis of the composite materials effectively. Galehdari et al [2] have optimised honeycomb structural parameters using SQP and genetic algorithm for minimising the weight to absorbed energy ratio to increase the crashworthiness. Park et al [3], have conducted structural linear analysis on a cantilever model and sliding contact analysis using CalculiX and Code_Aster comparing the results favourably with ANSYS commercial FE software. Therefore, in this paper, Salome platform was used for meshing the honeycomb composite structure and CalculiX FE solver was used for conducting structural analysis.

Methodology

The common failure modes of sandwich structures may happen due to severe shear force, intercellular buckling, core crushing, delamination in case of orthotropic composite facets,

shear crimping and punching shear [4]. The sandwich panel dimensions width, b , and length, l , are $0.2\text{m} \times 0.2\text{m}$ respectively, and the honeycomb top/bottom faces are fibre glass with thickness, t_f , honeycomb height, h , and with wall thickness, t_c . The sandwich panel is treated as a shell structure considering the length/width are significantly larger than the height [5]. The top/bottom faces consist of three laminates with a combined thickness of t_f mm, and a $[0^\circ/90^\circ/0^\circ]$ layup meaning that the in-plane/bending deformations are decoupled. The fibre glass composite micromechanics properties are computed using the Halpin-Tsai empirical approach. Moreover, the research methodology workflow is presented in Figure 1.

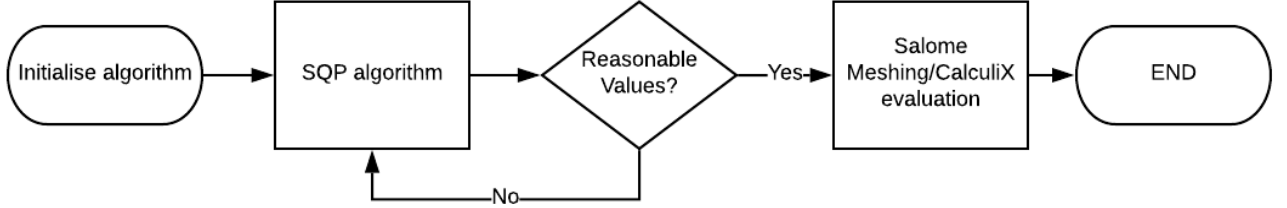


Figure 1: Block diagram of the research methodology

According to Bitzer [6] the equivalent bending stiffness of honeycomb sandwich panel D_{eq} can be computed using Eq. (1).

$$D_{eq} = \frac{E_1 h^2}{2\lambda} + \frac{E_1 t^3}{6\lambda} + \frac{E_c t_c^3}{12\lambda_c} \quad (1)$$

where; E_1 is longitudinal Young's modulus of faces and E_c is the honeycomb Young's modulus, λ is equal to $(1 - \nu_x \nu_y)$ and ν_x, ν_y are Poisson's ratio in longitudinal and transverse directions of composite layer, λ_c is $(1 - \nu_s)$, ν_s is Poisson's ratio of aluminum. The weight is $(g * b * l * (2 * \rho_f * t_f + \rho_{core} * h))$ where, g is gravity acceleration, b is breadth, l is length and ρ_{core} is honeycomb density and ρ_f is top/bottom face material density. As aforementioned, *Fmincon* function in MATLAB utilises sequential quadratic programming SQP algorithm to obtain the optimum minimum value. Therefore, the objective function is to minimise weight to bending stiffness which is formulated as in Eq. (2)

$$\text{Minimise } f(X) = \frac{\text{Weight}}{\text{bending stiffness, } D_{eq}} \quad (2)$$

The nonlinear constraints of the design are displacement δ and intercellular buckling P . The displacement at the panel centre should not exceed $span/100$ under concentrated force 5000N. The displacement of the panel at the centre can be computed by Lèvy's single series as shown in Eq. (3)

$$\delta = \sum_{m=1}^{\infty} Y_m \sin \frac{m\pi x}{a} \quad (3)$$

Since the panel is square of side a , Eq. (3) can be re-written as given in Eq. (4) [7], the serviceability limit state of displacement is $span/100$ and the intercellular buckling load must be less than critical value as computed in Eq. (5).

$$\delta = 0.00406 \frac{p a^4}{D_{eq}} \leq (span/100 = 2mm) \quad (4)$$

$$P < (P_c = K E_c (t_c)^3 / ((1 - \nu_s^2) * s)) \quad (5)$$

where P is the concentrated force at panel's centre, k is 5.75, E_c is the honeycomb Young's modulus, The upper/lower limits of the design variables are tabulated in Table 1. SQP function tolerance is 10^{-6} .

Table 1: Optimisation design variables with upper/lower bounds

Design Variable	$x(1)$	$x(2)$	$x(3)$
Geometric Parameter	t_f	h	t_c
Lower bound	0.0015	0.001	0.0001
Upper bound	0.002	0.010	0.001

As a side note, the positive definite Hessian matrix is a measure of function convexity over the domain [8]. Therefore, the eigenvalues of the Hessian have been computed and they are positive. After computations, a local minimum that satisfies the nonlinear constraints has been detected. Further, the variations of weight to bending stiffness ratio according to different honeycomb height and faces thickness are plotted in Figure 2. The iterations stopped as the objective function is non-decreasing in the feasible region. The buckling load factor (BLF) has been computed (i.e. $P_{critical} / P_{acting}$) and it is larger than 1 which indicates safety of the honeycomb cell wall under buckling.

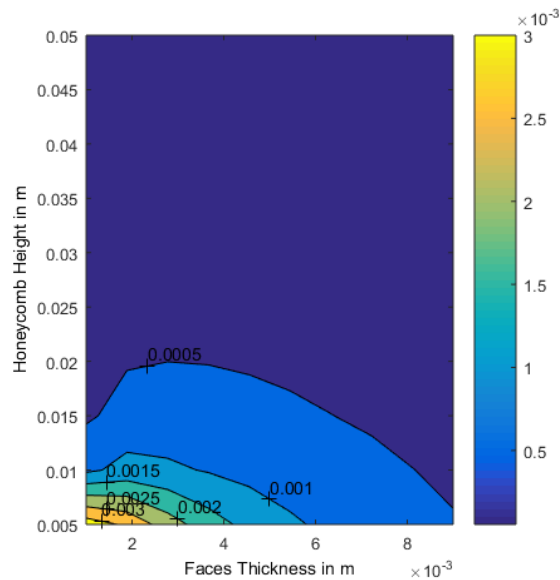


Figure 2: Weight to bending stiffness ratio for different height and face thickness

The optimum values are tabulated in Table 2. Furthermore, the MATLAB script used to obtain this result is provided at the end of this paper.

Table 2: Honeycomb optimum values

t_f (m)	H (m)	t_c (m)	W (N)	D_{eq} (N.m ²)	W / D_{eq} (m ⁻²)	Intercellular Critical Buckling (N)	Buckling Load Factor
0.0020	0.0100	0.0003	3.31564	5.8898e+03	5.6295e-04	1599.4	1.6

Finite Element Model

To evaluate the optimisation results, a honeycomb composite panel of zero thickness is processed in Salome Platform and meshed with “S6” and “S8R” shell elements [9] using Netgen 1D-2D option with maximum length 3 mm and minimum length 1.5 mm. Further, for better accuracy in solution, second order approximation for the meshing process is followed. However, care must be taken in meshing process as unlike commercial softwares, node-to-node connectivity is not assured for multiple surfaces automatically. Therefore, the sandwich panel must be partitioned into multiple shells and edges to assure the nodal connectivity. Yet, after partitioning it, the honeycomb core and top/bottom faces must be grouped and the two edges as well at the bottom face to form the elemental and nodal groups which will be used

later for materials definitions and boundary conditions in CalculiX code. The mesh is saved as “.unv” file to obtain a Python code of elements data. Afterwards, *unical* mesh converter in CalculiX is used to convert the (.unv) mesh file into input deck for further finite element analysis. Figure 3a) presents a block diagram of the FE process and 3b) shows the meshed honeycomb panel. It consists of 18,309 quadrangle elements “S8R” and 2,863 triangular elements “S6”. These elements expand to 3D quadratic brick elements and 3D wedge elements in modelling the top/bottom composite faces .

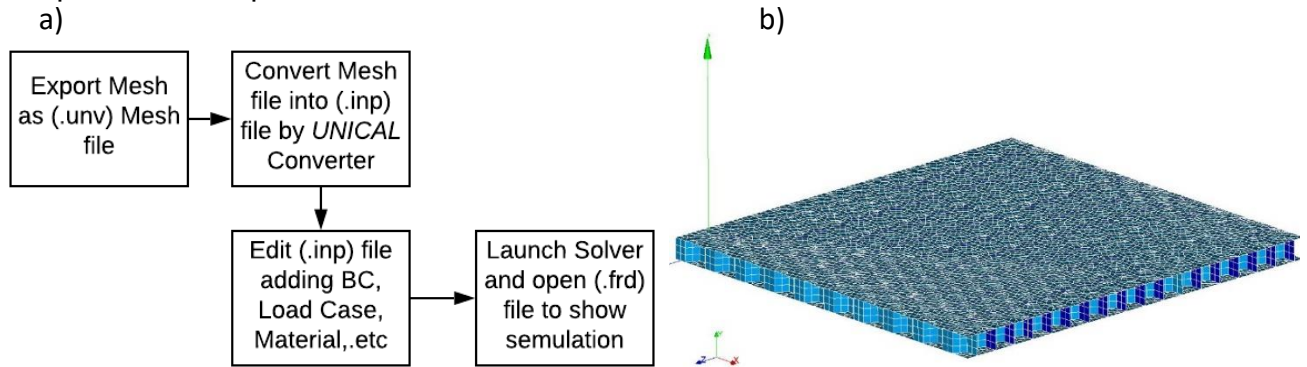


Figure 3: a) Finite element steps, b) Honeycomb Meshing in Salome Platform

The lateral concentrated force 5,000 N is positioned at the centre of the panel and structural static analysis is conducted. The maximum central displacement is 1.31 mm as shown in Figure 4a. Compared to the serviceability limit (i.e. span/100) which has been utilised within the optimisation, the maximum displacement obtained by CalculiX for the panel is desirably less. It is noteworthy to mention that in CalculiX section definition, the shell elements after expanding to build the required thickness may intersect at the corners as shown in Figure 4b. This intersection is dependent on the shell offset value and its normal direction whether negative or positive. Therefore, importantly, to assure that sides are interconnected.

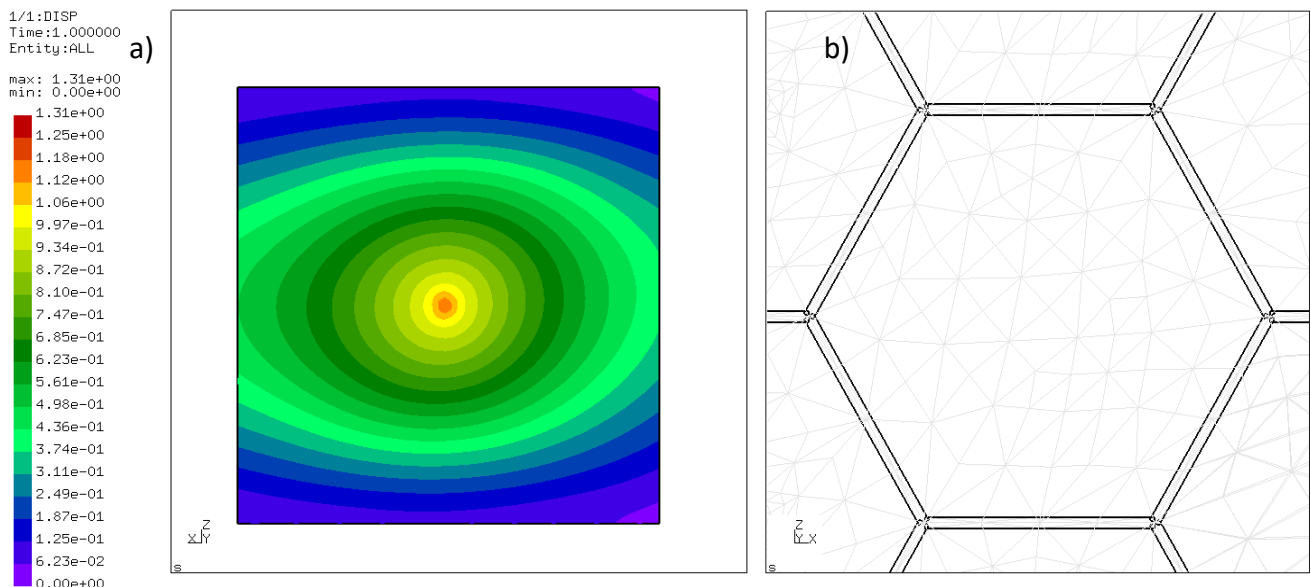


Figure 4: a) Maximum central displacement of the simply supported panel, b) the shell elements corner intersection after expanding

Conclusions

In conclusion, the honeycomb composite panel has been optimised using sequential quadratic programming. The ratio of weight to bending stiffness is minimised considering the intercellular buckling and lateral displacement as the main constraints functions. The optimum geometric parameters are the faces thickness, core height and core thickness. The buckling load factor

was computed, it was greater than 1 showing that the design would be safe under intercellular buckling. After the optimisation, a numerical model was processed and meshed with S8R/S6 shell elements in Salome platform then a structural static analysis has been carried out in the open source finite element solver CalculiX. Overall, it is demonstrated that coding with CalculiX is flexible, nevertheless care must be taken in the section definition within the CalculiX code. Mainly, the shell element offset and normal direction in the section card because the results are dependent on them. The maximum displacement retrieved from CalculiX was 1.31 mm which is less than the limiting value specified in SQP optimisation. Future research should be devoted to couple the SQP optimisation code within Salome Python code of the geometry/mesh to be processed after that in Calculix input deck. In addition, optimisation of honeycomb composite structure might prove an important area for future optimisation research so it is recommended that another optimisation technique such as Method of Moving Asymptotes MMA or Genetic algorithms is used and all optimisation results are examined.

Acknowledgements

This research is carried out within the PhD project entitled "*Investigation of Honeycomb Composite Structure for Wind Turbine Blades with Acoustics Emissions Damage Assessment*" funded by Newton-Mosharafa Fund in Egypt, *I.D: (NMJ 3/18)*. Many thanks to Prof Otto Ernst Bernhardt in Karlsruhe University of Applied Sciences, Germany, Hossem Elnachmie and Haoluan Li in Cardiff University for recommendations and discussions about some technical issues encountered in finite element modelling and optimisation.

References

- 1 F. A. Yapor Genao, E. J. Pineda, B. A. Bednarczyk and P. A. Gustafson, "Integration of MAC/GMC into CalculiX, an open source finite element code," in *AIAA SciTech Forum*, San Diego, California, 7-11 January 2019.
- 2 S. Galehdari, M. Kadkhodayan and S. Hadidi-Moud, "Analytical, experimental and numerical study of a graded honeycomb structure under in-plane impact load with low velocity," *International Journal of Crashworthiness*, vol. 20, no. 4, pp. 1754-2111, 2015.
- 3 S. K. Park, D.W. Seo, H. Jeong and M. Kim, "Performance evaluation of open-source structural analysis solver, CalculiX and Code_Aster, for linear static and contact problems," *ICIC Express Letters*, vol. 12, no. 7, pp. 655-662, 2018.
- 4 G. Lubin, *Handbook of Composites*, Springer Science & Business Media, 2013.
- 5 T. Kubiak, *Static and Dynamic Buckling of Thin-Walled Plate Structures*, Lodz, Poland: Springer, 2013.
- 6 T. N. Bitzer, *Honeycomb Technology: Materials, Design, Manufacturing, Applications and Testing*, Springer Science & Business Media, 2012.
- 7 S. P. Timoshenko and S. Woinowsky-Krieger, *Theory of Plates and Shells*, Singapore: McGraw-Hill Inc., 1959.
- 8 A. Messac, *Optimization in Practice with MATLAB® for Engineering Students and Professionals*, Cambridge: Cambridge University Press, 2015.
- 9 E. J. Barbero, *Finite Element Analysis of Composite Materials using Abaqus*, Taylor and Francis Group, 2013.

MATLAB M-script

```
%This code is written to perform
parametric optimisation using SQP
```

```
ub= [0.002,0.010,0.001];
nonlcon = @Constrains;
```

```

algorithm-All dimensions are in SI-
units~~After reading left hand
column to its end, continue reading
from top of right column to its
end. ~~File 1 consists of 3
sections.File 2 presents
constraints functions-File 1-
Section 1: Halpin-Tsai empirical
approach for micromechanics
computations & parameters
definitions
clc
rhof = 1800 ; % Faces density
rhos = 2700; % Aluminum density
% Material is Al honeycomb
L=0.2; % length
w=0.2; % breadth
g=9.81; % Gravity acceleration
E=60e9;
Ef = 73.1e9; %Fibre glass Young's
modulus
Em = 3.45e9;
vf=0.55; %volume fibre fraction
vm=0.45 ; % volume matrix fraction
uf = 0.22; % poisson ratio
fibreglass
um = 0.33; % poisson ratio Epoxy
Gf = 30e9; %Shear rigidity of fibre
Gm = 1.25e9 ; %Epoxy shear rigidity
v12 = uf*vf + um*vm ;
v21 = v12;
k = 0.9;%k:fibre misalignment
factor
E1 =k*(Ef*vf+Em*vm);%Longitudinal
Young's modulus
zeta = 2;
etae = ((Ef/Em)-1)/((Ef/Em)+zeta);
E2 = Em*(1+zeta*etae*vf)/(1-
etae*vf);%Longitudinal Young's
modulus
etaG= ((Gf/Gm)-1)/((Gf/Gm)+zeta);
G12 = Gm*(1+zeta*etaG*vf)/(1-
etaG*vf);
lambda = 1-v12*v21 ;
v_Al = 0.3 ; %Poisson ratio Al
lambdac = 1-v_Al;
s=0.0064;%Side length of cell
%File 1-Section 2:Optimisation
Formulation
f=@(x) 2*g*w*L*(rhof*x(1)+(x(2)*x(3)
*rhos/(s*(3^0.5))))/(((E1*x(1)*(x(2)
)+x(1))^2/(2*lambda))
+(E1*x(1)^3/(6*lambda))+(E*x(3)^3/(
12*lambdac))));
A = [];
b = [];
Aeq = [];
beq = [];
lb =[0.0015,0.001,0.0001];
x0 = [0.0018,0.002,0.0002] ;
%Initialisation point
options=optimoptions('fmincon','Algo
rithm','sqp','Display','iter') ;
[x,fval,exitflag,output,lambda,grad,
hessian]=fmincon(f,x0,A,b,Aeq,beq,lb
,ub,nonlcon,options);
disp (hessian);
e = eig(hessian);
[~,r] = chol(hessian);
disp (e)
disp (x)
M=2*g*w*L*(rhof*x(1)+(x(2)*x(3)*rhos
/(s*(3^0.5)))));
K = M/fval ;% stiffness at optimum
point
% File 1-Section 3: 3D plot of the
variables and corresponding
objective function
tfl = linspace(0.001,0.009,10) ;
h1 = linspace(0.005,0.05,10) ;
tc1 = linspace(0.0001,0.009,10);
[XX,YY] = meshgrid(tfl,h1);
[VV] = meshgrid(tc1);
WW=2*g*w*L.*(rhof*XX+(YY.*VV*rhos./(
s*(3^0.5)))));%Weight-various values
DD =(E1*XX.*(YY+VV).^2/ 2*0.9274)
+(E1*XX.^3/(6*0.9274))+(E*VV.^3/(12*
0.7))));%stiffness various values
Func = WW./DD ;
[FF] = meshgrid(Func);
%plot objective function vs design
variables core height&face thickness
figure
set(gcf, 'PaperPosition', [0 0 4
4]);
C = contourf(XX,YY,Func);
clabel(C,'FontSize',12)
xlabel('Faces Thickness in
m','FontSize',12,'Color','k');
ylabel('Honeycomb Height in
m','FontSize',12,'Color','k');
%File-2:Constraints.m File
function [c,ceq] = Constrains(x)
%Displacement at centre due to 5000
N concentrated force
c(1)=0.00406*5000*0.2^4/((3.758175e1
0*x(1)*(x(2)+x(1))^2/(2*0.9274))
+(3.758175e10*x(1)^3/(6*0.9274))+(6e
10*x(3)^3/(12*0.7)))-
0.002;%displacement
c(2)= 1000 -(5.75*60e9*x(3)^3/((1-
0.3^2)*0.0064)); %intercellular
buckling acting force on the side
ceq = [];
end

```

THE JOINT INFLUENCE OF CAVITIES PRESENCE AND RAPID DRAWDOWN CONDITION ON DISCHARGE RATE THROUGH EARTH DAMS

***Hawraa Alateya¹ and Alireza Ahangar Asr²**

¹School of Computing Science and Engineering, University of Salford, Manchester, United Kingdom

*h.alateya@edu.salford.ac.uk; a.ahangarasr@salford.ac.uk

Summary

Seepage measurement and control is one of the most significant considerations in designing and safety of earth dams. This numerical study aims to simulate the influence of cavities presence on seepage through earth dams taking into account rapid drawdown conditions. A series of two-dimensional finite element models were analysed using PLAXIS 2D software to examine the influence of various factors related to cavities which included (cavity shape and cavity position in horizontal and vertical directions). Hardening Soil and Mohr-Coulomb were adopted for modelling the behaviour of embankment and sub-soil. A single cavity in various position and depths in the subsoil of upstream and downstream slopes was considered in these simulations. The results of the analyses showed that the existence of cavities beneath the upstream side considerably increases the discharge rate through earth dam compared to their existence beneath downstream. The results of the numerical simulation also indicated that variation of the location of the cavities in the horizontal direction is more effective than the changes in position in the vertical direction, as well the cavity shape has an insignificant effect on flow rates through the dam.

Key Words: *Earth Dams; Seepage Analysis; Cavities; Finite Element; PLAXIS 2D*

1. Introduction

In recent years, computer software adopting numerical methods have been widely used for modelling different leakage conditions in dams. PLAXIS 2D is a software based on the numerical solution method (Abhyankar and Bhole, 2011). It is a powerful and easy to use finite element software designed to analyses two-dimensional problems of deformation and stability in soil and rock mechanics. The evaluation of the software began in 1987 at Delft University of Technology (Kahlstrm 2013). PLAXIS is utilized widely in different geotechnical engineering applications such as excavations, embankments and foundations, tunnelling, mining and reservoir geomechanics (Brinkgreve et al., 2018). In the present investigation, the influence of the cavity presence on seepage through the earth dam model has been examined numerically beneath rapid drawdown condition using PLAXIS 2D considering the effect of horizontal cavity position, cavity depth and the cavity shape.

2. Finite element modelling

2.1 Modelling of the earth dam and the cavity

To evaluate the combined influence of cavities presence and rapid drawdown condition on seepage through an earth dam. The soil was modelled using a fine elemental mesh with fifteen-node triangular elements plane strain. The height of the considered earth dam model was 15m from the crest to the sub-soil, a crest width of 6m, subsoil depth of 20m and the inclinations of both the upstream and downstream were 1Vertical: 2.5 Horizontal. The height of the initial water level of the reservoir was 12m from the sub-soil thereafter it was speedily reduced to the level of 4m during 5 days for simulating rapid drawdown condition. Figure 1 depicts the geometry of the earth dam model and the schematic finite element mesh. In this study, cavities were modelled using PLAXIS 2D code as idealized holes excavated away from the soil mass and assumed to have no lining. The seepage analyses were conducted

using two types of cavities; circular and irregular cavity shape models. To study the influence of the cavity location the cavities were assumed in positions which varied vertically and horizontally in the sub-soil of the upstream side of the dam.

2.2 Material modelling

The Hardening Soil constitutive model and the Mohr-Coulomb (MC) model were utilized for modelling the soil of dam body and sub-soil respectively. Mohr-Coulomb is a perfect linear elastic-plastic model. Because it is easy to understand, simple and requires fewer soil parameters specified by simple tests, it is more commonly used compared to other models (Obrzud, 2010). The input parameters encompass, unit weight of soil ($\gamma_{unsaturated} = 17kN/m^3$ and $\gamma_{saturated} = 21kN/m^3$), Poisson's ratio ($\nu' = 0.3$), cohesion ($C' = 5kN/m^2$), angle of dilatancy ($\Psi = 5^\circ$), internal angle of friction ($\Phi' = 35^\circ$), coefficients of permeability in horizontal and vertical directions (k_x and $k_y = 0.01m/day$), and the Young's modulus ($E' = 5.0E4$) (Brinkgreve et al., 2018). Hardening Soil model has more flexibilities in modelling and encompasses more input parameters in soil modelling (Keyvanipour et al., 2012). The Hardening Soil model is nonlinear elasto-plastic and its required input parameters include ($\gamma_{unsaturated} = 16kN/m^3$ and $\gamma_{saturated} = 20kN/m^3$), $\nu' = 0.3$, $C' = 25kN/m^2$, $\Psi = 1^\circ$, $\Phi' = 22.5^\circ$, and (k_x and $k_y = 10.0E - 4m/day$), soil stiffness parameters include reference modulus of primary loading in standard drained triaxial test ($E_{50}^{ref} = 25.0E3kN/m^2$), reference modulus of primary loading in drained oedometer test ($E_{ode}^{ref} = 25.0E3kN/m^2$), reference modulus of unloading /reloading in drained triaxial test ($E_{ur}^{ref} = 75.0E3kN/m^2$) (Brinkgreve et al., 2018).

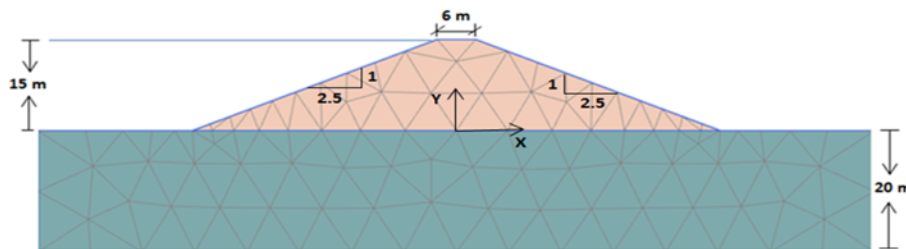


Figure 1: Earth dam model geometry and finite element mesh

3. Seepage Results and Analysis

3.1 Influence of existence and horizontal position of cavity

In order to investigate the influence of the variation of the cavity position in the horizontal direction on flow rate, eight horizontal positions of cavities were selected. These positions start from the dam centerline toward the end of the dam base and are 0, -8, -17, -20, -24, -28, -35 and -40m away from the centreline. The cavity horizontal position (X) is the horizontal distance from cavity centerline to earth dam centerline. The seepage analysis was implemented considering the existence of a single cavity model of the diameter of 60cm positioned at the depth of 1m in all considered horizontal locations. Figure 2 reveals a comparison between the effect of circular and irregular cavities on the flow rate through the earth dams. The results showed that the presence of circular cavity at location L2 (-8, -1) led to a great increase in the flow rate $459.2 \times 10^{-3} m/day$ compared to $2.58 \times 10^{-3} m/day$ for a cavity-free model. Generally, the increase in the flux rate ranged from $3.05 \times 10^{-3} m/day$ to $26.4 \times 10^{-3} m/day$ for locations L8 (-40, -1) and L1 (0, -1) respectively. It is worth mentioning that this impact decreases as the cavity position becomes closer to the end of the dam base toward the location L8 where the flow rate in this location amounted to $3.05 \times 10^{-3} m/day$ compared to $2.58 \times 10^{-3} m/day$ in the case of absence of cavities. It is seen from the results that presence of irregular cavities considerably increases the

flow rate, the flow rate increased from $3.127 \times 10^{-3} \text{m/day}$ for the model without cavities to $579.4 \times 10^{-3} \text{m/day}$ for the model with a cavity at location L2 (-8, -1). As it is clearly indicated by the results, the influence of cavities is associated with their horizontal position where the flow rate values range from $3.532 \times 10^{-3} \text{m/day}$ to $579.4 \times 10^{-3} \text{m/day}$ for models with a single cavity at locations between L8 and L2. The results also showed that the flow rate reduces as the distance between the dam centerline and the cavity centerline increase. The comparison indicated that the cavity shape has an insignificant effect on flow rates at all studied locations with the exception of location L2 (-8, -1) in which the flow rate increased by 26.17% when using an irregular cavity model compared to a circular cavity model with equivalent cross-sectional area.

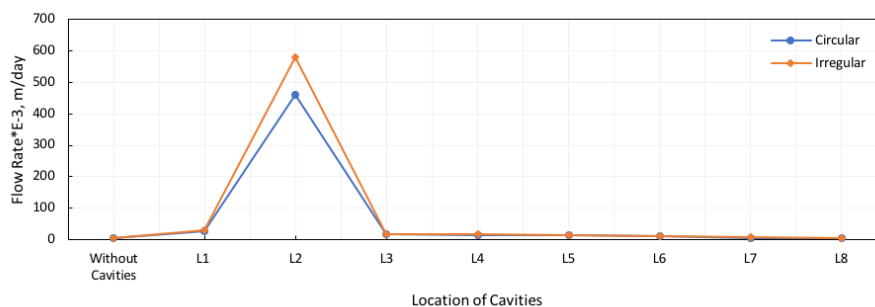


Figure 2: Comparison between the effect of presence of circular and irregularly shaped cavities in various horizontal positions and at the depth of 1m

3.2 Influence of cavity depth

To assess the influence of cavity depth on seepage through earth dams four depths for cavities were selected in the sub-soil of upstream $Y = 1\text{m}$, 2m , 3m and 4m keeping the same horizontal cavity positions as presented above. Cavity depth (Y) is the vertical distance from the dam base to cavity centreline. The results presented in Figure 3a exhibit the influence of depth of the circular cavity on the flow rate. As shown, the flow rate values increase slightly with increasing cavity depth from 1m to 4m. E.g. at locations L3 and L8 the flow rates increase from $15.47 \times 10^{-3} \text{m/day}$ to $19.13 \times 10^{-3} \text{m/day}$ and from $2.81 \times 10^{-3} \text{m/day}$ to $4.16 \times 10^{-3} \text{m/day}$ when the cavity depth changes from 1m to 4m respectively. This increase is more significant when the model contains a cavity situated at location L2, where the flow rate value increases from $459.8 \times 10^{-3} \text{m/day}$ at the depth of 1m to $721.2 \times 10^{-3} \text{m/day}$ at the depth of 2m and then reduces to $527.5 \times 10^{-3} \text{m/day}$ at the depth of 4m. Results in Figure 3b indicate the influence of depth of irregularly-shaped cavities on the flow rate. It is clear that the flow rate values increase somewhat with increasing cavity depth from 1m to 4m for all horizontal positions except positions X1(0) and X2 (-8). In X1 location there is a slight decrease in flow rates from $28.92 \times 10^{-3} \text{m/day}$ to $27.3 \times 10^{-3} \text{m/day}$ with increasing the depth, whilst the flow rate increases from $579.4 \times 10^{-3} \text{m/day}$ to $769.9 \times 10^{-3} \text{m/day}$ then reduces to $587 \times 10^{-3} \text{m/day}$ as the depth increases to 2m and then to 4m. It is clear that the horizontal cavity position is more influential on seepage rate through the earth dams compared to cavity depth.

Conclusions

Influence of cavities in terms of shape, horizontal position and depth on seepage through earth dams has been studied in the current investigation. Based on the results presented, the following key conclusions can be drawn:

- Presence of cavities in the sub-soil of an earth dam during rapid drawdown condition considerably increases the flow rates through the dam.

- Variation of cavity position horizontally significantly affects flow rates whilst relocation in the vertical direction does not seem to be as influential.
- Effect of the presence of cavities becomes less considerable on flow rate as the horizontal distance between the cavity centerline and the dam centerline increases.
- An increasing vertical distance between the centerline of the cavity and the base surface of the earth dam seems to have a smaller influence on the flow rate, even though with increasing the cavity depth, flow rate through the earth dam still increases.
- The cavity shape has an insignificant effect on flow rates through the dam.
- The horizontal cavity position (in X -direction) is the most effective factor on the seepage among all the studied factors in this research.

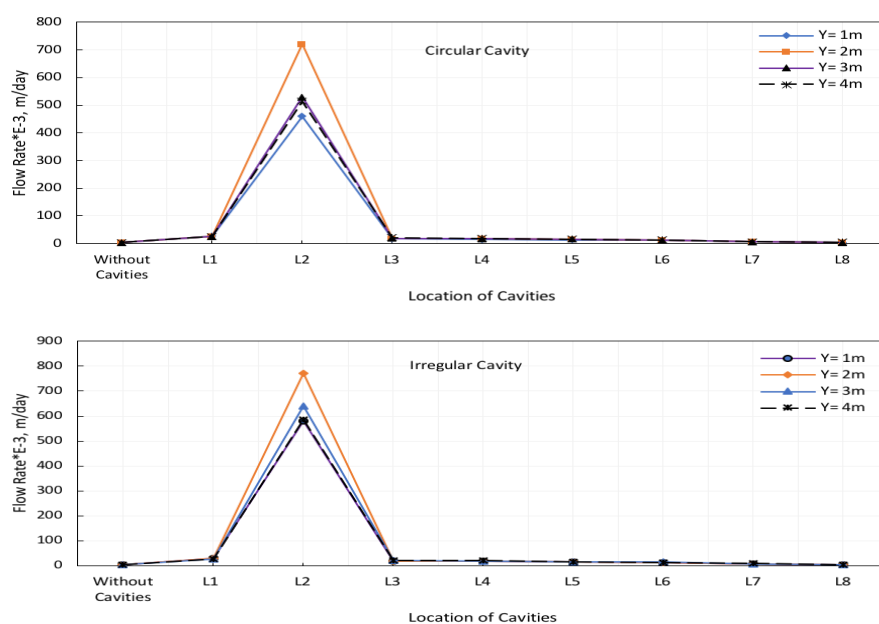


Figure 3: Flow rate vs. location of cavities for a: circular cavity model, b: irregularly-shaped cavity model at various depths

References

- 1 Abhyankar, S.P. and Bhole, S.D., 2011. Application of FEM in Civil Engineering applications. International Journal of Earth Sciences and Engineering, 4 (6) SPL, 2011, pp.748-751.
- 2 Brinkgreve, R.B.J., Kumarswamy, S.M, Swolfs, W.M. Foria, F. (2018). PLAXIS finite element code for soil and rock analysis. Delft University of Technology Plaxis bv, The Netherland.
- 3 Obrzud, R. F. (2010). On the use of the Hardening Soil Small Strain model in geotechnical practice. Numerics in Geotechnics and Structures, 15-32.
- 4 Kahlstrm M (2013). Plaxis 2D comparison of Mohr-Coulomb and soft soil material models.
- 5 Keyvanipour, M., Moharrampour, M., Faghieh, S. (2012). An Evaluation and Comparison of Bar Embankment Behavior with Instrumentation Data and Software PLAXIS. In International Conference on Environment Science and Engineering, Singapore (pp. 197-200).

AN AEROSTATIC APPROACH TO INCLUDE THE EFFECT OF ADAPTABLE WIND BARRIERS IN WIND-VEHICLE-BRIDGE INTERACTION ANALYSIS

Chrysanthi Stropouli¹, *Alfredo Camara² and Chetan Jagadeesh³

¹TOBIN Consulting Engineers, Clerkenwell, London, EC1R 0QB

²School of Mathematics, Computer Science and Engineering, City, University of London, EC1V 0HB

*alfredo.camara@city.ac.uk

Summary

Wind-driven vehicle accidents and traffic interruptions in long-span bridges represent a real problem in the UK and abroad. Recently, adaptable wind barriers that can rotate with the wind to protect the traffic and to avoid excessive forces on the deck have been proposed by the bridge aerodynamics research team at City, University of London (CUoL) [1]. This paper presents a simplified numerical approach to account for the effect of these barriers on the bridge and the traffic safety assessments. The interaction between the response of the vehicles, the vibration of the deck and the wind is captured by means of a semi-analytical model that solve the equations of motion for the deck, the vehicle and their coupling at every time step. The effect of the barriers is considered by means of aerodynamic coefficients that are obtained by means of computational fluid dynamic analysis. The methodology is applied to the Queen Elizabeth II Bridge.

Key Words: Bridge aerodynamics; traffic safety; wind barriers; wind-vehicle-bridge interaction

Wind-Vehicle-Bridge Interaction (W-VBI) model

The W-VBI analysis is a 3-stage framework that involves (1) the definition of the sources of vibration in the deck and in the vehicles, (2) the coupled solution of the differential equations of motion of the bridge and the traffic, and (3) the post-process of the wheel reactions and the accelerations in the structure and in the vehicle for the assessment of the driving safety and the comfort.

The wind speed time-histories at different points along the deck are generated from the mean wind speed and the turbulence properties. The simulation of these records follows the routines defined in [2] and results in three-directional wind velocity histories that are correlated in time and in space. The pavement irregularities are generated as the combination of harmonic signals that are correlated in the along-drive and the across-drive directions.

The second stage of the W-VBI framework involves the dynamic analysis of the deck and the vehicles crossing the bridge, which is coupled through the tyre-pavement contact forces. In addition, the wind acting on the deck and on the vehicle induces vibrations in both systems. Assuming no loss of contact of the wheels, the response of the bridge can be decomposed in different single degree of freedom systems associated with the relevant vibration modes of the structure. The governing equations of motion in the coupled structure-traffic system can be expressed in terms of the displacement of the bridge (\mathbf{q}_b) and the vehicles (\mathbf{q}_v), and in terms of their time derivatives:

$$\begin{bmatrix} \mathbf{M}_b & \mathbf{0} \\ \mathbf{0} & \mathbf{M}_v \end{bmatrix} \begin{bmatrix} \ddot{\mathbf{q}}_b \\ \ddot{\mathbf{q}}_v \end{bmatrix} + \begin{bmatrix} \mathbf{C}_b + \mathbf{C}_b^v & \mathbf{C}_{v,b} \\ \mathbf{C}_{b,v} & \mathbf{C}_v \end{bmatrix} \begin{bmatrix} \dot{\mathbf{q}}_b \\ \dot{\mathbf{q}}_v \end{bmatrix} + \begin{bmatrix} \mathbf{K}_b + \mathbf{K}_b^v & \mathbf{K}_{v,b} \\ \mathbf{K}_{b,v} & \mathbf{K}_v \end{bmatrix} \begin{bmatrix} \mathbf{q}_b \\ \mathbf{q}_v \end{bmatrix} = \begin{bmatrix} \Phi^T(\mathbf{f}_{b,r} + \mathbf{f}_{b,w}) \\ \mathbf{f}_{v,g} + \mathbf{f}_{v,r} + \mathbf{f}_{v,w} \end{bmatrix}, \quad (1)$$

where \mathbf{M}_i , \mathbf{C}_i and \mathbf{K}_i refer to the mass, damping and stiffness matrices for the bridge ($i = b$) and the vehicles ($i = v$), respectively. Note that the coupling damping and stiffness matrices ($\mathbf{C}_{v,b} = \mathbf{C}_{b,v}$

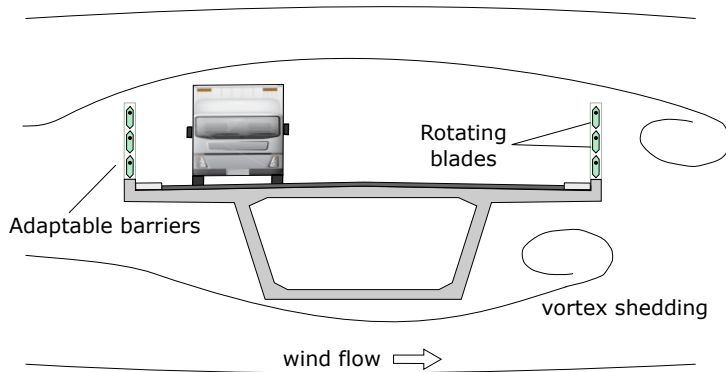
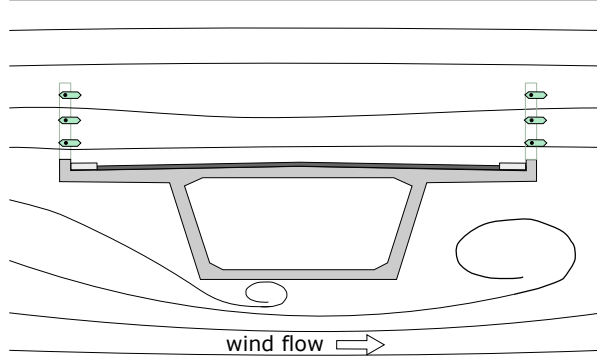
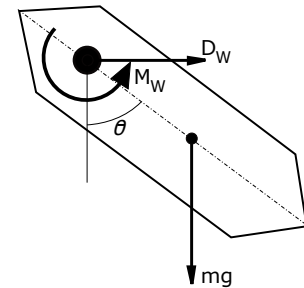
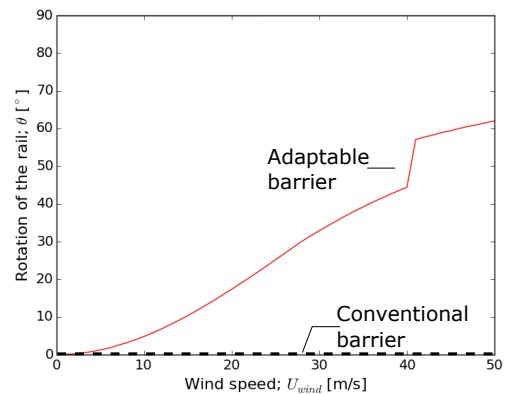
a) Adaptable barriers (moderate wind):b) Adaptable barriers (strong wind):c) Blade equilibrium:d) Blockage curves:

Figure 1: View of the adaptable wind barriers proposed in [1] under (a) moderate and (b) severe winds; (c) aero-static equilibrium in a blade; (d) rotation of a rail for different wind speeds.

and $\mathbf{K}_{v,b} = \mathbf{K}_{b,v}$, \mathbf{C}_b^v and \mathbf{K}_b^v) are time-dependent because they are influenced by the position of the vehicles on the deck [3]. The forcing vectors include the effect of the pavement irregularities ($\mathbf{f}_{b,r}$ and $\mathbf{f}_{v,r}$), the gravity force ($\mathbf{f}_{v,g}$) and the wind actions on the vehicles ($\mathbf{f}_{v,w}$) and on the bridge ($\mathbf{f}_{b,w}$). The effect of the adaptable wind barriers is introduced in $\mathbf{f}_{v,w}$ and $\mathbf{f}_{b,w}$, as it will be discussed in the following.

Adaptable wind barriers

The adaptable wind barriers proposed in [1] are composed of vertical posts connected by horizontal blades (or rails) that can rotate with the wind pressure. If the wind speed is low-moderate the barriers are in 'closed' position to protect the traffic (Fig. 1(a)). In the event of very strong winds, when traffic is not expected to cross the bridge, the blades rotate to protect the structure by reducing the wind pressure acting on the deck (Fig. 1(b)). A special blade/post connection and blade configuration have been developed at CUoL to ensure that the moment exerted by the wind on the blades is able to induce an optimum rotation θ with respect to the vertical line, as shown in Fig. 1(c). Considering a particular (and not necessarily optimum) design of the blades, Fig. 1(d) shows the results of the aerostatic equilibrium in which buffeting and aeroelastic effects have been ignored. The result illustrates that increasing the wind speed increases the rotation of the blades, reducing the drag on the deck.

Aerostatic approach to consider the adaptable wind barriers

In the W-VBI assessment it is proposed to include the effect of the adaptable barriers by means of aerodynamic coefficients for the deck and for the vehicles that depend on the mean wind speed (U)

under consideration. First, the drag, lift and (pitch) moment coefficients of the deck are obtained by means of CFD or wind tunnel testing for different values of the blade rotation angle (θ) and the angle of attack of the wind (α): $C_{d,j}(\theta, \alpha)$, with $j = D, L, M$ referring to the drag, lift and moment coefficients, respectively. The relationship of these coefficients with the wind speed is obtained through a quasi-static analysis of the rail such as the one presented in Fig. 1(d): $C_{d,j}(U, \alpha)$. This approach ignores local aeroelastic and buffeting effects of the wind in the barriers. The mean wind forces in the deck are then obtained as follows:

$$f_{d,w-s}^D = \frac{1}{2}\rho U^2 D C_{d,D}(U, \alpha), \quad f_{d,w-s}^L = -\frac{1}{2}\rho U^2 B C_{d,L}(U, \alpha), \quad f_{b,w-s}^M = \frac{1}{2}\rho U^2 B^2 C_{d,M}(U, \alpha), \quad (2)$$

where D is the depth and B is the width of the deck; ρ is the density of the air.

The aerodynamic coefficients in the vehicles can be obtained analogously at different lanes. The vehicle coefficients depend not only on the mean wind speed through the adaptable barriers but also on the position of the vehicle on the deck and on the instantaneous angle of incidence of the wind on the vehicles (ψ): $C_{v,j}(U, \psi)$, with $j = S, D, L, P, R, Y$ referring to the side, drag and lift forces on the vehicle, and to the pitch, roll and yawing moments in the vehicle, respectively:

$$f_{v,w}^{j1} = \frac{1}{2}\rho V_r^2 C_{v,j1}(U, \psi) A_v, \quad f_{v,w}^{j2} = \frac{1}{2}\rho V_r^2 C_{v,j2}(U, \psi) A_v h_v, \quad (3)$$

in which $j1 = S, D, L$ and $j2 = P, R, Y$; A_v and h_v are the front area of the vehicle and the distance between its centroid and the wheel-pavement contact. The resultant wind velocity acting on the vehicle (V_r) is a function of the instantaneous along-flow and along-drive wind speeds [2].

Application to the QEII Bridge

The above methodology was applied to the study of the QEII Bridge, a cable-stayed bridge located in Dartford. Fig. 2 shows the contours of kinematic energy at a certain instant of the CFD analysis conducted in ANSYS Fluent [4] for an angle of attack of the wind of $\alpha = 0^\circ$. The wind goes from left to right in this figure. The results also include the drag coefficient in the deck and the side coefficient in a typical heavy good vehicle ($A_v = 2.3 \times 2.3 \text{ m}^2$) that is centered in the windward lane. It is observed that when the barriers are closed ($\theta = 0^\circ$), for low wind speeds below $U = 5 \text{ m/s}$, the vorticity is concentrated at the top of the windward barrier and the vehicles are protected from wind actions by means of a 'bubble' of low wind pressures across the deck width (Fig. 2(a)). For wind speeds of up to $U \approx 25 \text{ m/s}$ the barriers considered for this bridge rotate up to $\theta = 30^\circ$, as shown in Fig. 1(d). In this case the bubble suppresses significantly the turbulence and the wind pressure across the road lanes (Fig. 2(b)). However, increasing the wind speed to $U \approx 40 \text{ m/s}$ results in $\theta = 60^\circ$ and the effective porosity of the barrier favours the fluid reattachment on top of the slab of the deck, which increases the wind pressure on the vehicles (Fig. 2(c)). In this situation traffic would not be allowed to cross the bridge but a vehicle is included in the analysis for illustration purposes. Fig. 2 presents the wind contour of wind pressures at the same instant of the CFD analysis.

In the CFD analysis the drag coefficient in the deck of the QEII Bridge was normalised as:

$$C_{d,D} = \frac{2f_{d,w-s}^D}{\rho U^2 D} \quad (4)$$

with $D = 2.24 \text{ m}$ is the depth of the deck without barriers; $\rho = 1.225 \text{ kg/m}^3$. The side coefficient of the vehicle was obtained ignoring its driving speed as:

$$C_{v,S} = \frac{2f_{v,w}^S}{\rho U^2 A_v} \quad (5)$$

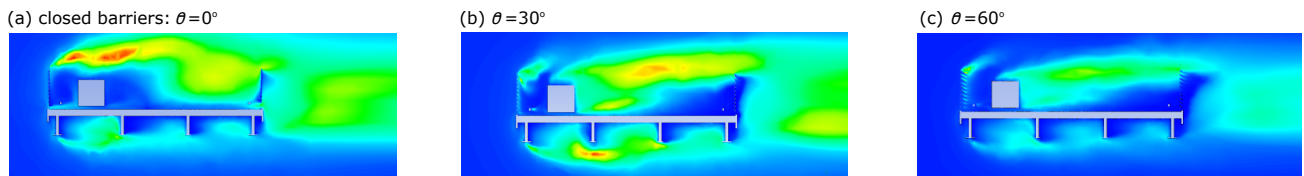


Figure 2: Kinematic energy field around the QEII Bridge deck with adaptable barriers with different inclination: θ .

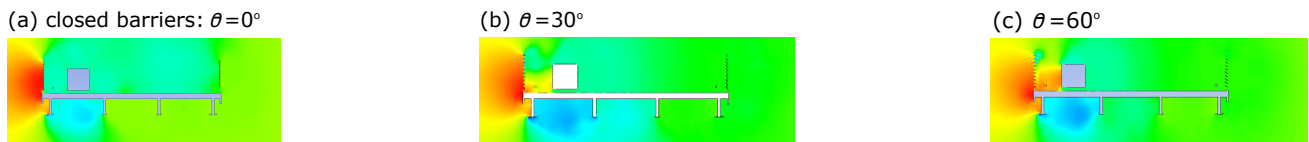


Figure 3: Pressure field around the QEII Bridge deck with adaptable barriers.

and it was calculated with and without barriers to observe their influence. The results indicated that the side coefficient of the vehicle when the deck has adaptable barriers, compared with the results obtained without them, is reduced by a factor of 37.8, 1.8 and 1.17 when the wind speed is $U \approx 5$, 25 and 40 m/s, respectively. This indicates that the barriers can efficiently protect the driving safety with angles of inclination below 60° .

Conclusions

This paper presents a simplified approach to include in the wind-vehicle-bridge interaction (W-VBI) problem the effect of adaptable barriers that can rotate with the wind. The method ignores the buffeting and the aeroelastic effects in the consideration of the local response of the blades of the barriers but they can be accounted for in the global 3D response of the coupled bridge/traffic system.

The results of a CFD analysis in the QEII Bridge are presented. It is observed that by increasing the wind speed the barriers rotate, decreasing the pressure on the deck and increasing the wind forces on the vehicles. Nevertheless, wind speeds below 40 m/s result in wind side forces on the vehicles that are smaller than those without barriers. More research on the lift and the moment coefficients of the deck and the vehicles for different angles of inclination of the barrier blades is being conducted.

References

- [1] A. Camara, "Smart wind barriers for traffic and bridge protection," tech. rep., City, University of London, Report for the Department for Transport (T-TRIG), 2018.
- [2] I. Kavrakov, A. Camara, and G. Morgenthal, "Influence of aerodynamic model assumptions on the wind-vehicle-bridge interaction," in *IABSE Symposium*, (Stockholm), 2016.
- [3] Y. Han, C. Cai, J. Zhang, S. Chen, and X. He, "Effects of aerodynamic parameters on the dynamic responses of road vehicles and bridges under crosswinds," *Journal of Wind Engineering and Industrial Aerodynamics*, vol. 134, pp. 78–95, 2014.
- [4] ANSYS, "Ansys fluent, version 19.2," 2019.

